

N° d'ordre: 41594



Thèse

Développement de renfort 3D multiaxial tissé pour les structures de composite

Technologie, modélisation et optimisation

Development of 3D multiaxis woven preforms for composite structures
Technology, modelling and optimisation

présentée par :

Ahmad Rashed LABANIEH

Pour obtenir le grade de Docteur de l'université de Lille 1

Discipline : Mécanique

Soutenue le 4 décembre 2014 devant la commission d'examen

Jury :

Lamine BOUBAKAR	Professeur à l'université de Franche-Comté, Président du jury
Laurence SCHACHER	Professeur à l'ENSISA, Rapporteur
Gilles HIVET	Professeur à l'université d'Orléans, Rapporteur
Sébastien COMAS	Professeur à l'école Centrale Nantes, Examineur
Damien SOULAT	Professeur à l'ENSAIT, Examineur
Vladan KONCAR	Professeur à l'ENSAIT, Directeur
Xavier LEGRAND	Maitre de Conférences à l'ENSAIT, Co-encadrant

Acknowledgements

First and foremost, praises and thanks to the God, most Merciful and perfect in knowledge, for His showers of blessings throughout my live.

I would like to thank sincerely my research supervisors, Prof. Vladan KONCAR, head of Research at ENSAIT, and Dr. Xavier LEGRAND for giving me the great honour to work my doctoral thesis under their supervision, for many fruitful discussions, ideas and their invaluable guidance and help during this research. I thank them also for their friendship and unconditional support. It has been a great privilege for me to work under their supervision.

I would also like to express my deepest gratitude and appreciation to Prof. Damien SOULAT for guidance, knowledge and advices. I benefit a lot not only from his intuition and readiness for discussing problems, but also his way of approaching problems in a structured way had a great influence on me.

My sincere thanks are due to the MTC research group members for their assistance. I also thank my friends and colleagues at ENSAIT including Eng. Boris DUCHAMP for his kindness and support.

I cannot forget friends who went through hard times together, cheered me on, and celebrated each accomplishment.

I would express a deep sense of gratitude to my father and mother who always put me and my sister and brother first. Thank you for your endless love and unconditional support. Thank you for inspiring me to walk in the research world. Thank you for teaching me to think freely and to be merciful in a society forgot these values. I am honoured to have you as my parents and I dedicated this work to you. I also thank my sister and brother for support and encouragement.

I would like to acknowledge all the teachers I learnt from since my childhood.

I also acknowledge the financial support by university of Aleppo – Mechanical department.

Table of Contents

1. General introduction	1
1.1. Problem statement.....	1
1.2. Thesis overview	2
2. State of the art.....	4
2.1. Introduction.....	4
2.2. Laminate fiber reinforced composites	7
2.3. Woven fiber reinforced composites.....	10
2.3.1. 2D woven fabric.....	10
2.3.2. Multilayered (or 3D woven) fabric	10
2.4. Stitched composites	14
2.5. Knitted composites.....	15
2.5.1. Non Crimp Fabrics	16
2.6. Braided composites	17
2.7. Z pinned composites	18
2.8. Conclusion	18
3. 3D multiaxis weaving technology.....	20
3.1. Introduction.....	20
3.2. Definition of multiaxis woven fabric	20
3.3. multiaxis weaving technology	20
3.3.1. 2D weaving process.....	21
3.3.2. 3D weaving process.....	22
3.3.3. Multiaxis weaving process	23
3.4. Developed multiaxis multilayer weaving loom	34
3.4.1. Warp yarns feeding	34
3.4.2. Bias yarns feeding.....	35
3.4.3. Bias yarns positioning mechanism	36
3.4.4. Binder yarns insertion	37
3.4.5. Filler yarns insertion	40
3.4.6. Beating up.....	43
3.4.7. Fabric control width and take up system.....	44
3.5. Weaving process.....	46
3.6. Manufactured prefomes	49
3.7. Geometrical characterization.....	49
3.7.1. Parameters of the 3D multiaxis woven preform.....	50

3.7.2. Experimental techniques.....	52
3.7.3. Results and Observations	58
3.8. Classification of the developed loom	67
3.9. Conclusion	69
4. Geometrical modelling of 3D multiaxis woven composite	71
4.1. Introduction.....	71
4.2. Modelling scales for woven composite	71
4.3. Literature survey about the meso-scale geometrical models of woven preform	73
4.3.1. Geometrical modelling type	75
4.3.2. The path and the cross section shapes of the yarn:	75
4.3.3. Geometrical models for 2D woven fabric	76
4.3.4. Geometrical models for 3D woven fabric	77
4.3.5. Textile Geometry Preprocessor.....	81
4.4. Road map.....	85
4.5. Predictive Geometrical Model.....	86
4.5.1. Hypothesis of the Model	87
4.5.2. Development of the Model	90
4.5.3. Results	95
4.6. Validation of the predictive geometrical model	100
4.7. Geometrical model.....	102
4.7.1. Hypothesis and method	102
4.7.2. Development of the model	106
4.7.3. Construction of the RVE	110
4.7.4. Results	111
4.8. Conclusion	113
5. Evaluation the elastic properties of 3D multiaxis woven composite.....	117
5.1. Introduction.....	117
5.2. Theory.....	117
5.2.1. Stress – strain relationship for composite materials	117
5.2.2. Coordinate transformation	119
5.2.3. Homogenisation concept	120
5.2.4. Micromechanics technique	120
5.2.5. Mechanic modelling of woven composite at mesoscale	122
5.2.6. Classical laminate theory.....	122
5.2.7. Interlaminar stresses	124

5.3. Methods	126
5.3.1. Evaluation of elastic modulus of developed 3D mutiaxial woven composite	126
5.3.2. Evaluation of elastic modulus of equivalent orthogonal woven composite.....	132
5.3.3. Evaluation of elastic modulus of equivalent laminate composite	133
5.3.4. Evaluation of in-plane off-axis properties.....	134
5.3.5. Evaluation of interlaminar stresses.....	135
5.4. Results	136
5.4.1. Elastic modulus.....	136
5.4.2. In-plane off-axis properties	140
5.4.3. Interlaminar stresses	141
5.5. Conclusion	143
6. General conclusion	145
6.1. Conclusion	145
6.2. Perspective	148
Reference	149
Appendix A	160
Sample-1.....	160
Sample-2	162
Sample-3.....	164
Sample-4.....	166
Sample-5.....	168
Sample-5C.....	170
Publication.....	173

List of figures

Figure 2.1: Three forms of the reinforcement; a) particle, b) flake, c) fibre (long fibre). (Kaw, 2006).....	4
Figure 2.2: Textile fiber- reinforcements, (Ko and Du 1998).	5
Figure 2.3: Classification of the fiber-reinforced composites in terms of the alignment plans of the constitutive fibers (Ko and Du 1998).....	6
Figure 2.4: Classification of the fiber-reinforced composites in terms of the orientation of the constitutive fibers (Fukuta et al. 1998).....	6
Figure 2.5: Laminate made by stacking laminas in different orientation (Robert 1999).....	7
Figure 2.6: Lamina fiber reinforced composite: on left lamina with unidirectional fiber, on right lamina with 2D woven fabric (Robert 1999).	7
Figure 2.7: Specific strength in function of specific modulus of fibre, lamina, laminate and metals, (Kaw, 2006).	9
Figure 2.8: Comparison of the in-plane tensile modulus, tensile strength and compressive strength to that in the through thickness properties for laminate composite materials, (Tong, 2002).	9
Figure 2.9: Degradation of the in-plane tensile and compressive strength after impact normalized to the strength before impact in function of the impact energy, (Tong, 2002, and the tensile and compressive data are brought from Dorey 1989, and Caprino 1984 respectively).....	10
Figure 2.10: Schematic representing conventional 2D weaving loom.	11
Figure 2.11: Typical 3D woven architectures; a) layer-to-layer angle interlock, b) through-thickness angle interlock, c) orthogonal.	11
Figure 2.12: Schematic representing 3D orthogonal weaving process with multiple filler insertion.....	12
Figure 2.13: Cumulative probability distribution of young's modulus (a) and tensile strength (b) of warp yarns at different weaving stages, (Rudov-Clark et al. 2003).....	13
Figure 2.14: Stitched composite; stacked 2D laminas sewed with modified lock stitch, (Tong et al. 2002).....	14
Figure 2.15: Schematics for the damages to laminates caused by stitching; a) crimping of the in-plane yarns, b) misalignment of in-plane yarns around stitch and formation of resin pocket, c) distortion of stitch due to heave compaction while curing, d) formation of resin pocket between the two strands of stitch heavily stretched. x1, x2 in-plane laminate direction and x3 through thickness direction, (Mouritz and Cox 2000).	15
Figure 2.16: schematic of a) weft knitted fabric, b) warp knitted fabric, (Ogin, 2000).	16
Figure 2.17: Principle of the warp-knit non-crimp fabric technology de developed by LEBA. (Kamiya et al., 2000).....	17
Figure 2.18: Schematic of the Z-pinning process of laminate composite, (Chang et al. 2008).....	19

Figure 2.19: Micrographs of laminate reinforced by pins illustrate caused microstructure damages; a) shows waviness of in-planes yarns around pins and the formation of resin rich region, b) shows crimp of in-plane yarns near pins, (Mouritz, 2007).....	19
Figure 3.1: Schematic of the multiaxis multilayer (3D) woven perform.....	21
Figure 3.2: Schematics of the conventional 2D weaving loom.....	22
Figure 3.3: Schematic representing formation of the shed on the 2D weaving loom.....	22
Figure 3.4: Schematic of the modified lappet multiaxis weaving by Ruzand and Guenet (1994) with produced architecture.	24
Figure 3.5: Multiaxis four layers woven fabric (a), one case of distribution the bias yarns by jacquard mechanism into upper movable reed and lower fixed reed (b), (Mood, 1996).....	24
Figure 3.6: Multiaxis four layers woven fabric (a) and the developed loom by Bryn (2004)(b) which is able to produce fabric in various cross section shape (c).	25
Figure 3.7: Multiaxis weaving machine developed by Nayfeh (2006).	25
Figure 3.8: a) scheme of multiaxis weaving machine developed by Lima et al. (2009), b) architecture of produced multiaxis 2D woven fabric.....	26
Figure 3.9: Scheme of lappet multiaxis weaving apparatus developed by Farley (1993). 1- filler yarns, 2- bias yarns, 3- needle's eye, 4- needles, 5- warp yarns.	26
Figure 3.10: a) Schematic of developed multiaxis multilayer weaving loom by Anahara et al. (1991) using screw shaft and rapier needle, b) produced architecture, c) path of a pair bias yarns layers during weaving process by screw shafts.....	27
Figure 3.11: Scheme of multiaxis weaving machine developed by Yasui et al. (1993) using guide blocks (b) to control the position of bias yarns with circularly moving for feeding mechanism.....	28
Figure 3.12: Scheme of multiaxis 3D weaving machine developed by Uchida et al. (1999) using guide blocks to control the position of bias yarns.	28
Figure 3.13: Tube rapier weaving method; a) scheme of developed multiaxis 3D weaving machine, b) representation of transversal movement of each assembly of tube rapier for one bias yarns layer, c) a unit cell of produced fabric illustrating of zig-zag path of bias yarns across fabric width, (Bilisik 1994, 2010).....	29
Figure 3.14: Tube carrier weaving method; a) scheme of developed multiaxis 3D weaving machine, b) representation of circular moving of each assembly of tube carrier for one bias yarns layer, c) a unit cell of produced fabric illustrating of edge to edge path of bias yarns across fabric width, (Bilisik 1995, 2010).....	30
Figure 3.15: Weaving zone on a developed multiaxis 3D weaving machine by Bilisik (1995, 2010) using tube carrier weaving method.....	30
Figure 3.16: a) Polar multiaxis weaving machine developed by Yasui et al. (1992), b) architecture of fabricated woven preform.	31

Figure 3.17: Cylindrical multiaxis 3D woven preform architecture (a), preform and weaving zone on polar loom (b), polar multiaxis 3D weaving loom, (Bilisik 2000, 2012).....	31
Figure 3.18: Schematic of the bias yarns path pattern: a) zig-zag pattern, b) edge to edge pattern, (Bilisik 2010).	32
Figure 3.19: Two patterns of bias yarns path, a) bias yarn is folded to next opposite bias layer, b) bias yarn is folded and kept on same layer.....	32
Figure 3.20: Isometric view of developed prototype of multiaxis weaving loom.	35
Figure 3.21: Bobbin holder on braider bobbin carrier used to supply warp and bias yarns (a) cut view along with the main carrier axis (b).	36
Figure 3.22: Bias yarns feeding mechanism.....	37
Figure 3.23: Bias yarns positioning mechanism.....	38
Figure 3.24: Three steps to displace guide blocks of bias yarns one step for a weaving cycle.....	38
Figure 3.25: arrangement of warp and bias yarns in the weaving zone by guide bar and guide blocks.....	39
Figure 3.26: Binder insertion mechanism in its two positions.....	39
Figure 3.27: Top view of weaving zone before and after transversal movement of bias yarns with illustration available gap created by crossing $+\theta$ and $-\theta$ bias yarns to insert binder needle.	40
Figure 3.28: Broken glass fiber when it was used as binder yarn.....	40
Figure 3.29: Isometric view of weaving zone.....	41
Figure 3.30: Top view of weaving zone illustrating the 5 steps of insertion the filler yarn.....	42
Figure 3.31: Side view of weaving zone illustrating the three created sheds.	43
Figure 3.32: Beating-up mechanism with illustration of the four movements of reed.....	44
Figure 3.33: Scheme of weaving zone on standard 2D weaving loom (a), multiaxis weaving loom (b).....	45
Figure 3.34: Scheme of multiaxis woven fabric illustrating shrinkage force resulting from tensioning forces applied on folded bias yarn.	45
Figure 3.35: Linear take-up mechanism with engaging hooks.	46
Figure 3.36: Diagram of weaving operations order for one weaving cycle on prototype multiaxis loom.	48
Figure 3.37: Representation of a unit cell of multiaxis 3D woven preform. (a) top view for the analyzed structure. (b) top view for the unit cell, (c) front view for the unit cell, (d) side view for the unit cell.....	51
Figure 3.38: a top cut view of the unit cell at the middle of bias yarn.	52
Figure 3.39: Illustration for the inclination of the binder tow in the throw thickness direction in a unit cell of the 3D multiaxis woven architecture. a) α is less than 90° . b) α is equal to 90°	52

Figure 3.40: Specified cut planes on which micrographs are captured for the multiaxis 3D woven samples. In this schema of the multiaxis woven preform only the bias and binder yarns are presented whereas warp and filler yarns are masked.	53
Figure 3.41: Micrographs of cross sections of sample-5, at cut plane “warp-b”, illustrates the different zones on the perimeter of the yarns cross section.	55
Figure 3.42: Micrograph of cross sections of sample-5 at cut plane “filler-a”, illustrates the two zones on the path of yarns.	55
Figure 3.43: Micrographs of cross sections of sample-5 at cut plane “warp-b” illustrates the undulation of warps yarns. Green line for the centre line of warp yarn, red outline for filler yarn and yellow outline for biases yarns.	56
Figure 3.44: Binarized black and white picture of the micrograph of yarn cross section used to measure the filament packing factor within the yarn (Lapeyronnie et al., 2011).	57
Figure 3.45: Micrograph of cross sections of sample-1 at cut plane filler-b, illustrates the measured yarns parameters and measured unit cell parameter.	58
Figure 3.46: Micrographs for the samples cross sections, a) for sample-3 at filler-b cut plane, b) for sample-1 at filler-b cut plane, c) for sample-3 at warp-b cut plane, d) for sample-1 at warp-b cut plane. Both samples 1,3 have the same manufacturing parameters but sample-3 have doubled unit cell dimensions resulting in higher yarn spacing.	61
Figure 3.47: Micrographs of cross sections of sample-2; at cut plane “warp-a” illustrates the two parts of binder yarn path (black line) and its inclination angle (α) to mid-plane (a). At cut plane “filler-a” illustrates the shape of binder yarn cross section on fabric outer surfaces (b).	62
Figure 3.48: Variation of the (j_2/j_1) ratio in function of the ratio of the bias yarn gap to that of filler-inner yarn (T_o/T_{fi}).	63
Figure 3.49: Micrographs of cross sections of sample-1 illustrates the variation of filler yarns cross sections, a) at cut plane warp-a, b) at cut plane warp-b.	64
Figure 3.50: Difference in area (a, b) and in AR (c, d) for the filler yarns cross sections in reference to the area and AR of “filler-I1” section on the two cut plane “warp-a” (a, c) and “warp-b” (b, d).	65
Figure 3.51: Difference in packing factor mean value for the filler-outer free “f-OF” and the filler-outer under binder “f-OZ” relative to the filler-inner “f-I”.	67
Figure 4.1: a) Opened-packing weave. b) closed-packing weave. (Hu, 2004 and Lin et al. 2012).	72
Figure 4.2: Hierarchy structure of textile reinforcement leads to three classified scales when study: a) macro-scale, b) meso-scale, c) micro-scale. (Boisse et al. 2010).	73
Figure 4.3: Durville’s model of 2D plain weave fabric, multi-scale (micro-meso) geometric model. (Durville 2005 and 2008)	74

Figure 4.4: Representative schema of the 2D plain weave fabric with illustration of the yarn centerline and its cross section.....	75
Figure 4.5: Micrographs for different fabrics with different yarn types and different architectures illustrates the yarns cross sections shape. a) plain weave, twisted yarns, circular cross section. b) plain weave, untwisted yarns, lenticular cross section. c) elliptical cross section. d) 3D fabric, angle interlock. e) 3D fabric, orthogonal. (Lin et al. 2012).	76
Figure 4.6: Peirce’s model for 2D plain weave fabric, circular cross section shape assumption. (Hu 2004)	77
Figure 4.7: Peirce’s model for 2D plain weave fabric, elliptical cross section shape assumption. (Hu 2004)	77
Figure 4.8: Kemp’s model for 2D weave fabric, racetrack cross section shape assumption. (Hu 2004)	77
Figure 4.9: Hearle and Shanahan’s model for 2D weave fabric, lenticular cross section shape assumption. (Hu 2004).....	77
Figure 4.10: Quinn’s model for 3D woven preform, idealized predictive geometric model. (Quinn et al. 2003).	78
Figure 4.11: Quinn’s optimized model for 3D orthogonal woven preform. (Quinn et al. 2003).....	78
Figure 4.12: Wu’s model for 3D orthogonal woven reinforced composite, a) plan view, b) side view. (Wu et al. 2002).....	79
Figure 4.13: Rao’s model for 3D orthogonal woven reinforced composite with two configurations for z-yarn, a) crowned configuration, b) uncrowned configuration. (Rao et al. 2009).....	80
Figure 4.14: Tan’s geometric laminate block model for 3D orthogonal woven reinforced composite with illustration of the rectangular cross section shape consideration. (Tan et al. 2000).	81
Figure 4.15: Nehme et al. ’s model for two angle interlock, a) a transverse micrograph of the composite and flatten ellipse shape consideration, b) constructed RVE. (Nehme et al. 2011)	81
Figure 4.16: Lapeyronnie et al. ’s model for layer to layer angle interlock, adaptation of the yarn cross section shape to lenticulare with keeping constant area. (Lapeyronnie et al. 2011)	81
Figure 4.17: Crimp intervals consideration in geometric modeling in WiseTex. (Lomov et al. 2008).....	82
Figure 4.18: Yarns interpenetration on the overlap zone in WiseTex software, left Figure, and the correction realized by M. Zako approach, the right Figure. (Lomov et al. 2008).....	83
Figure 4.19: a) fitting the yarns cross section to ellipse shape, b) spline with control point representing the yarn centerline in Texgen modeling, c) knot on the circumference of the yarn cross section. (Lin et al. 2012)	83

Figure 4.20: Hivet’s model, a) micrograph of 2D woven fabric with illustration of the cross section contact zones, b) general shape of cross section composed of 4 curves, c) simplification of shape to straight lateral and to 2 curves for low cohesion yarn. (Hivet and Boisse 2005)	84
Figure 4.21: Micrograph of 2D woven fabric with illustration of the contact zones of the yarn path. (Hivet and Boisse 2005)	85
Figure 4.22: Geometrical modelling road map.	86
Figure 4.23: Definition of the thickness of the RVE. (a) Crowned configuration. (b) Uncrowned configuration.	87
Figure 4.24: Flow chart for the optimization method dedicated to predict the cross section dimensions of constituent yarns.	91
Figure 4.25: Waviness of the through thickness part of the binder yarn for impregnated and cured multiaxis woven sample under 2bar, (McIlhagger et al. 2007).	92
Figure 4.26: Variation of the FVF of dry preform predicted by optimized predictive model with two configurations of binder yarns versus assumed value of packing factor.	97
Figure 4.27: Difference in the fiber volume fraction value computed in the uncrowned configuration to that computed in the crowned configuration in function of the total number of layer in preform and of the total thickness of preform in the uncrown configuration, (Labanieh et al. 2013).....	98
Figure 4.28: Assumptions concerning the cross section shape and path of the binder yarn.....	105
Figure 4.29: Assumptions concerning the cross section shape and path of the filler yarn at outer preform surfaces.	105
Figure 4.30: Front view of the RVE at filler-a cut plane illustrates the undulation of the filler yarn and the contact zone with warp yarn.	106
Figure 4.31: Assumptions concerning the cross section shape and path of the warp yarn near to extreme preform surfaces.	106
Figure 4.32: Computation approach in the geometric model to calculate yarns and unit cell parameters.....	107
Figure 4.33: Transversal cut view for the RVE of sample-5 parallel to mid-plane, illustrating the path of the bias yarns and its position relative to binder and filler yarns.	108
Figure 4.34: Computation approach to calculate filler_ under Z (1, 2) cross sections dimensions and binder path parameters.....	109
Figure 4.35: Path of the binder yarn and the sections of filler yarns at different position relative to binder yarn.....	109
Figure 4.36: Three possible cases for the filler-under Z cross section.....	110
Figure 4.37: Isometric view of the constructed RVE of sample-5.a) construction of the matrix as a first step, b) formation the yarns inside the matrix.	111

Figure 4.38: Isometric view of a representative volume of the preform illustrates the alternative movement and position of the binder yarns. 112

Figure 4.39: Comparison of the constructed RVE for sample-5 at four cut planes to the corresponding section of the real composite 115

Figure 4.40: Comparison of the constructed RVE for sample-5C at four cut planes to the corresponding section of the real composite. 116

Figure 5.1: the origin of interlaminar stresses (σ_{yz}, σ_{zz}) in cross-ply laminate (Mallick 2007). 125

Figure 5.2: the 3D stresses distribution along with the “y” axis at the mid-plane interface of laminate subjected to uniaxial extension in “x” direction, (Pagano and Pipes, 1971). 125

Figure 5.3: 3D volume solid model of RVE of: 3D multiaxis woven composite (a), multiaxis architecture-2 (b), equivalent 3D orthogonal woven composite (c). 127

Figure 5.4: Local coordinate system ($1^{\wedge}, 2^{\wedge}, 3^{\wedge}$) of the binder yarn elements and global coordinate system (1, 2, 3). 129

Figure 5.5: Partitioning the upper bias yarn face. 130

Figure 5.6: Illustration of transformation angle (α). 134

Figure 5.7: Displacement fields in the FE model of 3D multiaxis woven composite under the six BC cases. 138

Figure 5.8: Tensile elastic modulus of 3D multiaxis woven composite (noted: M), of 3D multiaxis-Inv woven composite (noted: M_Inv) and 3D orthogonal woven composite (noted: O) using both FE method and CLT. 139

Figure 5.9: Shear elastic modulus of 3D multiaxis woven composite (noted: M), of 3D multiaxis-Inv woven composite (noted: M_Inv) and 3D orthogonal woven composite (noted: O) using both FE method and CLT. 139

Figure 5.10: Poisson’s coefficients of 3D multiaxis woven composite (noted: M), of 3D multiaxis-Inv woven composite (noted: M_Inv) and 3D orthogonal woven composite (noted: O) using both FE method and CLT. 139

Figure 5.11: Polar representation for variation of the E_x and G_{xy} modulus of equivalent laminate to multiaxis architecture (a) and equivalent laminate to orthogonal architecture orthogonal (b) in function of angle between extension axis and warp yarns axis. 141

Figure 5.12: Comparison between equivalent laminate to multiaxis architecture and equivalent laminate to orthogonal architecture orthogonal relative to the variation of the tensile modulus E_x (a) and shear modulus G_{xy} (b) in function of angle between extension axis 141

Figure 5.13: Evaluation of caused interlaminar stresses on FE model of multiaxis woven composite along with path-2 after applying uniaxial extension $\varepsilon_1 = 1 \times 10^{-3}$ 142

Figure 5.14: Evaluation of caused interlaminar stresses on FE model of multiaxis-Inv woven composite along with path-2 after applying uniaxial extension $\epsilon_1 = 1 \times 10^{-3}$ 143

Figure 5.15: Evaluation of caused interlaminar stresses on FE model of orthogonal woven composite along with path-2 after applying uniaxial extension $\epsilon_1 = 1 \times 10^{-3}$ 143

List of tables

Table 3.1: Classification the multiaxis weaving technologies introduced in the literature;.....	33
Table 3.2: Manufacturing and weaving parameters of five produced samples* .	49
Tableau 3.3: Definition of the manufacturing and weaving parameters.	50
Table 3.4: Fiber Volume Fraction percentage of the dry preforms and VARTM impregnated sample.	58
Table 3.5: Crimp percentage [%] of warp yarns in the five samples.....	60
Table 3.6: Yarns gap mean values for the in-plane yarns.	61
Table 3.7: Angle of binder yarns to mid-plane and the ratio of the two parts width	62
Table 3.8: Coefficient variation of the area and the AR of bias, warp and filler yarns measured at each cut plane.	65
Table 3.9: Coefficient variation of the area and the AR of bias and warp yarns across the four cut planes.	66
Table 3.10: Mean values of the computed packing factor.	66
Table 3.11: Comparison developed 3D multiaxis weaving loom prototype and the impregnated sample-5C to the two 3D multiaxis weaving looms of Bilisik (2010) and the produced composite by these looms.	68
Table 4.1: Comparison the predicted fiber volume fraction (FVF) and preform thickness (H) by Buchanan’s model (2010-b) to the measured values with two considerations for the packing factor (Pf) value.	89
Table 4.2: Investigation of interpenetration between yarns in case of computation of the yarns cross section dimensions by Buchanan’s model by verifying the geometric conditions of multiaxis structure expressed by equations (4.2 and 4.6).....	89
Table 4.3: The considered cross section shapes.	92
Table 4.4: fiber volume fraction and thickness of the dry preform and composite predicted by optimized predictive model with two configurations for filaments arrangement (Pf=0.7854) and (Pf=0.9069) also two configurations for binder yarn (crowned and uncrowned). The predicted values are compared to measured one.	96
Table 4.5: The dimensions of the yarns cross section for the five manufactured dry preform, computed by the optimized predictive model.	99
Table 4.6: Comparison of the component yarns parameters computed by geometric model for impregnated sample-5C with rectangular cross section shape consideration to the measured values.....	100
Table 4.7: FVF of the different sample computed by geometric model with variant cross section consideration for in-plane yarns and compared to measured value.	104
Table 4.8: Optimized value of the yarns packing factor leading to obtain FVF of geometric model equal to measured value.	112
Table 4.9: Geometric parameters of the constructed RVE for sample 5.	114
Table 5.1: Elastic modulus of used materials.....	128
Table 5.2: Six boundary condition cases	130
Table 5.3: The applied displacement on each boundary surfaces for each boundary condition cases	131
Table 5.4: Number of elements and nodes for FE models.....	132

Table 5.5: Geometric parameters and geometric properties of the RVEs of 3D orthogonal woven composite and 3D multiaxis woven composite..... 133

Table 5.6: Elastic modulus of multiaxis, multiaxis-Inv and orthogonal architectures of woven composite computed by FE method and that of equivalent laminates computed by CLT. The modulus values are expressed in GPa. 137

Table 5.7: Difference in the elastic modulus of multiaxis relative to the orthogonal obtained by two methods FE and CLT..... 140

Table 5.8: Maximum interlaminar stresses values and its location along path-1 and path-2 for the three structures. 142

1. General introduction

1.1. Problem statement

Laminated composite materials have been used widely for structural applications because of their high specific stiffness and strength, high-specific energy absorption, and excellent fatigue performance. These structures are constituted by laying up different laminas (unidirectional ply or 2D woven ply) in different orientations. However, the incapability to have fibre reinforcement in the through the thickness direction of the laminate by this technology, to combine the constitutive laminas, results in poor damage tolerance, poor impact resistance and poor delamination resistance comparing to the 3D composites, which can cause disastrous failures. Otherwise, the 3D composites exhibit high impact damage resistance and low velocity impact protection. Consequently, a lot of works have concerned the potential of mechanical characteristics of the 3D preforms that explains the growing interest of industrials. Different textile technologies are used to produce 3D preforms such as weaving, knitting, braiding and stitching.

In the 3D weaving technology, the constitutive in-plane layers are linked together by fibre reinforcement during the weaving process (layer formation). That is contrary to the stitching technology which is performed after laying-up process to form the dry laminate. Then, the constitutive layers of the laminate are combined together by fibre reinforcement yarns in form of stitches in means of needles insertion. As a result of this insertion, it is noticed a degradation of the in-plane fibre properties, a deflection of the in-plane yarns around the stitch and formation of resin pockets. However, the 3D weaving technology is limited relatively to a possibility to insert in-plane yarns oriented other than 0° and 90° . Thus, the 3D woven preforms have only two sets of the in-plane fibres, the warp and the filler yarns (oriented in 0° and 90° respectively). That results in poor in plane off axis tensile properties and poor shear in-plane resistance. Therefore, the multiaxis 3D weaving technology has been developed in order to enable having bias in-plane yarns layers.

In the last two decades, several patents were published dedicated to development of this technology that is however still under-development. The essential technical obstacles are related to sequencing the in-plane yarn layers, bias yarns feeding system, bias yarns transversal movement and controlling the fabric width in the weaving zone. Furthermore by the developed 3D multiaxis weaving techniques, pairs of opposite ($+/-\theta^\circ$) bias in-plane layers are formed without the possibility to separate them by a warp yarn layer in order to decrease the angle between layers that causes important interlaminar stresses. Furthermore, few works were published related to characterisation of the geometrical and mechanical properties of produced preforms by this technology. In the presented thesis, these problems are dealt with and a novel technical solution is presented.

On the other side, elaboration of fibre-reinforced composites involves a precise understanding of its mechanical behaviour on the macro and meso scales. The numerical modelling gives the possibility to understand phenomena on two scales. This understanding enables reduction of the experimental tests number, which are required necessarily to characterize the manufactured final composite, numerical conception of the preform suitable for specified application conditions, study the formability and the permeability of the dry preform and prediction of the defects, which could appears in the final products. Consequently, that allows optimizing and saving design time and cost of the composite. Otherwise, a numerical modelling allows classifying the present developed 3D multiaxis

woven composite among the other equivalent architecture developed in the same application field.

The geometrical characterization is indispensable to evaluate the geometrical properties of the manufactured samples using newly constructed loom. Also, the geometrical properties refer to the geometrical parameters of the constitutive yarns, the unit cell and the yarns geometry (cross section shape and path) inside the structure. Thus, by the geometrical characterization a detailed description of the constitutive yarns and the unit cell could be obtained. This description is inherently required to develop the numerical modelling. A measurement of geometrical properties of the produced samples allows the evaluation of the technical development in comparison with the similar manufactured 3D multiaxis woven preforms reported in the literature.

The predictive geometrical model, is indispensable design tool, provides an approximate estimation of the fibre volume fraction, the preform total thickness and the proportion of each yarn set in the dry preform or final composite. This type of geometrical model is developed with simplified hypothesis concerning the cross section shape and the path of yarns inside the structure as well as the ratio between two principle yarns cross section dimensions and the packing factor value of the filaments arrangement within the yarn are assumed. Regarding the present 3D multiaxis woven architecture, a few works are published in the literature. An optimized geometrical predictive model is presented in the thesis based on the published models. However, this model does not allow construction of an accurate geometric model at the meso-scale ensuring a consistent estimation of the stress field in the structure by the numerical mechanical modelling. Wisetex (Lomov et al. 2001, 2005, 2007 and 2008), Texgen (Lin et al. 2012) and Hivet's approach (Hivet and Boisse, 2005 and 2008 and Wendling, 2014) allow geometrical model construction of the 3D woven dry preform and composite with significant accuracy. However, because of the specialty of the analyzed 3D multiaxis woven architecture, these modelling approaches could not be implemented directly. The assumed hypothesis and the modelling approach dedicated to compute model parameters should be adapted for the present architecture in association with the geometrical characterization results. That enables construction of a representative volume element (RVE) of the present textile preform at meso-scale.

Evaluation of the bias yarns effect, inserted in multiaxis woven preform, on the elastic properties and on the out-of axis stiffness of the composite is essentially required. Also, it should be compared to the equivalent composite. Furthermore, the influence of the in-plane layers sequence on the induced interlaminar stresses at the composite free edges should be investigated by estimation of the 3D stress-strain field in the structure. Moreover, the strength, failure initiation and failure mechanism should be evaluated for this type of textile fibre reinforcement.

1.2. Thesis overview

The present thesis is devoted to development of 3D multiaxis weaving technology for composite structure application and optimization of the geometrical and mechanical modeling approaches implemented to estimate the geometrical properties and elastic stiffness of manufactured 3D multiaxis woven composite.

The next chapter (**chapter 2**) is a review for the fibre reinforced composite. The basic concept of the used technology, the essential advantages and disadvantages from structural and mechanical point of view are treated.

The **chapter 3** is dedicated to 3D multiaxis weaving technology. The fundamental principles of this technology are defined. The published patents in the literatures in this field are

analyzed with complete classification. The optimized and improved mechanisms of the developed 3D multiaxis weaving prototype loom are detailed. The geometrical parameters of the manufactured samples are measured and the characterization geometrical methods are presented. The geometrical properties of the developed composite sample are compared to those reported in the literature.

In the **chapter 4**, the geometrical modelling approaches developed in the literature are explored. A predictive geometrical model is improved, based on the published predictive models. The assumed hypothesis and the development of the model are detailed. The model results are compared to those of the geometrical characterization. Optimized geometrical modelling approach is developed in association with measured parameters in order to construct as accurate as possible representative volume element (RVE) of this structure. The assumed hypothesis and the followed approach to compute the model parameters are detailed.

The **chapter 5** is dedicated to present the mechanical modelling approach used to estimate the elastic stiffness and out off axis elastic properties of a sample of 3D multiaxis woven composite then compare it to that of the equivalent composite. The influence of the in-plane yarn layers on the induced interlaminar stresses at the composite free edge is investigated and the applied method is presented.

The last chapter is devoted to the conclusions and perspectives of this thesis.

2. State of the art

2.1. Introduction

The reinforced composite material, which is also called “Advanced composite material”, are used increasingly after the Second World War as structural engineering material tanks to its light weight, high specific stiffness, high specific strength, excellent corrosion resistance, fatigue resistance and impact resistance compared to common metallic alloys. Furthermore, its ability to be manufactured in complex shape reduces the number of parts in an assembly. All those reasons explain its interest, despite high fabrication cost, compared to conventional metal alloys, (Kaw, 2006).

The reinforced composite material is a subgroup of the composite material class, which is one of the four engineering material classes (metals, polymers, ceramics and composites), (Ogin, 2000). The composite material is defined as multiphase material composed of two or more constituents, with distinct boundary and different properties, combined together to optimize one or more specific properties, (Peters 1997, Gay 1997, Berthelot and Cole 1999, Ogin 2000, Vasiliev and Morozov 2001 and Lucas and Zanella 2007). The reinforced composite material is composed of reinforcing phase embedded in continuous matrix phase. The matrix fixes the reinforcement in position, transfers and distributes the loads between the reinforcing components by the shear adhesion forces and preserves the reinforcement from the external environment conditions, (Peters, 1982). The typical matrix materials are thermoset polymer, thermoplastic polymer, metal, carbon and ceramic. The reinforcement plays the important role to control the stiffness and strength properties of the composite structure. It could be in three forms, (Figure 2.1): particle, flake and fiber, which could be short (discontinuous) fiber or long (continuous) fiber, (Kaw, 2006). This work deals with the composite materials reinforced by continuous fiber, which could be of different materials. The typical used fiber material is carbon, glass, quartz, metal, boron and organic (natural and synthetic) fibers. Furthermore, the continuous fiber reinforcement could be tailored in various architectures, according to the final product application conditions (type and orientation of the loads that the product will support).

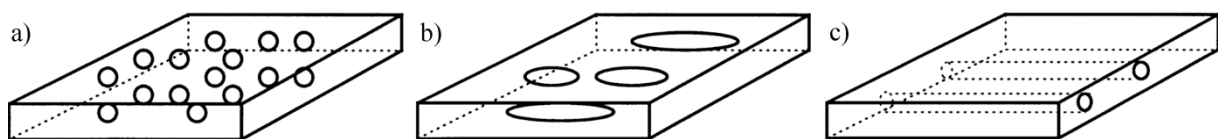


Figure 2.1: Three forms of the reinforcement; a) particle, b) flake, c) fibre (long fibre). (Kaw, 2006)

The architecture of the reinforcement refers to the position of the fibers in the reinforcement relative to a defined coordinate system. Different classifications are introduced in the literature for the architecture of the textile reinforcement depending on the fabrication technology; the alignment plans of the constitutive fibers and the orientation of the constitutive fibers. Regarding the fabrication technology, the conventional textile technologies are used to design and manufacture fiber-reinforcements such as weaving, knitting, stitching and braiding, Figure 2.2. Furthermore, several novel technologies were also developed to produce special shaped composite, Risicato et al. 2014.

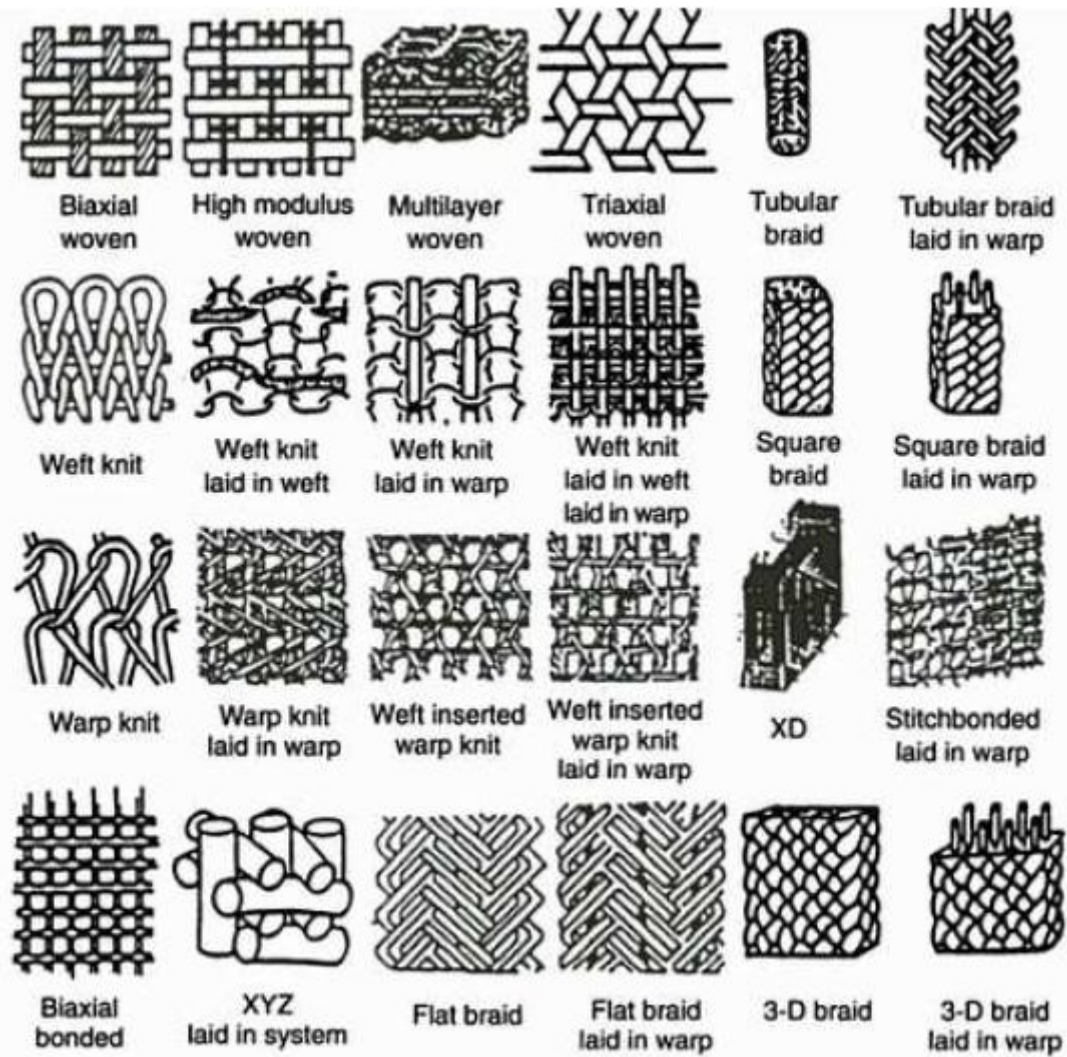


Figure 2.2: Textile fiber- reinforcements, (Ko and Du 1998).

In terms of the alignment plans of the constitutive fibers, the fiber-reinforced composites are classified into three groups, as illustrated in the Figure 2.3:

- 1D fiber reinforced composites: in which the fiber are parallel and aligned in one direction.
- 2D fiber reinforced composites: in which the fiber are aligned on one plane of the structure (XY plane).
- 3D fiber-reinforced composites: in which, in addition to the aligned fibers on XY plane of the structure, another set of fiber is aligned along the orthogonal axis (Z axis) corresponding to through thickness axis of the structure denoted through-thickness fiber reinforcement or Z fiber.

Regarding the orientation of the main axis of constitutive fibers, the fiber-reinforced composites are classified into non-axial, mono-axial, biaxial, triaxial and multi-axial structure, as presented in Figure 2.4.

2. State of the art

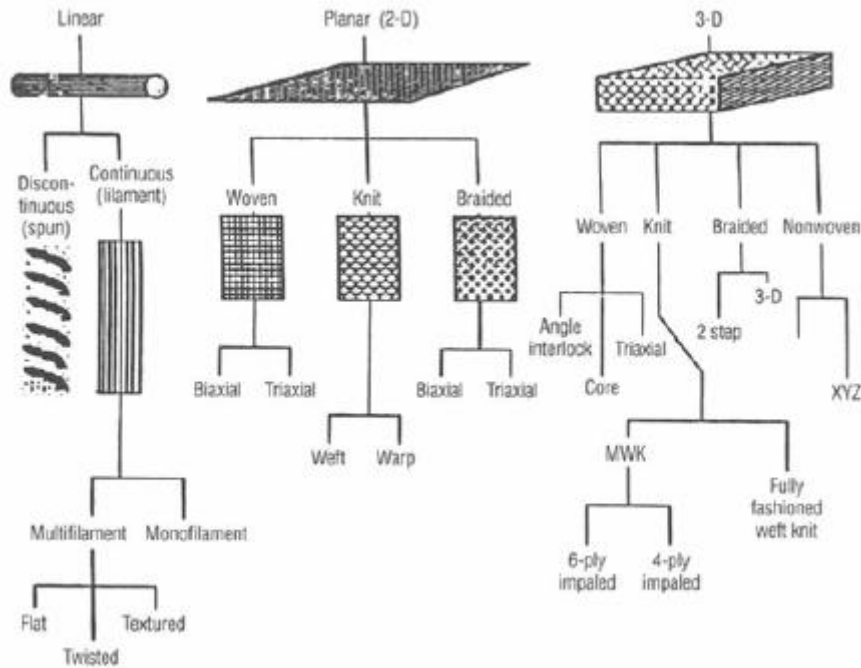


Figure 2.3: Classification of the fiber-reinforced composites in terms of the alignment plans of the constitutive fibers (Ko and Du 1998).

AXIS Dimension		Non-axial	Mono-axial	Biaxial	Triaxial	Multi-axial
		1D		Roving yarn		
2D		Chopped	Pre-impregnation sheet	Plane weave	Triaxial weave	Multi-axial
3D	Linear element	Strandmat	3D braid	Multi-ply WEAVE	Triaxial 3D weave	Multi-axial 3D weave
	Plane element		Laminate type	H or I beam	Honeycomb type	

Figure 2.4: Classification of the fiber-reinforced composites in terms of the orientation of the constitutive fibers (Fukuta et al. 1998).

In the present manuscript, the preform expression is used to mention the dry state of the fiber-reinforcement before being impregnated into the matrix.

In following paragraphs, architectures of the 2D/3D fiber reinforced composites produced by different textile technologies, in addition to their advantages and disadvantages, are briefly presented. Then, the necessity to elaborate novel 3D multiaxis woven reinforcement architectures, which are the focus of this work, is presented.

2.2.Laminate fiber reinforced composites

The laminate fiber reinforced composites are 2D structures, made by stacking various laminas one upon the other in specific order and specific relative orientation, as illustrated in the Figure 2.5, (Robert 1999). Each ply can be a unidirectional layer of juxtaposed long continuous fibers (filaments) aligned on one plane, or it could be a layer of conventional 2D woven fabrics, Figure 2.6. The 2D woven fabric will be presented in the next section. The orientation of the lamina is expressed by the orientation of the longitudinal axis of the fibers in the case of unidirectional lamina or by the orientation of the longitudinal axis of the warp yarns in the case of woven fabric relative to referencing coordinate system. The orientation of stacked laminas could vary between -90° and $+90^\circ$.

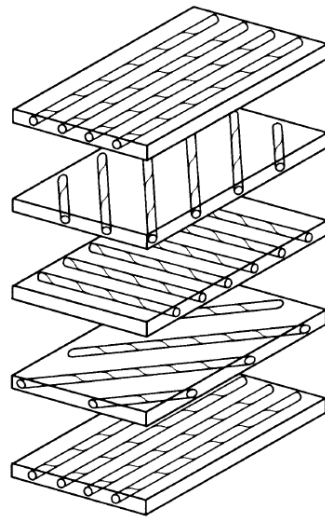


Figure 2.5: Laminate made by stacking laminas in different orientation (Robert 1999).

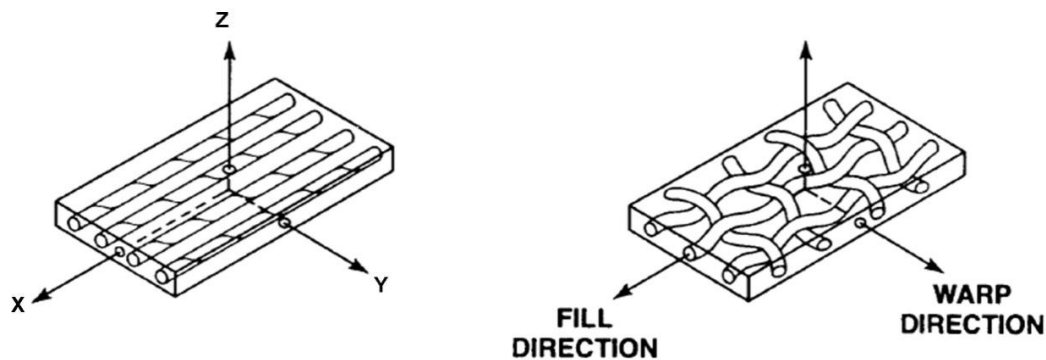


Figure 2.6: Lamina fiber reinforced composite: on left lamina with unidirectional fiber, on right lamina with 2D woven fabric (Robert 1999).

The filaments of the unidirectional lamina are often saturated with resinous material, which will be used subsequently as matrix, without consolidation in order to maintain the aligned filaments in parallel and to be handled easily in the next lay-up process. Such laminas are called “prepregs”.

The two basic steps to fabricate the laminate fiber-reinforced composite materials are lay-up and curing (Robert 1999). The lay-up process consists of laying down the filaments in specific orientation to form the laminas then stacking them to form the laminates, whereas the curing process consists of solidification of the matrix material to get the final rigid desired shape. The principal lay-up processes are winding, laying and molding. However, the lay-up

process implies high amount of skilled labor. Furthermore, the cost of fabrication and the number of parts in the assembly increase when forming a complex part shape by the laminate (Tong et al. 2002).

The laminate composite materials are used in various applications from sport equipments to the spacecrafts as result of their favorable properties resulting from the combination of the properties of advanced fibers with that of the matrix. These advantages could be summarized in:

1. High in-plane specific strength (strength to density) and high in-plane specific stiffness (stiffness to density) for the laminate composite comparing to metallic materials, as illustrated in Figure 2.7 where the specific strength and specific modulus of graphite fiber, unidirectional graphite/epoxy lamina and cross-ply graphite/epoxy laminate are compared to that of steel and aluminum, (Kaw, 2006).
2. Low amounts of defects (fiber breakage, fiber misalignment, resin pocket) are caused. Such defects, which are usually associated to textile process (weaving, stitching, braiding...) used usually to produce fiber reinforcements, contribute to pull down the mechanical properties of final composite products.
3. Low cost in comparison with the metallic material, where the initial cost of the laminate composite materials (cost of raw material, design, fabrication and assembly) as well the operating cost is lower, (Robert 1999).
4. Saving weight resulting from high specific strength and specific stiffness leading to lower operating cost such as the fuel cost for transport applications.
5. Contrariwise, this structure is a directional material, its mechanical properties are not identical in all direction and they depend on the fibers directions. Further, many drawbacks are reported for the laminated composite structure. When forming a complex part shape using the laminas the cost increases because of increasing the parts count in the assembly and that increases the labor cost, (Robert 1999). Moreover, the laminated composite has high thermal and moisture expansion coefficient and low operating temperature when using polymer matrix, (Kaw, 2006). However, the principal drawback relating to the reinforcement architecture is the absence of the through-thickness fiber reinforcement, which is the origin of the poor strength and strength properties in the through thickness direction. This affects strongly its delamination resistance leading to low impact resistance and low post impact properties (Anabara et al. 1992, Chou 1992 and Sih and Skudra 1986). As presented by Tong (2002), the strength and stiffness properties, in the through thickness direction of the laminate, are often less about 10% of the in-plane properties, Figure 2.8. Tong also mentioned poor post impact mechanical properties of the laminates by showing the degradation of the in-plane tensile and compressive strength after impact, as illustrated in Figure 2.9. It was proposed, as a recommendation in view of the poor post impact properties, to increase the ply count but that, on other side, increases labor and cost. Otherwise, the 3D reinforced structures can be considered as alternative materials since they are delamination-free and damage tolerant (Kamiya at al. 2000, Cox et al. 1993 and Bilisik 2010-a, b).

2. State of the art

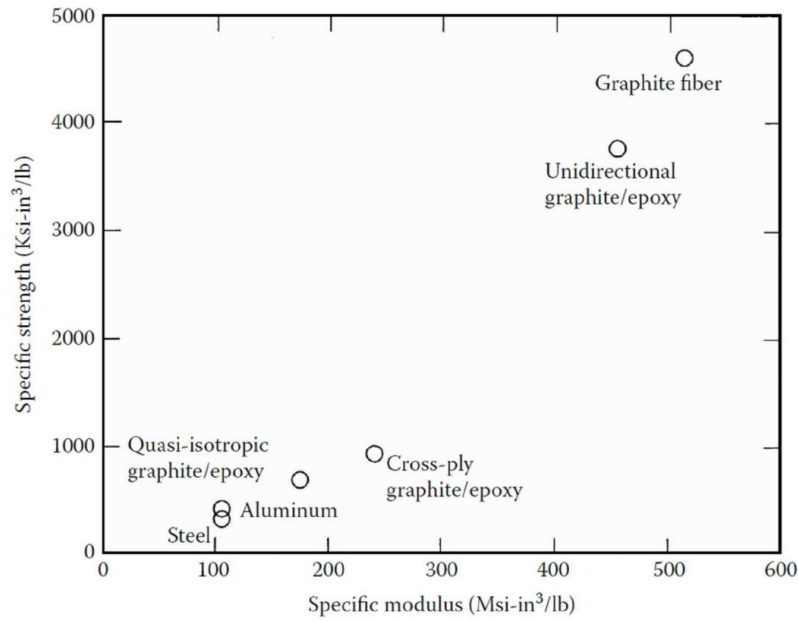


Figure 2.7: Specific strength in function of specific modulus of fibre, lamina, laminate and metals, (Kaw, 2006).

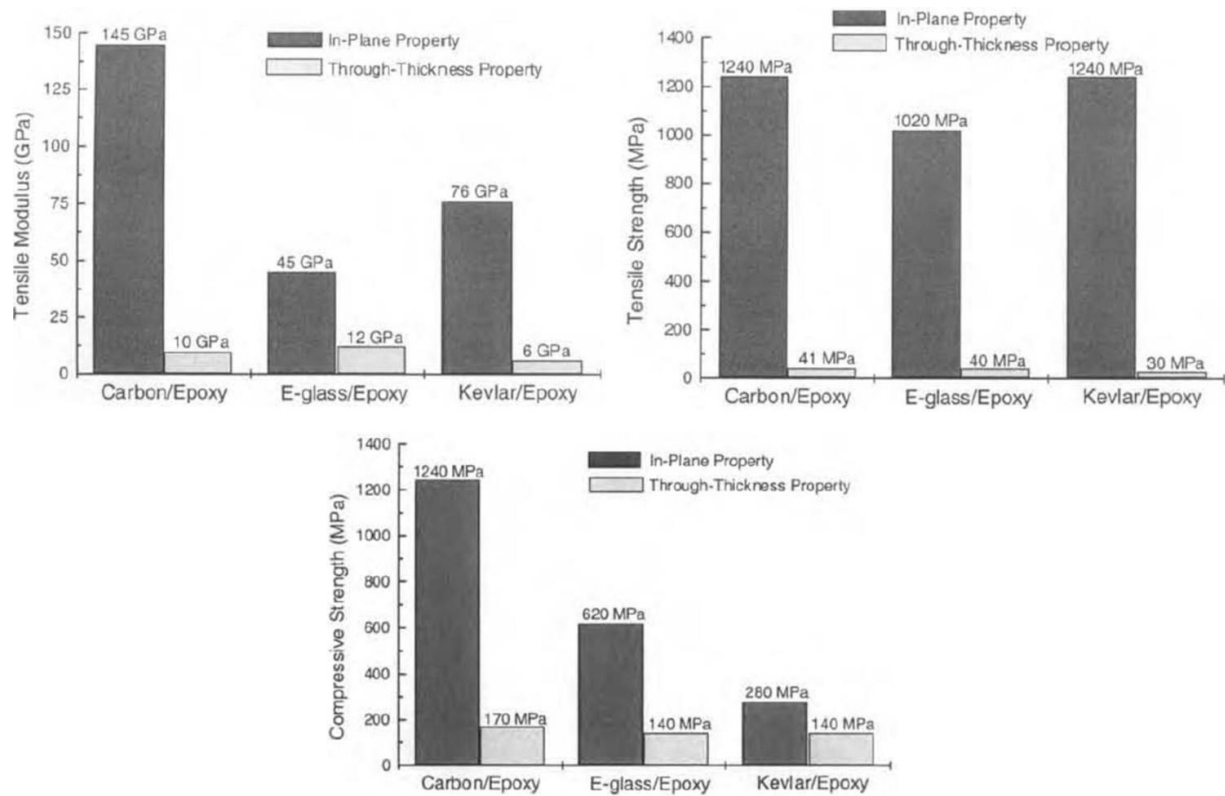


Figure 2.8: Comparison of the in-plane tensile modulus, tensile strength and compressive strength to that in the through thickness properties for laminate composite materials, (Tong, 2002).

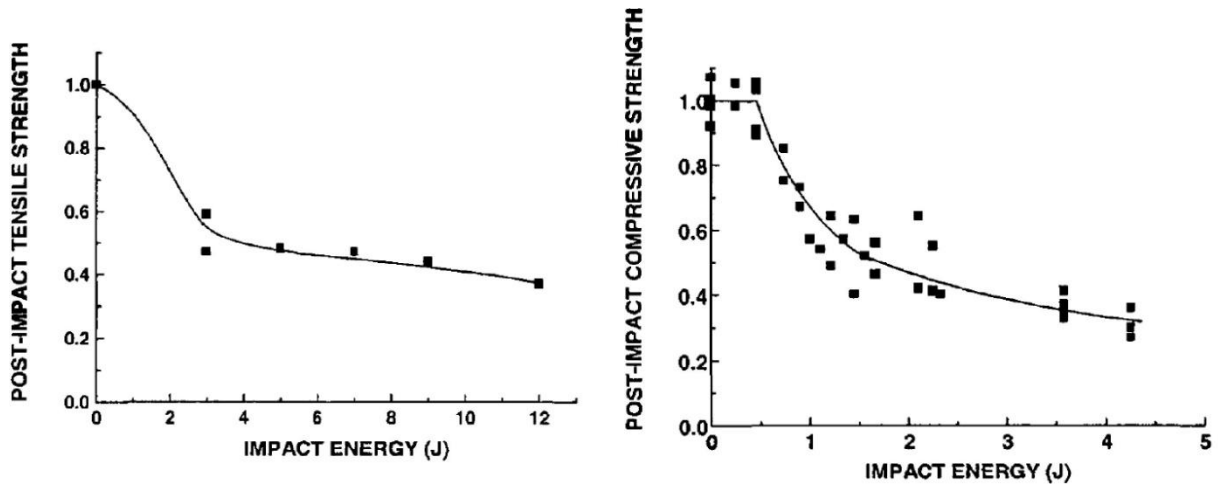


Figure 2.9: Degradation of the in-plane tensile and compressive strength after impact normalized to the strength before impact in function of the impact energy, (Tong, 2002, and the tensile and compressive data are brought from Dorey 1989, and Caprino 1984 respectively).

2.3. Woven fiber reinforced composites

2.3.1. 2D woven fabric

The 2D woven fabric is made by conventional weaving process consisting of interlacing two orthogonal sets of yarns; warp 0° and weft 90° , (Behera and Hari 2010). However, it is not possible to have yarns in other in-plane orientation on the conventional 2D weaving loom, Figure 2.10. The 2D weaving process is detailed in the section (3.3.1).

The weaving loom technology is well developed providing high productivity and reducing the manufacturing cost of composites. The interlacement of yarns attributes to the lamina stability when handling and conformability to form complex shape with no gaps. Therefore it is not necessary to pre-impregnate preforms. Thereby one manufacturing step is bypassed in comparison to preperg, (Ogin, 2000). However, bending and sliding against loom machineries causes abrasion and fiber breakage, further, the interlacement of yarns induces to crimping them. That reduces the yarns strength and leads to reduction of the lamina strength and toughness in comparison with equivalent cross ply (0° - 90°) unidirectional laminate, as shown by Curtis and Bishop (1984).

2.3.2. Multilayered (or 3D woven) fabric

The multilayered fabric is composed of several in-plane woven layers linked together by yarns passing in the through thickness direction of the fabric called binder yarns or weaver yarns. The aim of developing this woven architecture was to overcome the disadvantage of laminate by combining the different layers of structure via through thickness fiber reinforcement (Rao 2009, Mahadik 2011, Ansar 2011, Buchanan 2010, Chen 2011, Nehme 2011, Boussu 2011). The composite made of this preform is classified as 3D woven fiber reinforced composites.

Generally, the in-plane yarns of the 3D woven preform are oriented in 0° and 90° (warp and filler yarns), like the 2D woven preform. However, several technologies are developed recently to obtain 3D multiaxis woven preform containing in-plane yarns oriented in a direction other than 0° and 90° . This architecture and the used technologies are the axis of the next chapter.

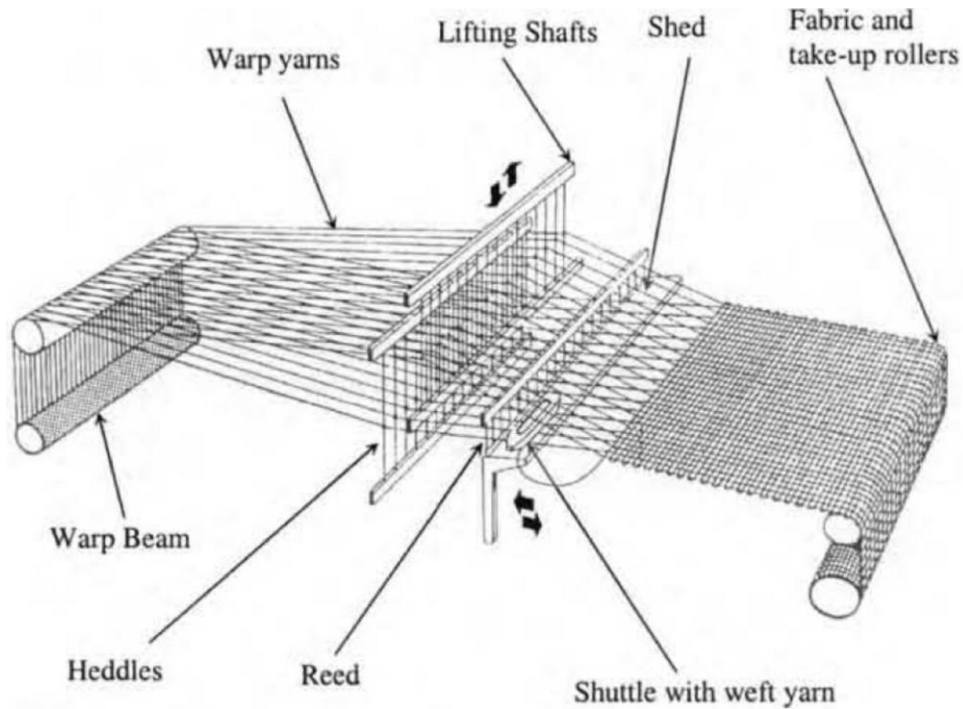


Figure 2.10: Schematic representing conventional 2D weaving loom.

Different weave patterns for the binder yarns are used to link the fabric layers (Lomov et al. 2005), it could be classified into three weaving architectures categories:

- *Layer-to-layer angle interlock*: when the binder yarn passes from layer to adjacent one, then it returns to the first layer thus it links just two adjacent layers, Figure 2.11-a.
- *Through-the-thickness angle interlock*: when binder yarn passes through whole the thickness of the fabric across more than two columns of weft yarns, Figure 2.11-b.
- *Orthogonal*: when binder yarn passes through whole the thickness of the fabric for each column of weft yarns, Figure 2.10-c. Here, there is no interlacement between warp and weft yarns where the alternate layers of virtually un-crimped in-plane yarns (warp and weft) are combined together just by the binder yarns, (Leong et al. 2000).

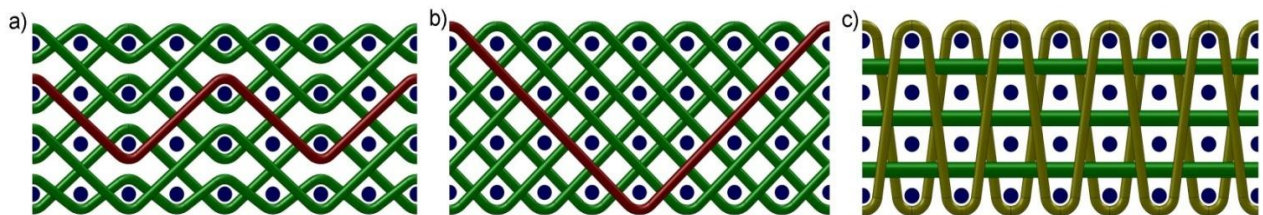


Figure 2.11: Typical 3D woven architectures; a) layer-to-layer angle interlock, b) through-the-thickness angle interlock, c) orthogonal.

The formation of one weft yarns column in the through-the thickness of the multilayered woven preform involves multiple weft yarn insertions. That could be achieved on the 2D weaving loom even with conventional weft insertion apparatus by adapted weave pattern involving multiple successive shedding operations for one weft yarns column. However, this multilayer weaving process requires higher number of fed warp yarns comparing to 2D conventional weaving process. That raises the manufacturing cost and multiple weaving cycles (Solden and Hill 1998, Chen et al. 2011, Lefebvre et al., 2013).

2. State of the art

Specialized 3D weaving looms for orthogonal architecture are also developed enabling simultaneous multiple weft yarns insertion at each weaving cycle, Figure 2.12. That limits the required shedding operation to make one weft yarns columns to one. Consequently, reduction of the abrasion incurred on warp and binder yarns by heddles while shedding operation.

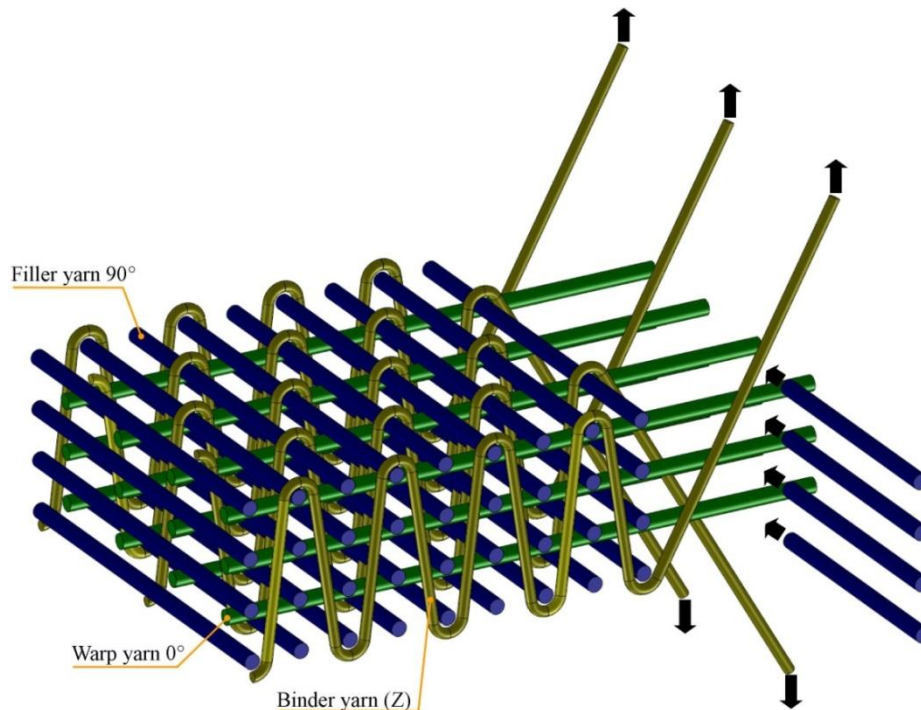


Figure 2.12: Schematic representing 3D orthogonal weaving process with multiple filler insertion.

In addition to the flat woven preforms either 2D or 3D, more complex three dimensional shapes, such as I-beam, could be produced on the conventional 2D weaving loom by means of programmable shedding apparatus executing adequate weave pattern, (Solden and Hill 1998).

The manufacture cost of the 3D woven composite is higher than that of laminates for many applications, where the woven composite is not produced in large commercial quantities (Tong, 2002).

As it was mentioned for 2D woven preform, the weaving process causes strength reduction for the warp, weft and binder yarns especially for brittle yarns, because of abrasion and breakage of fibers resulting from bending and sliding the yarns against the loom machineries. Rudov-Clark et al. (2003) analyzed the damage on warp yarn and binder yarn of glass fiber arisen while weaving 3D preform on 2D jacquard loom. They noticed a strength reduction of about 30% and 50% for warp yarn and binder yarn respectively with a loss of 5 – 7% in the young's modulus, Figure 2.13. The main reason of this reduction is attributed to the abrasion, therefore; it was suggested to coat the loom apparatus with wear resistant material having low coefficient of friction.

The waviness in through-the-thickness direction of the yarns, resulting from the interlacement of yarns when weaving, affects strength, ductility and fatigue life of woven composite, (Cox et al., 1992, 1994, 1995-a and b). The waviness magnitude varies between yarns sets depending on their tension while weaving. Generally, filler yarns are suffering from crimp higher than warp yarns. Furthermore, the waviness magnitude depends upon the yarn path associated with the weave pattern. Therefore the crimp is relatively high in

2. State of the art

layer-to-layer architecture of 3D woven fabric whereas it is less in the through thickness angle interlock architecture and least in orthogonal architecture, (Cox et al., 1995-b).

Two types of defect regions could be found in the 3D woven composite: the first is a region of high-fiber content making infiltration of viscous resin difficult while consolidation process resulting in formation of porosity and the second is a region of rich resin (low-fiber content) formed after the consolidation process resulting from crimp and push aside of the in-plane yarns by the binder yarns, (Leong et al., 2000).

Tong et al. (2002) analyzed the experimental results provided from researches about characterization of the mechanical properties of 3D woven composites. He founded that the young's modulus of 3D woven composite is within 20% (improved or degraded) of that of equivalent 2D laminates. Further, either the content of the binder yarns or the 3D weave pattern (angle interlock or orthogonal) has no significant effects on the Young's modulus of 3D woven composite. The same results were revealed for compressive strength of 3D woven composite in comparison with 2D laminates, whereas the tensile strength is mostly lower, but no more than 20%. Cox et al. (1994) and Callus et al. (1999) found that the plastic straightening of heavily crimped in-plane yarns at low strain is the origin of the beginning of softening the stiffness of 3D woven composite which continues with straightening all yarns while raising the strain. Likewise, the plastic deformation of the resin within the crimped yarn is the cause of the formation of kink band responsible of failure compression.

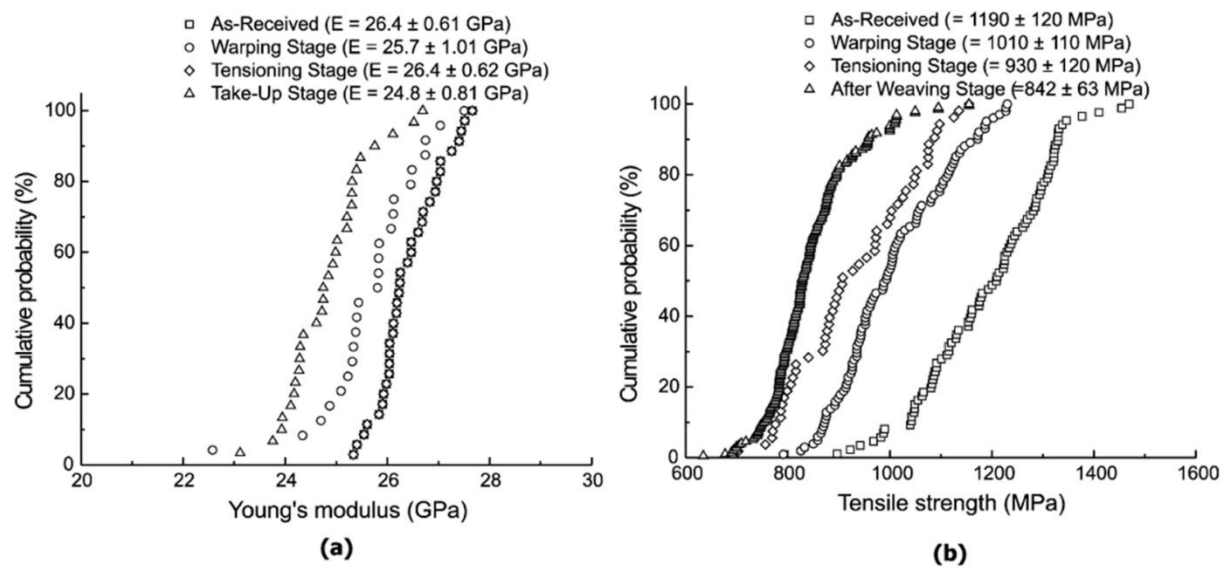


Figure 2.13: Cumulative probability distribution of young's modulus (a) and tensile strength (b) of warp yarns at different weaving stages, (Rudov-Clark et al. 2003).

Contrary to the laminate composites, the 3D woven composites have high fracture toughness and high delamination resistance due to the through thickness fiber reinforcement (binder). Guénon et al. (1989) showed that even for low binder yarns content about 1% in 3D carbon/epoxy composite the delamination toughness for mode I is about 14% higher than for 2D carbon/epoxy prepreg laminates. In the same manner, Liu et al. (1989) found that the 1% content of binder yarns leads to delamination toughness for mode II 2 or 3 times higher. Cox et al. (1994) studied the failure mechanisms of 3D woven carbon reinforced polymer composites on tension, compression and bending. They observed that the 3D woven composites exhibit high strain to failure in tension resulting from very large pullout lengths for failed yarns, so high work of fracture. As well in compression the

geometrical flaws favors high strain to failure. Lomov et al. (2009), compared between non-crimp 3D orthogonal woven composites and four-ply laminates of plain weave. He noted a higher strength, failure strain and damage initiation thresholds for 3D woven composites. Further, he mentioned that the delamination between plain weave plies of laminates initiate at applied strain between 1.5% and 2%, whereas it never arises in the 3D woven composites. The high delamination resistance gives better damage resistance to 3D woven composites. That results in higher post impact mechanical properties for 3D woven composite than 2D laminates, (Tong 2002, Agrawal 2013, Seltzer 2013).

2.4. Stitched composites

The stitched composites are 3D fiber reinforced composites produced by sewing high tensile yarns through stacked 2D conventional laminas as illustrated in Figure 2.14, (Tong et al., 2002). The stitching technology is used to manufacture special shaped composite structure such as T-joints, (Stickler 2000). The typical reinforcing yarns used for stitching are of carbon, glass or Kevlar. Different configuration of stitch could be sewed such as lock stitch, modified lock stitch and chain stitch, but the most used is modified lock stitch, (Tong et al., 2002). And different sewing process parameters have important effects on resultant products such as stitches density per unit area, needle diameter, stitching yarn linear density and its tension.

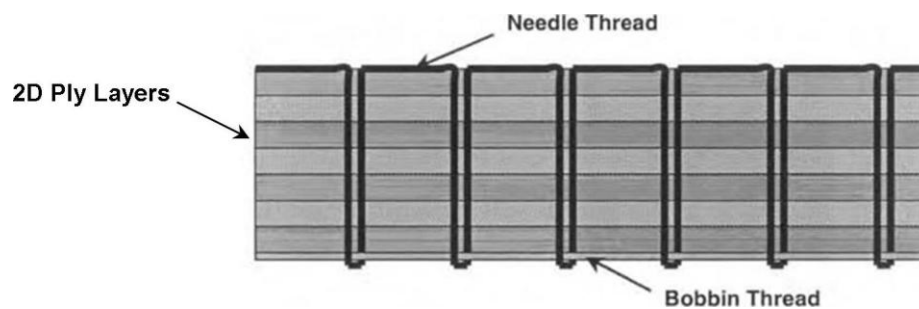


Figure 2.14: Stitched composite; stacked 2D laminas sewed with modified lock stitch, (Tong et al. 2002).

The insertion of the stitching needle and yarn into through the thickness of stacked layers causes microstructure damages to stacked laminas. Mouritz and Cox (2000) and Tong et al. (2002) have summarized these damages in, Figure 2.15:

- Breakage of the in-plane fibers due to the needle insertion.
- Crimp of the in-plane yarns into the preform through-the-thickness direction due to stitching yarn tension.
- Misalignment of the in-plane yarns around the stitch.
- Stitch distortion caused by resin rich region (resin pocket) associated to misalignment and crimp in the case of heavy compaction while curing.
- Micro-cracking resulting from mismatch of the thermal expansion coefficients of stitches and surrounding materials and compaction of the laminate.
- Degradation of stitching yarns mechanical properties due to bending and sliding against sewing machineries during stitching process.

As result of these microstructure damages, Mouritz and Cox (2000) revealed that it is common reduction of the in-plane strength and fatigue life of stitched laminate in comparison with equivalent un-stitched laminate by up to 20%. Nevertheless, the sewing effect on the in-planes Young's modulus, compressive strength and flexure is within 20% (improved or degraded). And a slight dependence of mechanical properties upon the stitches density is reported for stitched laminate. However, post-impact mechanical

properties are improved with large stitches density. The interlaminar shear strength of the laminates can be enhanced or degraded by stitches in a range of 15-20%, according to Mouritz and Cox (2000). The stitch prevents the delamination crack growing up. Contrariwise the initiation of the failure crack is around a stitch where is the most distorted yarn that could be the reason of the reduction in the interlaminar shear strength. However, high mode I delamination resistance is prompted to stitched laminate compared to un-stitched one by bridging action of stitches. Likewise, the mode II delamination resistance of stitched laminate is promoted but the improvement rate is less important. The influence of stitching parameters on the mode I and II interlaminar failure toughness and impact behavior is investigated by Tan et al. (2012), Koziol (2012, 2013) and Vallons et al., (2014).

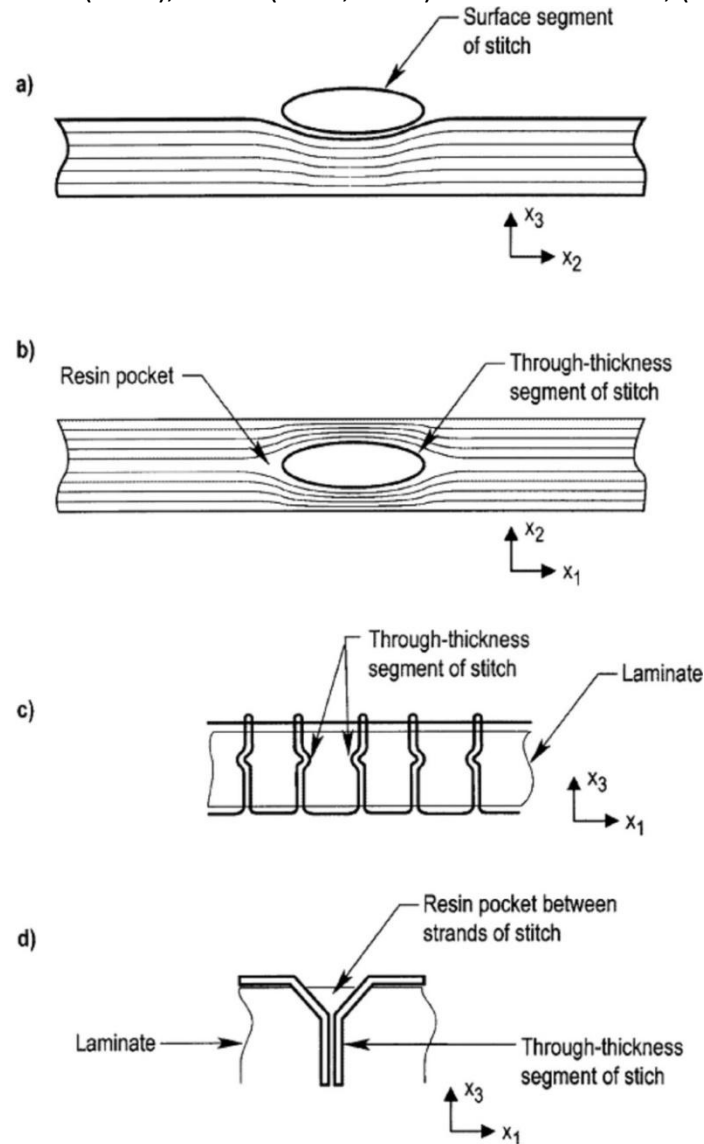


Figure 2.15: Schematics for the damages to laminates caused by stitching; a) crimping of the in-plane yarns, b) misalignment of in-plane yarns around stitch and formation of resin pocket, c) distortion of stitch due to heavy compaction while curing, d) formation of resin pocket between the two strands of stitch heavily stretched. x_1 , x_2 in-plane laminate direction and x_3 through thickness direction, (Mouritz and Cox 2000).

2.5.Knitted composites

Two basic types of knitting processes are; warp knitting and weft knitting, Figure 2.16. In warp knitting process multiple yarns are fed into the longitudinal direction of the machine

and each yarn forms line of knit loops in the fabric direction. While, in the weft knitting process, single yarn is fed into the transversal direction of the machine and it forms a row of knit loop, (Tong et al. 2002). The loop form gives the structure high conformability to cover complex shape surface without wrinkles or need to cut and overlap sections. Further, the knitting process enables to produce net shape or near net shape performs.

From the experimental study investigating the in-plane properties of weft knit preforms, It is seen a similar performance between weft knitted composite and random mat composite, further its in-planes performance is much lower than that of conventional 2D woven composite, (Ramakrishna et al. 1997 and Huang et al. 2001). However, knitted composite exhibits fracture toughness greater than conventional 2D woven, unidirectional or random mat composite, (Mouritz et al., 1999). Similarly, knitted composite showed higher damage tolerance and impact energy absorption, (Pandita et al. 2002).

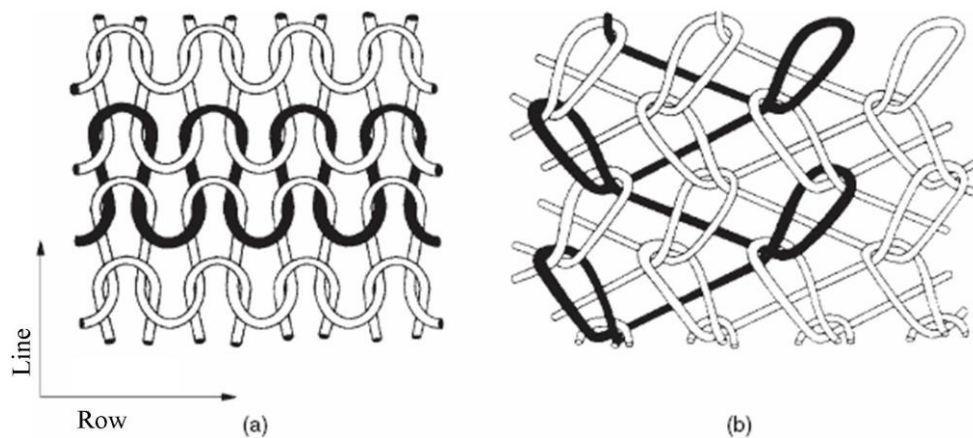


Figure 2.16: schematic of a) weft knitted fabric, b) warp knitted fabric, (Ogin, 2000).

2.5.1. Non Crimp Fabrics

The non-crimp fabric (NCF) technology is a subgroup of knitting technology. This process consists of aligning technical yarns in specific orientation and in successive plies without inducing crimp to yarns then the warp knitting technique is used to link these plies using sharp-head needles, as illustrated in the Figure 2.17; schematic for the principle of this technology elaborated by LIBA manufactory, (Kamiya et al. 2000). By the NCF machine of LIBA, the maximum number of plies, could be obtained, is 8 with orientation of the last ply in 0° .

The warp knit, linking the fiber unidirectional plies, makes manipulating and handling the preform in the next step of manufacturing the composite materials easier and reduces the amount of labor required to hand lay-up of laminas (Tong et al 2002). The NCF reinforcement overcomes the disadvantage of the applying the 2D woven fabric lamina in terms of reduction of in-plane properties resulting from the crimp associated of woven fabric (Hogg et al. 1993). However, insertion the needles into through the thickness of the plies causes damage to in-plane fiber, misalignment of in-plane yarns around the through thickness part of loop knit and crimp of in-plane yarns into the through thickness of the preform. Therefore, polyester knitting yarns with low linear density are used to minimize these damages.

The non-crimp composites have inferior tension, compression and flexure properties than equivalent laminate composites made from unidirectional laminas, because of the damage incurred by warp knitting process to in-plane yarns, (Hogg et al., 1993, Wang et al., 1995,

Bibo et al., 1997 Bibo et al., 1998 and Edgren et al. 2008). Bibo et al. (1997) observed similar fracture mechanism for non-crimp composite to equivalent laminate composite with improved resistance to inter-ply failure and separation due to the knitting yarns.

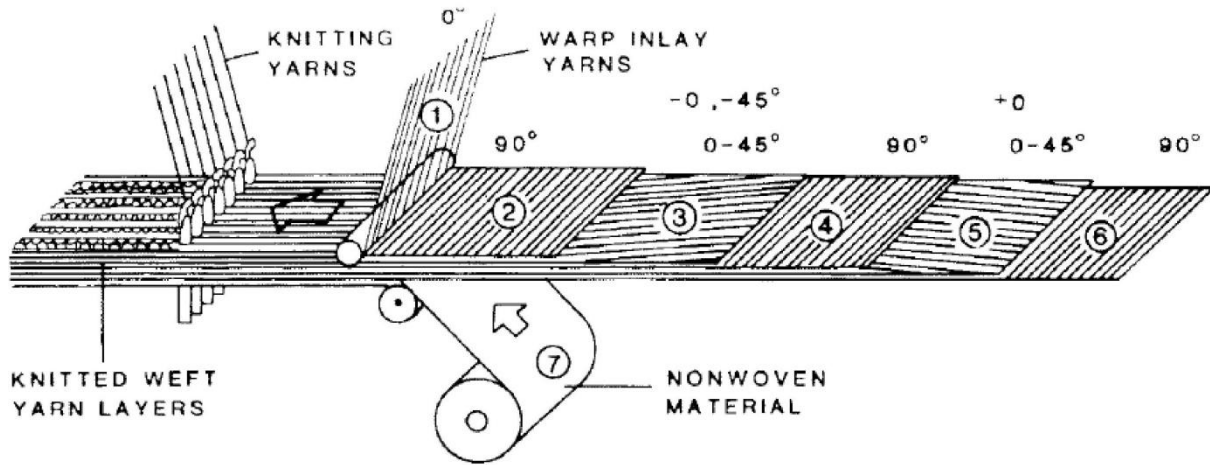


Figure 2.17: Principle of the warp-knit non-crimp fabric technology developed by LEBA. (Kamiya et al., 2000).

2.6. Braided composites

The standard 2D braiding process consists of intertwining two sets of yarns in $\pm \theta^\circ$, in addition to the possibility to introduce axial yarns 0° , (Ogin 2000, Byun et al. 1991-2000 and Head et al. 1989), Figure 2.18. Thereby, unlike woven fabric, the braided fabric contains $\pm \theta^\circ$ and 0° yarns but no 90° yarns could be introduced by standard braiding process. As well, braiding process is not suitable to fabricate wide fabric as weaving process and it is suitable to fabricate narrow width flat or tubular fabric (Tong et al. 2002). Four-step 3D braiding, two-step 3D braiding and multilayer interlock braiding are developed to produce 3D braided preform also to form a quite complex shape, (Du and Popper 1994 and Bilisik 2013).

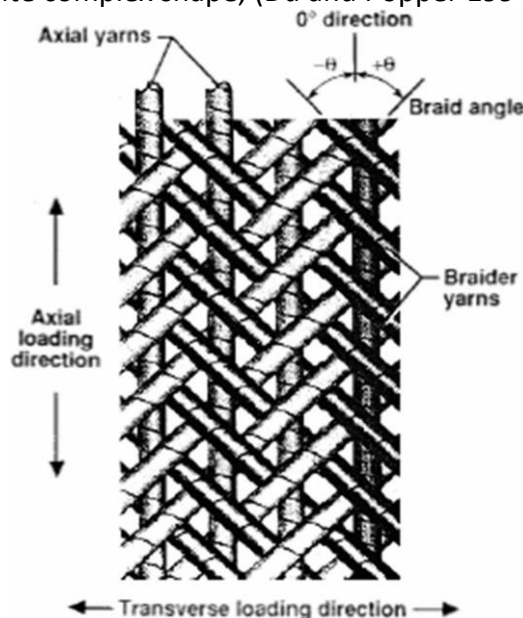


Figure 2.18: Schematic of braided fabric, (Ogin, 2000).

The mechanical properties of the braided composite depend largely on the amount of axial yarns and their properties, the angle of braided yarns and their braiding pattern. The presence of axial yarns improves the axial tensile compressive and flexure properties.

Moreover, decrease the braiding angle improves the axial tensile and compressive properties, but at the sacrifice of the transverse one (Tong et al., 2002). Gause and Alper, (1987) compared 1x1 and 1x1x1/2F 3D braided composites (1/2F signifies the presence of axial yarn with half amount to braid yarns) to equivalent laminate composite formed by stacking unidirectional lamina. The 3D braid showed a less tensile strength in both directions and less transverse tensile modules, whereas the longitudinal compressive properties and tensile modulus were better than laminate. Crimp of braid yarns reduces the performance of braided composite relative to unidirectional lamina as well it contributes to degrade the fatigue performance of the 3D braided composite compared to laminate, but the presence of axial yarns improves the resistance to shattering fatigue damage. The 3D braided composite exhibits greater damage resistance and tolerance than laminate composite, (Tong et al., 2002).

2.7. Z pinned composites

In the Z-pinned composite, thin pins are inserted in the through thickness direction of laminate using manual or automated pinning process, (Mouritz, 2007). The z-pinning process is presented in Figure 2.17. The diameter of the pin is between 0.1 mm and 1 mm, while the volume content of the laminate is between 0.5% and 5%. And the pin is made of high stiffness and high strength material, such as fibrous carbon composites or titanium alloys, (Mouritz 2007).

The pins increases the delamination toughness, damage tolerance and the through thickness properties of the laminate, (Cartié 2006, Mouritz 2007 Nanayakkara 2012 and Koh et al. 2012). However, insertion of the pins in the through-thickness of the laminate causes microstructure damages: in-plane waviness, out-of-plane crimping and breakage of fibers, resin-rich regions and swelling of the laminate (to accommodate the pins), Figure 2.18. That decreases the fiber volume fraction in addition to preventing the compaction of laminate while curing by the stiff pins, (Mouritz, 2007 and Mouritz and Cox, 2010). These microstructure damages lead to important reduction of the in-plane strength, stiffness and fatigue life of composite in comparison with equivalent laminate. Moreover, this reduction increases with the volume content increase and diameter of pines increase, (Chang et al. 2006 and 2007).

2.8. Conclusion

The low delamination resistance, poor through the thickness properties and poor toughness properties of laminates composite material are a result of the absence of the fiber reinforcement in through the thickness direction of composite structure. Therefore, different textile technologies were used to enable the fabrication of preform containing through-the-thickness fiber reinforcements denoted 3D composite. The weaving and the stitching technologies are used to manufacture planar 3D composite structure. The braiding and the weft knitting technologies are adapted to produce 3D complex shape composite products.

Although the improvement of through-the-thickness behavior and toughness properties of the 3D textile composite structure comparing to laminated composite, an important degradation of the in-plane properties is observed as a result of the microstructure damages induced by textile machinery and the yarn geometry inside the structure attributed to the specification of each textile technology. The woven composites show poor in plane off-axis properties and poor in-plane shear properties because of absence of in-plane biases yarns. Further, crimp of in-plane yarns into the through thickness of preform contributes to

2. State of the art

decrease in-plane properties. Nevertheless, the stitching technology has no restriction concerning orientation of in-plane yarns but it causes important microstructure damages to in-plane yarns.

The 3D multiaxis weaving technology is developed to overcome the drawbacks of standard weaving process by enabling aligning in-plane yarns in biases direction in addition to warp and filler yarns with minimization of the weaving machineries damage effects on fibers. However, this technology still under development and few of works have been dedicated to characterize the geometrical properties and the mechanical performance of preforms produced by this type of technology. This is the axis of this research developed in next chapters.

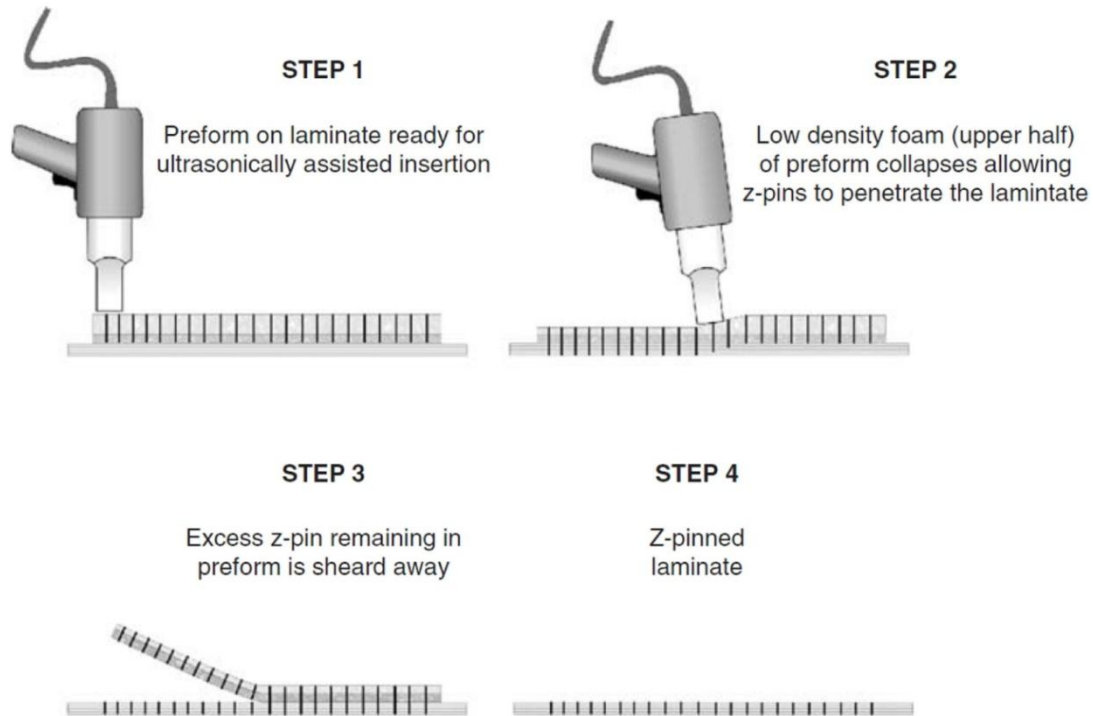


Figure 2.18: Schematic of the Z-pinning process of laminate composite, (Chang et al. 2008).

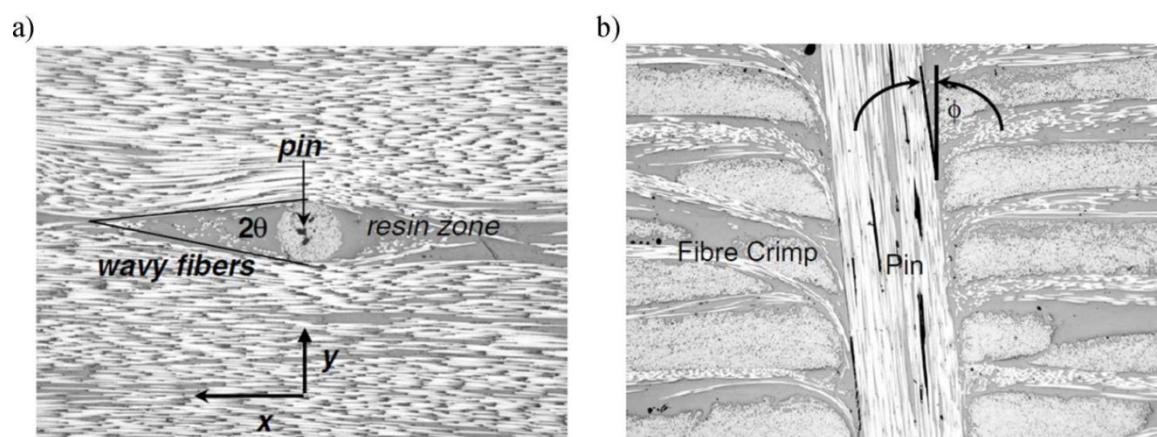


Figure 2.19: Micrographs of laminate reinforced by pins illustrate caused microstructure damages; a) shows waviness of in-planes yarns around pins and the formation of resin riche region, b) shows crimp of in-plane yarns near pins, (Mouritz, 2007).

3. 3D multiaxis weaving technology

3.1. Introduction

As it was concluded in the chapter 2, the insertion of in-plane yarns oriented in a direction other than 0° and 90° during the weaving process could provide a structural solution to improve the in-plane mechanical properties of 3D woven composite. That is investigated deeply in the chapter 5. The technology consecrated to enable this insertion is called multiaxis weaving technology including the 2D weaving and the 3D weaving processes.

In the last two decades, several patents were published dedicated to development of this technology that is however still under-development, Kowalski (2010). Furthermore, few works were published related to characterisation of the geometrical and mechanical properties of the produced preform by this technology.

This chapter focuses on the work realized on the development of the multiaxis weaving technology. The requirements for this process are defined through exploring the conventional 2D and 3D weaving operations and by identifying the differences. Then, the technical solutions proposed in this work are detailed and the multiaxis weaving loom prototype that has been designed and produced in GEMTEX laboratory is presented.

Using the developed 3D multiaxis weaving prototype loom, several samples have been manufactured. The geometrical parameters of the constitutive yarns and the unit cell of these preforms are measured. Furthermore, the geometry of the yarns inside the preform is observed. This characterization provides the essential details to develop predictive geometrical modeling approach serving in the design of this multiaxis structure. Also, it contributes to construct the accurate geometrical model for RVE of this structure, serving in the mechanical modeling. That will be treated in the next chapter.

Finally, the weaving setting of the developed 3D multiaxis weaving prototype loom is compared to that of Bilisik's looms; "tube-rapier" and "tube-carrier" 3D multiaxis weaving looms (1994, 2000, 2010). Also, the geometrical properties of composites samples produces using these looms are compared.

3.2. Definition of multiaxis woven fabric

The textile preform could be classified relatively to the orientation of constitutive fibers main axis, (Fukuta et al. 1986), Figure 2.4. The 2D fabric is defined as 2-axial structure referred to the two constituent sets of in-plane yarns: warp yarns and filler yarns oriented in 0° and in 90° respectively. The multilayer or 3D fabric is classified as 3-axial structure due to the presence of through the thickness yarns in addition to two sets of in-plane yarns. The 2D woven preform that possesses in-plane yarns oriented in a direction other than 0° and 90° called bias yarns in addition to warp and filler yarns is classified as four axial structure and it is called 2D multiaxis fabric. Similarly, the 3D woven fabric composed of multilayer of four in-plane yarns sets (0° , 90° and $\pm\theta^\circ$) combined together by through the thickness reinforcing yarn is called 3D multiaxis woven fabric. A configuration of this structure is presented in Figure 3.1 in which the axes of the constituent yarns are illustrated.

3.3. Multiaxis weaving technology

The conventional 2D and 3D weaving processes do not enable insertion of bias yarns ($\pm\theta^\circ$) to get multiaxis woven fabric. So, special technique is required to achieve this insertion with adaption of other conventional weaving operations. The technology dedicated to achieve these requirements is called multiaxis weaving technology including the techniques employed to produce 2D and 3D multiaxis woven fabric.

3. 3D multiaxis weaving technology

First, since the 2D conventional weaving process is the base to develop the multiaxis technology, a brief presentation of the essential operations on the 2D loom is pointed out. Then, the differences of 3D weaving technology compared to the 2D weaving process are revealed. Finally, the differences and the requirements of the multiaxis weaving relative to 2D and 3D weaving processes are specified with presenting the developed multiaxis technique in the literature.

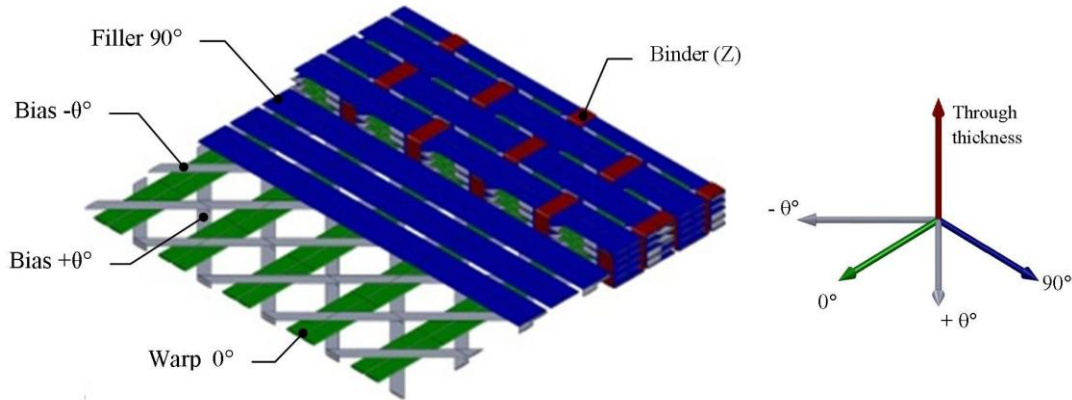


Figure 3.1: Schematic of the multiaxis multilayer (3D) woven perform.

3.3.1. 2D weaving process

On the conventional 2D weaving loom, Figure 3.2, a fabric is made by interlacing two sets of yarns (warp and filler), which are perpendicular, with specific weave pattern by a series of weaving operations in a following order, (textile handbook, 2001):

1. **Warp left-off:** Warp yarns are winded in parallel with even tension on warp beam. The beam is turned a specific step for each weaving cycle, corresponding to demanded filler yarns count per unit length, to feed warp yarns into weaving zone under controlled tension with the aid of tensioning devices.
2. **Shedding:** each warp yarn passes through a heddle eye (one heddle for one warp). These heddles are attached to lift shafts. Warp yarns which have the same state in weave pattern (that means same sequence of interlacement up/down with filler yarns) their heddles are attached to the same shafts. For each weaving cycle, a part of lift shaft moves up while the others move down to separate the warp yarns into two layers creating appropriate space between them across the loom, called shed, Figure 3.3. The shed allows insertion of filler yarn across loom width. This proper space is essentially required to avoid crossing and rubbing warp yarns while insertion the filler yarn. The distribution of the warp yarns on lift shafts and the sequence of lifting the shafts (up/down) across weaving carry out the demanded weave pattern for fabric.
3. **Filler insertion:** For each weaving cycle, a filler yarn is inserted through created shed and it passes across the loom width. Different apparatus are used to carry filler yarn such as shuttle, rapier, projectile, air-jet and water-jet.
4. **Beating:** the filler yarn, after being inserted, is packed tightly to the fabric by means of reed which is closed combs through the gaps created between its blades the warp yarn are passed. And the number of warp yarns in one space in addition to the count of blades per unit length defining the count of warp yarns per unit length of fabric on loom. The reed has alternative movement, it moves back away from the fabric

3. 3D multiaxis weaving technology

formation line in order to allow creating the shed and insertion the filler yarn then it moves forward toward the fabric formation line to pack the inserted filler yarn.

5. **Fabric take-up:** The new packed filler yarn is pulled from the weaving formation zone by rolling up the fabric on fabric beam. The take-up roller and the fabric beam turn one step corresponding to the filler yarns count per one unit length of fabric.

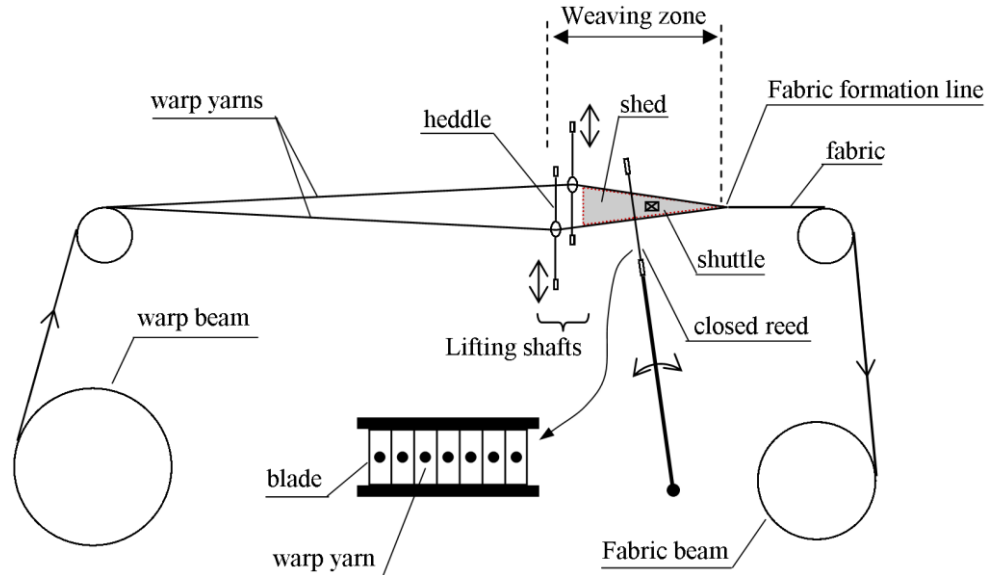


Figure 3.2: Schematics of the conventional 2D weaving loom.

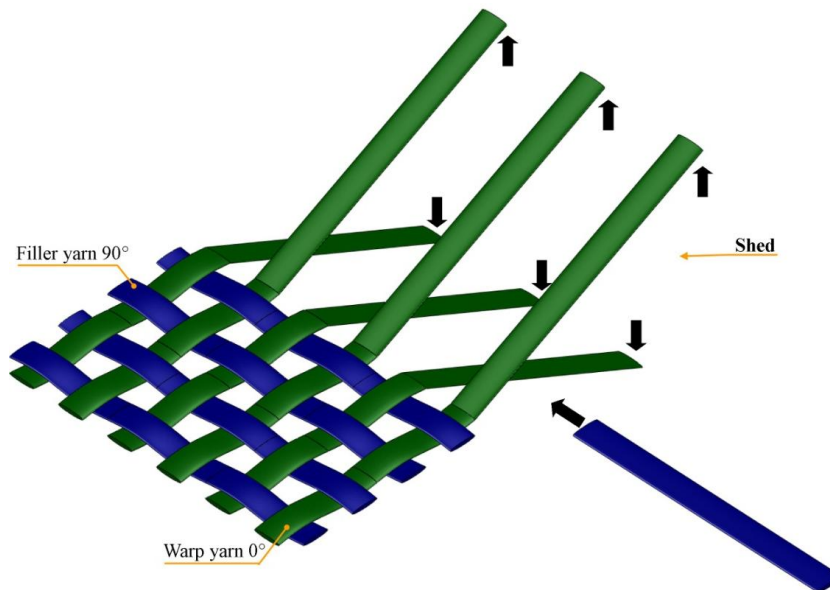


Figure 3.3: Schematic representing formation of the shed on the 2D weaving loom.

3.3.2. 3D weaving process

Contrary to the 2D woven fabric, the 3D woven preform is characterized by multilayer of in-plane yarns through the thickness of the preform linked together by binder yarns (Z-yarns) inserted via weaving process (Lomov et al. 2005, Chen et al. 2011). The 3D woven structure could be produced on the conventional 2D weaving loom to profit from its high productivity (Solden and Hill 1998, Chen et al. 2011, Lefebvre et al., 2013). However, some adjustments are required (Tong, 2002). Firstly, it is necessary to equip the loom with multi-warp beams, one beam for each warp yarns layer, because of the difference in required tension between

warp layers while weaving cycles. Binder yarns are also fed from a separate beam because of the difference in its path in the structure comparing to warp yarns so dissimilar tension is required. Secondly, since on the 2D loom only one shed could be created enabling one insertion of filler yarn, a succession of shed formations and filler insertions are required to make one column of filler yarns in the through the thickness of the preform corresponding to one weaving cycle. The number of filler insertion per weaving cycle corresponding to the number of rows in one column of fabric is equal to the filler layers number. The formed fabric is pulled out of weaving zone for one step at the end of each weaving cycle and not at the end of each filler insertion operation. The multilayered woven fabric is characterized by important thickness regarding to the 2D woven fabric. Consequently, the use of the conventional take-up device consists in winding the formed fabric on fabric beam causes distortion of the formed layers. Therefore, the linear take-up device is preferred here.

However, the formation of multiple successive sheds for one weaving cycle increases the microstructure damages incurred on warp yarns by rubbing this yarns with the heddle's eye and by abrasion to the other loom machineries. That reduces the mechanical properties of warp yarns, (Rudov-Clark et al. 2003, Lefebvre et al., 2013), as explained in the previous chapter. Furthermore, the higher number of fed warp yarns and of the multiple filler insertion for one weaving cycle decreases the loom productivity and raise the manufacturing cost. Therefore, some researchers worked on construction of a special 3D weaving loom enabling formation multiple sheds allowing simultaneous insertions of multiple filler yarns, Figure 2.12, meaning one column by one stage.

On a 3D loom used to produce special 3D architectures such as 3D orthogonal woven preform, where the in-plane yarns are not interlaced and are bonded together only by the binder yarns, the sheds are fixed (no change warp level), that minimizes warp yarns rubbing by heddles.

3.3.3. Multiaxis weaving process

On 2D/3D loom, warp yarns are fed parallel to loom axis (0° orientation) and they advance, while weaving process with keeping this orientation. On the contrary, the bias yarns have to be displaced for each weaving cycle one step transversally to loom main axis in order to get θ° orientation within the fabric relative to warp yarns axes. That is the essential difference of multiaxis weaving process comparing to conventional 2D and 3D weaving process. To achieve this insertion, mechanisms dedicated to feed bias yarns and to control their position in the weaving zone are required in addition to adapt the other conventional weaving operations to these requirements.

3.3.3.1. Two dimensional multiaxis weaving

Ruzand and Guenot (1994) proposed lappet-weaving apparatus, by modifying standard 2D weaving machine. That enables forming a pair of symmetric bias yarns layer on the top and /or bottom faces of woven fabric. Heddle hooks (one for each bias yarn) are disposed on segmented transversal bar called lappet bar, Figure 3.4. The heddle hook has also two movements; first, the vertical one allowing insertion of filler yarns and it is driven away to enable beating up by reed, and the second, horizontal movement to put the bias yarns in right orientation. However, the bias yarns are not interlocked to filler and warp yarns where they are maintained in position within the fabric by the interlacement between filler and warp yarns. The two lappet bars on each side of the fabric move oppositely in transversal direction. The length of the lappet bar is greater than the fabric width. Once the yarns of one segment of lappet bar reach the fabric edge, they are gripped between the selvedge and the guide and they are cut then this segment is transferred to the opposite lappet bar and it is

3. 3D multiaxis weaving technology

reattached. The bias layers cover the entire width of the fabric and the boundary bias yarns are folded to next layer. Consequently, edge to edge uniform bias yarns layers is formed. Moreover, disposing pair of opposing bias yarns layer (one at 45° and the other on -45°) creates balanced fabric. But it is not possible by this technique to arrange the bias layers other than the two outer faces of the fabric. As well, this technology solution is limited to fabricate layer to layer interlock, as reported by Kamiya (2000).

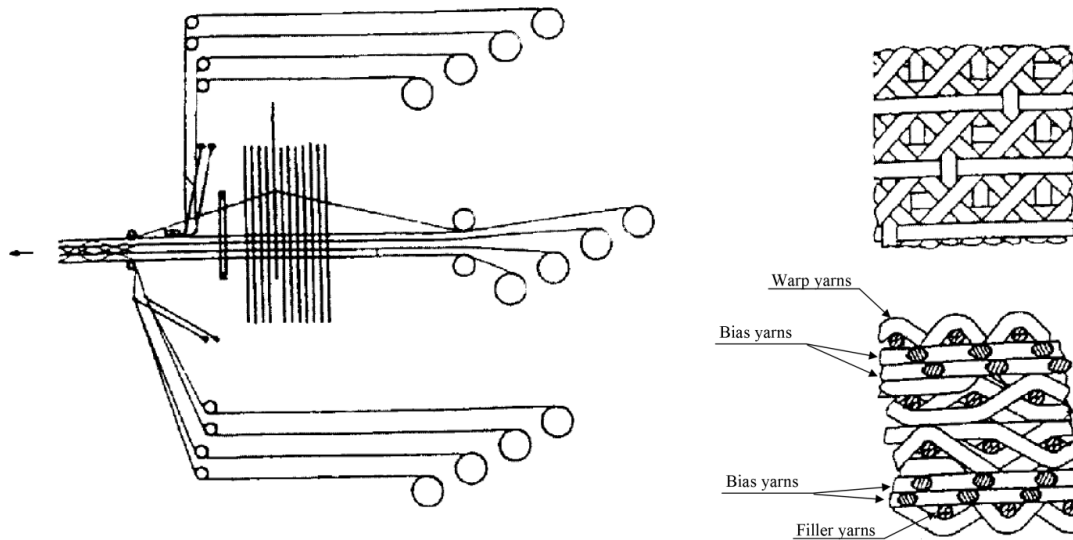


Figure 3.4: Schematic of the modified lappet multiaxis weaving by Ruzand and Guenot (1994) with produced architecture.

Mood (1996) worked also on modifying the 2D weaving loom to produce four layers multiaxis woven fabric (warp, filler, + and - bias) by means of special split reed and jacquard shedding mechanism, Figure 3.5. The reed is split into open upper reed which is able to move transversally to loom main axis and open lower one which is fix. The bias yarn passes through the eye of one especial jacquard heddle. To shift the bias yarns transversally, they are selected by jacquard mechanism and placed in the upper reed or in the lower reed. The jacquard mechanism also creates required shed for insertion filler yarn to be interlaced with warp yarns then the filler yarns is beaten to the fabric by other reed. Thereby, the + and - bias yarns are locked in position between warp and filler yarns. However, the large shedding motion could cause higher fibre damage as reported by Kamiya (2000). Furthermore, using this technique to fabricate multilayer multiaxis fabric could be too complicated for higher production rate.

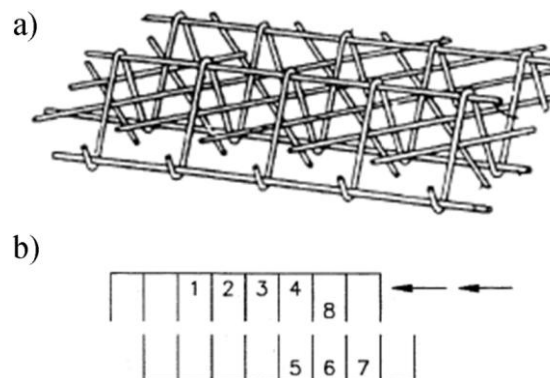


Figure 3.5: Multiaxis four layers woven fabric (a), one case of distribution the bias yarns by jacquard mechanism into upper movable reed and lower fixed reed (b), (Mood, 1996).

3. 3D multiaxis weaving technology

Bryn et al. (2004) also worked on producing four layers multiaxis fabric in various cross section shapes, Figure 3.6, based on multilayer narrow weaving principle. Individual hook is used to control the position of one bias yarns. When bias yarn reaches the fabric edge, it will be folded to next opposite bias yarns layer. Comparing to the four layers multiaxis fabric fabricated by Mood (1996), on Bryn's loom the + and - bias yarns are also interlaced with warp and filler yarns. The length of produced fabric is restricted by the length of bias yarns so the continuous manufacturing of fabric is not available on this loom, (Bilisk, 2011).

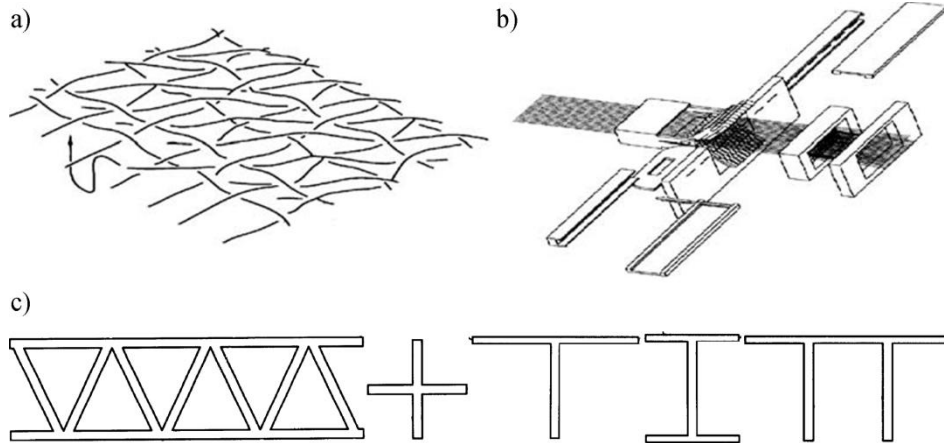


Figure 3.6: Multiaxis four layers woven fabric (a) and the developed loom by Bryn (2004)(b) which is able to produce fabric in various cross section shape (c).

Nayfeh et al. (2006) used the braider carrier to feed bias yarns on 2D multiaxis weaving loom, Figure 3.7. The carriers are equipped with controlling tension device able to maintain the tension of bias yarn during the weaving process. They move along predetermined path according to desired fabric cross section. A shuttle is used to insert the filler yarn into the formed shed. Then, an open reed is used to pack the inserted filler yarn into the fabric.

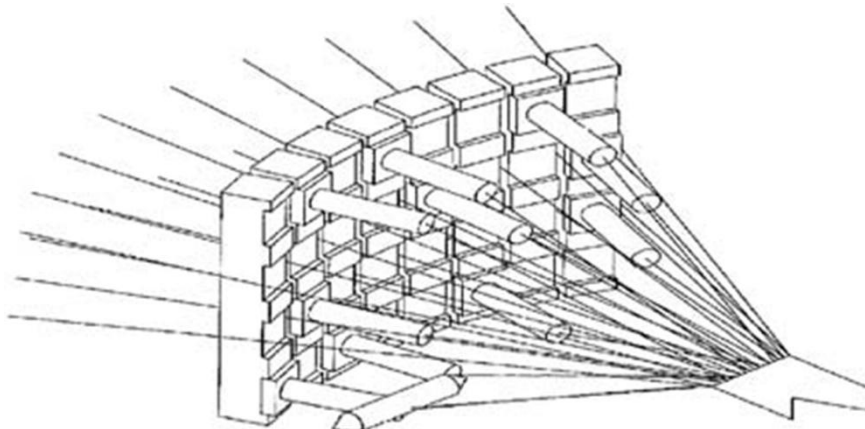


Figure 3.7: Multiaxis weaving machine developed by Nayfeh (2006).

Lima et al. (2009) developed a 2D multiaxis weaving loom, Figure 3.8-a. The manufactured fabric is composed of four yarn sets: warp, filler, + and - bias yarns. The bias yarns are fed from two rotating beams, then they pass through special tension compensation device. By stepwise transversal movement for bias yarns, they form pair of two opposite parallel uniform layers. For each weaving cycle a layer of warp yarns is raised and form with bias yarns layers a shed to insert filler yarns. However, the produced fabric is in open weave architecture, Figure 3.8-b, resulting in low fibre volume fraction obtained when it is impregnated. Furthermore, this machine is limited to 2D woven fabrics.

3. 3D multiaxis weaving technology

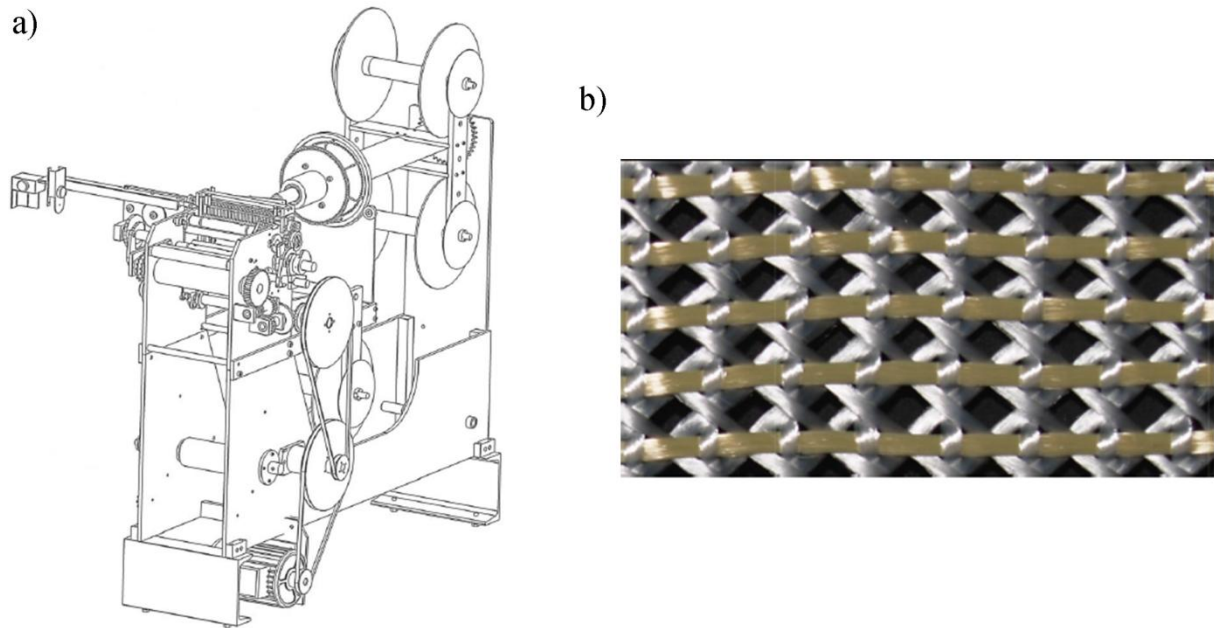


Figure 3.8: a) scheme of multiaxis weaving machine developed by Lima et al. (2009), b) architecture of produced multiaxis 2D woven fabric.

Farley (1993) presented a lappet weaving apparatus enabling insertion of bias yarns during the weaving process. This apparatus consists of needles disposed on transversal rack holding also bias yarns supply, where one bias yarn passes through needle's eye as illustrated in Figure 3.9. The holding rack is placed in front of the shedding device and it has two movements: firstly, it moves up and down forming a shed to pass filler yarns, secondly, the bias moves transversally relative to loom axis. Thereby, bias yarns are interlaced with filler yarns so an interlocked bias ply structure could be produced without limitation concerning the number of layers and bias yarns ply could be placed in any layer through the thickness. Further, this apparatus produce edge to edge bias yarns ply, but there are no details about the uniformity of produced bias layers. However, there is no possibility, by the proposed apparatus, to produce multilayer woven architecture. Otherwise, high crimp is noted for bias yarns.

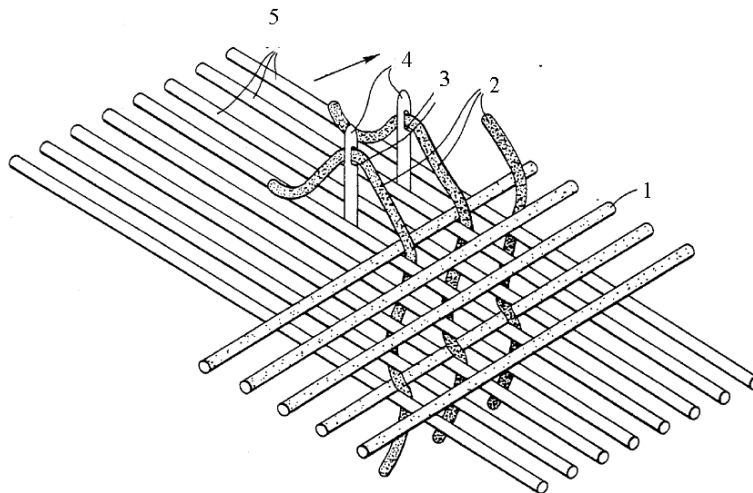


Figure 3.9: Scheme of lappet multiaxis weaving apparatus developed by Farley (1993). 1- filler yarns, 2- bias yarns, 3- needle's eye, 4- needles, 5- warp yarns.

3.3.3.2. Multilayer multiaxis weaving

Anahara et al. (1991) worked on developing a multilayer multiaxis weaving machine using screw shafts and rapier needles apparatus, Figure 3.10. The screw shafts displace the bias yarns transversally across the entire width of fabric forming edge-to-edge layer. However, as illustrated in Figure 3.10-c, a pair of non-uniform bias layers in opposite orientation is formed. The screw shafts for each weaving cycle dispose the bias yarns at right position forming proper gaps to insert rapier needle holding binder (Z) yarns in the through thickness direction of fabric. Thereby, the four in-plane yarn sets (warp, filler, + and – bias) are locked in position within the fabric by the binder yarns. So, five-axial woven structure is manufactured. Multiple screw shafts could be used on the loom to get multiaxis multilayer woven fabric.

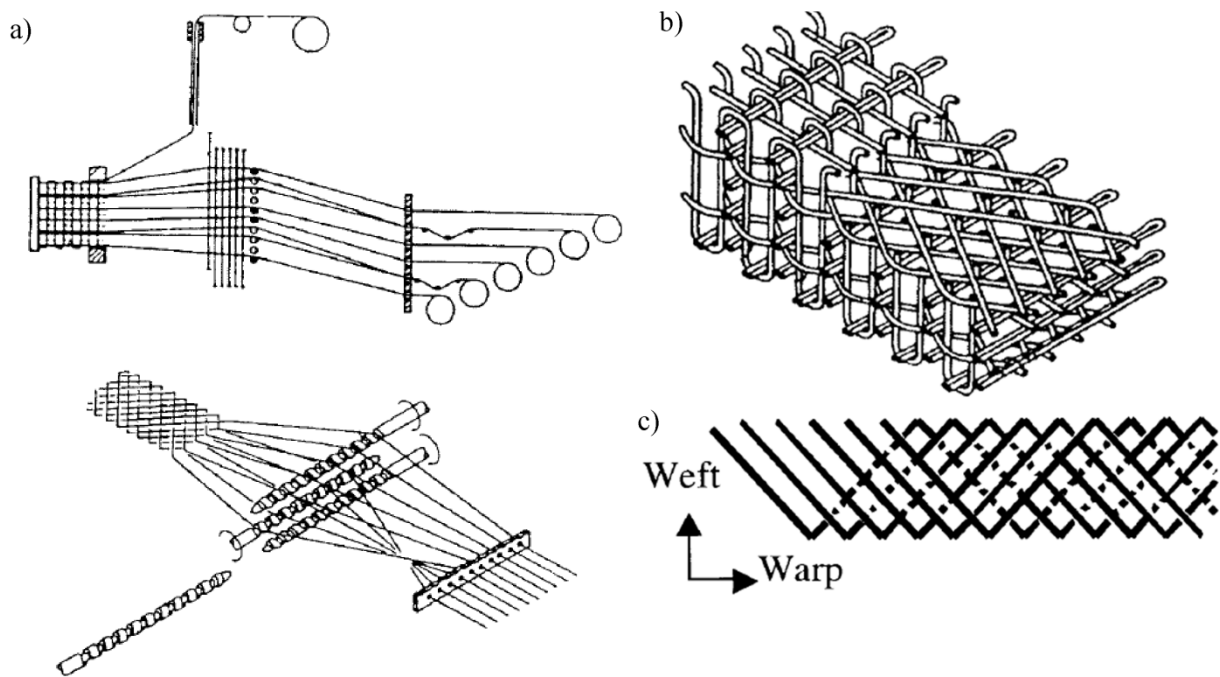


Figure 3.10: a) Schematic of developed multiaxis multilayer weaving loom by Anahara et al. (1991) using screw shaft and rapier needle, b) produced architecture, c) top view of the bias yarns path in the formed pair layers during weaving process by screw shafts.

Yasui et al. (1993) also developed 3D multiaxis weaving machine, but they used movable guide blocks to displace the bias yarns in the weaving zone instead of screw shafts, Figure 3.11. The guide blocks are actuated to move in closed cycle, Figure 3.11-b, resulting in formation of pair of uniform bias yarns layers in opposite orientation. However, that obligates to rotate the bias yarns supplying apparatus for continuous fabric production without intertwining the bias yarns. The bias yarns extend the entire fabric width that allows producing edge-to-edge layers. The rapier needles are also used to insert binder yarns in the through thickness direction to fabricate orthogonal multilayer fabric. According to Kamiya et al. (2000) using this technique to insert the fibre reinforcement into the through-thickness causes considerable damage to in-plane yarns.

Uchida et al. (1999) used as well the guide blocks to control the position of bias yarns in the weaving zone. Different method, Figure 3.12, is used to actuate the guide blocks where special means are used to displace guide blocks sideways (transversally) and shift them up or down to fold the bias yarns once they reach the fabric edge so alternating its orientation

3. 3D multiaxis weaving technology

from $(-\theta/+ \theta)$ to $(+\theta/- \theta)$ but bias yarn still in the same layer. As a result, a pair of edge to edge non-uniform bias yarns layer is formed. Thereby, there is no need for circularly moving of bias yarns supply mechanism and the bias are fed from beam. In order to control the variation of their tension during the weaving process, a tension device is developed. A pair of chain conveyors is used at the interval of fabric width to retention woven fabric in order to stabilize its width after weaving zone and to prevent high shrinkage caused by folded bias yarns.

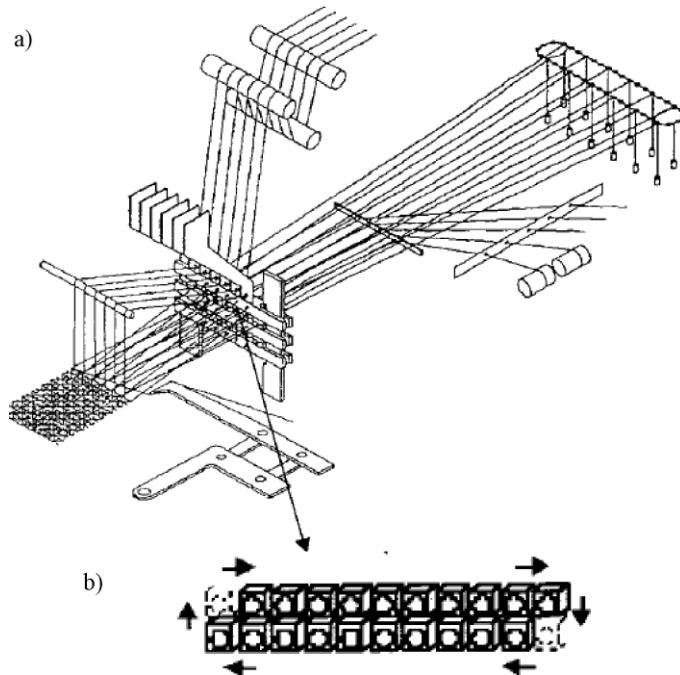


Figure 3.11: Scheme of multiaxis weaving machine developed by Yasui et al. (1993) using guide blocks (b) to control the position of bias yarns with circularly moving for feeding mechanism.

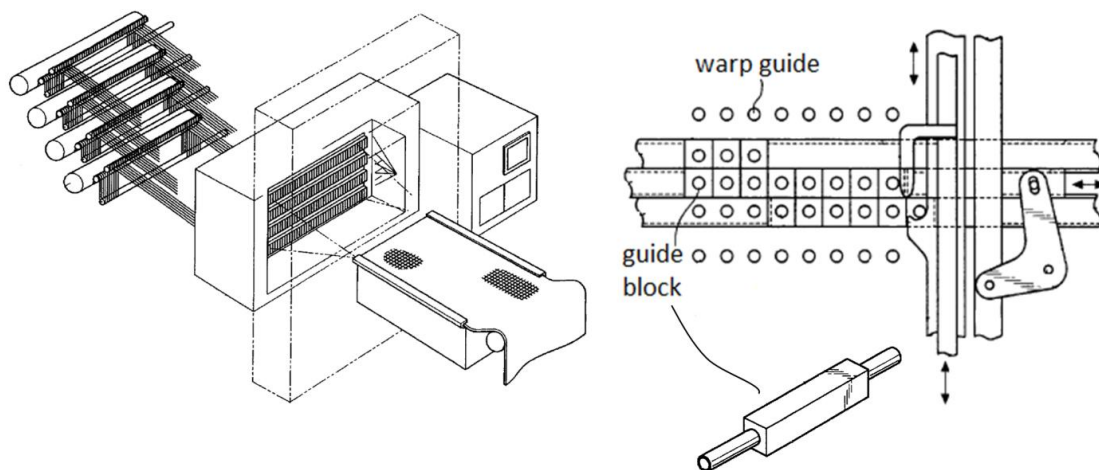


Figure 3.12: Scheme of multiaxis 3D weaving machine developed by Uchida et al. (1999) using guide blocks to control the position of bias yarns.

Bilisik and Mohamed (1994) developed a tube rapier weaving method to produce multiaxial three-dimensional fabric. Both warp and bias yarns pass through tube rapiers, Figure 3.13-a, which are arranged in a matrix corresponding to a cross section shape of demanded preform. Filler and binder yarns are inserted by needles passing between the tube rapiers of

3. 3D multiaxis weaving technology

bias and warp yarns. That reduces the damage incurred by insertion of the needles to warp and bias yarns met in other technologies. Tube rapiers of bias yarns displaces only transversally with respect to the loom main axis, Figure 3.13-b. The yarns are folded when it reaches the fabric edge but they are still in the same layer resulting in zig-zag non-uniform bias yarns layer, Figure 3.13-c (Bilisik, 2010). On this loom, the bias yarns layer could be placed in any layer in through the thickness of the fabric allowing producing a 3D multiaxis woven fabric.

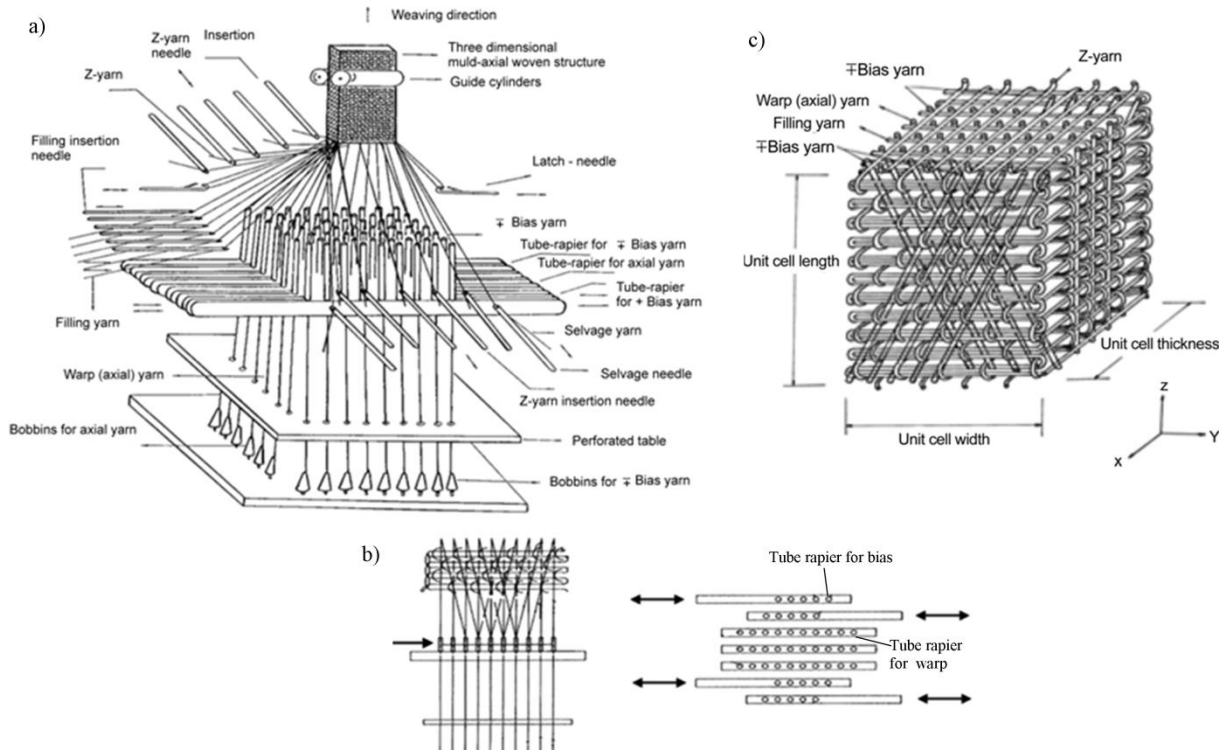


Figure 3.13: Tube rapier weaving method; a) scheme of developed multiaxis 3D weaving machine, b) representation of transversal movement of each assembly of tube rapier for one bias yarns layer, c) a unit cell of produced fabric illustrating of zig-zag path of bias yarns across fabric width, (Bilisik 1994, 2010).

In order to get pair of opposing uniform edge to edge bias yarns layer within multiaxis 3D woven fabric, Bilisik and Mohamed (1995, 2010) developed another weaving method using a tube carrier. So each bias yarn is feed from individual bobbin then it passes through one tube. The tubes move transversally inside a box and when one tube reaches fabric edge, it is shifted up or down to the next opposite bias yarns layer so it changes its orientation from $(-\theta/+ \theta)$ to $(+ \theta/- \theta)$ Figure 3.14-b. Thereby, the tubes are in a circular movement requiring circular moving for feeding bobbins. The filler yarns and the binder yarns are inserted in the same manner as tube rapier weaving method by means of rapier needles. The applied tension on folded bias yarns while weaving process leads to high shrinkage for fabric width and trapezoidal weaving zone as illustrated by Figure 3.15; the difference between the fabric width and weaving zone width. As consequence, the standard reed, having fix gap width between its blades, could not be used because of high friction between the inclined bias yarns and reed blades. Therefore, a special reed is used to beat the filler yarn into fabric formation line. In this reed, the distance between its blades decreases as it advances toward the fabric. However, this type of reed still causes important friction with in-plane yarns (Bilisik and Mohamed 2010) and rotation of blades around its axis is also required. Otherwise, the needles rapiers damage also the in-planes yarns.

3. 3D multiaxis weaving technology

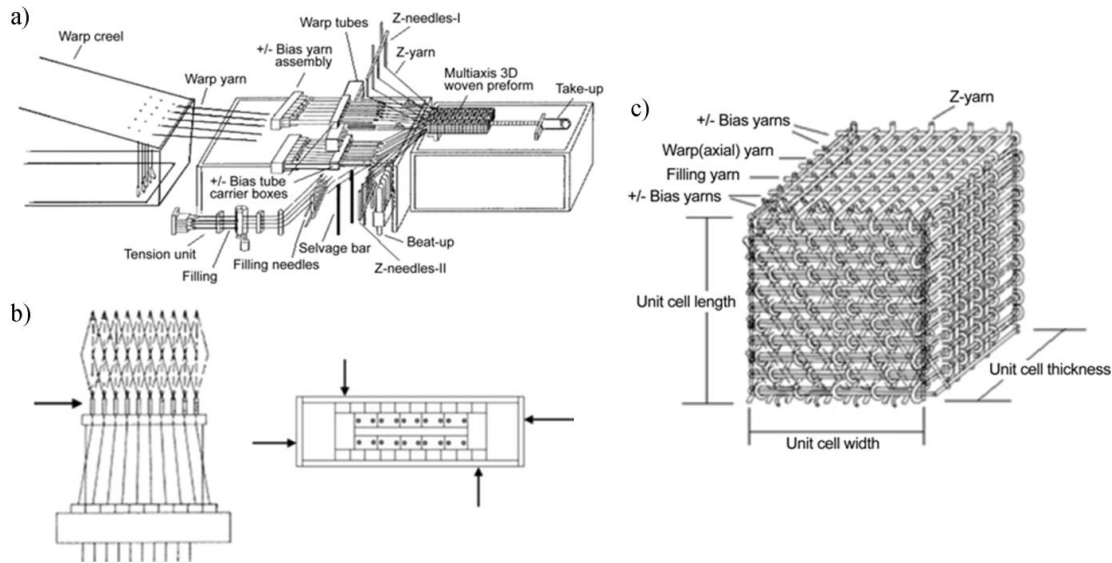


Figure 3.14: Tube carrier weaving method; a) scheme of developed multiaxis 3D weaving machine, b) representation of circular moving of each assembly of tube carrier for one bias yarns layer, c) a unit cell of produced fabric illustrating of edge to edge path of bias yarns across fabric width, (Bilisik 1995, 2010).

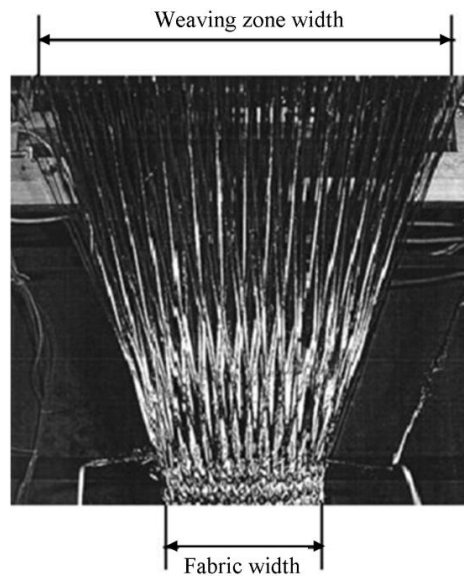


Figure 3.15: Weaving zone on a developed multiaxis 3D weaving machine by Bilisik (1995, 2010) using tube carrier weaving method.

3.3.3.3. Polar multilayer multiaxis weaving

Yasui et al. (1992) developed a polar multiaxis 3D weaving loom, Figure 3.16-a. This machine is capable of fabricate preforms made of 24 layers (circumferential filler yarns, bias yarns and axial warp yarns) with through the thickness fibre reinforcement (radial yarns). That is carried out by 144 yarn bobbins exchanged between two disks which are able to rotate and translate. Nevertheless, the large shedding motion resulting from exchanging the bobbins between the two disks could cause fibres damages. Further, concerning this method, it seems to be complex for high production rates.

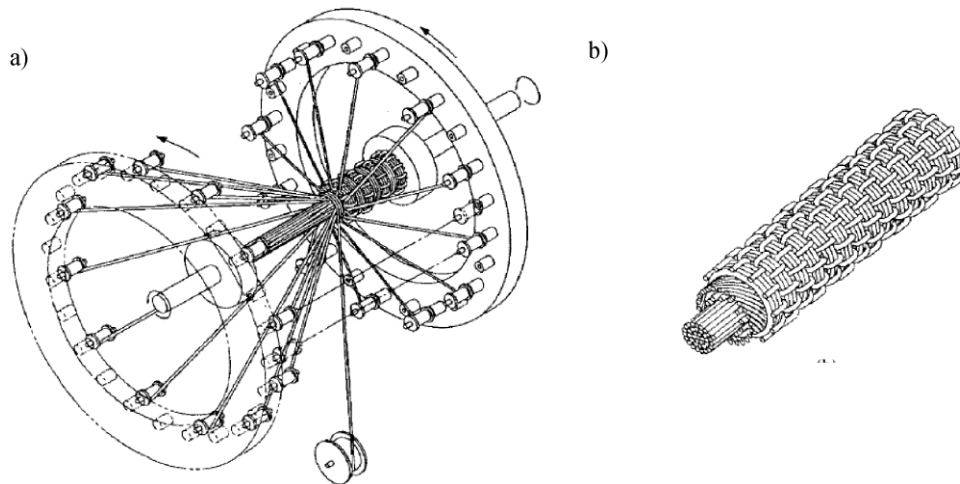


Figure 3.16: a) Polar multiaxis weaving machine developed by Yasui et al. (1992), b) architecture of fabricated woven preform.

Bilisik (2000) developed a multiaxis 3D circular weaving loom based on the 3D braiding principle, Figure 3.17. The axial yarns form warp yarns and circumferential yarns form filler yarns while the bias yarns are fed by braider bobbins and placed only on the outside and inside surfaces of cylinder. The radial yarns form through the thickness yarn linking the different layers and they are inserted by means of special carrier units. This machine could produce thick and thin cylinders and the presence of bias yarns improves its torsion properties, as reported by Bilisik (2012).

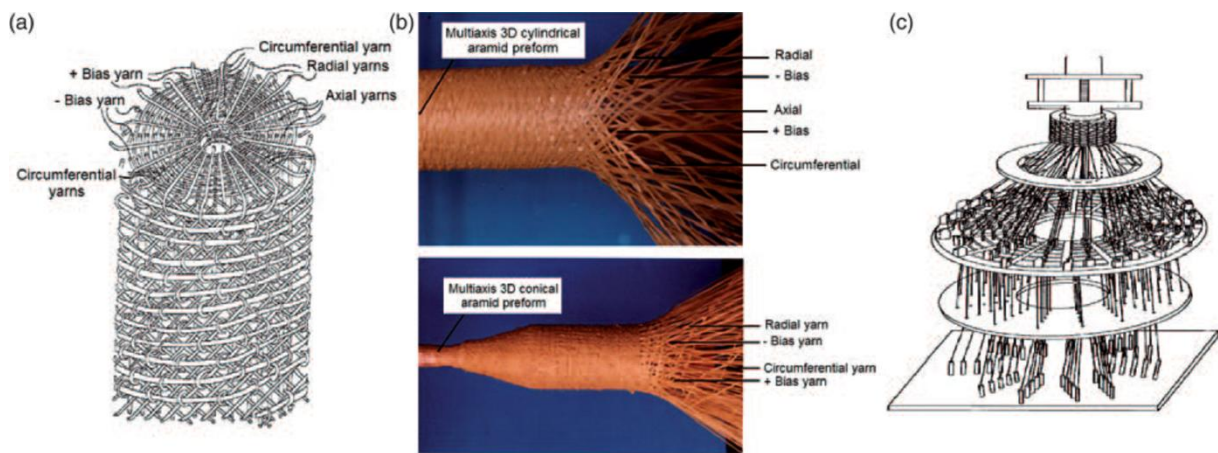


Figure 3.17: Cylindrical multiaxis 3D woven preform architecture (a), preform and weaving zone on polar loom (b), polar multiaxis 3D weaving loom, (Bilisik 2000, 2012).

3.3.3.4. Characteristics of bias yarns layer within multiaxis woven fabric

Across different developed weaving methods, dedicated to produce multiaxis woven fabric, various architectures dedicated to form bias yarns layers and fabric are obtained. The essential architecture characteristics of bias yarns layer could be summarised as follows:

- One single layer or pair of inherent opposite (- and + θ) layers of bias yarns is formed.
- Number and position of bias yarns layers in through the thickness of fabric produced on the loom.
- Bias yarns path pattern across the fabric width. The bias yarns do not extend across the entire fabric width “zig-zag pattern”, Figure 3.18-a. Or they extend across the entire fabric width “edge to edge pattern”, Figure 3.18-b, (Bilisik 2010).

- Uniformity of bias yarns orientation. The bias yarn alternates its orientation from $(-\theta/+ \theta)$ to $(+ \theta/- \theta)$ as it reaches the fabric edge and it is folded to next bias layer, Figure 3.19-a, resulting in formation uniform bias layers. On the contrary, if the bias yarn is folded and kept in the same layer, Figure 3.19-b, a non-uniform bias yarn is formed, (Kamiya et al 2000). Otherwise, producing uniform bias layers requires necessarily circularly moving of bias yarns feeding system to prevent intertwining of bias yarns while fabric progress. However, that is not required for producing non-uniform bias layers, but tension-controlling system is needed to maintain constant yarns tension during the weaving process as bias yarns path changes.

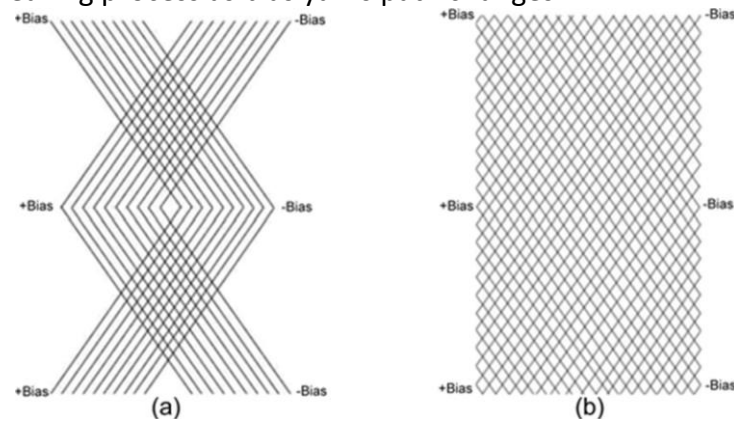


Figure 3.18: Schematic of the bias yarns path pattern: a) zig-zag pattern, b) edge to edge pattern, (Bilisik 2010).

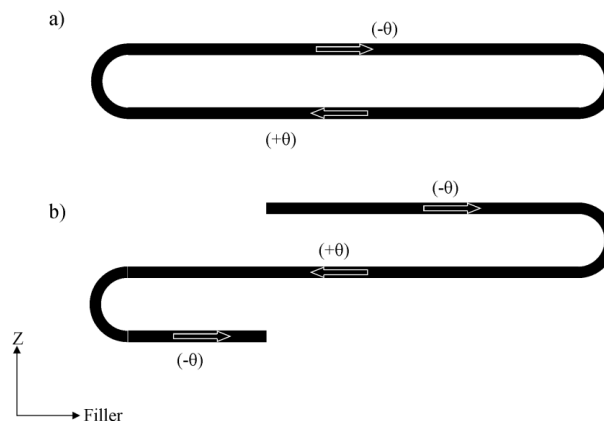


Figure 3.19: Two patterns of bias yarns path, a) bias yarn is folded to next opposite bias layer, b) bias yarn is folded and kept on same layer.

3.3.3.5. Classification of innovated multiaxis weaving techniques

Different criteria and parameters used to classify multiaxis weaving techniques are mentioned in the literature. Kamiya et al. (2000) takes into account the uniformity of bias yarn layers, the presence of through the thickness reinforcements and an ability to produce multilayer fabric as criteria in his classification. Whereas, Bilisik (2012) based his classification on the produced fabric properties including number of yarns sets and their orientations, type of their interlacements, possible fibre volume fractions and machine development stage. Here, in order to obtain general classification of developed techniques the two aforementioned classification techniques are combined and reformulated, table 3.1.

3. 3D multiaxis weaving technology

Table 3.1: Classification the multiaxis weaving technologies introduced in the literature;

Multiaxial weaving loom	Yarn sets	Interlacement of bias with other in-plane yarns	Multiple layers	Uniformity of bias layer	Fiber volume fraction ^a	Development stage ^a	technique comments
Ruzand and Guenot (lappet)	warp/filler/±bias	No, bias locked by warp and filler interlacement	No (4)	Yes	Low or medium	Commercial	±bias only on fabric faces
Mood (split reed)	warp/filler/±bias	No, bias locked by warp and filler interlacement	No (4)	Yes	<i>No data</i>	<i>No data</i>	High large shedding motion
Bryn (hook)	warp/filler/±bias	Yes, bias interlace with warp and filler	No (4)	Yes	Low or medium	Prototype	various cross section, no continuous
Nayfeh (braider bobbins)	warp/filler/±bias	No, bias locked by warp and filler interlacement	No (4)	Yes	Low or Medium	Prototype	special preform cross section
Lima (rotating beam)	warp/filler/±bias	No, bias locked by warp and filler interlacement	No (4)	Yes	Low	Prototype	open weave
Farley (lappet)	warp/filler/±bias	Yes, with warp and filler, (angle interlock)	Yes	Yes	<i>No data</i>	<i>No data</i>	High bias crimp, single bias layer
Anahara (screw shaft)	warp/filler/±bias/Z	No, orthogonal	Yes	No	Low	Prototype	
Yasui (guide block)	warp/filler/±bias/Z	No, orthogonal	Yes	Yes	Medium	Prototype	
Uchida (guide block)	warp/filler/±bias/Z	No, orthogonal	Yes (5)	No	Low	Prototype	maintain fabric width
Bilisik (tube rapier)	warp/filler/±bias/Z	No, orthogonal	Yes	No	Medium (33.9 %) ^b	<i>No data</i>	zig-zag ±bias layers
Bilisik (tube carrier)	warp/filler/±bias/Z	No, orthogonal	Yes	Yes	Medium or high (38.5-47.5) ^b	Prototype	high fabric ratio ^c
Yasui (Polar)	axial/circumferential/±bias /radial	No, radial links layers	Yes (24)	Yes	<i>No data</i>	<i>No data</i>	cylindrical preform
Bilisik (Polar)	axial/circumferential/±bias /radial	No, radial links layers	Yes	Yes	High	Early prototype	cylindrical preform

a: according to Bilisik's (2012) classification, b: according to produced samples by Bilisik (2009). c: fabric ratio = weaving zone width/fabric width.

3.4. Developed multiaxis multilayer weaving loom

The aim of this project is the construction of a prototype loom consecrated to fabricate planar multiaxis multilayer woven performs. The interest of this performs comparing to other woven preform architectures, as mentioned earlier in the chapter 2, is getting a symmetric bias ($\pm\theta^\circ$) fibre reinforcement layers allowing to overcome poor shear in-plane properties of conventional woven composite, (Bilisik, 2012). Like other multilayer woven architectures (orthogonal and interlock), through the thickness fibre reinforcement is inserted during the weaving process to link the different in-plane layers. That allows to obtain a good delamination and impact resistance and to improve post-impact properties (Guénon et al. 1989, Liu et al. 1989, Cox et al., 1993), contrary to laminate composite made by stacking of unidirectional fibre reinforcement laminas or 2D woven fabric without through the thickness fibre reinforcement.

On another side, as mentioned earlier stitching technology could be also employed to insert fibre reinforcement through the thickness of laminate with the possibility to vary the orientation of in-plane lamina and to get good in-plane mechanical properties. Though, important degradation for in-plane properties of perform is incurred because of needle insertion and stitch loop, (Mouritz and Cox 2000). That explains why the weaving technique was preferred here.

Among 3D weaving architectures, an orthogonal one is preferred due to its less incurred crimp for in-plane yarns comparing with other interlock architectures, resulting finally in less reduction of in-plane properties (Leong et al. 2000).

Regarding the mechanics of laminate composite structure, Mallick (2008) and Halal et al. (2012) noted that the high angle between successive lamina causes high delamination stresses at the free edge of the structure. That is why high angles should be avoided in the design and manufacture phases. Similarly, for 3D woven composite structure, high angle between successive layers should be also avoided. However, by the developed 3D multiaxis weaving techniques explored earlier pair of successive opposite ($+\theta^\circ$ and $-\theta^\circ$) bias yarns layers is formed without the possibility to insert warp or filler yarns layer between them. Therefore, a modified guide blocks technique is developed enabling insertion pair of opposite uniform bias yarns layers separated by a warp yarns layer. The effect of this architecture modification will be investigated more deeply in the chapter 5. Furthermore, the used guide block mechanism is simplified as well as other weaving mechanisms in order to minimize the corrosion and the degradation induced to warp and bias yarns by moving machinery.

Series of operations is realized on prototype multiaxis weaving loom in order to produce desired architecture. These operations are performed by mechanisms, Figure 3.20, whose functions and composition are detailed as following.

3.4.1. Warp yarns feeding

Multiple layers of warp yarns are required for multilayer weaving. That is what differentiates this technology from the conventional 2D weaving. The thickness of the fabric is directly proportional to the number of layers used.

Here, beams are not used to stock and supply totality of warp yarns as on conventional 2D loom. Each warp yarn is fed from single bobbin mounted on braider bobbin carrier equipped with tension compensation device serving on maintain constant yarn tension while weaving process, Figure 3.21-a. The lock of tension compensation device prevent the bobbin from rotation to supply more yarn until the yarn tension (F) overcome the moment applied by the

3. 3D multiaxis weaving technology

spring on the movable bar and the pivot segment as illustrated in Figure 3.21-b. The yarn tension (F) could be loaded by the choice of spring rigidity used for tension compensation device. Using of this braider carrier instead of beam gives flexibility for this prototype loom stage regarding manage number of warp yarns per unit length and number of warp yarns per layer as well as number and sequence of layers.

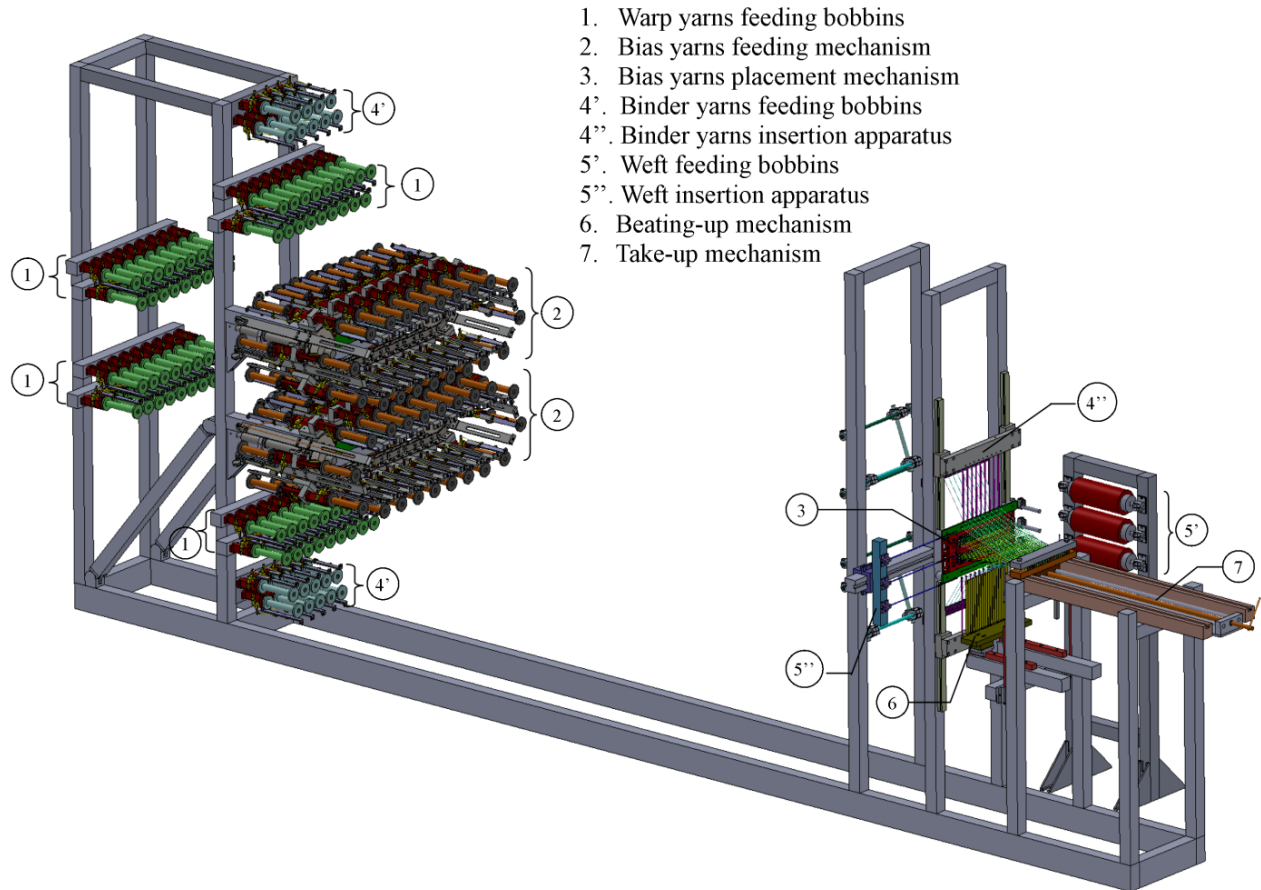


Figure 3.20: Isometric view of developed prototype of multiaxis weaving loom.

The warp yarns run in machine direction (main loom axis) from feeding bobbins to formed fabric. As there are no interlacements between warp and weft yarns for designed architecture, instead of using heddles mounted on movable harnesses to control yarns positioning in the weaving zone, fixed guide bars with a row of eyes are used and through these eyes the warp yarns are passed, Figure 3.22 and Figure 3.25. The bars eyes are circular and smooth helping to minimize the friction in case of brittle high performance fibres. The number of eyes per unit length on guide bar is associated to the number of warp yarns per unit length on fabric.

3.4.2. Bias yarns feeding

Like the warp yarns, each bias yarn is fed from single bobbin mounted on braider bobbin carrier equipped also with tension compensation device to maintain constant tension. However, contrary to braider bobbins of warp yarns, which are unmovable and attached to loom support, those of bias yarns are mounted on rotative chain Figure 3.22. That enables transversal movement of bias yarns in the weaving zone, without entangling the yarns near the bobbins. Therefore, uniform bias yarns layers could be obtained. The braider bobbins are disposed on two sides of the chain to keep its equilibrium. Thereby, guide roller is used to direct back bobbin yarn to weaving zone Figure 3.22. The chain moves one step for each

weaving cycle. On the chain the yarns of upper bobbins form bias fibre layer oriented in a direction θ° within fabric while the yarns of lower bobbins form opposite bias layer (oriented in a direction $-\theta^\circ$). Guide bar is used to keep warp yarns between two opposite bias yarns layers in correct path without intersecting with chain or braider bobbins support. Two chains are mounted on prototype loom. Hence, four bias yarns layers could be obtained within produced fabric.

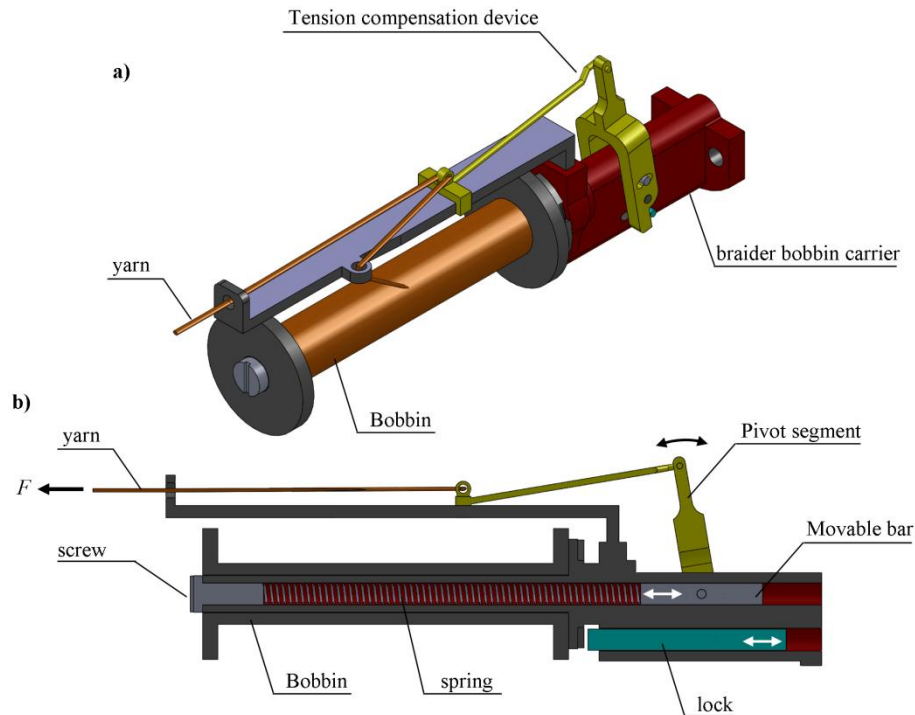


Figure 3.21: Bobbin holder on braider bobbin carrier used to supply warp and bias yarns (a) cut view along with the main carrier axis (b).

3.4.3. Bias yarns positioning mechanism

As mentioned earlier, the transversal displacement with respecting loom axis is required for bias yarns to be oriented in $\pm \theta^\circ$ within the fabric. This displacement should be realized with appropriate positioning for bias yarns in the weaving zone to assure right insertion of the binder yarns needles and the open reed without intersecting with bias yarns.

By exploring developed multiaxis weaving technique responding to this requirement, guide block technique appears as convenient technique for production uniform multiaxis multilayer woven preform. Therefore, it was applied for the present prototype weaving loom. Some modifications are however required enabling the insertion of a warp layer between two opposite bias yarns layers as well as to simplify actuating mechanism and minimise yarns-machineries friction.

One guide block is used for each bias yarn which passes through its central eye. The guide block is made in particular shape, Figure 3.23 that facilitates its sliding along closed frame with adjacent blocks and around central warp yarns guide bar. To displace the blocks within the closed frame, four sliding sticks are used to push the blocks one step transversally. Also two sticks, moving up/down, are used to translate a block from a layer to the opposite one. Thus, the displacement of the guide blocks inside the frame is along with a closed rectangular path around a central warp yarns guide bar kept into fixed position. For each weaving cycle the guide blocks displace one step. This displacement is executed by three moving steps for the actuating sticks. These steps are illustrated in Figure 3.23 and Figure

3. 3D multiaxis weaving technology

3.24 with tracking the position of the blue guide block as reference. As shown in Figure 3.25 the guide blocks are divided into two level, the bias yarns of guide blocks of upper level will obtain $+ \text{ or } - \theta^\circ$ direction within the fabric whereas those of lower level will obtain opposite orientation. The totality of bias yarns passing through guide blocks attached to one frame are fed from braider bobbins mounted on one chain. Thereby, number of bias yarns feeding chain is equal to that of frame holding guide blocks. For the designed architecture on present prototype loom two frames are mounted. The number of frames could be modified, but it should be even to get symmetric structure to its mi-plane.

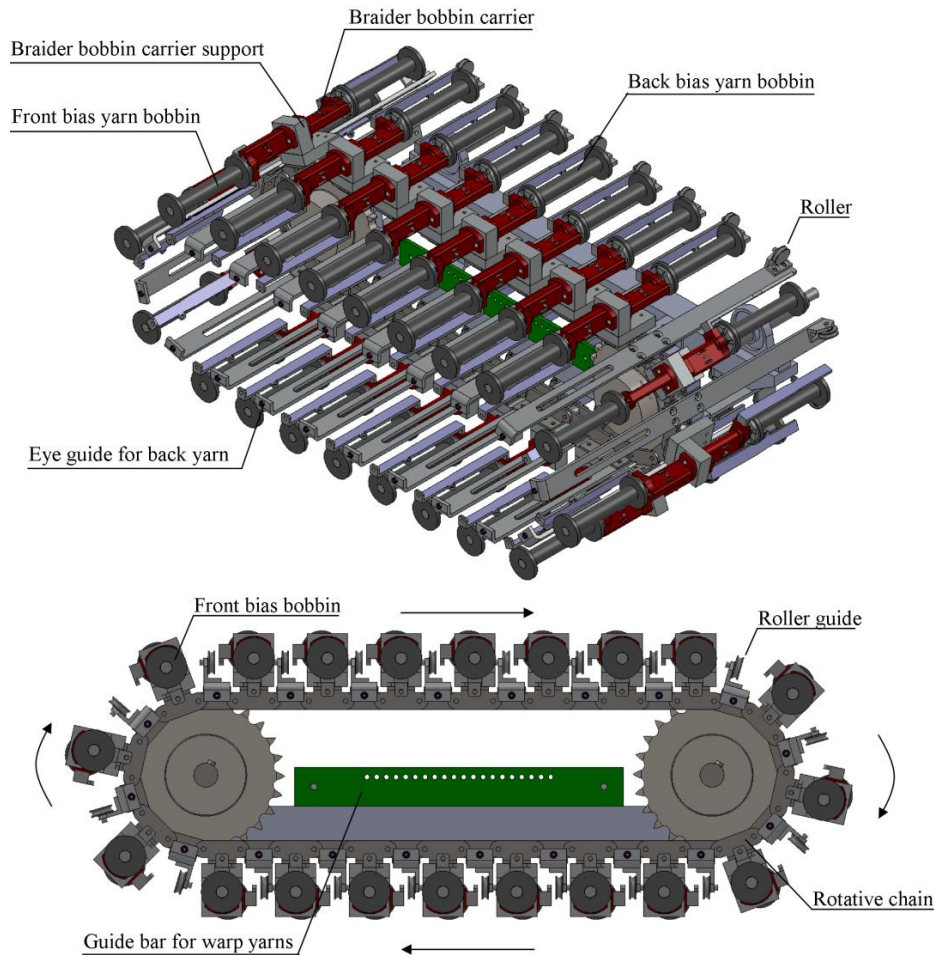


Figure 3.22: Bias yarns feeding mechanism.

3.4.4. Binder yarns insertion

In order to bind the different layers of fabric, binder yarns are inserted in through the thickness of the fabric and interlaced with the outer filler yarns. Like the warp yarns, single braider bobbin supplies one binder yarn with controlled tension into weaving zone. Since the weave pattern of the designed fabric is orthogonal architecture, just two alternative positions on the two faces of fabric are required for binder yarns while weaving process. Thus, two sheds are created alternatively on the two outer faces of fabric between binder yarn and last warp yarns layers to insert two filler yarns. Therefore, it is not necessary to position the binder yarns and to create shed inside the structure (between in-plane layers).

3. 3D multiaxis weaving technology

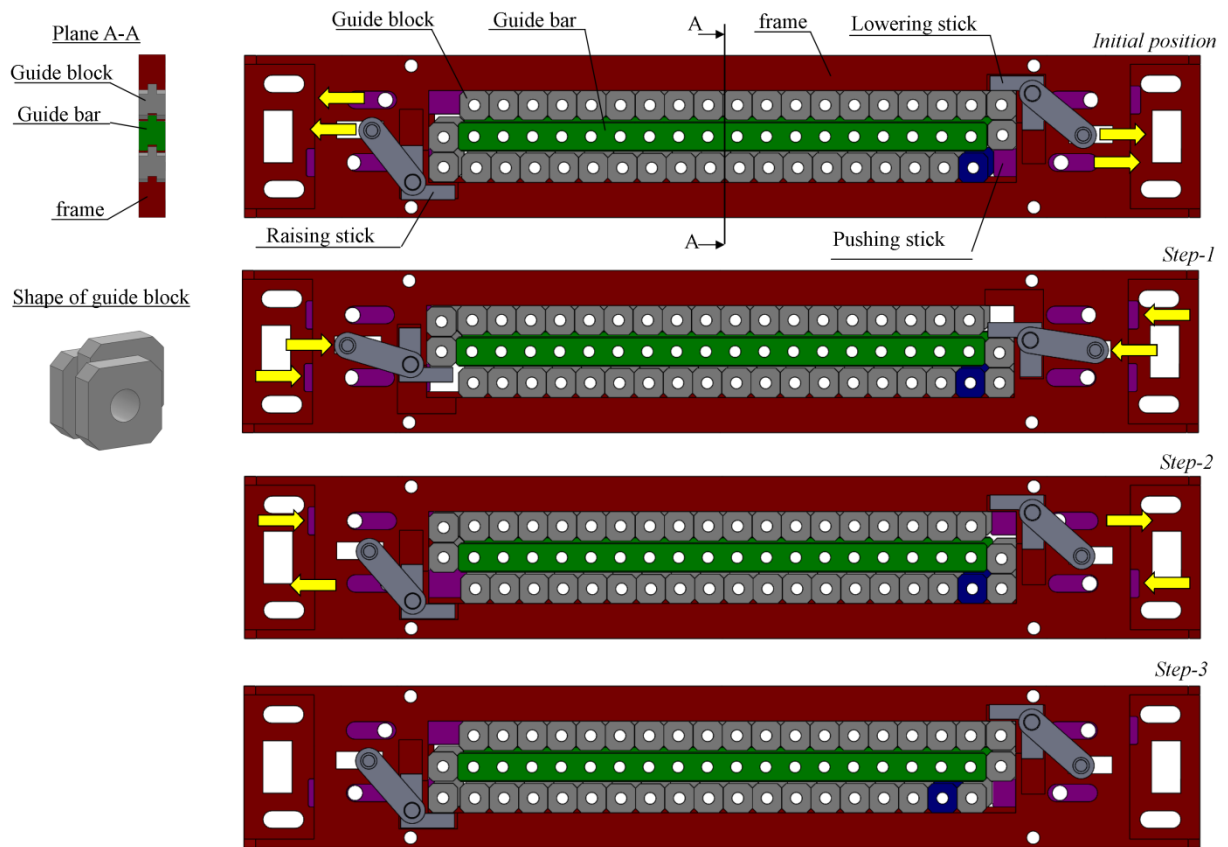


Figure 3.23: Bias yarns positioning mechanism.

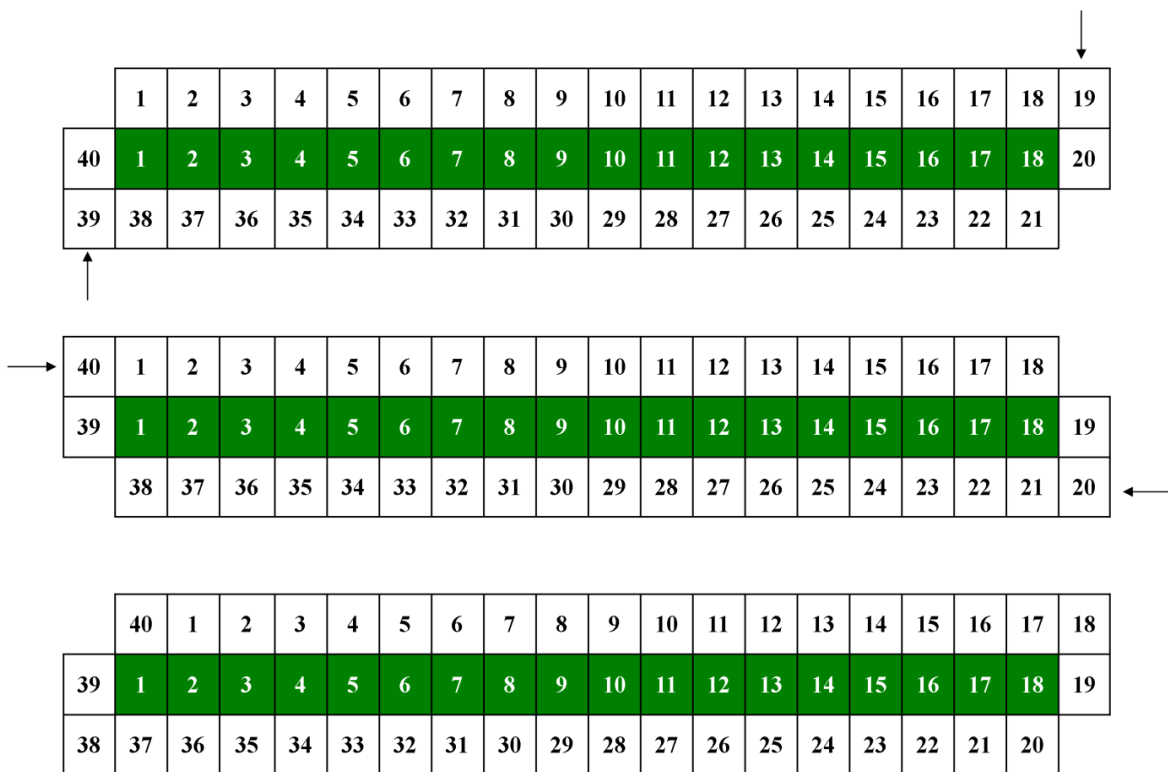


Figure 3.24: Three steps to displace guide blocks of bias yarns one step for a weaving cycle.

3. 3D multiaxis weaving technology

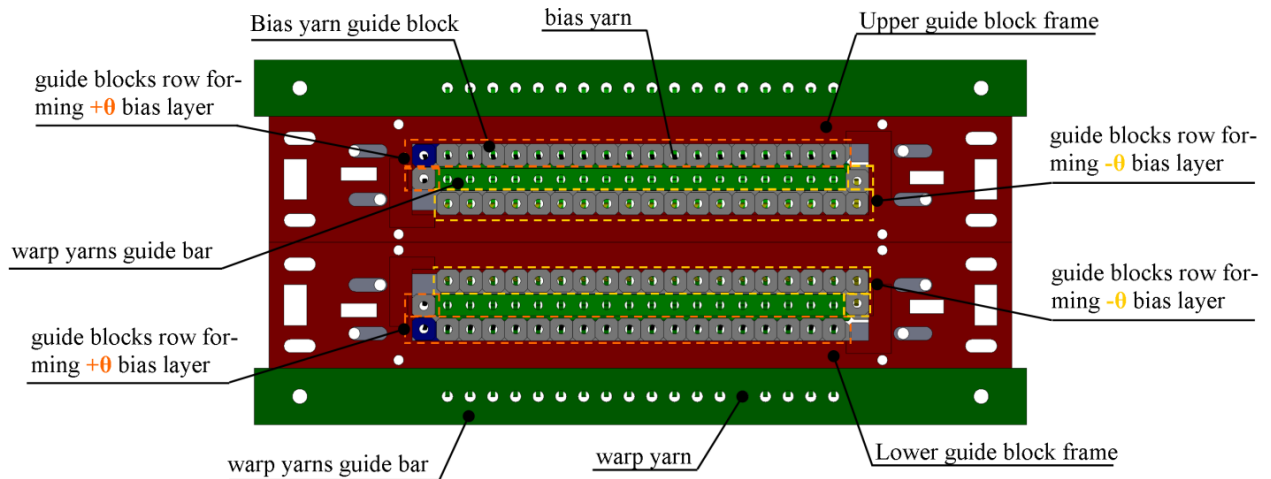


Figure 3.25: arrangement of warp and bias yarns in the weaving zone by guide bar and guide blocks.

For insertion of binder yarns, a type of needle is used instead of heddles. The needles are attached to the loom from one end in order to move the binder yarns up and down between the warp and bias yarns whereas heddles are attached from their two ends. And that prevent transversal movement of bias yarns in the weaving zone. One end of the needles are fixed to transversal bar moving up/down via two Guide-ways attached to loom support, Figure 3.26. Two groups of needles are used, one on each fabric faces, with alternative distribution of needles between these two groups. That enables two simultaneous insertions of filler yarns resulting in symmetrical filler yarns layers to fabric mid-plane.

As a result of transversal movement of bias yarns, the $+\theta$ and $-\theta$ bias yarns are crossed in the weaving zone, Figure 3.27, and small gaps are created between them. Through these gaps the binder needles are inserted and its largest width is at bias yarns guide blocks plane. However, insertion too near to guide blocks increasing the bending curvature. That is why for fibre having low flexibility as glass fibres, a high bending stress is generated and it is broken during a weaving process, Figure 3.28. The binder yarns have recoil motion by applying weights to take back the extra binder yarn to maintain tension.

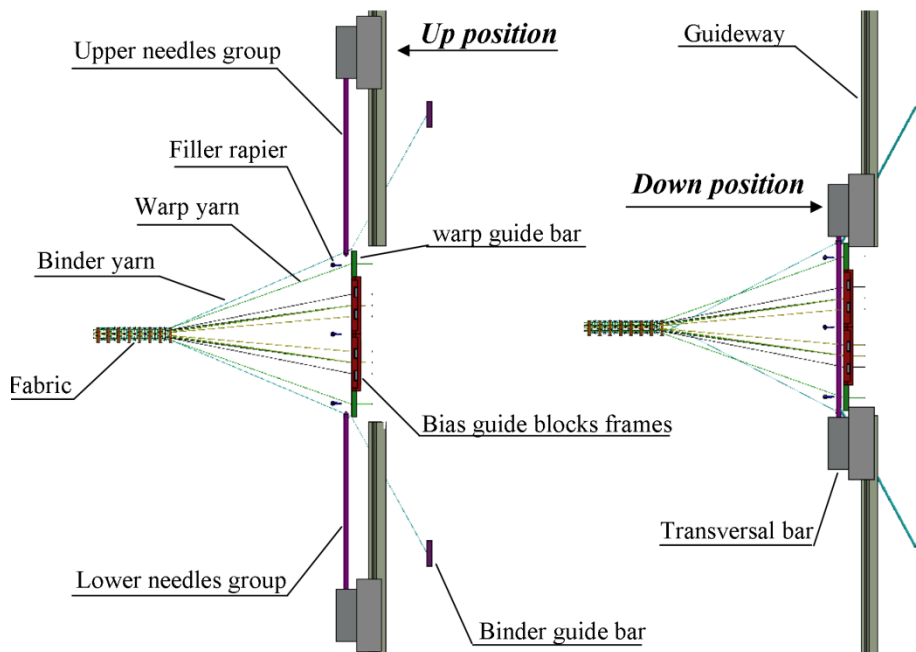


Figure 3.26: Binder insertion mechanism in its two positions

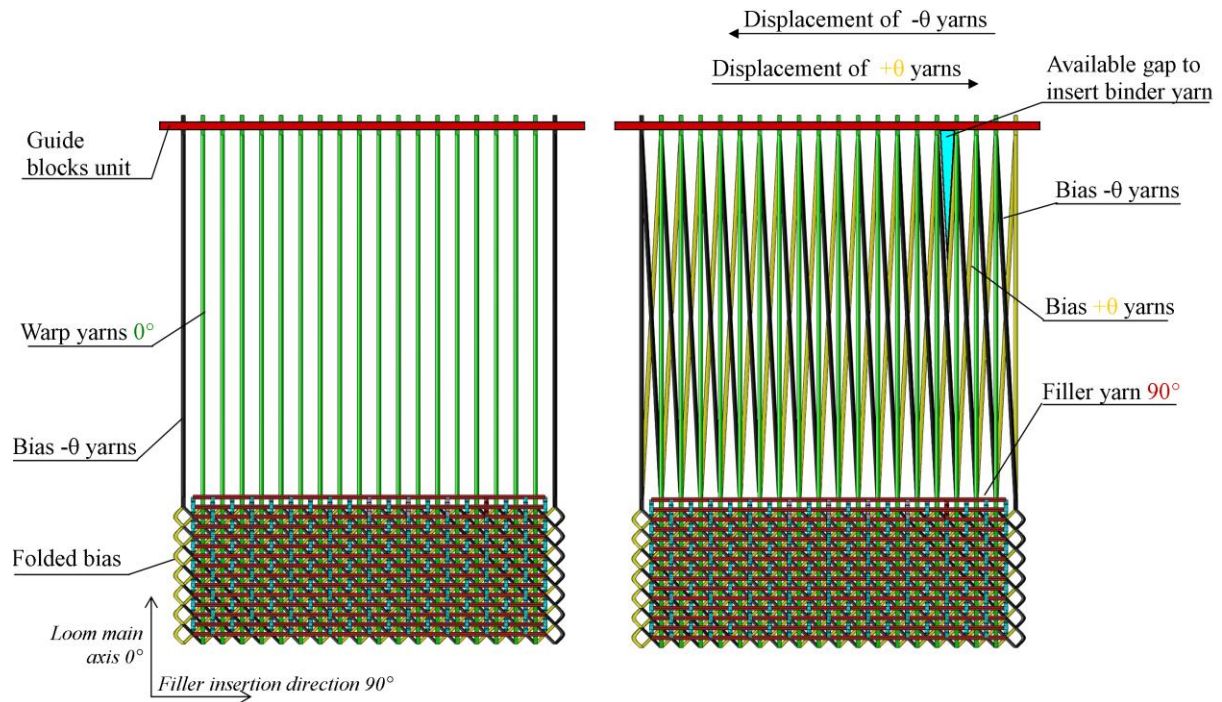


Figure 3.27: Top view of weaving zone before and after transversal movement of bias yarns with illustration available gap created by crossing $+\theta$ and $-\theta$ bias yarns to insert binder needle.

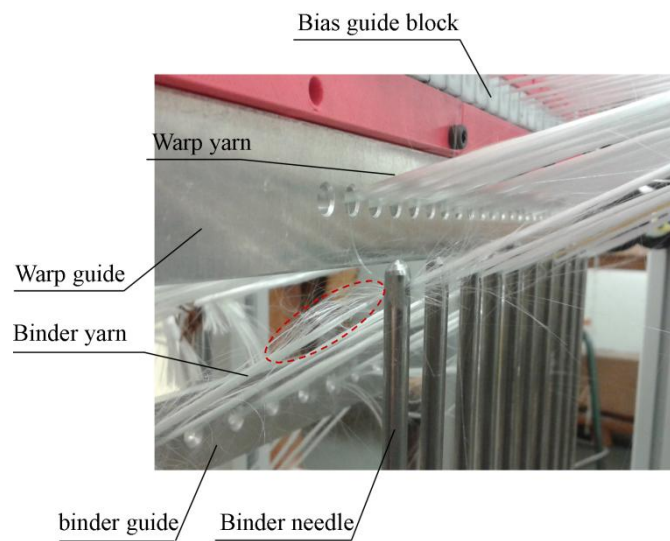


Figure 3.28: Broken glass fiber when it was used as binder yarn.

3.4.5. Filler yarns insertion

The filler insertion is done by standard rapier method. The rapier with hook head shape passes through created shed across the weaving zone width to pick up filler yarn, Figure 3.29. Then, the rapier moves back taking filler yarn. As a result, a loop of filler yarn (double filler) is inserted and the filler yarn is continuous along fabric, Figure 3.30. To achieve this insertion properly two engaging rods are used. The first one (engaging rod -1) is at the fabric edge on the side of filler bobbin. The second one (engaging rod -2) is on the opposite side where the rapiers apparatus. Engaging rod -1 is positioned at the fabric formation line and it has one vertical motion (up/down). Engaging rod -2 has two motions: firstly horizontal motion where it alternates its position along fabric edge between fabric formation line and front bias yarns guide blocks, secondly vertical up/down motion.

3. 3D multiaxis weaving technology

For present architecture three sheds are created, Figure 3.31; the first one is on the top of the outer face of fabric between last warp yarns layer and one group of binder yarns, the second one is at the mid-plane of fabric between the two symmetric bias yarns layers and the third one is on the bottom outer face of fabric between last warp yarns layer and second group of binder yarns. Three simultaneous insertions are achieved via three rapiers. Each rapier pull one filler yarn fed from individual bobbin located on the opposite side of loom. The three rapiers are fixed to vertical bar sliding one horizontal Guide-way, Figure 3.29. Filler bobbins are positioned on the right side of loom while rapiers are on the left one. To insert a loop of filler yarn, five steps should be executed as shown by Figure 3.30.

1- Following last filler insertion engaging rod -1 is moved up to maintain last inserted filler yarns into position and prepare next insertion while engaging rod-2 is driven down and in front of bias guide blocks.

2- Rapiers are inserted through sheds across loom width. They pick up filler yarns via their hook head.

3- Rapiers move back to their initial position taking filler yarns in form of loop.

4- Engaging rod-2 moves up to catch yarns that are released from rapier head.

5- Engaging rod-2 advances toward fabric to hold inserted filler yarns while it is beating up by reed. And engaging rod-1 moves down to release the previous filler yarns then it moves up again to maintain the new inserted filler yarns. Finally engaging rod-2 moves down and come back to its initial position in front of guide blocks frames

The number of filler insertion forming one column of filler yarns through the thickness of the fabric could be varied on this prototype loom.

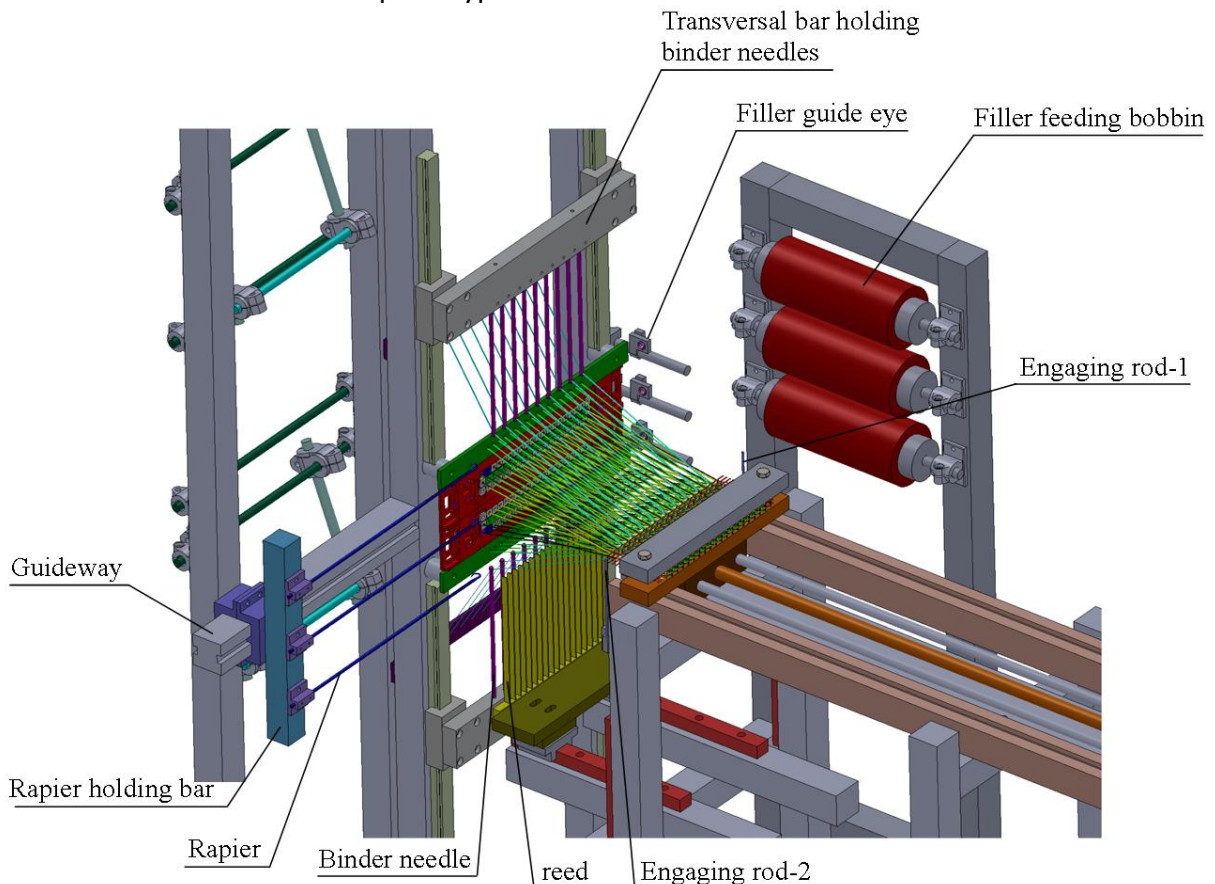


Figure 3.29: Isometric view of weaving zone.

3. 3D multiaxis weaving technology

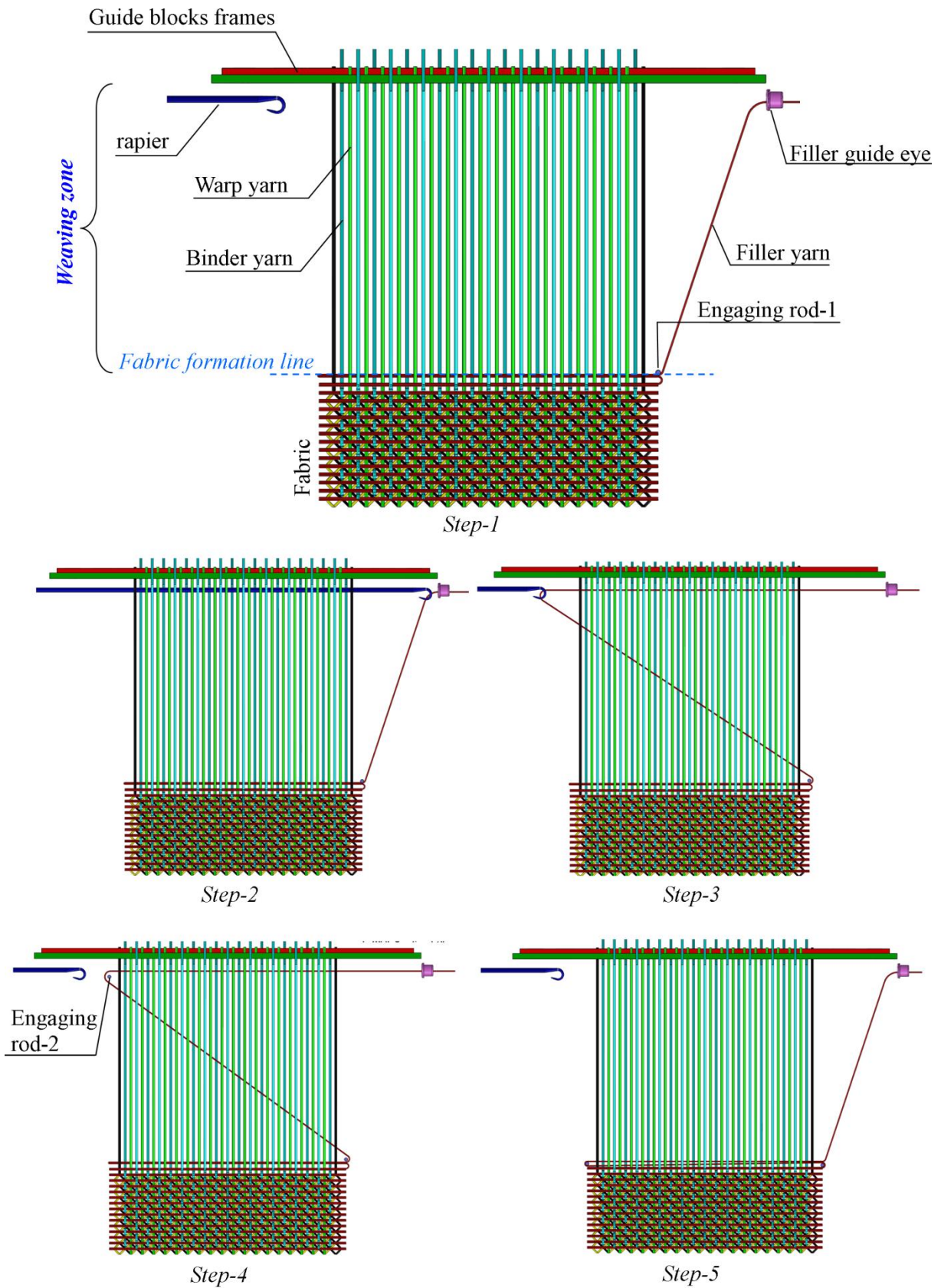


Figure 3.30: Top view of weaving zone illustrating the 5 steps of insertion the filler yarn.

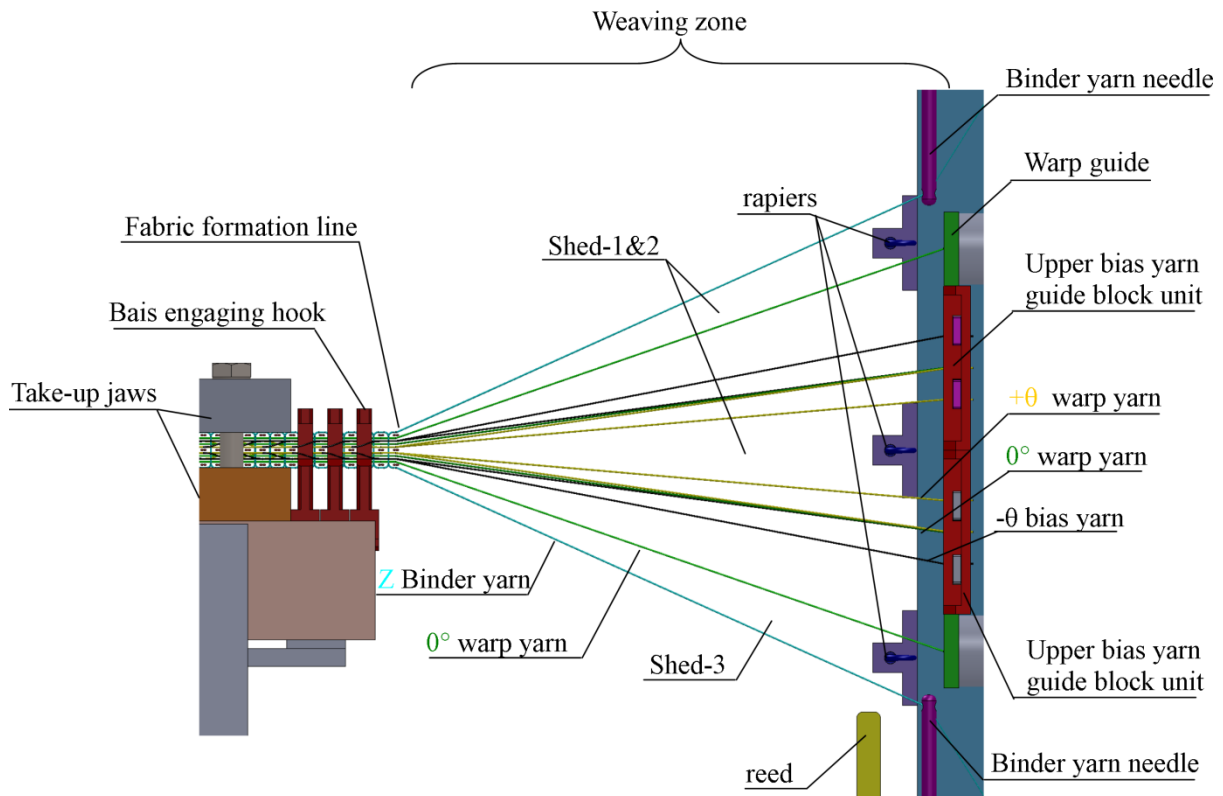


Figure 3.31: Side view of weaving zone illustrating the three created sheds.

3.4.6. Beating up

On 2D and 3D loom, a reed is employed to beat-up inserted filler yarns to formed fabric. This reed consist of arranged parallel blades separated by even distance and maintained from two (up and bottom) sides forming closed reed, Figure 3.32. In the gaps between blades warp yarns are inserted and they are enclosed there as long as a weaving process is on. Reed oscillates between two positions in the weaving zone (back position near heddles and front position at line fabric position). However, this type of reed does not conform to multiaxis weaving process because of the transversal displacement of bias yarns in the weaving zone for each weaving cycle. The bias yarns could not be enclosed in reed gaps as well the reed should be driven out of weaving zone after each beat-up operation. Open reed is employed here for which blades are maintained just from one side that enables insertion and remove the reed in/from weaving zone. Further, location of insertion point is restrained by location of gaps formed by crossing + with $-\theta^\circ$ bias yarns too near binder yarns needles insertion point. So, the motion of reed consists of four steps as illustrated in Figure 3.32:

- 1- move up to be inserted into the weaving zone through created gaps between crossing bias yarns.
- 2- advance towards fabric from back position.
- 3- move down out of weaving zone
- 4- move back toward rear position close to bias guide blocks frames.

Thereby, in the multiaxis weaving process beating-up operation in addition to pack filler yarns to fabric, it serves on packing bias yarns to fabric with given orientation and they are kept into position within the fabric by binder yarns interlaced with filler yarns.

To execute the four steps, the open reed is attached to two horizontal Guideways enabling horizontal motion from near bias guide block frames toward fabric and inversely. And these Guideways are attached to two other vertical Guideways enabling up/down motion.

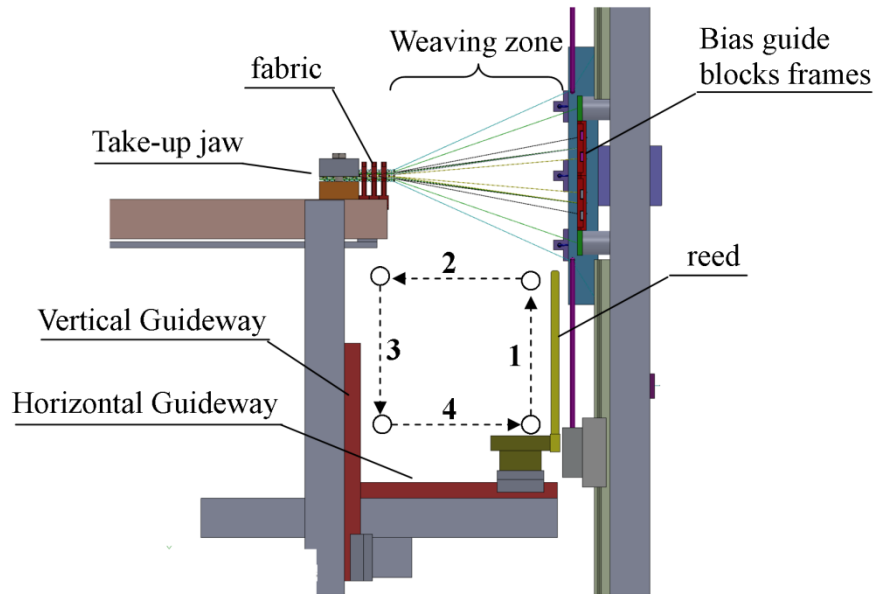


Figure 3.32: Beating-up mechanism with illustration of the four movements of reed.

3.4.7. Fabric control width and take up system

Multiaxis woven fabric suffers from higher width shrinkage on loom (fabric width ratio between weaving zone plane and fabric formation line) comparing to 2D and 3D woven fabric, as illustrated by Figure 3.33. On 2D weaving loom, the fabric shrinkage results from filler yarns waviness as it is beaten to fabric because of higher warp yarns tension. This width shrinkage (fabric width less than weaving zone width) induces higher friction between warp yarns and reed blades and it augments gradually toward fabric edges as warp yarns inclination increasing. Therefore, it is used to realize, on a 2D weaving loom, two temples holding the two fabric side in order to maintain fabric width at formation line equal to weaving zone width at the harness. That minimizes warp yarns degradation incurred by friction. Whereas, the width shrinkage ratio, on multiaxis weaving loom, is much more important because of folding bias yarns on two fabric edge as they are tensioned by feeding system and fabric take up device, Figure 3.34. Thus, the folded bias yarns over last binder yarns press fabric literary toward its centre. Furthermore, a temple could not be used to hold fabric side because of multilayer and folding bias yarns. Consequently, using standard reed (having fix distance between its blades) while weaving of high density multiaxis multilayer fabric cause important degradation for warp and bias yarns because of high corrosion with reed blades. Furthermore, warp and bias yarns density will be distorted and uneven across the fabric width. Bilisik (1995, 2010) developed for tube carrier weaving loom a special reed reducing the distance between its blades as it advances towards fabric from its back position. However, Bilisik (2010) reported that important corrosion still occurred even though of using this special complicated reed because rotation of blades around their own axis.

Therefore, on present developed prototype loom, a small engaging hook is inserted between last two bias yarns on the two fabric edges before displace them again for next weaving cycle. As a result, bias yarn on the fabric edge will be folded over the inserted engaging hook instead of being folded around last binder yarn, Figure 3.35. That operation prevents the folded bias yarns to press fabric literary causing width shrinkage. Thereby, fabric width is held equal to weaving zone edge and standard open reed with fix blades distance could be used with minimized corrosion. At the beginning of each weaving cycle two engaging hooks

3. 3D multiaxis weaving technology

are inserted (one for each side edge of fabric). The hooks are guided with the old ones by special shaped profile and accompanying the fabric along take-up apparatus. On other side, as a result of the important thickness of woven fabric, the standard rotate take-up mechanism utilized on conventional 2D loom could not be employed here to avoid fabric distortion. A linear take-up mechanism is used. A fabric end is climbed by jaw whose lower part is attached to long screw thread, Figure 3.35.

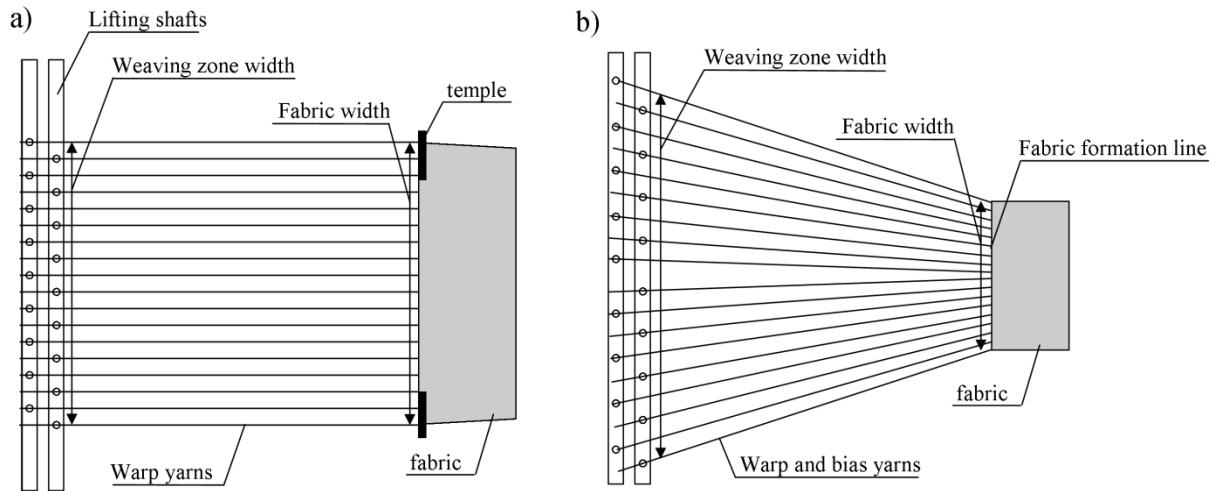


Figure 3.33: Scheme of weaving zone on standard 2D weaving loom (a), multiaxis weaving loom (b).

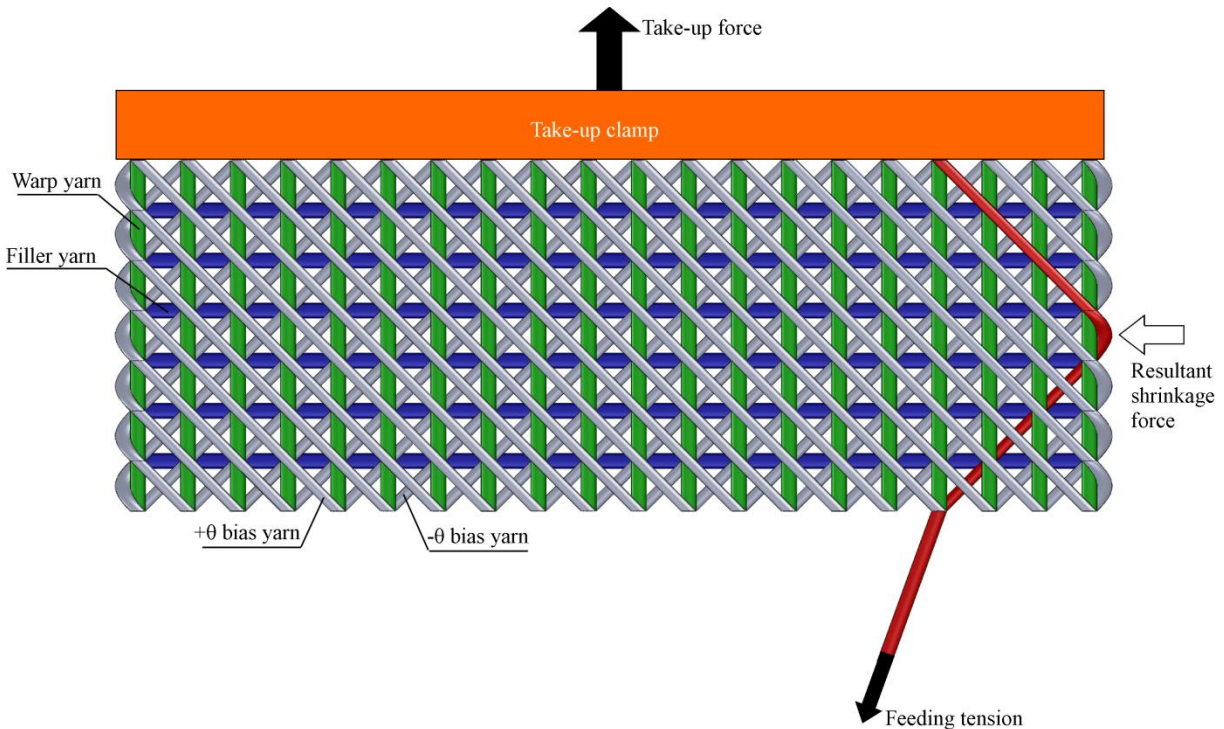


Figure 3.34: Scheme of multiaxis woven fabric illustrating shrinkage force resulting from tensioning forces applied on folded bias yarn.

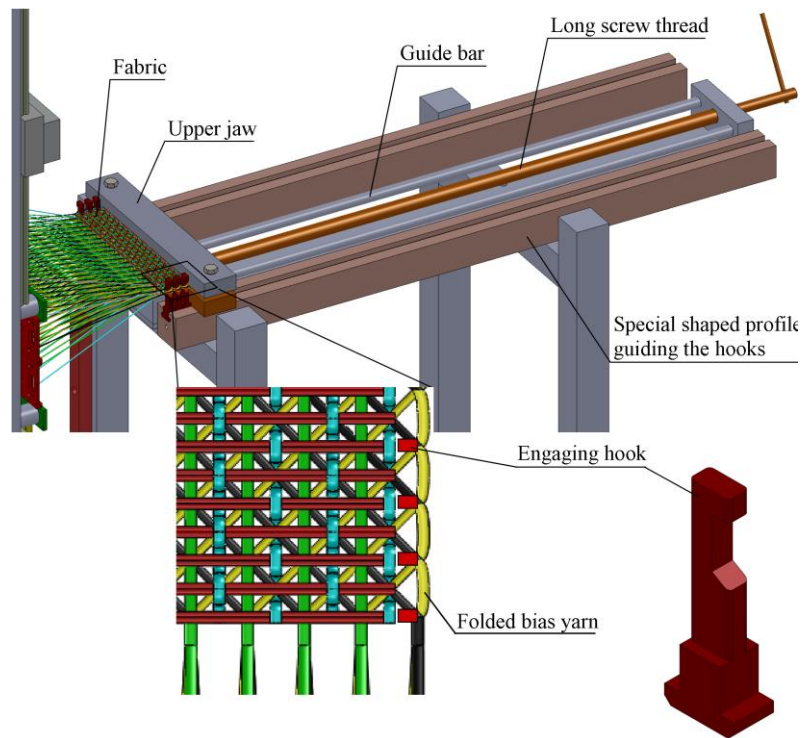


Figure 3.35: Linear take-up mechanism with engaging hooks.

3.5. Weaving process

The weaving process consists of repeating a series of weaving operations, called weaving cycle, realized in defined order with adequate synchronization beginning by changing lifting shafts position and finishing by take-up formed fabric from weaving zone. Generally, on conventional 2D loom one weaving cycle involves one filler yarns insertion operation since just one shed could be created. Here, for multiaxis weaving process in order to maintain bias yarns inside the fabric with given orientation in the aid of binder yarns two filler insertion operations are required. Thereby, the weaving cycle for this multiaxis multilayer woven architecture is considered for two filler yarns insertion operations and formation one unit cell of fabric.

Weaving zone is called the zone located on the loom between bias guide blocks frames and fabric formation line, Figure 3.36. It is the zone where bias yarns orientation, binder insertion, filler insertion and reed beating-up operation are executed.

The series of operations are done to complete one weaving cycle of multiaxis woven architecture on developed prototype loom series of weaving following:

1st step

Following last weaving cycle, the warp and bias yarns are parallel to loom axis and the binder needles, weft rapiers and the reed are out of weaving zone. As a result of last fabric take-up motion, tension of warp and bias yarns increased so that their braider bobbins release some length of yarns corresponding to keep constant yarns tension.

Two hook rods are inserted between last two bias yarns on the two edges of fabric. Thus, bias yarns fold around these hooks instead of last binder yarns.

2^{ed} step

The guide blocks of upper frame move one step to displace the bias yarns transversally with respect to loom axis, as mentioned by Figure 3.23. Similarly, bias yarns guide blocks of lower frame move also one step but in opposite direction in order to getting two pair of bias yarns

layers symmetrical to fabric centre plane. This movement is accompanied with rotation of the chain of bias yarns feeding bobbins one step to avoid entangling bias yarns between bobbins and guide block frames.

3^{ed} step

The engaging rod-1 for filler yarn is in its upper position beside fabric edge at fabric formation line. While, engaging rod-2 is in lower position front guide blocks frames. The rapiers of filler yarns is inserted throw the three sheds from left side of loom to right side. The filler yarns are hinged into rapier hooks.

4th step

Rapiers move back to their initial position on the left side of loom taking with them filler yarns. Inserted filler yarns are in form of loop, and double filler yarns are inserted through each shed. After releasing filler loops from rapier hooks engaging rod-2 is moved up to front guide blocks frames. At same time, reed is moved up front guide blocks frames.

5th step

Reed advances toward fabric to pack-up inserted filler yarns. Simultaneously, engaging rod-2 advances also toward fabric accompanying filler loops. Ones reed beat-up filler yarns to fabric, engaging rod-1 moves down to release inserted filler yarns, then it moves up again to be inserted between last inserted filler yarns and filler guides. That to keep last inserted filler yarns into position at fabric formation line and prepare to nest filler insertion. Reed and engaging rod moves down.

6th step

Reed moves down and binder needles change their level to be inserted through in-plane yarns arranged in the weaving zone. Also engaging rod-2 moves down and back to its initial position away of fabric releasing filler loops.

7th step

Reed moves horizontally away from fabric to its initial position front guide blocks frames. Then new filler yarns insertion operation is made.

8th, 9th and 10th steps

The binder needles are driven out of weaving zone. Then the same operations realized in the 5th, 6th and 7th by engaging rod 1 and 2 and by reed to pack-up the new inserted filler yarns are repeated. Finally, take-up jaws climbing the fabric displace by long screw thread one step corresponding to required number of filler yarns per unit length. As consequence, tension of warp and bias yarns increases so braider bobbin carriers release some length of yarns recompensing pulled length of fabric by take-up device in the manner the tension of yarns is still constant.

3. 3D multiaxis weaving technology

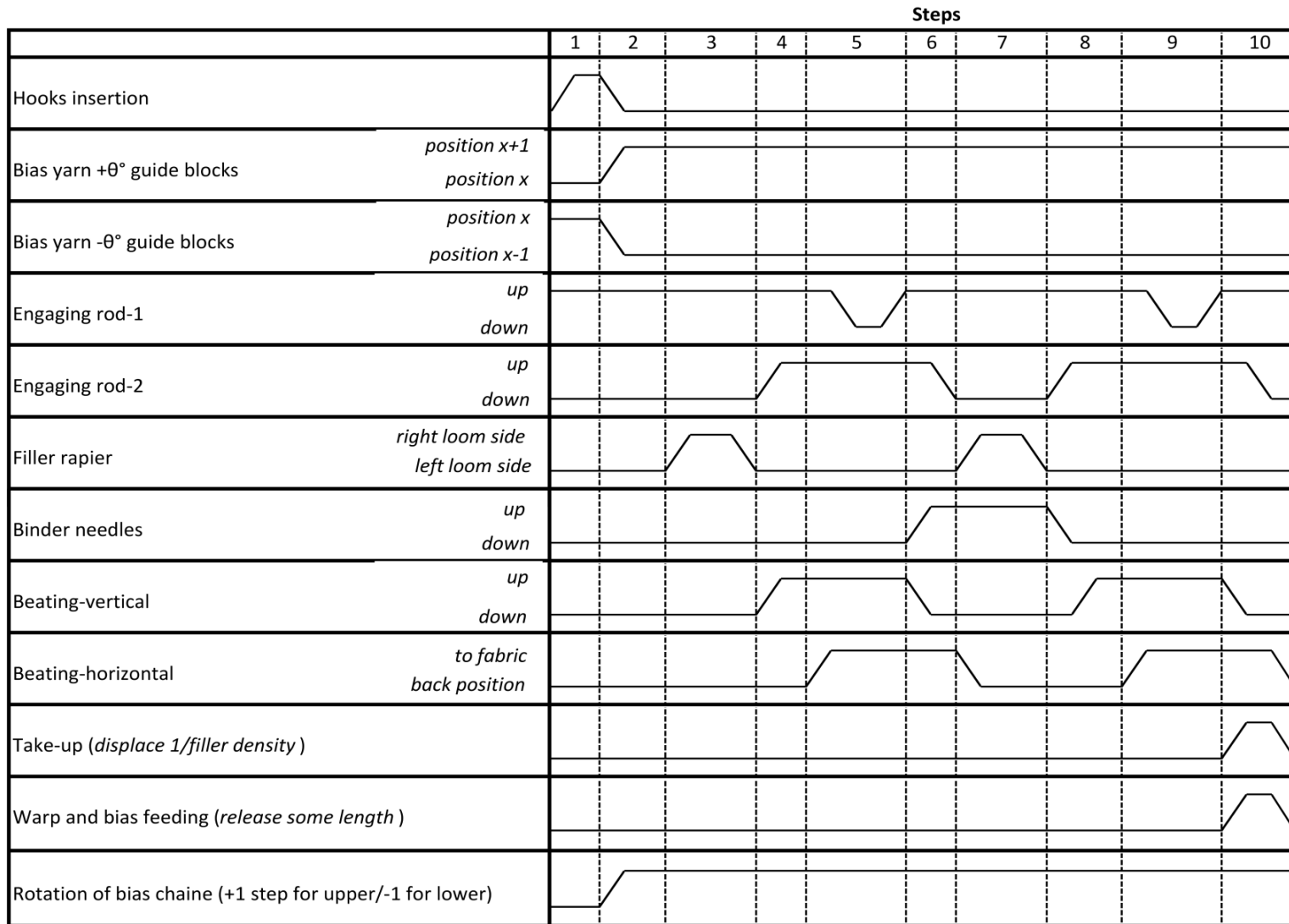


Figure 3.36: Diagram of weaving operations order for one weaving cycle on prototype multiaxis loom.

3.6. Manufactured prefomes

Using the developed 3D multiaxis weaving prototype loom, five samples have been manufactured. The manufacturing parameters together with the weaving parameters for these samples are given in the table 3.2. In this table, both biases yarns, which are oriented in $+θ° -θ°$, have the same manufacturing and weaving parameters for all samples. The difference between samples is noticeable in terms of the linear density of yarns, the number of yarns per unit cell and the yarns number per the unit length (unit cell dimensions in warp and filler directions). For five samples, the sequence of the in-plane layers is as following: $[90/0/θ/-θ/0/90]_s$ (angle representing the angle of the yarn layer axis relative to warp yarns axis).

The last sample was impregnated with the resin epoxy SR 8200 in the vacuum assisted resin transferring mold (VARTM) method. This resin is hardened by SD 7206 hardener at 80° degrees for 8 hours. This sample is denoted “sample-5C”.

Table 3.2: Manufacturing and weaving parameters of five produced samples*.

	yarns	material	Sample 1	Sample 2	Sample 3	Sample 4	Sample 5
Linear density [g/m] x number of yarn per unit cell	Warp	E-Glass	0.9 x 3	0.9 x 3	0.9 x 3	2.4 x 2	2.4 x 3
	Filler	E-Glass	0.9 x 4	0.9 x 4	0.9 x 4	2.4 x 4	2.4 x 4
	Biases	E-Glass	0.9 x 1	0.9 x 2	0.9 x 1	2.4 x 1	2.4 x 2
	Binder	Aramid	0.172	0.172	0.172	0.172	0.172
binder per cm	<i>in warp direction</i>		1,628	1	1	1	1
	<i>in filler direction</i>		2	1	1	1	1

*All samples composed of 4 layers of warp yarns, 3 layers of filler, 2 layers of bias at $+θ°$ and 2 layers of bias at $-θ°$.

3.7. Geometrical characterization

The geometrical characterization for five manufactured dry preforms is necessarily required to evaluate geometrical parameters of the constituent yarns and of the unit cell after the weaving process. Moreover, the geometrical properties of last sample are evaluated after the impregnation process. This characterization helps also to identify the geometry of the yarns (cross section shape and path) within the structure. Also it help to evaluate and develop the applied predictive geometrical modeling approach serving in the design of this multiaxis structure. Furthermore, it contributes to construct the accurate geometrical model for RVE of this structure, serving in the mechanical modeling.

The geometrical characterization involves the microscopic observation of the component yarns inside the structure and measuring the characterizing geometrical parameters of the unit cell (fiber volume fraction, proportion of each yarn sets, preform thickness, unit cell dimensions) and of the yarns (cross section dimensions and area, crimp of yarns).

At the beginning, the parameters describing the structure are defined and classified. The principles of the experimental techniques are explained, then the results and the observation of the procedure are reported. The geometrical properties of the produced samples in this work are compared to those reported in the literature for multiaxis woven preforms produced by other technologies.

3.7.1. Parameters of the 3D multiaxis woven preform

The characterizing parameters of the 3D multiaxis woven preforms could be classified into two groups; firstly the manufacturing and weaving parameters, which are defined before production of the preform, secondly the geometrical parameters, which characterize the produced preform.

Indeed, the definition of these parameters is essential in geometrical modeling to determinate the input parameters (which are defined before weaving process) and output parameters (that are demanded for manufactured preform and required to construct a RVE serving in the mechanical modelling).

3.7.1.1. Manufacturing and weaving parameters

The manufacturing parameters are defined as the nominal geometrical parameters of used yarns provided by manufactures (such as linear mass density, material Volumetric mass density,..).

The weaving parameters are defined as the geometrical parameters of woven preform resulting from the weaving process settings (such as yarn layers number and its order, weft yarns per centimeter, warp yarns per centimeter,).

The manufacturing and weaving parameters are listed in table 3.3.

Tableau 3.3: Definition of the manufacturing and weaving parameters.

Manufacturing parameters:		
$\mu_w, \mu_f, \mu_b, \mu_\vartheta$	g/m	Linear mass density of warp, filler, binder and biases (oriented at +/-45° degree) yarns respectively
$\rho_w, \rho_f, \rho_b, \rho_\vartheta$	g/cm ³	Volumetric mass density of the warp, filler, binder and biases yarns material respectively
Weaving parameters:		
$n_w^{uc}, n_f^{uc}, n_\vartheta^{uc}$		Number of warp, filler, biases yarns respectively in one unit cell
$\lambda_w, \lambda_f, \lambda_\vartheta$	yarns/cm	Number of warps, filler and bias per unit length perpendicular to yarn direction
λ_b^w	yarns/cm	Number of binder yarns per unit length along the warp direction
λ_b^f	yarns/cm	Number of binder yarns per unit length along the filler direction
L_w, L_f	mm	Length of unit cell in the <i>warp</i> and <i>filler</i> directions
n_w, n_f, n_ϑ		Number of warp, filler and biases layers in the unit cell.

3.7.1.2. Geometrical parameters

The geometrical parameters of a woven preform describe the geometry of the yarns inside the preform and the characterizing parameters of the unit cell. Hence, the geometrical parameters could be subdivided into: yarn parameters and unit cell parameters.

Yarn parameters:

They include the following parameters:

- The area of the yarn cross-sections denoted (S).
- Two major and minor dimensions of the yarn cross-sections, which represent the width (l) of the yarns cross-sections and its height (h). These two parameters are mentioned in the Figure 3.37.

3. 3D multiaxis weaving technology

- The aspect ratio, denoted (AR), between the width and the height of the yarn cross section. This parameter helps in monitoring the variation of the shape of the yarns cross section.
- Packing factor of the composed filaments inside the yarns denoted (Pf).
- The angle of orientation of biases yarns inside the structure denoted (θ). It could be defined as the angle between the axis of the bias yarn and the axis of the warp yarns as mentioned in the Figure 3.38. This angle could be evaluated by the two dimensions of the unit cell (L_w and L_f) as in the following equation:

$$\tan \theta = \frac{L_f}{L_w} \quad (3.1)$$

- The yarn crimp percentage in the through-thickness direction, denoted e.
- The angle of inclination of through the thickness part of the binder yarn relative to the mid-plane of the preform, denoted (α) and mentioned in the Figure 3.39.

N.B.; the symbols of these parameters are followed by subscript indicating the yarn type. (w, f, b, o; warp, filler, binder and biases in +/- θ respectively)

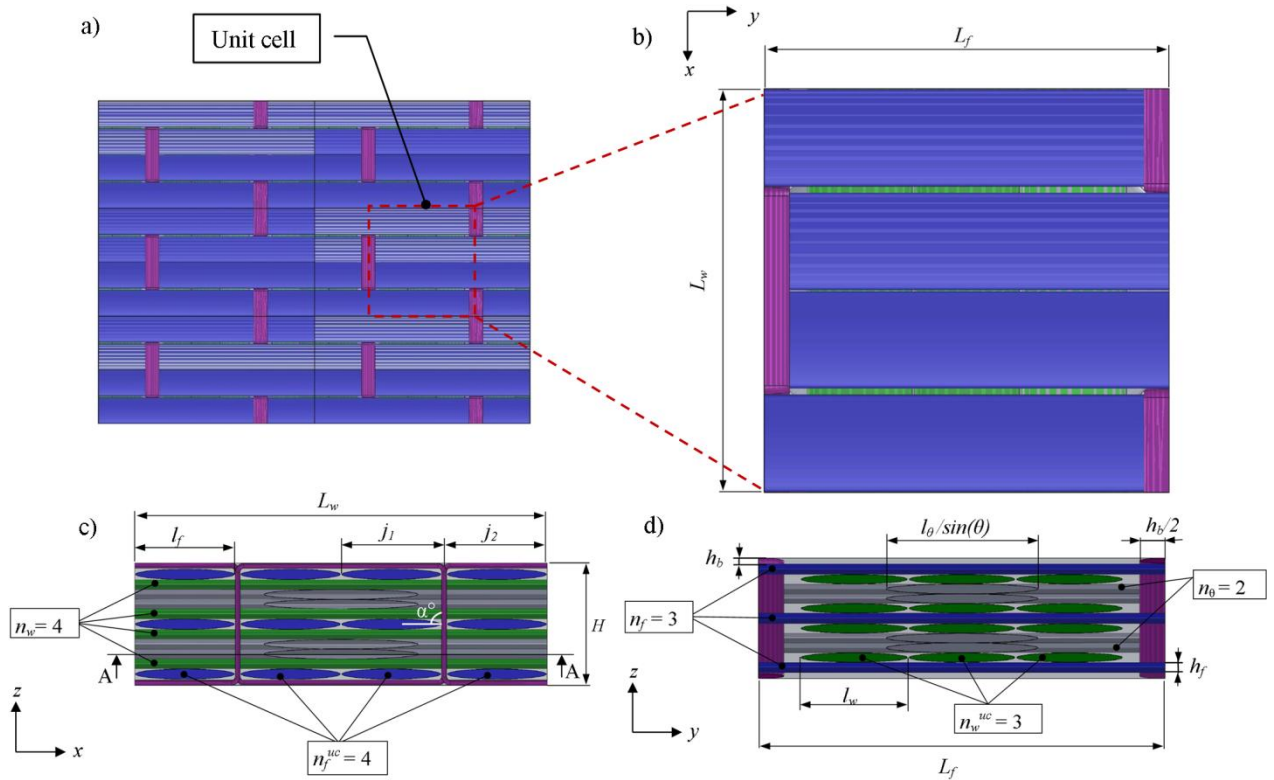


Figure 3.37: Representation of a unit cell of multiaxis 3D woven preform. (a) top view for the analyzed structure. (b) top view for the unit cell, (c) front view for the unit cell, (d) side view for the unit cell.

Unit cell parameters

The unit cell parameters include the following parameters characterizing the preform:

- The unit cell length in warp and filler yarns directions denoted L_w and L_f respectively, Figure 3.37. These two dimensions are related to the number of warp and filler yarns per centimeter (λ_w, λ_f) and number of these yarns per unit cell (n_w^{un}, n_f^{un}) as in the equation

$$L_w [mm] = \frac{n_w^{un} [yarns]}{\lambda_w [\frac{yarns}{cm}]} \cdot 10, \quad L_f [mm] = \frac{n_f^{un} [yarns]}{\lambda_f [\frac{yarns}{cm}]} \cdot 10 \quad (3.2)$$

- The total unit cell thickness denoted H, Figure 3.37.

3. 3D multiaxis weaving technology

- Areal density of the preform denoted S^{uc} quantifies the mass of the dry textile preform per one square centimeter.
- The fiber volume fraction, denoted FVF, quantify the fiber volume relative to the unit cell volume.
- The proportions of each component yarns type (V_{fw} , V_{ff} , V_{fb} , V_{fo} , V_{f-o} ; for warp, filler, binder and biases in $\pm\theta$ respectively) are evaluated relative to the total volume of fibers.

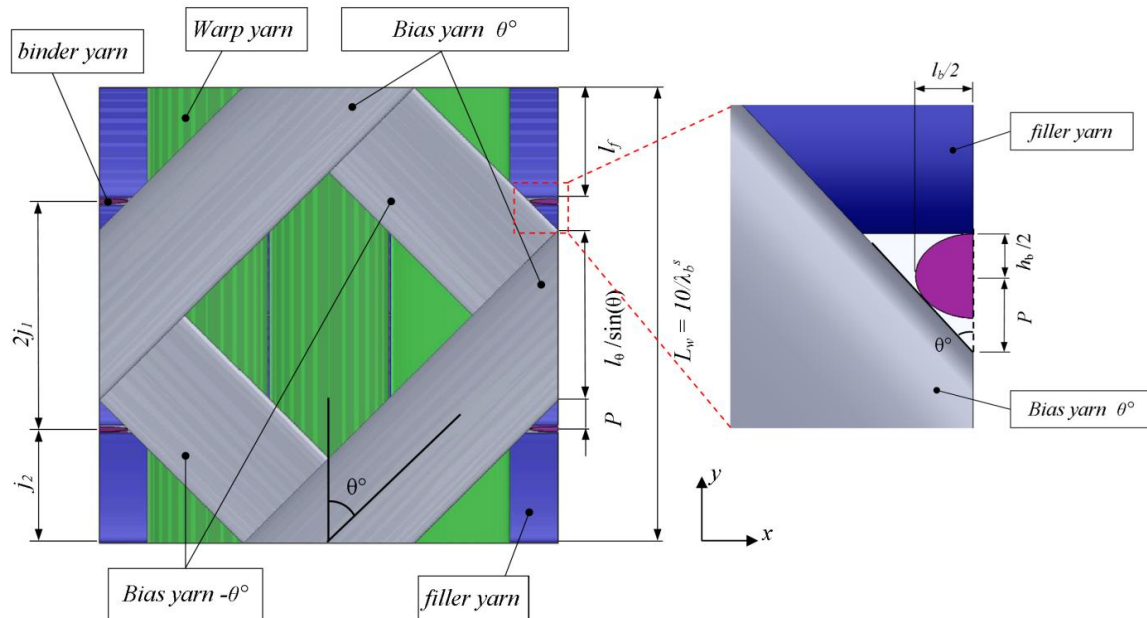


Figure 3.38: a top cut view of the unit cell at the middle of bias yarn.

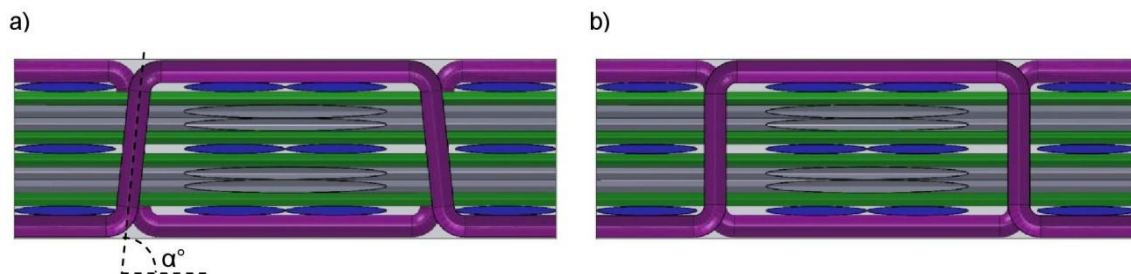


Figure 3.39: Illustration for the inclination of the binder tow in the throw thickness direction in a unit cell of the 3D multiaxis woven architecture. a) α is less than 90° . b) α is equal to 90° .

3.7.2. Experimental techniques

3.7.2.1. Microscopic observation

The optical method could be used to observe the path and the cross section of the yarns inside the dry preform by capturing images for the preform cross sections. But, cut and manipulate the dry preform lead to distort the shape and the positions of yarns because of the poor cohesion between filaments within the yarn. Therefore, the dry samples are impregnated using a transparent resin, allowing the distinction between the yarns crosses sections on captured micrographs, then the samples are cut to get micrographs for their cross sections. The resin is poured over samples without applying pressure, as in an RTM procedure (or in VARTM procedure) to keep the original shape and position of yarns inside the preform without causing deformations on them. In spite of the fact that the penetration of the resin inside yarns and between filaments disrupts a little bit the position of fibers, the

3. 3D multiaxis weaving technology

results obtained by this method are supposed representative to discipline the yarns geometry inside dry preform. That makes able to evaluate the properties of dry preform after the weaving stage.

The micro-tomography could also be used to obtain 3D virtual model of the preform instead of the 2D cross section micrograph. The 3D virtual model is made up of a 3D array of voxels (3D pixels). However, the low resolution (18 μm), as reported by Sherburn (2007), makes difficult identifying the yarns cross-sections; outline and the boundary between two crossing yarns.

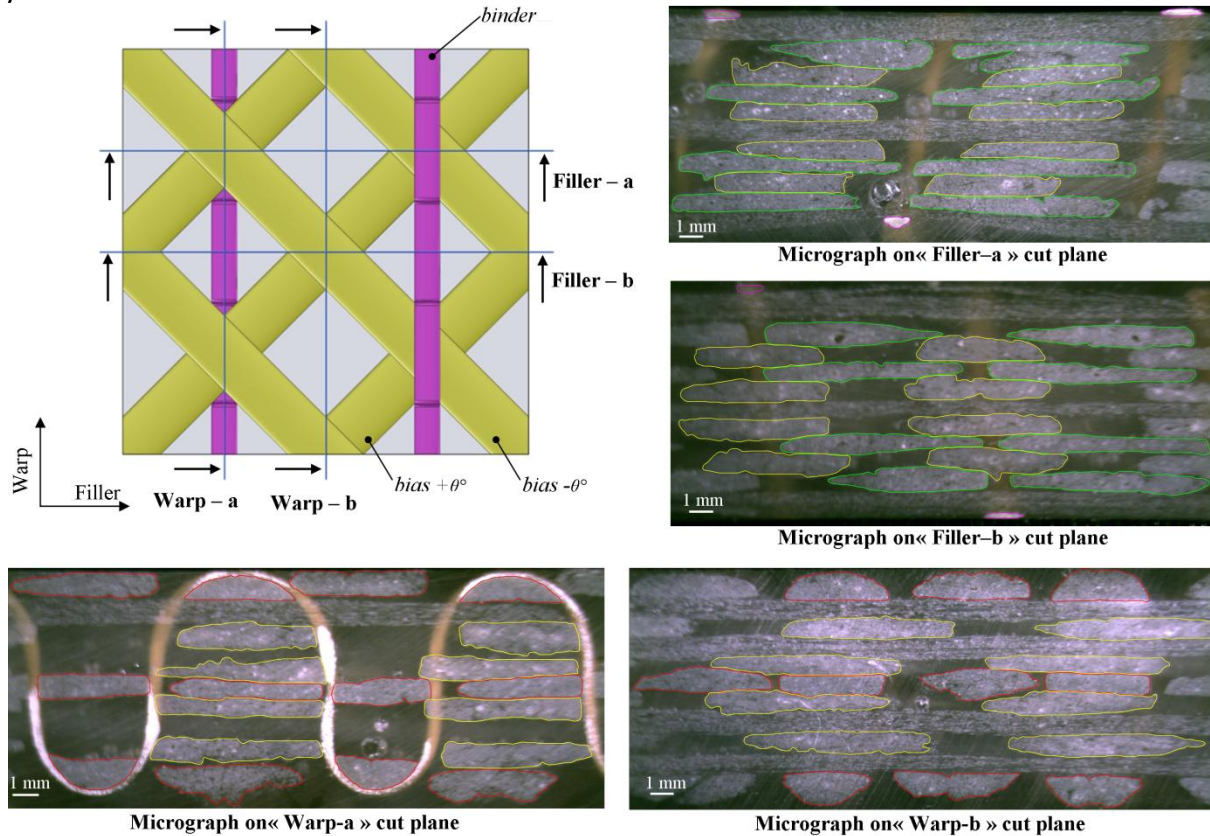


Figure 3.40: Specified cut planes on which micrographs are captured for the multiaxis 3D woven samples. In this schema of the multiaxis woven preform only the bias and binder yarns are presented whereas warp and filler yarns are masked.

So to characterize the geometrical properties of dry preforms, we impregnated the samples using Resina Cristal Enrobage A Froid (Méthylméthacrylate colorless): Liquid and hardener in the ratio 2:1. The 3D preform was kept in a frame and resin was poured over it ensuring, as possible, that the resin penetrates into the yarns bundle and no air bubbles are formed. The used resin has low viscosity and that helps to ensure the good impregnation of textile samples. The samples were allowed to dry for 24 hours and the composite was made ready for the microscopic analysis.

For both groups of impregnated samples (with transparent resin without pressure and with resin epoxy applied via VARTM) each sample are cut and polished at four specific planes then micrographs for the sample cross sections are captured on each cut plane. Two cut planes are in warp direction and two in filler direction. They are specified depending on the position of the binder yarn and the crossing point between the two opposite biases yarns, as illustrated in Figure 3.40. For the two cut planes in warp direction, one is through binder yarn (denoted "warp-a") and the other is at the middle between two binder yarns (denoted

“warp-b”). For the two planes in filler direction, one is when the crossing point of the two opposite biases yarns ($+\theta^\circ$ and $-\theta^\circ$) is in the plane of binder yarn (“filler-a”) and the other is when this crossing point is between two binder yarns (“filler-b”).

3.7.2.2. Yarn contacts

The interaction between the adjacent yarns within the preform governs the shape and the area of their cross-sections as well their path in addition to the axial tension applied on. The filaments are reorganized inside the yarn in function of the pressure applied on yarn surface. Hence, to describe the geometry of the yarns, the contact surfaces between yarns should be defined. Hivet and Boisse (2005) proposed a 3D geometric model for 2D woven fabric based on characterizing the contact surface between interlaced yarns. When defining the yarns cross-section geometry, they distinguished between three zones: a contact zone, a contact-free zone and lateral zone. For the yarns path, they distinguished also between two parts: contact zone (supposed to be parabolas) and contact-free zone (supposed to be straight). Here, for the 3D woven preform, on the perimeter of each yarn cross section, the same three zones could be also defined depending on its contact with adjacent yarns: contact zone, contact free zone and lateral zone, Figure 3.41. Also, for the yarn path two parts could be distinguished: contact zone and contact-free zone, Figure 3.42. This classification, for the contacts surfaces zone of the yarn cross-section and the yarn path with the adjacent yarns, helps in the definition of the yarn geometry and its cross section shape inside the structure.

3.7.2.3. Fiber volume fraction

Two approaches could be used to evaluate the fiber volume fraction of a composite:

Experimental approach: two experimental methods mentioned by Curtis P. T., (1988) could be followed:

- The density measurement method: this method involves the measurement of the density of the produced composite part in addition to the density of the component yarns and that of the resin. Then, the following equation (3.3) could be applied to evaluate the fiber volume fraction, (Vasiliev and Morozov 2001).

$$\begin{aligned}
 m_c &= m_f + m_r \\
 \rho_c V_c &= \rho_f V_f + \rho_r V_r \\
 \rho_c V_c &= \rho_f V_f + \rho_r (V_c - V_f) \\
 V_f (\rho_f - \rho_r) &= V_c (\rho_c - \rho_r) \\
 FVF &= \frac{V_f}{V_c} = \frac{\rho_c - \rho_r}{\rho_f - \rho_r} \tag{3.3}
 \end{aligned}$$

Where, ρ_c , ρ_f and ρ_r is the density of composite sample, fiber and resin respectively. m_c , m_f and m_r is the masse of composite sample, fiber and resin respectively. V_c , V_f and V_r is the volume of composite sample, fiber and resin respectively. FVF is the fiber volume fraction. However, it is an approximate method because of ignoring the porosity could be existed in the manufactured composite.

- The resin removal method: this method involves removing the resin from produced composite sample to make able quantify the mass of existed fiber in the composite sample. Three ways could be used to remove the resin depending on its type; Sulphuric acid/hydrogen peroxide digestion, Nitric acid digestion or Resin burn-off.

Geometric computation approach: the fiber volume fraction is computed in this approach based on the measured parameters (yarns parameters and unit cell parameters) and on the calculation of the length of yarns inside the structure. Assumptions are made to define the path of the yarns associated with the analyzed preform architecture. This approximation method should be verified by comparing with experimental methods. Otherwise, by this method the proportion of each type of the component yarns could be evaluated also this method could be applied in the predictive models to estimate the fiber volume fraction in the composite while the designing procedure. This method is detailed in the next chapter (4.5.2.2).

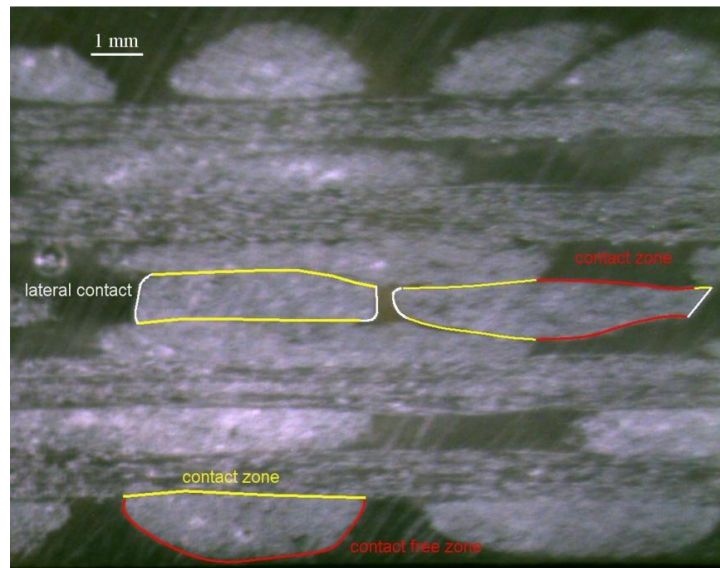


Figure 3.41: Micrographs of cross sections of sample-5, at cut plane “warp-b”, illustrates the different zones on the perimeter of the yarns cross section.

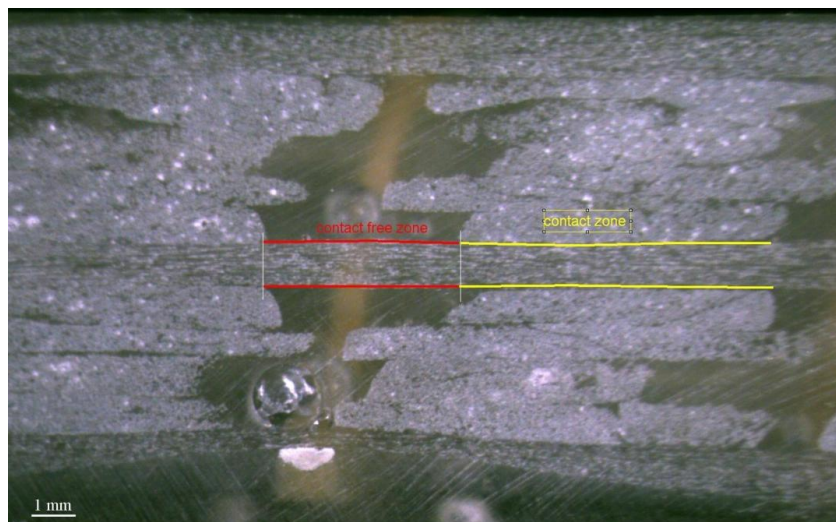


Figure 3.42: Micrograph of cross sections of sample-5 at cut plane “filler-a”, illustrates the two zones on the path of yarns.

3.7.2.4. Crimp measurement

The yarns are undulated into the through thickness of the fabric and they do not keep a path in the fabric plane, due to the interlacement between the warp and filler yarns as in the 2D fabric or between warp and filler yarns from different layers of fabric as in the 3D angle interlock. Further, the in-plane yarns could be misaligned in the fabric plane due to

inappropriate weaving setting. Crimp percentage term is used to express the measurement of this waviness in yarns (Booth J. E., 1968). Generally the crimp percentage of a yarn in a specified fabric length (L) is defined by the mean difference between the length of yarn (L') after extracting from fabric and straightening to the specified fabric length. (3.4)

$$\text{Crimp \%} = \frac{(L' - L)}{L} 100 \quad (3.4)$$

The crimp percentage of a yarn depends on its tension during weaving process as well on the tension of the second interlacing yarn. Also, it depends on the linear density of the two yarns and their density (number of end and pick per unit length). The crimp of in-plans yarns into the through thickness of fabric could be generated also in the 3D orthogonal fabric, which has no-interlacement between in-plane yarns, because of the tension applied on binder yarn that pushes filler yarns into through thickness direction. Moreover, the applied pressure during consolidation process leads to increase the crimp percentage of in-plane yarns.

The waviness in through the thickness direction of the yarns affects strength, ductility and fatigue life of woven composite, Cox et al. (1992, 1994-b, 1995-a and b). Further, the misalignment of in-plane yarns from load direction contributes to the formation of the kink band when compression of composite structure, Cox et al. (1992, 1994-b). Therefore, it is important to quantify the crimp of in-plane yarns in the composite architectures. Cox et al. (1995-b) found that the waviness magnitude varies between yarns sets depending on their tension during the weaving. Therefore, filler suffering from crimp higher than warp, and between weave architecture relating on the path of yarns within the structure, so it is relatively high in layer to layer angle interlock architecture, less in the through thickness angle interlock and least in orthogonal architecture. In addition to the importance of the crimp quantification to estimate the related influence of the multiaxis weaving architecture and process on the mechanical performance, also this quantification aids to define the path of the yarns within the structure through construction the geometric model.

In this characterization the crimp percentage for warp yarns, resulting from waviness in through thickness direction of preform, is measured on the captured micrographs. On the cut plane “warp-b” for all produced samples, the length of centre line of the warp yarns (L') is measured on a known straight distance (L). The centre line is defined by spline passing through the midpoint of vertical segments defining the thickness of the yarn, as illustrated in Figure 3.43. Then the crimp percentage is computed by equation (3.4). In the same manner, the crimp of filler yarns was measured on the cut plane “filler-a” and “filler-b”.

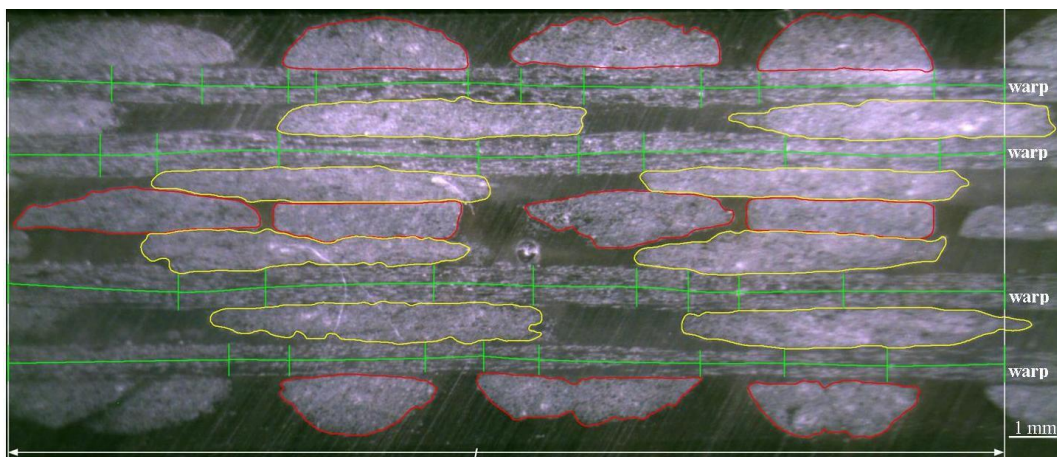


Figure 3.43: Micrographs of cross sections of sample-5 at cut plane “warp-b” illustrates the undulation of warps yarns. Green line for the centre line of warp yarn, red outline for filler yarn and yellow outline for biases yarns.

3.7.2.5. Yarn gap

The yarn gap (T) represents the distance from the yarn edge to the corresponding edge of the adjacent yarn. This parameter indicates the lateral restriction to which the yarns are subjected. Further, if the fabric is tight (closed-packed fabric) the gap is null or the fabric is opened-packed and the gap isn't null. The yarn gap (T) could be calculated for the in-plane yarns from the yarn cross-section width and the corresponding unit cell length as following:

$$\begin{aligned} \text{For warp yarn: } T_w &= (L_{yf} - l_w)/L_{yf} \\ \text{For bias yarn: } T_o &= (L_{yf} - \frac{l_o}{\cos(\theta)})/L_{yf} \\ \text{For filler-inner yarn: } T_{fi} &= (L_{xw}/2 - l_f) L_{xw}/2 \end{aligned} \quad (3.5)$$

3.7.2.6. Packing factor of filaments

The arrangement of the filaments within the yarns in the woven composite depends upon the contact pressure of adjacent yarns, Figure 3.44. Increasing this contact pressure (as in the interlacement zone of two yarns under tension) decreases the gaps between the filaments within the yarn. That means that the filaments are more packed and the contact between them is more important. Consequently, the cross section area of the yarns decreases and the volume of matrix occupying the gaps between filament inside yarns decreases also, vice versa. This effect is evaluated using packing factor (pf) parameter which compares the total volume of filaments to the yarn volume. Thereby, at this microscale the packing factor represents the fiber volume fraction parameter for impregnated yarn as composite material (consists of the two phases; filaments and matrix). So it serves the micromechanics models to evaluate the stiffness matrix of yarn as homogeneous material, as it will be explained in section (5.2.5).

The packing factor could be evaluated experimentally by binarizing to black and white of yarns cross section micrograph as followed by Lapeyronnie et al. (2011), Figure 3.44, and Xu et al. (2013).

Otherwise, the packing factor could be computed based on the measured area of the yarns (S [mm²]), the linear density of the yarns (μ [g/Km]) and the fiber density (ρ [g/cm³]).

$$pf = \frac{\mu 10^{-3}}{S \rho} \quad (3.6)$$

The maximum value could be obtained for the packing factor is pf=0.9069 when all filament are in contact and they are in hexagonal arrangement with considering that the filament are non comprisable, (Ansar et al. 2011).

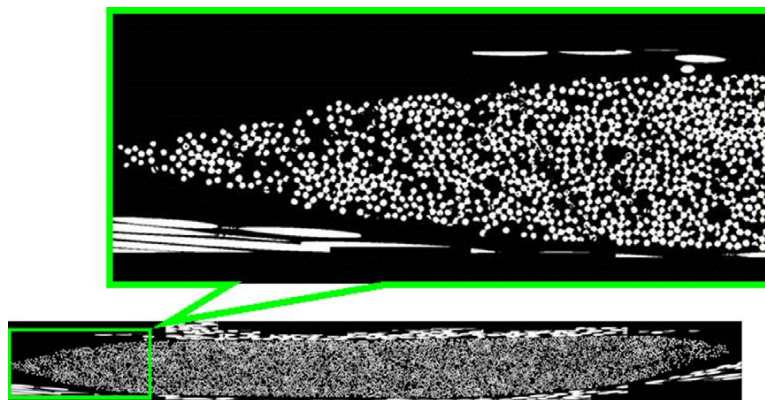


Figure 3.44: Binarized black and white picture of the micrograph of yarn cross section used to measure the filament packing factor within the yarn (Lapeyronnie et al., 2011).

3.7.3. Results and Observations

3.7.3.1. Measured geometric parameters

On each micrograph, the yarns cross section is outlined and its area is measured using image-j software. Also, the two dimensions; width (l) and height (h) of each yarn cross section are measured then the aspect ratio (AR) between these two cross section dimensions is computed. The dimensions of the unit cell (L_w , L_f , H) for each sample are measured using the measurement tools provided by image-j software, Figure 3.45. The mean and the coefficient of variation of the measured parameters are computed at each cut-plane. The details of the measurement results with the micrographs of each sample are presented in appendix-A. A variation in order of 3.5% to 7% was noted for the total thickness values when it was measured on the four micrographs of each sample. The higher thickness value is at “filler-a” and “warp-a” planes where the binder yarn passes over the crossing of the two biases yarns ($-\theta^\circ$ and $+\theta^\circ$), whereas the lower thickness value is at “filler-b” and “warp-b” where the crossing of the two biases yarns is between two binder yarns.

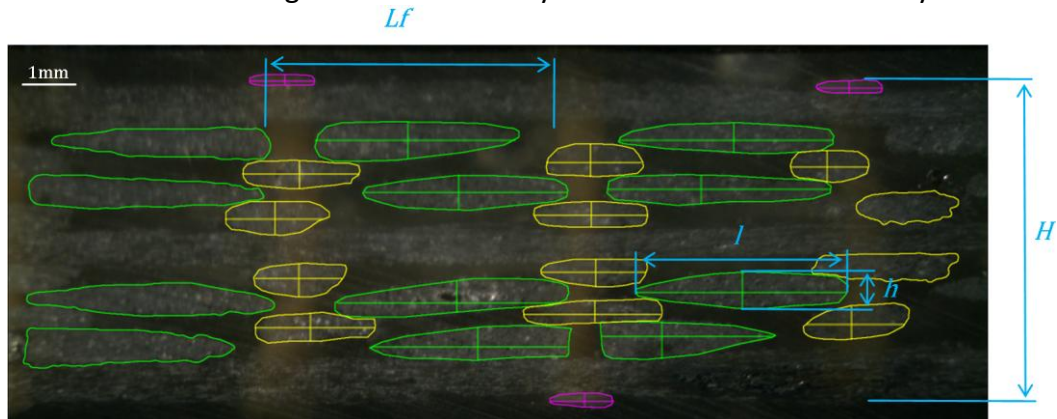


Figure 3.45: Micrograph of cross sections of sample-1 at cut plane filler-b, illustrates the measured yarns parameters and measured unit cell parameter.

3.7.3.2. Fibre volume fraction

The fiber volume fraction of the five preforms was measured by “the density measurement method”, and the results are reported in the table 3.4. And the measurement incertitude of FVF was $\pm 1.2\%$. This method was also used by McIlhagger et al. (2007) for the produced multiaxis woven preform. The density of the E-glass fiber and aramid fiber was 2.58 g/cm^3 and 1.44 g/cm^3 respectively, from the provided data sheet. The density of the used matrix (Methylmethacrylate) is 1.142 g/cm^3 and that of the resin epoxy is 1.1 g/cm^3 . The densities of the composite samples (ρ_c) are measured and listed also.

Table 3.4: Fiber Volume Fraction percentage of the dry preforms and VARTM impregnated sample and the mean of the measured unit cell dimensions with the standard deviation (SD) of the measurement.

	sample-1	sample-2	sample-3	sample-4	sample-5	sample-5C
$\rho_c \text{ [g/cm}^3\text{]}$	1.56	1.47	1.49	1.59	1.62	1.77
FVF [%]	31.12	25.02	26.35	33.13	34.95	45.47
$L_w \text{ [mm] (SD)}$	6.14 (0.1)	9.08 (0.28)	10.42 (0.8)	9.97 (0.19)	10.5 (0.27)	10.28 (0.29)
$L_f \text{ [mm] (SD)}$	5.66 (0.09)	9.4 (0.3)	9.49 (0.37)	9.92 (0.19)	9.8 (0.3)	9.86 (0.28)
$H \text{ [mm] (SD)}$	5.8 (0.18)	5.43 (0.26)	4.04 (0.14)	7.32 (0.44)	9.35 (0.16)	6.99 (0.15)
$\theta \text{ [deg.]}$	42.6	45.9	42.3	44.8	43	43.28

Because of the pressure applied during the VARTM process the fiber volume fraction (FVF) increases about 30.5% whereas the preform thickness (H) decreases about 25%. This observation would be more verified in future work through different samples.

The two geometric modeling approaches (FVF-weight and FVF-volume) introduced in the literature, as detailed in the next section (4.5.2.2), are implemented to compute the FVF of the dry preform sample-5 and the impregnated sample-5C. In the FVF-volume method the resin volume inside the yarn is not considered so it represents the ration of yarns volume to the composite volume. So this method allows evaluating the volume between yarns. Contrary to the FVF-volume method, in the FVF-weight method the resin volume inside the yarn is considered.

The FVF values of the sample 5 and the sample 5C evaluated by weight method (4.14-a) are 34.83% and 45.47% respectively. Whereas the FVF values of these two samples evaluated by volume method (4.14-b) are 68.3% and 62.74% respectively. The result obtained by weight method accords the measured values. The difference in the FVF computed by weight between the two samples (5 and 5C) is 30.5%. That means that the applied pressure on the dry sample before resin infusing during VARTM impregnation process compacts the preform resulting in reduction inter-fibre gap. Otherwise, this deviation between the samples relative to the FVF computed by volume is -8%. That means that this compaction is essentially between the fibres inside yarns whereas the yarns gaps is affected slightly. That could be noted by following the packing factor values of the constituent yarns of the two (dry and impregnated) samples as listed in the table 3.10. This observation would be more verified in future work through different samples.

3.7.3.3. Crimp percentage of in-plane yarns

The crimp percentage of the warp yarns and of the weft yarns have been measured via the captured micrographs. The mean and the standard deviation of the results are listed in the table 3.5.

In the 3D multiaxis woven architecture, there is no interlacement between the in-plane yarns resulting in low crimp percentage for the in-plane yarns. In comparing with 2D plain fabric, Xu et al. (2013) reported that the crimp percentage for 2D twill weave fabric made of carbon fiber 3K and 12 K are 0.85% and 0.28% respectively. Thus, the warp yarns could be considered as kept straight in the in-plane of the preform for this architecture. The same result is noticed for the middle (inner) weft yarns whereas the extreme (outer) one show higher crimp resulting from the binder yarn, passing over it. With less yarns gap, the extreme filler yarn experiences higher waviness at filler-b plane where the biases yarns crossing is not on binder yarn plane, so binder is more able to press extreme weft yarns toward the preform centre. That is corresponding to the thickness measurement where lower thickness value is obtained on filler-b plane.

The impregnaation process via VARTM causes augmentation of the crimp percentage for warp yarns because of the pressure (about 1 bar) applied during resin infusion. While, less effect is observed on filler yarns (both outer and inner).

3. 3D multiaxis weaving technology

Table 3.5: Crimp percentage [%] of warp and filler yarns in the five samples.

		crimp percentage [%] (SD)						
		sample-1	sample-2	sample-3	sample-4	sample-5	sample-5C	
Warp yarn	cut plane							
	warp-a	0.04(0.04)	0.14(0.06)	0.19(0.03)	0.10(0.08)	0.07(0.05)	0.14(0.08)	
Filler yarn	filler-a	outer	0.02	0.23	0.08	0.13	0.08	0.1
		inner	0.01	0.16	0.05	0.13	0.07	0.06
	filler-b	outer	0.21	0.05	0.03	0.29	0.28	0.28
		inner	0.04	0.04	0.01	0.01	0.00	0.12

3.7.3.4. Yarn gap

For five dry samples and impregnated one, the yarn gap value is computed but it has high variation on one cut-plane and between four cut-planes. This variation, which is related to the variation of the cross-section dimensions, is treated in the three next sections through monitoring the variation of the yarns cross-section area and shape. Thus in this section only the mean value of the yarn gap is presented to illustrate the influence of the difference between the five dry samples regarding the manufacturing and weaving parameters on the yarn gap value. As it is indicated in the equation (3.5) the yarn gap values depend on the unit cell dimensions (which is related to n_i^{un} , λ_i) and the yarns cross-section width (which is related to μ_i , Pf_i and yarns tensions).

During the weaving process, we have a possibility to control the number of yarns per unit cell, the width of the produced preform as well as the step of fabric advancing per weaving cycle. That makes able controlling the density of yarns (count per unit length) in the two unit cell directions (warp and filler).

The yarn gap values are computed by equation (3.5) and listed in the table 3.6. To see the influence of yarns cross-section width the yarn gap values are divided on the associated unit cell dimension.

Because of the double filler yarns insertion per weaving cycle so two filler yarns per unit cell, less gap value is created between filler yarns comparing to the warp and bias yarns. No important difference in the gap values of filler yarns between the samples although the difference in the filler yarn linear density because of tightly packing of filler yarns on the loom by reed with the same advancing fabric step. That is resulting in reduction of AR (aspect ratio) of filler yarns as the filler yarns linear density increasing. The gap between filler yarn is equal to the thickness of the through thickness part of the binder yarn as in the case of the closed packed preform. We should re-mention here that number of warp and bias yarns per unit cell is one although of multi yarns, as mentioned in table 3.2, because of passing warps yarns (also the bias yarns) of one unit cell through the same eye guide block resulting in packing the multi yarns in the weaving zone as one yarn.

The gap between warp yarns increases inversely to its linear density and its number per unit cell with constant unit cell dimensions, as illustrated in table 3.6 in association with the table 3.2. The sample 3 has double unit cell dimensions with the same other manufacturing and weaving parameters comparing to the sample 1. That leads to same T_w/L_f ratio. Thus in the sample 3 the warp yarns are less restricted laterally while they are subjected to a through the thickness pressure caused by the binder yarns. So, the yarns will be relocated within the unit cell, as illustrated by Figure 3.46-a where the warp and bias yarns are displaced transversally relative to the initial weaving arrangement, to have more equilibrium state.

3. 3D multiaxis weaving technology

This re-arrangement causes also less-uniformity for cross section shape and dimensions across one plane of the unit cell, section (3.7.3.7). Contrariwise, in the case of sample-1, 5, where a poor warp yarns gap, the warp yarns are more restricted and they maintain their initial weaving location as illustrated by Figure 3.46-b.

The gap between bias yarns in the same layer is much more important and it increases inversely to bias yarns linear density and its number per unit cell with constant unit cell dimensions. This high gap restricts the proportion of bias yarn volume that could be obtained within the preform. The reason of this gap is attributed to the multiaxis architecture where to obtain the inclined orientation of the bias yarns inside the structure two insertions of binder yarn is required per one weaving cycle, as shown by Figure 3.46-c on “warp-a” cut plane.

Table 3.6: Yarns gap mean values for the in-plane yarns.

	sample-1	sample-2	sample-3	sample-4	sample-5	sample-5C
T_w [mm]	0,29	0,47	0,49	0,33	0,14	0,28
T_o [mm]	0,64	0,52	0,65	0,52	0,38	0,35
T_{fi} [mm]	0,04	0,05	0,06	0,03	0,04	0,006
T_w/L_f	0.051	0.049	0.051	0.032	0.014	0.029
$T_o/(L_w/\cos(\alpha))$	0.077	0.04	0.046	0.036	0.0261	0.024
T_{fi}/L_w	0.007	0.005	0.006	0.003	0.0038	0.0006

For the gaps between the filler yarns are much less important comparing to that of the bias and the warp yarns. That is because of the high number of filler yarns per unit length.

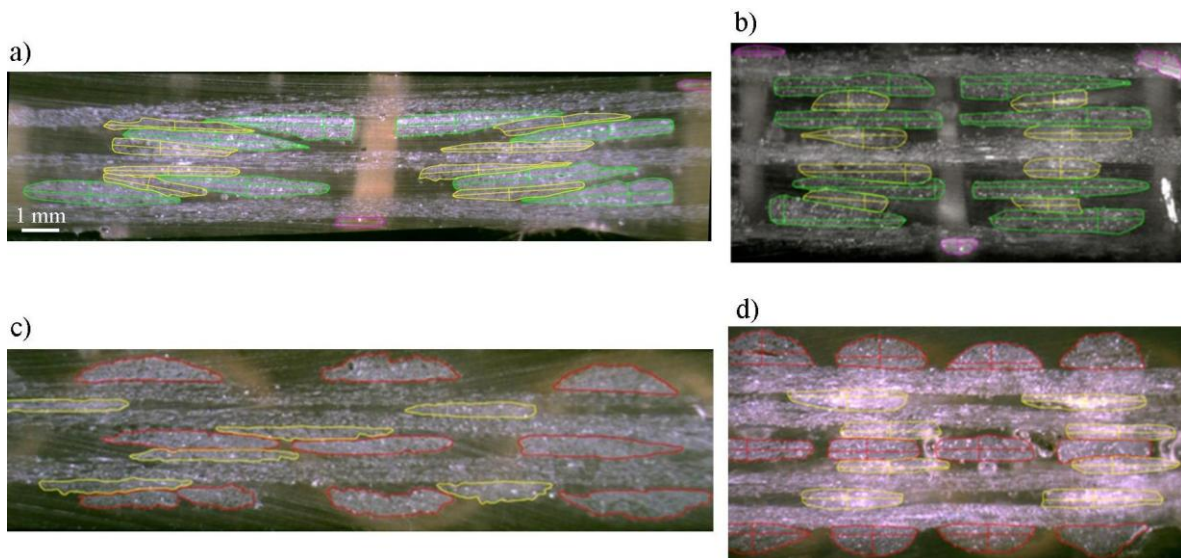


Figure 3.46: Micrographs for the samples cross sections, a) for sample-3 at filler-b cut plane, b) for sample-1 at filler-b cut plane, c) for sample-3 at warp-b cut plane, d) for sample-1 at warp-b cut plane. Both samples 1,3 have the same manufacturing parameters but sample-3 have doubled unit cell dimensions resulting in higher yarn spacing.

3.7.3.5. Binder yarn

As illustrated in Figure 3.47-a, the binder yarn could be divided into two parts; through the thickness part and crown part (passing over filler yarn and appears on the top and bottom surfaces of preform). The inclination angle (α) of through the thickness part of binder yarn

3. 3D multiaxis weaving technology

relative to horizontal mid-plane of preform could be measured as shown in Figure 3.47-a. This angle is affected essentially by the count per unit length and the linear mass density of the filler and biases yarns in a unit cell of the structure, the preform thickness. Also this angle is affected by the compression applied during the impregnation process. The angle (α) is evaluated for the five samples as presented in Table 3.7.

Otherwise, the shape of the binder yarn cross section varies along its trajectory. By following the path of binder yarn on Figure 3.47-a, we can notice this variation through monitoring its thickness. At through the thickness part, the binder has thickness more important than at crown part. The through the thickness part has lateral contact with the surrounding yarns (biases and filler) on whole its perimeter, whereas the crown part has contact just on one side with filler yarn. Moreover, because of applied tension on binder yarn during the weaving process, its cross section at crown part becomes flat (or semi elliptic), as shown in Figure 3.47-b. An important variation for the shape of the binder cross section along its path and between the two parts is noted.

Table 3.7: Angle of binder yarns to mid-plane and the ratio of the two parts width

	sample-1	sample-2	sample-3	sample-4	sample-5	sample-5C
α (SD) [deg.]	93.5 (1.89)	80.4 (1.18)	62.2 (4.87)	82.3 (3.99)	89.2 (0.55)	101.7 (0.58)
j_2/j_1 (SD)	0.76 (0.07)	0.76 (0.03)	0.74 (0.04)	0.87 (0.05)	0.65 (0.05)	0.61 (0.07)
T_o/T_{fi}	14.66	11.24	10.50	17.28	9.30	14.66

From Figure 3.47–a made at the cut-plane “warp-a” the width of the two parts of unit cell ($2j_1, 2j_2$) corresponding to the path repeat of the binder yarns are not even. The difference is attributed to the alternative crossing of bias yarns with binder yarns. By other words, at the “warp-a” cut plane crossing of the two opposite bias yarns is located and repeated only at “filler-a” cut-plane. That is why j_1 is higher than j_2 . The table 3.7 lists the mean of the (j_2/j_1) ratio for all analyzed samples. It is noticed that this ratio is influenced by the unit cell length in warp direction, the linear density and number of yarns per unit cell for both bias and filler yarns. This influence could be indicated by compare (j_2/j_1) ratio to the ratio of the bias yarn gap to that of filler-inner yarn (T_o/T_{fi}), as shown in Figure 3.48 for the dry preform. Where, increasing the yarn gape ration leads to increase the (j_2/j_1) ratio.

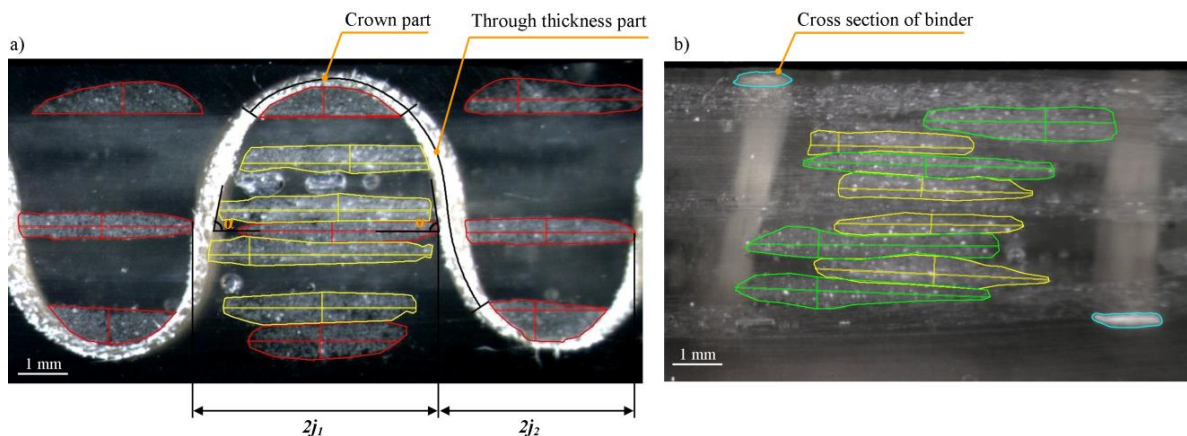


Figure 3.47: Micrographs of cross sections of sample-2; at cut plane “warp-a” illustrates the two parts of binder yarn path (black line) and its inclination angle (α) to mid-plane (a). At cut plane “filler-a” illustrates the shape of binder yarn cross section on fabric outer surfaces (b).

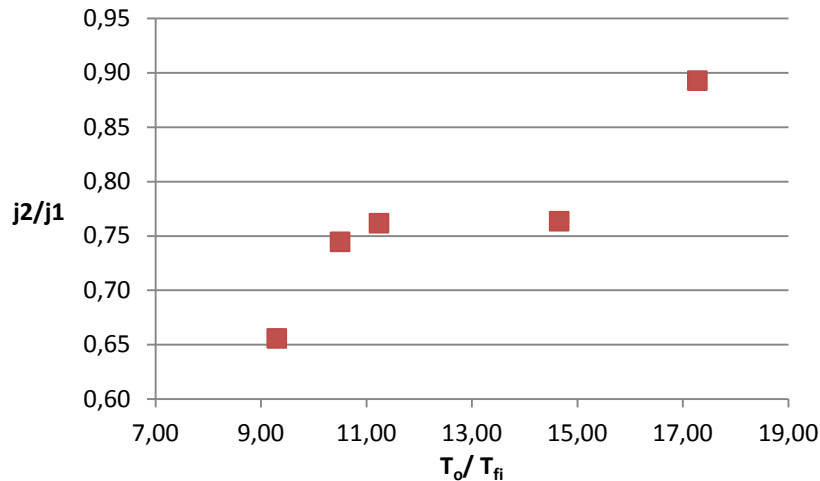


Figure 3.48: Variation of the (j_2/j_1) ratio in function of the ratio of the bias yarn gap to that of filler-inner yarn (T_o/T_{fi}) .

3.7.3.6. Filler yarns cross section

The shape and the area of the filler yarns cross section, on the same cut-plane, vary in function of its location through the thickness of the preform due to the interaction and the contact with surrounding yarns. On the cut plane “warp-a”, five cross sections for filler yarns could be distinguish and they are indicated in Figure 3.49-a.

At the mid-plane of preform, the inner filler yarn, denoted “filler-I”, has lateral contact with binder yarn and contact on its upper and lower surfaces with bias layers. So, it has more rectangular cross section shape. However, because of the difference in the width of the two parts of binder yarns (j_2, j_1) , which were treated in the previous section, the area and the AR of the inner filler yarns could vary. Thus two distinct cross section “filler-I1” and “filler-I2” are named for the inner filler yarns.

The outer filler yarn at the two preforms outer surfaces has two distinct sections regarding its position relative to the binder yarn, as shown on Figure 3.49-a. Both of these two sections have one contact surface with the adjacent warp yarn layer. When binder yarn passes over, the filler yarn, denoted “filler-OZ”, takes semi-elliptical cross section shape and important contact pressure is applied on yarn outer surface. Like the inner filler yarn, because of the difference in the width of the two parts of binder yarns (j_2, j_1) the area and the AR of the outer filler yarns could varies. Thus two distinct cross section “filler-OZ1” and “filler-OZ2” are named for the inner filler yarns. But, as no binder yarn passing over the next filler yarn, less contact pressure is applied on the outer surface of this filler yarns and its section is called “filler-OF”.

3. 3D multiaxis weaving technology

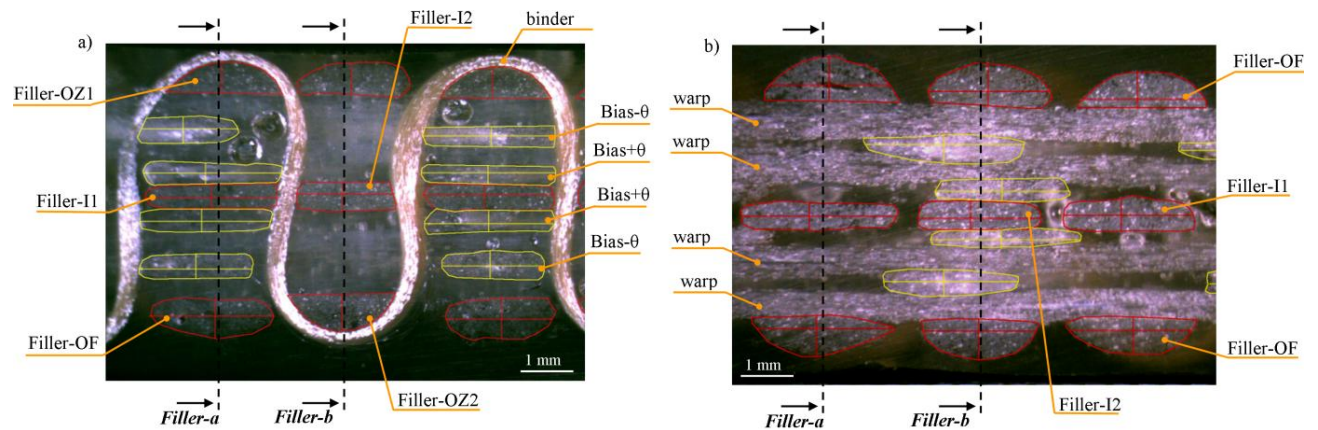


Figure 3.49: Micrographs of cross sections of sample-1 illustrates the variation of filler yarns cross sections, a) at cut plane warp-a, b) at cut plane warp-b.

Otherwise, on the cut plane “warp-b”, Figure 3.49-b, only three sections are distinguished the “filler-I1” and “filler-I2” sections for inner filler yarns and “filler-OF” section for the outer filler yarns. That is because the absence of the binder yarn at this cut plane. Thus, the outer filler yarns cross section alternates between “filler-OZ1”/“filler-OZ2” and “filler-OF” sections along its path in association with binder yarn path.

The difference in the area and the AR between these five cross sections of the filler yarns at the two cut-planes is investigated in reference to the area and AR of the “filler-I1” section as shown in Figure 3.50. On “warp-a” cut plane too low difference in the area is found between “filler-I1” and “filler-I2” less than 5% except for “sample-3”, whereas this difference is much more important regarding the AR value, reach to -50% for sample-5 and -70% for sample-5C, that increases as linear density of bias yarn increases. This result is associated to the inverse of the variation of (j_2/j_1) ratio between samples. However, on “warp-b” cut plane the difference in the area is become more important (about 20%) while the difference in the AR decreases, as shown in Figure 3.50-b,d.

Like the inner filler yarns sections “filler-I1” and “filler-I2” the difference between the two sections “filler-OZ1” and “filler-OZ2” of outer filler yarn regarding the area is too small less than 6%, as well as the difference in the AR which is more important about 58% for sample-5 and it relies also on the inverse of the (j_2/j_1) ratio. Otherwise, the two outer filler yarns under binder yarn “filler-OZ1” and “filler-OZ2” have cross section area smaller than the inner filler yarn, about -10% depending the density of the preform and binder yarn tension. That is due to the contact pressure applied by binder yarn on the outer filler yarns leading to compress their section “filler-OZ”. While the outer filler yarn with no binder yarn, “filler-OF”, has cross section area more important comparing to the inner filler yarns, about +25% on “warp-a” cut plane and about +40% comparing to outer filler under binder “filler-OZ”. But, the difference between outer filler yarn section “filler-OF” and inner filler yarns “filler-I1” decreases decrease on the cut plane “warp-b”. The same results are noted concerning the difference in the AR between these two sections on the two cut planes.

3. 3D multiaxis weaving technology

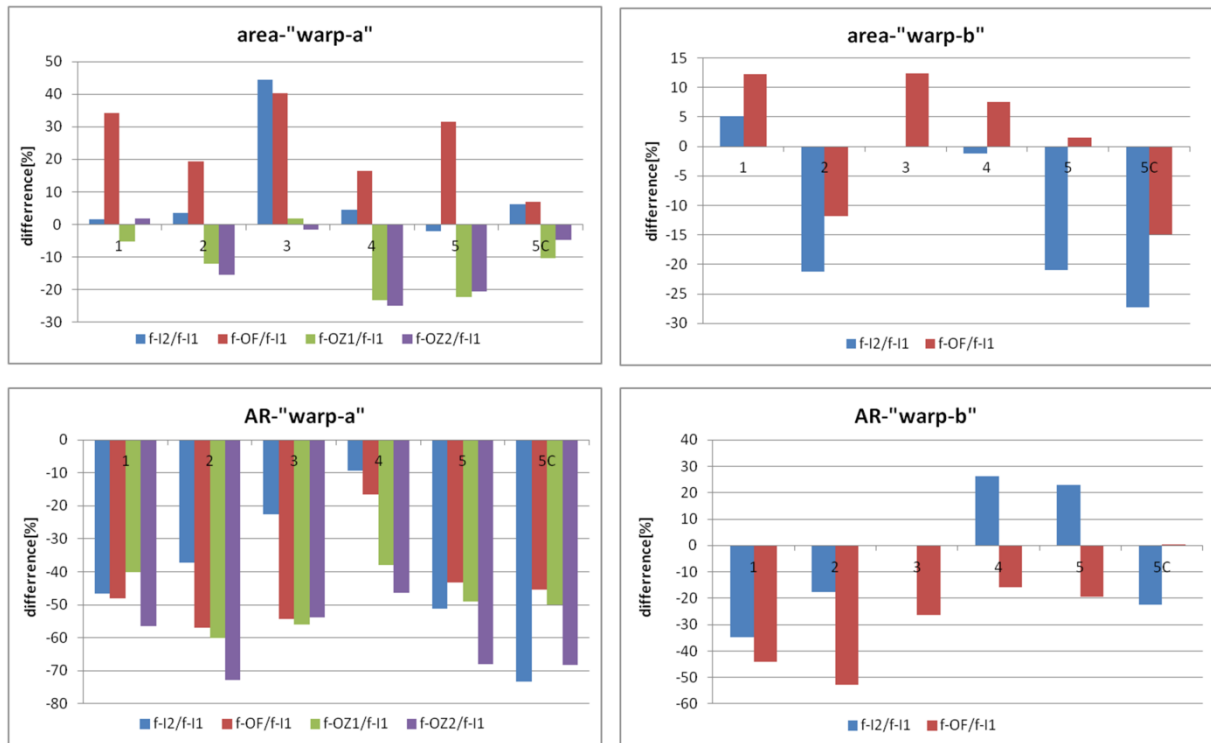


Figure 3.50: Difference in area (a, b) and in AR (c, d) for the filler yarns cross sections in reference to the area and AR of “filler-I1” section on the two cut plane “warp-a” (a, c) and “warp-b” (b, d).

3.7.3.7. Warp and biases yarns

The repeatability of the area and the AR values of the bias and warp yarns cross section at the same cut-plane are observed as well as their regularity across the different cut-planes, which signifies along yarns path. This observation is made by monitoring the coefficient of variation CV % for the area and the aspect ratio measured on the same cut plane (table 3.8) and between different cut-planes (table 3.9).

Table 3.8: Coefficient variation of the area and the AR of bias, warp and filler yarns measured at each cut plane.

cut-plane		Area_CV [%]						Aspect Ratio_CV [%]					
		1	2	3	4	5	5C	1	2	3	4	5	5C
Bias yarn	Warp-a	12.96	7.98	13.5	7.82	5.87	1.3	28.42	11.04	27.37	17.09	15.7	14.4
	Warp-b	13.17	11	13.1	6.76	7.19	10.5	17.91	15.69	30.15	9.57	12.1	14.6
	Filler-a	9.63	9.98	7.74	10.5	4.83	2.5	31.81	28.28	21.31	15.85	11.8	16.3
	Filler-b	9.92	9.97	8.28	7.79	8.77	6.6	23.62	24.75	33.52	19.53	15.4	15.8
Warp yarn	Filler-a	10.98	3.99	13.12	5.32	4.21	7.9	14.98	6.15	37.62	33.13	19.7	20.5
	Filler-b	6.73	9.28	10.43	7.76	9.13	5.4	18.37	28.38	30.38	22.38	15.9	19

Concerning the repeatability at the same cut-plane and between the unit cells, the variation of the area for the bias and warp yarns is approximately about 10%, while the variation of the AR is more important and more dispersed. That is could be referred to the yarns gap parameters, where the variation is less important with poor yarn gap, as it was mentioned earlier in the section (3.7.3.4) by comparing between samples 1 and 3, Figure 3.46. Also that is related to the weaving process because of the manual functioning of the mechanisms.

3. 3D multiaxis weaving technology

Table 3.9: Coefficient variation of the area and the AR of bias and warp yarns across the four cut planes.

	Bias yarn		warp yarn	
	S_CV [%]	AR_CV [%]	S_CV [%]	AR_CV [%]
Sample-1	3.26	21.28	5.56	11.10
Sample-2	5.28	23.37	7.63	6.19
Sample-3	5.37	17.11	3.92	4.95
Sample-4	5.91	21.44	9.48	4.95
Sample-5	7.12	12.18	2.19	15.49
Sample-5C	5.54	16.68	11.8	29

Concerning the regularity, between the cut planes, we notice that the variation of area of the bias and warp yarns cross section is less than 7.12% and 11.8% respectively. Otherwise, the variation of AR for bias yarns cross section is more important and dispersed; further, it could be related oppositely to yarns counts per unit cell. However, the variation of AR for warp yarns cross section is less important than in bias yarns and it is more stable between the two planes, except for sample-5C. The difference in AR value indicates the variation of the shape of yarns cross section. In the case of biases yarns, the high variation in the shape, in comparing to the less variation for warp yarns, refers to the variation of the contact with surrounding yarns along its trajectory inside the structure due to the passage under binder yarns. Where, as shown in cut plane type “a” (“warp-a” and “filler-a”), the bias yarns pass between two through thickness parts of binder yarns so higher lateral pressure resulting in lower AR. However, in cut plane type “b” (“warp-b” and “filler-b”), no binder yarns so too less lateral pressure resulting in higher AR and elliptical cross section shape. By comparing the coefficient variation of the area and AR between the sample-5 and sample-5C to see the influence of the impregnation process, it could be noticed the augmentation of the coefficient variation of AR after impregnation.

3.7.3.8. Packing factor

The packing factor of the constituent filaments of each yarn is predicted by equation (3.6) and listed in table (3.10). The packing factor value is presented only for three filler yarns sections: “filler-I”, “filler-OZ” and “filler-OF” as a poor deviation in the cross section area was observed between the two inner filler yarns section “filler-I1” and “filler-I2”. And similarly for the two outer filler yarn sections “filler-OZ1” and “filler-OZ2” under binder yarn.

Table 3.10: Mean values of the computed packing factor.

Yarns	sample-1	sample-2	sample-3	sample-4	sample-5	sample-5C	dif.*[%]
Warp	0,51	0,43	0,44	0,51	0,47	0,73	54,1
Filler-inner	0,54	0,48	0,53	0,52	0,52	0,58	11,4
Filler- outer free	0,41	0,39	0,42	0,44	0,39	0,55	41,7
Filler- outer under binder	0,56	0,55	0,77	0,67	0,65	0,65	-0,4
Bias	0,48	0,46	0,45	0,52	0,55	0,62	12,3
Binder	0,40	0,39	0,34	0,34	0,38	0,9	141,2

*dif.: represent the difference in percentage of the packing factor value of the yarns of the sample-5C relative to the values of the sample-5 to evaluate the influence of impregnation process.

3. 3D multiaxis weaving technology

From the table 3.10 and in association with the figure (3.49), a remarkable difference could be noted in the packing factor value for the three filler yarns sections: “filler-I”, “filler-OZ” and “filler-OF” referred to filler yarn position inside the structure. This difference is attributed to the yarn-to-yarn contact interaction. The filler yarn under binder yarn “filler-OZ” subjected to high contact compressing by the binder yarn alternating its position to the next outer preform layer. This compaction is related to the binder yarn count and its tension during weaving process. As a result of the compressing contact on the two yarns surface, the filaments inside the yarn section re-arrange with less gaps between them resulting in increase the packing factor value associated to decrease the cross section area. Contrariwise, the opposite filler yarn “filler-OF” in the opposite outer layer is less compacted where no binder yarn. So less packing factor value is resulted.

This difference in the packing factor for the both outer filler yarns “filler-OF” and “filler-OZ” with respect to the inner filler yarns is more explored in Figure 3.51. It could be deduced from this Figure that as the yarns linear density and their number per unit cell increase the difference in the packing factor between the outer and inner filler decrease.

Comparing the mean value of the packing factor of the impregnated sample-5 by VARTM method to that of the dry preform allows see the influence of the pressure applied during the impregnation process on the yarn cross section area and packing factor. The difference in the packing factor value between the two stats is listed in table (3.10). It could be noted also from the Figure 3.50 that the difference in packing factor between outer and inner yarns decreases after impregnation.

The area cross section measurement for the binder yarns is made on the crown part, outlined in the figure 3.47. As the crown part is on the two outer faces of the preform, it is more subjected to the pressure applied during impregnation process. That could explain the high compaction of the binder yarn filaments resulting in the maximum packing factor value (0.9096) corresponding to the hexagonal array arrangement of the filaments with total filament-filament contact. This observation would be more explored in the future work.

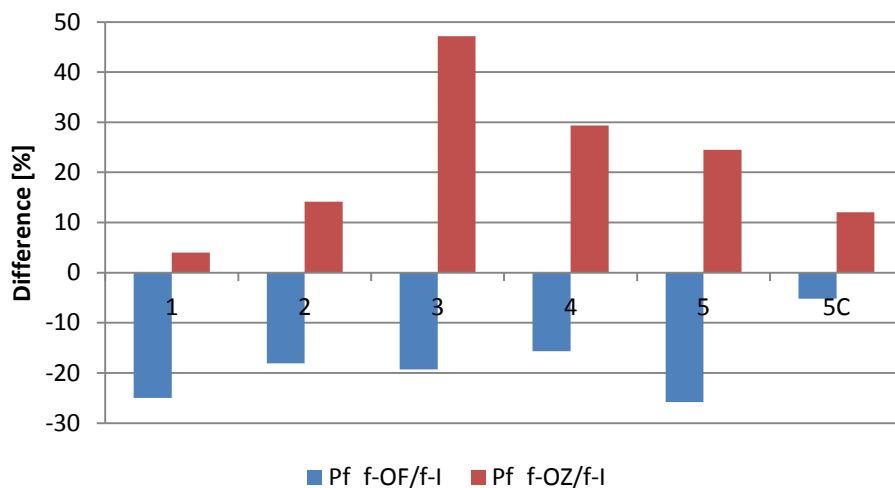


Figure 3.51: Difference in packing factor mean value for the filler-outer free “f-OF” and the filler-outer under binder “f-OZ” relative to the filler-inner “f-I”.

3.8. Classification of the developed loom

To better show the technical solutions developed in this project for the 3D multiaxis weaving technology, the specifications of the built prototype loom is compared to the tube-rapier

3. 3D multiaxis weaving technology

and the tube-carrier 3D multiaxis weaving looms developed by Bilisik et al. (1994, 2000, 2010). Also the manufacturing, weaving and geometrical parameters of the manufactured composite (sample-5C) are compared to the samples manufactured by the Bilisik's looms. Three composite samples provided by Bilisik (2010) were impregnated by compression molding process with 900 kg of applied pressure on the mold at 80 °C and for 60 min. The used resin was Tactix 123 and it was cured at 177°C for 120min.

This comparison is made in reference to the Bilisik's work because it is the unique published 3D multiaxis weaving technology with providing the parameters of the manufactured composite. And, it is listed in table 3.11.

Table 3.11: Comparison developed 3D multiaxis weaving loom prototype and the impregnated sample-5C to the two 3D multiaxis weaving looms of Bilisik (2010) and the produced composite by these looms.

	Sample-5C	tube rapier	tube carrier	
in-plane yarns material	glass	carbon	carbon	
binder yarns material	kevlar	carbon	carbon	
μ_s [g/m] x n_w^{uc}	2.4x3	0.398 x1	0.398 x1	
μ_f [g/m] x n_f^{uc}	2.4x4	0.198 x2	0.198 x2	
μ_θ [g/m] x n_θ^{uc}	2.4x2	0.398 x2	0.398 x2	
μ_b [g/m]	0.172	0.198	0.198	
<i>Guide elements in weaving zone</i>				
warp yarns	18 x 4 layer	32 x 2 layer	32 x 2 layer	
bias +/- θ yarns	20 x 4 layer	32 rows x 2 layer	32 rows x 2 layer	
binder yarns	19	32	32	
filler yarn per insertion	double picks x 3 layers	double picks x 3 layers	double picks x 3 layers	
Bias yarns path pattern	edge-to-edge	zig-zag	edge-to-edge	
Uniformity of bias yarns orientation	uniform	non-uniform	uniform	
Bias yarns feeding	rotative braiders	fix bobbins	rotative braiders	
Bias yarn layers placement in the preform thickness	any layer	any layer	only top and bottom	
layers sequence	[90/ θ /0/- θ /0/90]s	[90/ θ /- θ /0/90]s	[90/ θ /- θ /0/90]s	
possibility to separate opposite bias layers by warp layer	yes	no	no	
width ratio	1/1	1/4.5	1/5.55	1/8.23
preform width [mm]	190	77.25	62.36	42
bias yarn orientation +/- θ [degree]	43.80°	34°	30°	40°
H [mm]	6.99	2.26	2.73	3.1
FVF [%]	45.47 ±1.2	33.9	38.5	47.5
warp /unit cell [%]	15.88	8.45	10.5	13.7
filler /unit cell [%]	14.68	4.82	5.42	4.77
bias /unit cell [%]	7.26	8.62	9.43	11.7
binder /unit cell [%]	0.41	3.36	3.67	5.61

3.9. Conclusion

A novel prototype loom has been constructed enabling weave multiaxis multilayer preform. The guide blocks technique was used to control bias yarns position in the weaving zone and achieve the required transversal displacement. The bias yarns would be maintained into position inside the preform by binder yarns and their orientation in $\pm\theta^\circ$ would be obtained by controlling number of binder per unit length in warp and weft direction. These two parameters could be managed by developed loom so bias yarns orientation could be varied. Uniform layers of bias yarns are obtained in means of closed rotative motion of guide blocks inside frames and rotative motion of feeding bobbins since they are mounted on rotative chain. Further, bias layers are edge to edge across fabric width. Symmetric structure regarding layers order is produced relative to mid-plane of structure. As well the number of layers could be managed on this loom and for the present architecture samples are made of 11 layers.

Warp yarns layer could be inserted between two opposite $+\theta^\circ$ and $-\theta^\circ$ bias layers contrary to all other developed multiaxis loom. That reduces the risks of the delamination fracture occurs at the preform free edge resulting from the high interlaminar stresses could be generated in case of high angle between layers. That will be investigated in the chapter 5.

Controlling bias yarns folding at the fabric edge minimized the fabric width shrinkage. Thus beating inserted filler yarns is achieved with minimum friction between reed blades and warp and bias yarns.

The delicate fibre, which has low flexibility such as glass fiber, could not be used as binder yarns because of the high bending curvature induced by insertion system of the binder yarn. Where, the available gaps between crossing opposite bias yarns to insert binder needles is too close to bias guide blocks frames resulting in high bending curvature for binder yarns.

The characterizing parameters of the 3D multiaxis woven preform have been defined and classified into three groups: manufacturing, weaving and geometrical parameters. Five samples of the 3D multiaxis woven preform have been fabricated on the developed loom with variation of the manufacturing and weaving parameters to evaluate their influence on the geometrical parameters. Further, the geometry of the yarns involving the shape, area and AR of the yarns cross section and the yarns path inside the structure have been also investigated. The five samples have been analysed in the dry state (after loom). The last sample has been also impregnated with resin epoxy using VARTM method then its geometrical parameters and yarns geometry have been investigated to evaluate the influence of the impregnation process.

Low crimp percentage has been observed for the in-plane yarns of this architecture since no interlacement between these yarns. The contact interaction between adjacent yarns governs the yarns cross section shape and dimensions inside the structure. The cross section area and shape of filler yarns are related inherently to its position relative to binder yarn. Low variation of the yarns cross section area along its path has been noticed for the five samples. However, the variation of the AR value of the yarns cross section along its path is more important and its related to the yarns gap value. The high yarn gap value causes rearrangement of the yarns inside the structure resulting in high variation of the yarns cross section shape and AR value. The packing factor of the constituent filaments inside the yarns is inversely proportional to the yarn cross section area. Regarding the outer filler yarns (on the two outer preform faces) the packing factor value is affected by its position and the tension applied on the binder yarns.

3. 3D multiaxis weaving technology

The pressure associated with the impregnation process causes compaction of the preform thickness without remarkable influence on the in-plane unit cell dimensions. That is resulting in increasing the FVF of the impregnated sample relative to dry state about 10%. By using the two computation methods of FVF (FVF-weight and FVF-volume), this increasing in the FVF is attributed to the compaction of the yarns cross section referred to reduction the filament-filament gaps inside the yarns more than the structure compaction referred to reduction the yarn-yarn gaps.

The developed prototype loom is not automated that limited the sample production. In the future work, this obstacle could be resolved enabling more detailed study of the manufacturing and weaving effect and the impregnation process effect on the geometrical properties of the final composite.

4. Geometrical modelling of 3D multiaxis woven composite

4.1. Introduction

The geometrical modelling consists of methods and algorithms used to define and predict the geometrical characteristics of an object and to provide its numerical representation. There are various applications of the geometrical modelling, as reported by Frain et al. (2002), such as in the scientific visualization: engineering design and mechanical analyses (CAD/CAM), and computer animation. In the textile industry, the tools are required to describe the complex geometry and architecture of the textile products (woven, braided and knitted fabric). Concerning the manufacturing of composite materials, the geometrical modelling is indispensable tool helping to design the textile reinforcement architecture and to develop mechanical modelling in order to evaluate the mechanical properties and performances, either for the dry preform or for the final composite. Design of the textile reinforcement architecture consists of defining interlacements and arrangements of the component yarns, according to the final use conditions of the composite.

In this chapter, the geometrical modelling approach is developed and adapted to 3D multiaxis woven reinforcements in order to estimate their geometrical properties and to construct geometric model necessary for the mechanical modelling of the structure intended to estimate its mechanical properties. Our modelling approach is developed based on the previous works presented in the literature for the 2D and 3D woven performs. A predictive geometrical model is developed, as a first step, helping to design this structure, determinate the influencing production parameters on the final geometrical properties and define the technological requirements to develop the weaving process. Secondly, the predictive model is evaluated in light of comparing the observed yarns geometry and measured geometrical parameters of manufactured samples via the geometrical characterization presented in the previous chapter. Thirdly, the geometrical modelling approach is optimized based on the obtained results from the geometrical characterization presented in the chapter 3. This optimization leads to construct a geometrical model of the architecture with sufficient accuracy ensuring a consistent mechanical modelling.

The geometrical model could be created on different scales as the hierarchical structure of textile preform as it will be explained in section 4.2. The different modelling methods proposed in the literature for woven preforms will be explored in the section 4.3. Then, the road map proposed to construct a RVE (Representative Volume Element) of this composite structure is presented in section 4.4. In the section 4.5, a predictive model, proposed in the literature for 3D woven preforms, has been optimized and adapted to our 3D multiaxis woven architecture. The validation of the predictive model by comparing it to results of the geometrical characterization is investigated in the section 4.6. Finally, the optimized geometrical model, based on the acquired observations and the measurements for produced preforms, is developed in the section 4.7.

4.2. Modelling scales for woven composite

The woven fabric is made up by interlacing distinct sets of yarns, in terms of the orientation of their main axis, in specified weave patterns. For the 2D woven fabric, the weave pattern specifies the relative position of the warp and filler yarns (up or down) at the crossover and also the number of the warp and weft yarns in the repeated pattern.

4. Geometrical modelling of 3D multiaxis woven composite

The woven fabric could be classified relative to its geometric dimensions and properties into *balanced fabric* when the properties are identical in the both warp and filler directions and *unbalanced fabric* when they are different. Also, the fabric is considered as *opened-packing weave*, Figure 4.1-a, when there is a gap between the adjacent yarns, on the other side, it is considered as *closed-packing weave*, Figure 4.1-b, when the fabric is tightly woven, which means no gap between yarns, Tan et al. (1997).

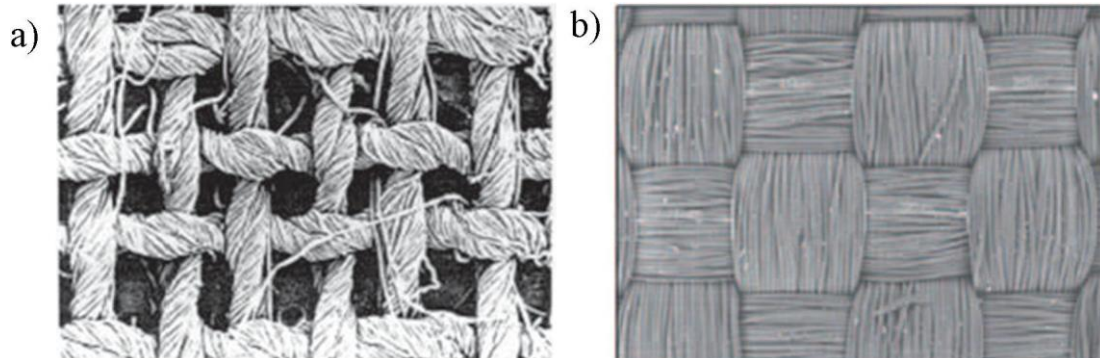


Figure 4.1: a) Opened-packing weave. b) closed-packing weave. (Hu, 2004 and Lin et al. 2012)

The yarn, in its turn, is composed of an assembly of fibres combined together by different spinning methods depending on their characteristics and the final use conditions. The fibres could be classified in terms of their lengths into short fibres and very long fibres (continues) denoted filaments. The short fibres are twisted together to increase the inter-friction between them providing sufficient cohesion to form the yarn (Gegauff 1907 and Lomov et al. 2005). On the other side, the filaments could be entangled or juxtaposed; also they could be twisted together (with poor turns number per unit length comparing to the case of short fibres) or sized to make the weaving process easier, (Scardino 1989).

In view of the hierarchy structure of the woven textile reinforcement, three distinct scales are introduced in the literature when modelling the geometry and analysing the mechanical performance of this preform and/or the obtained composite. Selection of the scale is associated with which mechanical property is intended to be evaluated or which response is investigated for this structure. On each scale, the origin of the heterogeneity of the built composite should be taken into consideration when dealing with. The scales, represented in the Figure 4.2, are:

- ***Micro-scale***: the properties of the fibres and the interaction between them and surrounding matrix are studied on this scale. That helps to define the orthotropic stiffness and strength properties of the yarns. The heterogeneity of the composite on this scale resulting from the fibre-matrix microstructure, Lief (2007), Figure 4.2-c.
- ***Meso-scale***: the effect of the interlacement and the arrangement of the yarns on the local mechanical properties of composite also on the permeability of the dry preform are evaluated on this scale. Often one unit cell of the structure is modelled on this scale because of the material and geometry periodicity of the woven reinforcement on this scale and, the responses of unit cell are the same in despite of their location in the reinforcement plates, (Karkkainen and Sankar 2006, Barbero 2013). The unit cell is defined as the smallest unit of the fabric representing one repeat of the weave pattern. Otherwise, according to certain literature definitions; the unit cell represents also the repeated volume/mass of the yarns across the fabric. The yarns are considered as homogenous and continuous material on this scale and their

properties are computed from the analyses made on the micro-scale level. The heterogeneity here is attributed to the waviness of the constituent yarns in the preform and the resin pockets separating the distinct yarns, Lief (2007), Figure 4.2-b.

- **Macro-scale:** The global performance of the preform, for example the large deformation of fabric (formability and drapability), is analysed on this scale. The computed properties of the unit cell on the meso-scale are served on this scale to assign the anisotropic material properties of the preform and the composite. The orientation of the yarns within the structure is the origin of the heterogeneity on this scale, Lief (2007), Figure 4.2-a.

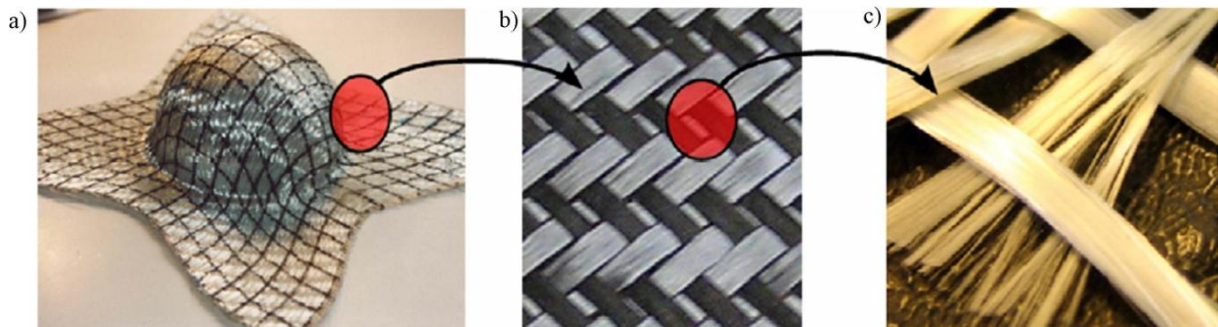


Figure 4.2: Hierarchy structure of textile reinforcement leads to three classified scales when study: a) macro-scale, b) meso-scale, c) micro-scale. (Boisse et al. 2010)

Certain of studies are made on multi-scale combining two scales as in the work of Durville (2005, 2008) who developed a geometrical model of 2D woven and of braided fabric on micro/meso-scale. On this twofold scale, the yarns are represented as a bundle of filaments instead of continuous solid as in meso-scale geometric models, Figure 4.3. That allows bypassing the required identification for yarns state inside the structure. Also that allows including the local phenomena between the filaments when analysing the mechanical performance of the structure on the meso-scale. In this model just a few number of filaments is modelled as 3D solid volume beam instead of the huge number of filaments composing the yarns in order to reducing the numerical computation cost. A contact detection algorithm between the filaments, which could be occurred at any point along the filament, is developed. However, the high computation cost of this modelling approach is still an obstacle.

In this study, since we focus on developing the multiaxis 3D weaving technology and on evaluating the effect of the new yarns arrangement on the mechanical properties of the produced 3D woven composite, so the geometric and mechanical modelling are developed on the meso-scale.

4.3. Literature survey about the meso-scale geometrical models of woven preform

Different geometric modelling approaches are developed in the literature. The sophistication of the developed models depends on the type and the aim of the next mechanical modelling. Where, the mechanical modelling could be intended for evaluation of mechanical performance of dry preform or of composite, for evaluation of forming behaviour of dry preform or for evaluation of permeability of dry preform. Otherwise, the built mechanical models are generally subdivided into two principal types; analytical model or numerical model.

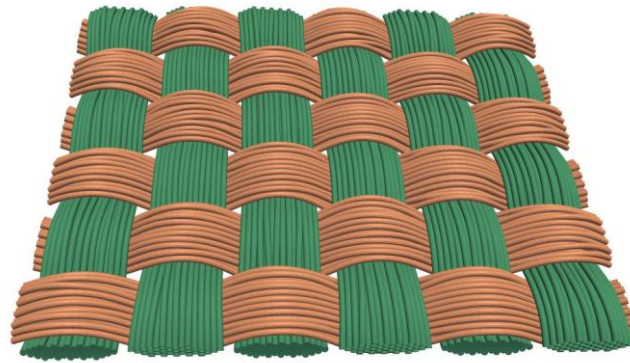


Figure 4.3: Durville's model of 2D plain weave fabric, multi-scale (micro-meso) geometric model. (Durville 2005 and 2008)

The **analytical models** are generally developed based on classical laminate theory and rule of mixture (Tan et al., 1997). The two basic analytical models are the orientation-averaging model (Kregers AF, and Melbardis YG. 1978) and the mosaic model (Ishikawa, T. and Chou, T. W., 1982). In both models, a unit cell of the structure is discretized to strips composed of unidirectional segments, which represent either fibres in specific orientation with matrix or pure matrix. Then, in orientation averaging model, the volume averaging method is applied with the iso-stress and iso-strain assumptions to predict the global stiffness constants of structure. While, in the mosaic model, the parallel model or series model were formed with iso-stress and iso-strain assumptions to compute global structure stiffness. The parallel model gives the upper bound solution of the stiffness constants while the series model gives the lower bound. In the mosaic model the fibres continuity and undulation was neglected. Therefore, the fibre undulation model (Ishikawa, T. and Chou, T. W., 1983) was proposed where, the fibres continuity and undulation were respected for yarns in loading direction while they were neglected for yarns perpendicular to loading direction.

On the other side, Cox et al. (1994) proposed the binary model using the finite elements method to predict the elastic properties of 3D woven interlock composite. In this model, the axial properties of the yarns are represented by line element, while; the transverse and shear properties are represented by eight nodes iso-parametric solid element called also "effective medium elements". The binder yarns are represented by spring and the weave pattern is represented by node pattern. The macroscopic elastic constants of this assemblage, binary model, are computed by the finite element method and an acceptable agreement is noted in comparison to the experimental results for the in-plane properties.

Consequently, the analytical models provide good predictions for fibre dominated properties (e.g. in-plane on-axis modulus), but for matrix dominated properties like shear and out-of-plane properties they are predicted with significant errors as reported by (Prodromou AG., et al. ; 2011). However, these models could not find the stress/strain fields so the fracture evaluation could not be predicted. On the other side, the analytical models are easy to implement, computationally inexpensive and they do not require detailed description of the yarns geometry within the preform or composite. Only the geometrical properties of the unit cell are required.

On the other side, the **numerical models** are counting on construction of a RVE (Representative Volume Element) of the structure based on detailed geometric description then implementing the finite element analysis to predict the internal stress/strain fields, in addition to evaluation of the thermo-elastic composite properties with moderate to good

accuracy. That allows using this approach for progressive damage analysis, (Prodromou AG., et al., 2011). However, these models are costly computationally and the accuracy of the obtained stress/strain field depends on the consistence of the geometric modelling and the created RVE relative to the real structure.

4.3.1. Geometrical modelling type

Among the proposed geometric models, two types of models could be distinguished:

1. Predictive geometric modelling relies on mathematical geometric model, based on simplifying assumptions for the cross section shape and the path of the constitutive yarns and it counts on the manufacture parameters of yarns and the weaving parameters as an input data. This model is used to predict the geometric properties of the designed preform before its production. That aids essentially in the design of the final product and evolving adequate technique to produce novel structure.
2. A more realistic geometric modelling is based on detailed geometric description of the produced preform. This model is indispensable to create accurate mechanical modelling. Thus, a geometrical characterization is essentially required before construction this model to describe the real geometry of the yarns within the preform and to measure the yarns and the unit cell parameters. This type of modelling could not be used in the design phase. However, it serves as a back-data to optimize the predictive model for next production.

4.3.2. The path and the cross section shapes of the yarn:

The construction of a geometrical model involves determination of path, cross-section shape and placement of the constitutive yarns inside the structure, in addition to defining the yarns and the unit cell parameters. The path of the yarn inside the woven fabric is the path of the yarn centerline. The cross section shape of the yarn is defined on a plane perpendicular to its centerline, Figure 4.4. The path and the cross section shape of the yarn is governed by different materials, manufacture and weaving factors such as the yarn formation method, the yarns material properties, the unit cell parameters that influence also on the interaction between the fibres inside the yarns and the interaction between the adjacent yarns. The Figure 4.5 shows the reorganization of the fibres inside the yarns in functions of the fibre type, yarn formation method and weave pattern.

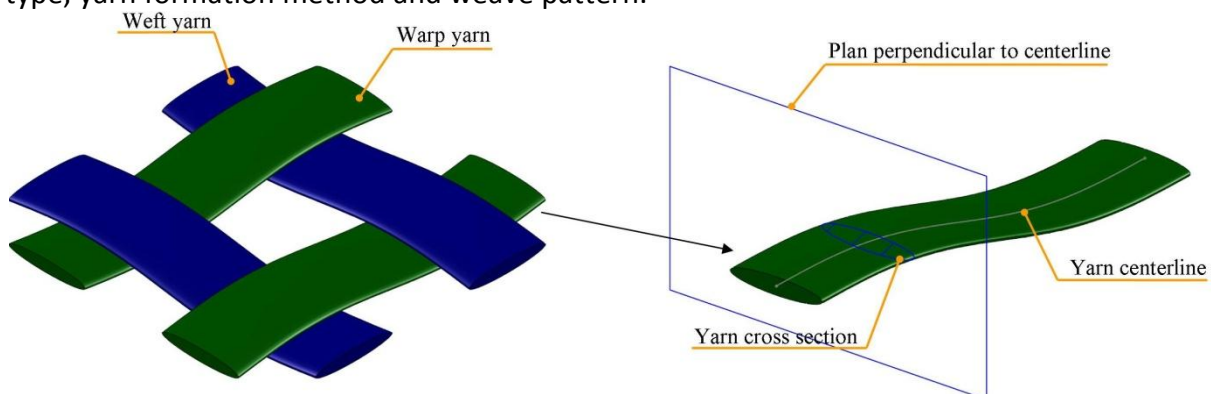


Figure 4.4: Representative schema of the 2D plain weave fabric with illustration of the yarn centerline and its cross section.

On the other side, the fibrous structure of the yarns gives them a high flexibility resulting in a complex path for yarns inside the preform. As well, it gives to the cross section of the yarns high sensibility and deformability to the outline contact and interaction with the surrounding

yarns. These flexibility and transversal deformation sensibility are inversely related to the cohesion forces between fibres inside the yarns in addition to the mechanical and physical properties of fibre material. The low cohesion forces, like in the case of just juxtaposed filaments, leads to high flexibility and deformability. Contrariwise, the high cohesion forces for the same fibre mechanical properties, like in the case of twisted yarn, leads to less flexibility and deformability. That makes the geometrical modelling of fibrous structure too difficult in terms of the consideration of the cross section shape and the path of the component yarns.

In view of the various influencing factors and the fibrous structure of the yarn, different hypothesis and approximation concerning the path and cross section shape of the yarn are assumed associated with the analysed weaving architecture.

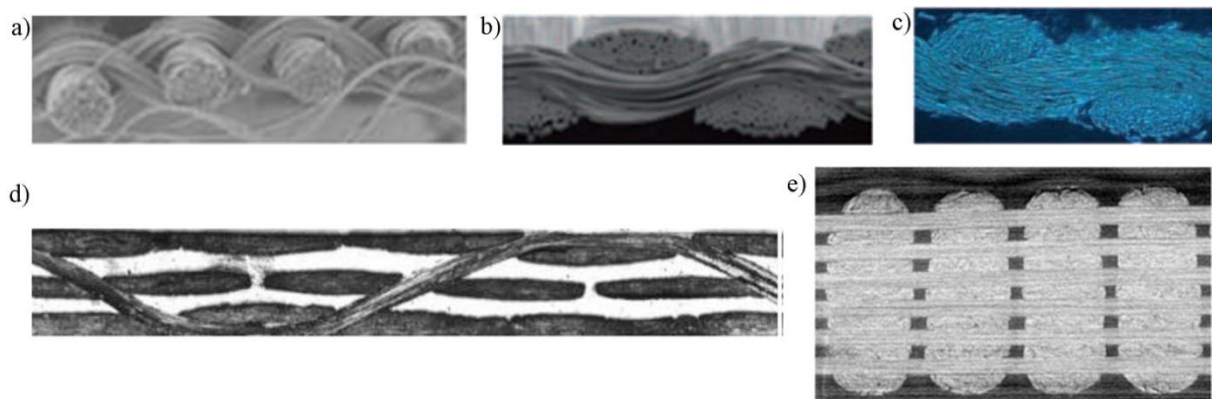


Figure 4.5: Micrographs for different fabrics with different yarn types and different architectures illustrates the yarns cross sections shape. a) plain weave, twisted yarns, circular cross section. b) plain weave, untwisted yarns, lenticular cross section. c) elliptical cross section. d) 3D fabric, angle interlock. e) 3D fabric, orthogonal. (Lin et al. 2012).

4.3.3. Geometrical models for 2D woven fabric

The first work done in this domain was focused on 2D plain weave fabrics by Peirce (1937). He proposed an idealized geometrical model, the cross section shape of yarns was considered circular and highly incompressible but at the same time perfectly flexible. The path of the yarns was built up by superimposing linear and circular yarn segments, Figure 4.6 (Hu, 2004). This model is valid in very open weave but the assumptions of circular cross-section shape and incompressibility and perfect flexibility of yarns are unrealistic causing the limitation of the application of this model (Jinlian, 2004). Peirce re-proposed an elliptical cross-section instead of circular to make more realistic model representing the yarn flattening resulting from the inter-yarns pressures induced during weaving, Figure 4.7 (Hu, 2004). Kemp (1958) used the racetrack section for the yarns cross section to represent the yarns flattening instead of the elliptical section in the Peirce model. The racetrack section is a rectangle section with two circular arcs on its two ends, Figure 4.8 (Hu, 2004). Hearle and Shanahan (1978) proposed a lenticular section, which is defined as an intersection of two circles of equal radius offset by a given distance, Figure 4.9 (Hu, 2004). This assumption provides a good accuracy and fit the yarns geometry for many 2D woven fabrics (Sherburn, 2007). Searles et al., (2001) used two splines to represent the upper and lower halves of the yarns. The idea of using two splines instead of one is to break the first order continuity at edges of the yarns and that gives a better fit. However, large number of parameters obtainable by image analysis are required in this representation.

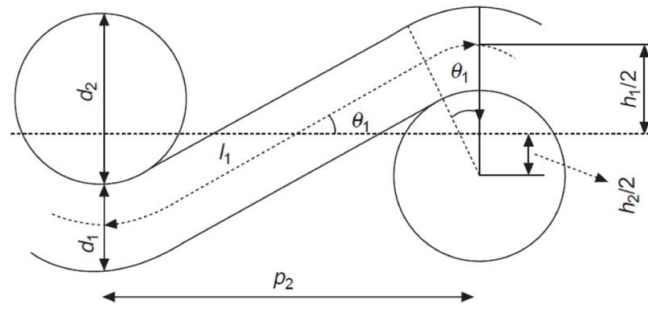


Figure 4.6: Peirce's model for 2D plain weave fabric, circular cross section shape assumption. (Hu 2004)

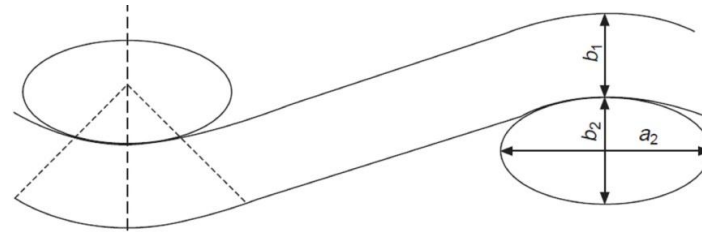


Figure 4.7: Peirce's model for 2D plain weave fabric, elliptical cross section shape assumption. (Hu 2004)

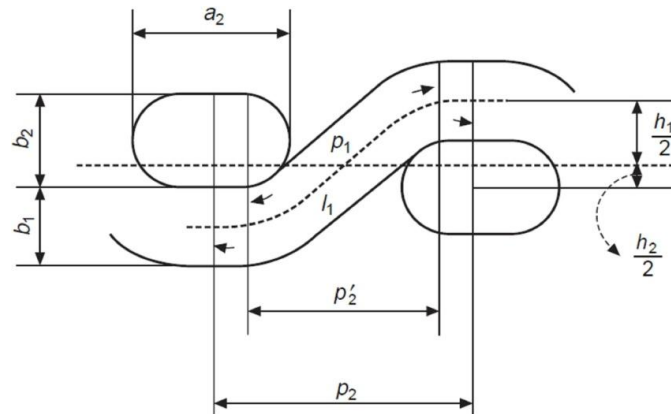


Figure 4.8: Kemp's model for 2D weave fabric, racetrack cross section shape assumption. (Hu 2004)

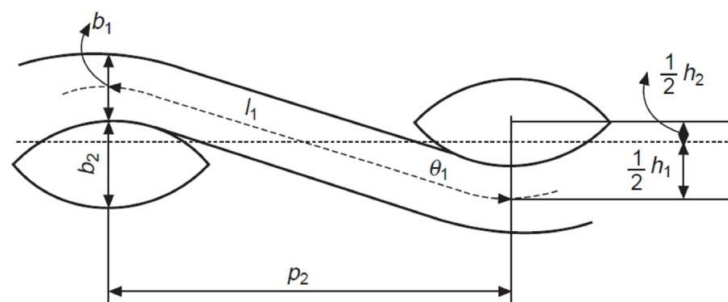


Figure 4.9: Hearle and Shanahan's model for 2D weave fabric, lenticular cross section shape assumption. (Hu 2004)

4.3.4. Geometrical models for 3D woven fabric

Concerning the 3D woven preform (angle-interlock, layer to layer interlock and orthogonal 3D weave architecture), several researchers worked recently on to face the need of design and understand the geometrical and mechanical properties of these preforms, used in composite applications. Among the proposed models, Quinn et al., (2003) proposed an idealized predictive geometrical model for the 3D woven preform. In this model, the path of yarns was considered straight even for binder yarns, where it was composed of two straight

4. Geometrical modelling of 3D multiaxis woven composite

segments with a right angle between them, Figure 4.10. The first segment is vertical in the through the thickness direction of the preform and the second one is horizontal in the 0° direction on the upper and lower surfaces of preform. The lenticular cross section shape was assumed for all constitutive yarns (warp, weft, binder) and the yarns count and an assumed packing density determined the major and minor dimensions of cross sections. In this idealized model, the correlation between experimental and predicted properties for orthogonal architecture was found reasonable, but it was less accurate for interlinked (orthogonal) architecture. Quinn re-proposed a lenticular-based model as an optimization for the idealized model. In this model, the path of binder yarns was composed of arcs around the lenticular cross-section of the weft yarns and straight segments. In this case the through thickness part has angle less than 90° relative to preform plane, Figure 4.11. This last optimized model showed more realistic assumption for the binder yarn path also a more accurate correlation, between predicted and experimental parameters, was found for the fibre volume fraction and total preform thickness comparing to the idealized model.

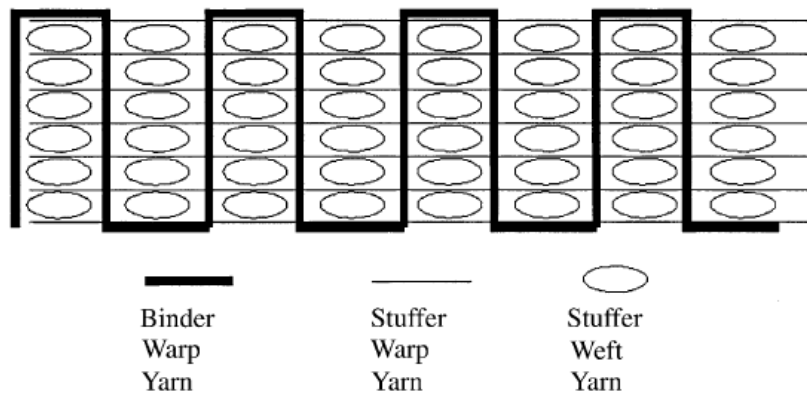


Figure 4.10: Quinn's model for 3D woven preform, idealized predictive geometric model. (Quinn et al. 2003).

Wu Z. (2009) developed an analytical model to predict the stiffness properties of orthogonal 3D woven composite based on a predictive geometric model. In his model two cross-section shapes for yarns were assumed rectangular and ellipsoidal. The yarns path was assumed straight even for binder yarns, Figure 4.12. The consideration of the straight yarns path bases on the very low crimp of the in-plane yarns, which could be neglect, as no interlacement between in-plane yarns in the orthogonal architecture. The effects of the number of warp yarns in the layer to the binder yarns, the number of filler yarns that binder yarn passes over them and the number of the warp and filler yarns layers on the elastic constants were investigated.

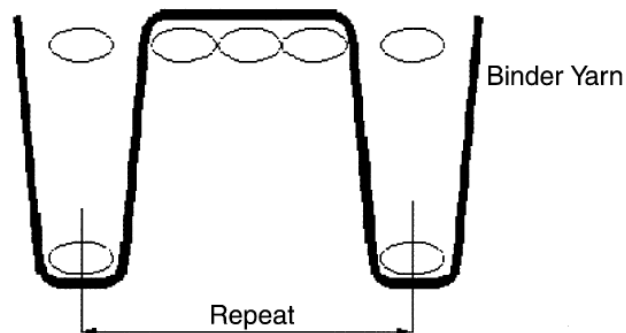


Figure 4.11: Quinn's optimized model for 3D orthogonal woven preform. (Quinn et al. 2003).

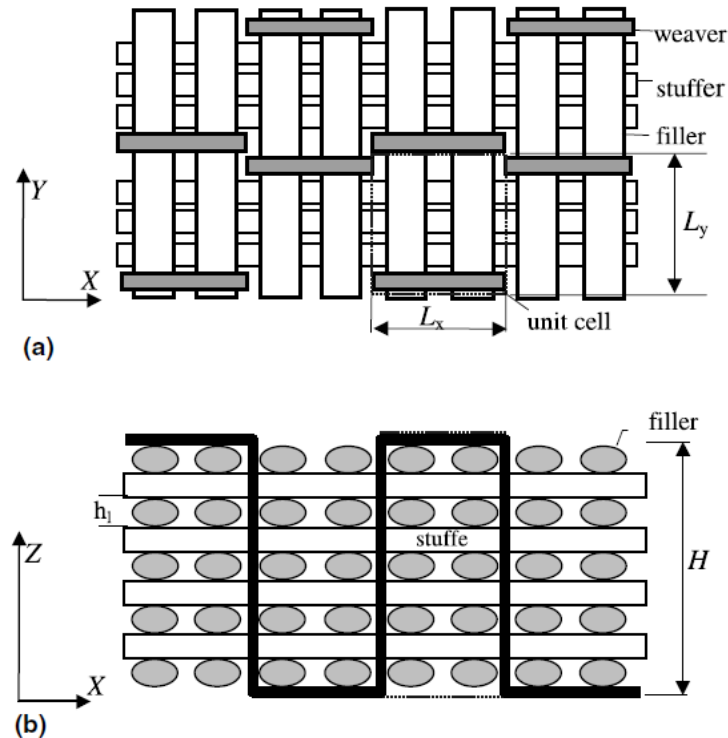


Figure 4.12: Wu's model for 3D orthogonal woven reinforced composite, a) plan view, b) side view. (Wu et al. 2002).

Buchanan et al., (2010-a) proposed a predictive model for the 3D orthogonal woven preform. As the idealized model of Quinn et al., (2003), the yarn path was considered straight but the ellipsoidal cross section shape was assumed for all yarns and the aspect ratio between the major and minor dimensions of yarns cross sections was considered constant and equal to 11 for warp and filler yarns and 4 for binder yarn. The total thickness of preform was calculated without taking into consideration the thickness of binder yarns, in other word, the 0° direction segment of binder yarn was not taken into consideration in the computation of the preform thickness. Better correlation is obtained between the experimental parameters (viz. fibre volume fraction and preform thickness) and the predicted one computed by Buchanan's model in comparison to Quinn's (2003) model. The noted error is related to the binder yarns length inside the unit cell.

Rao et al., (2009) studied by finite element method the influence of the consideration or not the 0° oriented segment of the binder yarn (crown part) at the two outer surfaces of composite on the elastic constants of an orthogonal 3D woven composite, Figure 4.13 illustrates the two configurations; crowned and uncrowned binder yarn. Knockdown was noted on the in-plane elastic constants when take the crown part into account because of the rich resin zone associated with the crown part. An additional layer of matrix is considered on the two outer surfaces of the RVE in the case of crowned configuration to avoid meshing difficulty in the FE.

The three predictive models provided a good approximation regarding prediction of the fibre volume fraction in the preform, the preform total thickness and the proportion of each yarns volume. That aids the designer to define the input parameters (viz. manufacture parameters and weaver parameters). However, in these models, the area and the two principle dimensions of the yarns cross sections are computed (as output parameters) by assuming the value of the filaments packing factor and the aspect ratio. Hence, the geometry of the

4. Geometrical modelling of 3D multiaxis woven composite

yarns inside the structure is not represented accurately through these models. Thus, they could not be used to construct an accurate RVE serving in mechanical modelling to evaluate the stress/strain field before validating this model relative to the real geometry of the yarns inside the preform.

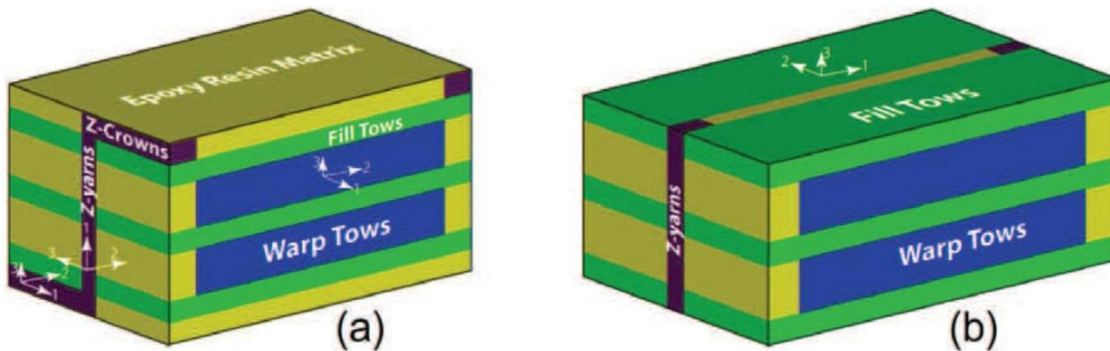


Figure 4.13: Rao's model for 3D orthogonal woven reinforced composite with two configurations for z-yarn, a) crowned configuration, b) uncrowned configuration. (Rao et al. 2009).

On the other side, the more complex model requires more detailed geometric parameters and characterization for the yarns and unit cell geometry. This type of models costs numerically and it induces complex meshing process in time of the finite elements analysing. Tan et al. (2000), proposed a geometrical laminate block model for 3D orthogonal woven reinforced composites aiding to predict the stiffness and strength properties using analytical and FE methods. Experimental study is made first with a geometrical characterization. It is noted that the coefficient variation of the measured width and height of weft and warp yarns cross-sections at the same micrograph is among 6.7% and 15%. In the geometric model, the shape of the yarns cross section is approximated to rectangle, and the yarn path is considered straight within the structure, as illustrated in Figure 4.14.

Nehme et al. (2011), developed a 3D solid geometric model for two angle interlock woven reinforced composites to analyse the mechanical performance of these structures by the FE. The developed model is based on the measured parameters such as the width and the height of yarns cross-section and the distance between two adjacent yarns in addition to the observed arrangement of the yarns within the structure. Whereas, the measured area of the yarns cross section is not taken as basic factor to define the geometry of the yarns. The shape of the yarns cross section is assumed to be a flatten ellipse (combination of ellipse and rectangle, Figure 4.15-a) and it is considered constant along the path. The undulation of the weft yarns was not taken into consideration and its path is considered straight as a simplification, as illustrated in the constructed RVE in Figure 4.15-b. To solve the problem of the yarn contact, an additional matrix layer separating the contacting yarns at overlap zone is considered. It was not mentioned the adjustment made to take the influence of the additional layer on the geometrical properties and the mechanical performance as well the correlation between constructed RVE and real composite in term of the fibre volume fraction and other geometrical properties.

Lapeyronnie et al. (2011), proposed a 3D solid geometric model, for layer-to-layer angle interlock architecture of 3D woven reinforced composite, aids to evaluate the mechanical properties of this structure by a developed homogenization method using the FE. The shape is adjusted to equivalent lenticular shape with holding the cross section area constant as criteria, Figure 4.16. The shape and the area are considered constant along the yarns path.

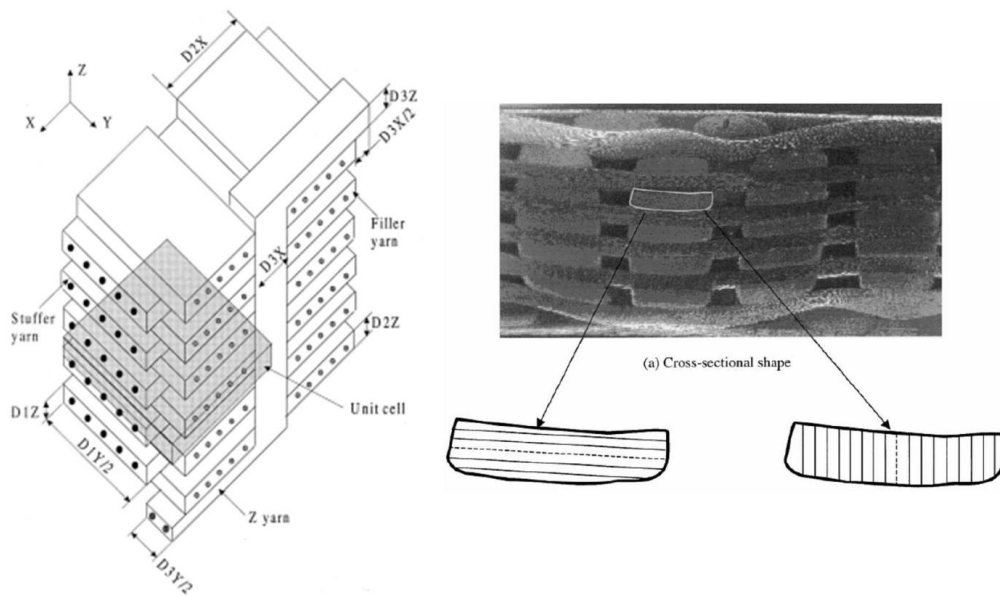


Figure 4.14: Tan's geometric laminate block model for 3D orthogonal woven reinforced composite with illustration of the rectangular cross section shape consideration. (Tan et al. 2000).

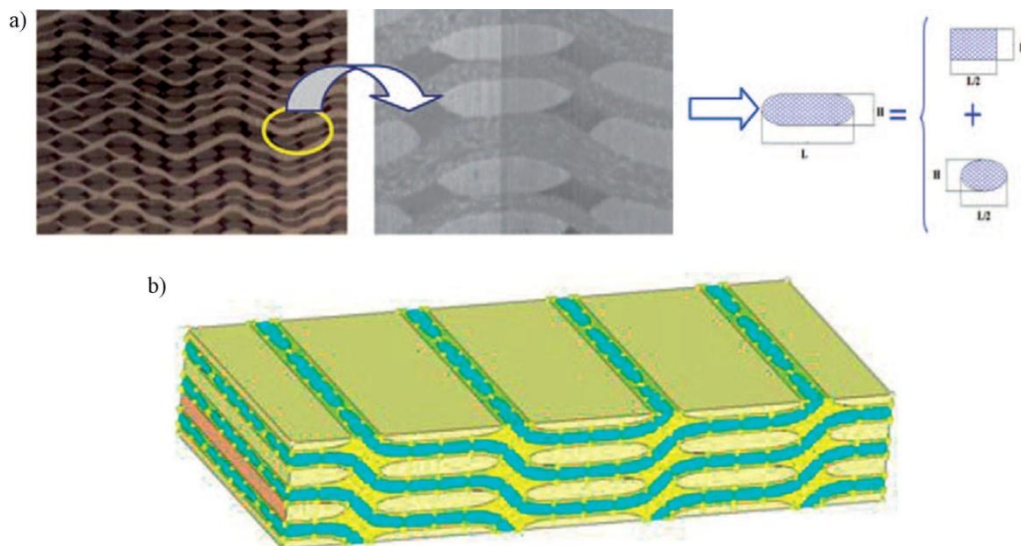


Figure 4.15: Nehme et al.'s model for two angle interlock, a) a transverse micrograph of the composite and flatten ellipse shape consideration, b) constructed RVE. (Nehme et al. 2011)



Figure 4.16: Lapeyronnie et al.'s model for layer to layer angle interlock, adaptation of the yarn cross section shape to lenticular with keeping constant area. (Lapeyronnie et al. 2011)

4.3.5. Textile Geometry Preprocessor

All the previous models were idealized meaning that the complex yarn path and the variations of the shape and the area of the yarn cross section along its path were not taken into consideration. As well, each model was proposed for specified fabric architecture and geometry and it could not be generalized. Therefore, different textile geometry preprocessors (TGP) were programmed to provide a designing and geometric modelling tool

4. Geometrical modelling of 3D multiaxis woven composite

that could be used to construct a geometrical model of a unit cell for any woven 2D fabric even for knit and stitched laminate textile structures. Among these software, WiseTex package, developed by Lomov and co-workers (2001, 2005, 2007 and 2008), is providing tools serving in geometric modelling, constructing and meshing a RVE and mechanical evaluation of the following types of fabrics: 2D and 3D woven, 2 and 3-axial braided, knitted and multiaxis multiply stitched (non crimp fabric). In our work the focus is on the proposed approach for the geometric modelling of woven fabric. The required data in this model are classified in three groups. The first are the yarns properties including: geometry of the yarns cross-section and the fibrous content together with its mechanical properties (tensile, compression, bending and friction). The second one is defined by the weaving pattern of the modelled architecture. The last data group is the yarn spacing in the weave pattern. Additional input data is required in case of the 3D woven fabric defining the shift between the weft layers. Symmetrical prescribed shape (elliptical, lenticular or rectangular) is assigned to the yarns cross section. The paths of the yarns are represented by the centreline of the yarns and they are subdivided in intervals of crimp, Figure 4.17. Then, the minimum bending energy is applied to find the optimal path. The same method “minimizing the bending energy” could be implemented to determine the geometry of the deformed fabric. In this modelling approach, regarding the consideration for the yarns cross section; a symmetrical and constant shape along the yarn path are not realistic where the yarn shape is in function of the interaction with the outline yarns. Also, in the contact zone between yarns the yarns cross section dimensions are calculated by ensuring a constant distance between the contacting yarns centrelines. That may cause a penetration between yarns when meshing in FE.

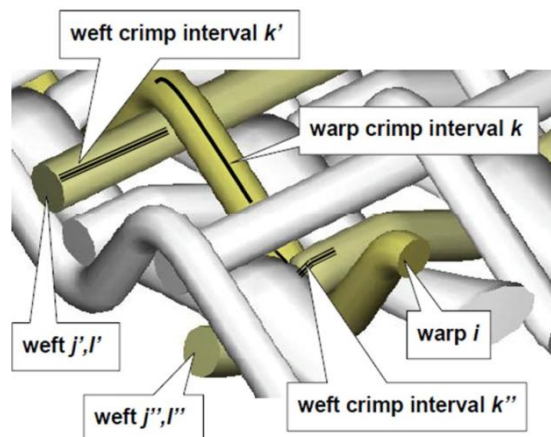


Figure 4.17: Crimp intervals consideration in geometric modeling in WiseTex. (Lomov et al. 2008)

To eliminate this interpenetration, a local re-dimensioning is proposed for yarns cross section in the contact zone in the case of orthogonal penetration or an intermediate FE approach developed by Zako (2003) could be applied, Figure 4.18. Xu et al. (2013) implemented WiseTex software to create a RVE of a 2D plain weave reinforced composite in order to study damages issue of this structure. For the created RVE, and to avoid the problem of the contact between the weft and warp yarns, additional thin layer of matrix is added to separate the two contacting yarns and to overpass the arisen consequence the area of the yarns are decreased about 10% with increasing the associated packing factor value. In despite of these approximations, an accurate estimation of the mechanical properties is obtained for different 3D composite structure using the RVE constructed by this

4. Geometrical modelling of 3D multiaxis woven composite

geometrical approach. However, in the present study, Wisetex software could not be implemented to construct geometric model for the developed 3D multiaxis woven preform because its restriction to 2D and 3D conventional weave pattern and there is no possibility to introduce bias yarn in the weave pattern.

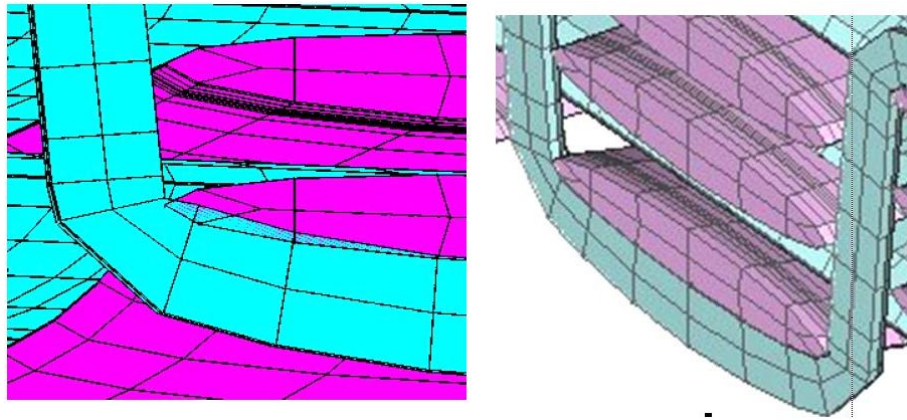


Figure 4.18: Yarns interpenetration on the overlap zone in WiseTex software, left Figure, and the correction realized by M. Zako approach, the right Figure. (Lomov et al. 2008)

The other remarkable TGP in this field is TEXGEN, open source software, developed at the University of Nottingham, Lin et al. (2012). This software could be implemented to model 2D or 3D woven, knitted, knotted or non-crimp fabric, where the two basic element to construct the geometric model (path and cross section shape of constituent yarns) are determined independently. In the experiments, the cross section of yarns is fitted to symmetrical shape (elliptical, lenticular) or to hybrid shape, Figures 4.19-a, while the centreline of yarns is defined based on the measured parameters of the geometry of the yarns and the unit cell. Spline (Bezier, natural or periodic cubic) is used to represent the centreline with knot (control point), Figure 4.19-b. These knots allow control the centreline path. The section is assigned at these knots. So the yarns are represented as a series of defined sections that will be lofted to build a solid yarns volume. In this method, interpenetration could be occurred between contacting yarns. To avoid the appeared interpenetration, knots are considered on the circumference of the yarns cross-section, Figure 4.19-c, making able the adjustment of the cross sections according to the contact conditions. However, the yarn/yarn contact zone is not assured in this method that could affect the stress/strain field in the structure, the interlaminar stresses created at yarn contact zone and the estimation of the strength properties.

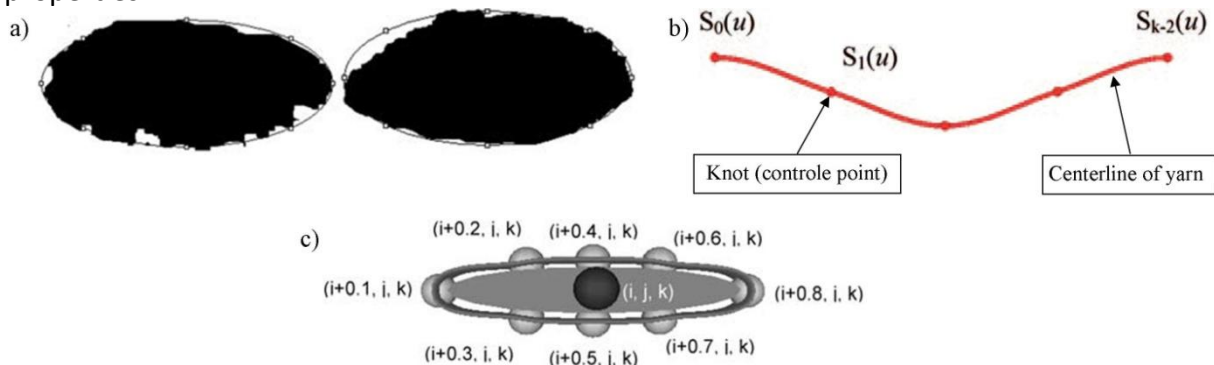


Figure 4.19: a) fitting the yarns cross section to ellipse shape, b) spline with control point representing the yarn centerline in Texgen modeling, c) knot on the circumference of the yarn cross section. (Lin et al. 2012)

4. Geometrical modelling of 3D multiaxis woven composite

To overcome the problem of the interpenetration between contacting yarns in TGPs resulting from the followed methods, which do not take into consideration the conditions of the contact zone as a constructing element when defining the path and the cross section of yarns, Hivet and Boisse (2005, 2008) and Wendling (2014) proposed a consistent 3D geometric modelling for 2D and 3D woven fabrics. In this modelling approach, the variation of the shape of the yarns cross section along its path is taken into consideration. The shape is defined based on the boundary condition of the contacting yarns; thereby three zones identifying the cross section of the yarn: a contact zone, a contact-free zone and a lateral zone, that are reduced to two zones for low cohesion yarn case, Figure 4.20-a. The shape is considered as composition of 4 curves referred to 3 contacts zones, Figure 4.20-b, whereas, it is simplified to lenticular shape composed of two dissymmetric curves linked at two points in case of low cohesion between constituent filaments, Figure 4.20-c. Therefore, the geometrical characterization involving identifying the contacts zones of the yarns cross section with the transverse yarns is necessary. The path of the yarns represented by their centreline, divided into two parts: straight segment where no contact (free-contact zone) and parabola segment taking the shape of the cross section of the transverse yarn (contact zone), Figure 4.21. The cross section shape is assigned on the yarn centreline at specified control point defined in function of the overlap zone between contacting yarns. Then, the 3D solid yarns volume is created using the swept blend functions provided on CAD software. Mathematical equations are developed describing the structure, based on the explained strategy, enabling to compute the model parameters from the yarns and the unit cell measured parameters as input data and the number of required and implemented parameters determinate the sophistication of the constructed model. In this method, it was assumed that the cross section curves ensure the tangential conditions with rectangular envelope representing the measured yarns cross-section dimensions.

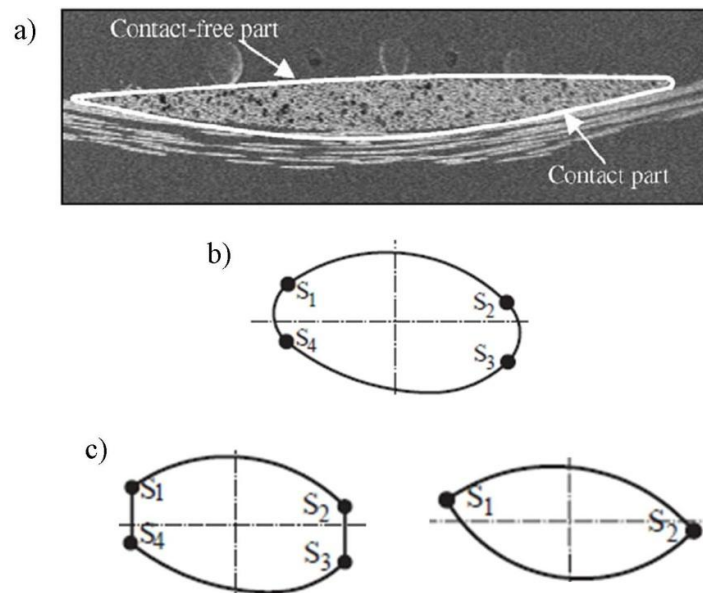


Figure 4.20: Hivet's model, a) micrograph of 2D woven fabric with illustration of the cross section contact zones, b) general shape of cross section composed of 4 curves, c) simplification of shape to straight lateral and to 2 curves for low cohesion yarn. (Hivet and Boisse 2005)

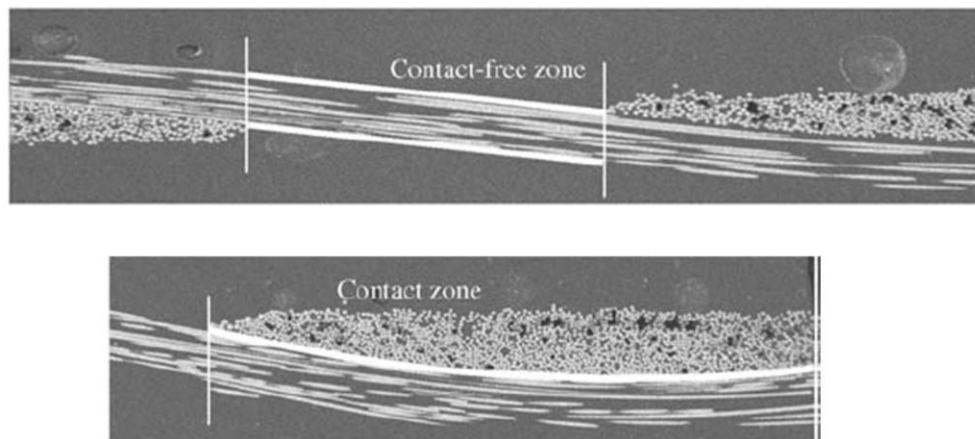


Figure 4.21: Micrograph of 2D woven fabric with illustration of the contact zones of the yarn path. (Hivet and Boisse 2005)

On the other side, it was not mentioned in the reported publications of the two TGP (Wisetex and Texgen) and Hivet's model the correlation between the constructed RVE and the real dry preform or composite in term of the fibre volume fraction (as essential criteria to compare) and of the other geometric parameters (yarns area, packing factor, fabric thickness...).

Otherwise, through the explored geometrical models for 3D woven fabric in the literatures, all of these models are created for the 3D interlock woven fabric and no models are created for the multiaxis 3D woven fabric, which is the axe of this work. In the work of Buchanan et al. (2010-b) who developed a predictive geometric modelling it is possible to predict the geometrical properties of the designed preform by following the same hypothesis proposed in his model for the 3D interlock woven fabric. As well, in this model the arrangement of the filaments inside the yarn is assumed either in rectangular or hexagonal array, which aids to assume the packing factor value. Also, this model is adequate just for closed-packed fabric.

4.4. Road map

In order to develop an RVE for a unit cell of the multiaxis 3D woven performs on the meso-scale (allowing the construction of an accurate mechanical modelling able to predict the elastic properties of textile reinforcement architectures), the following steps were undertaken, (Figure 4.22).

1. Before building up the weaving machine prototype and produce the novel samples, the process parameters and the characterizing geometrical parameters of the yarns and of the unit cell for the produced preform, are defined and classified, as detailed in the section (3.7.1.2).

2. A predictive geometrical modelling is developed by optimizing and adapting the geometrical models developed in the literature for 3D interlock woven reinforced composites and Buchanan's predictive model developed for multiaxis woven reinforced composite. That helps to:

- Design the desired 3D multiaxis woven preform.
- Estimate the influence of the manufacturing parameters and the weaving parameters on the geometrical properties of the produced preforms.
- Determinate the weaving process requirements associated with multiaxis architecture that should be respected when developing weaving machine mechanisms.

In this model-simplifying hypothesis are proposed to develop a mathematical model allowing computing the predicted geometrical properties.

3. The geometry of the constituent yarns and of the unit cell of the dry preform and of the composite are characterized. The method and the results of this characterization have been already presented in section (3.7).

4. The measured and observed geometric parameters via the geometrical characterization are compared to that obtained by the predictive model based on assumed hypothesis.

5. To create a more realistic geometrical model of the designed architecture serving in accurate mechanical modelling, the geometric modelling has been optimized. The invalid hypotheses of the predictive model are re-considered based on the geometrical characterization and observations. Therefore, the mathematical model describing the structure is re-developed to compute the geometrical properties and the model parameters through the manufacturing parameters, the weaving parameters and the measured parameters. Hereby, an RVE of the structure is re-built by the computed model parameters with the aid of an appropriate approach and CAD software.

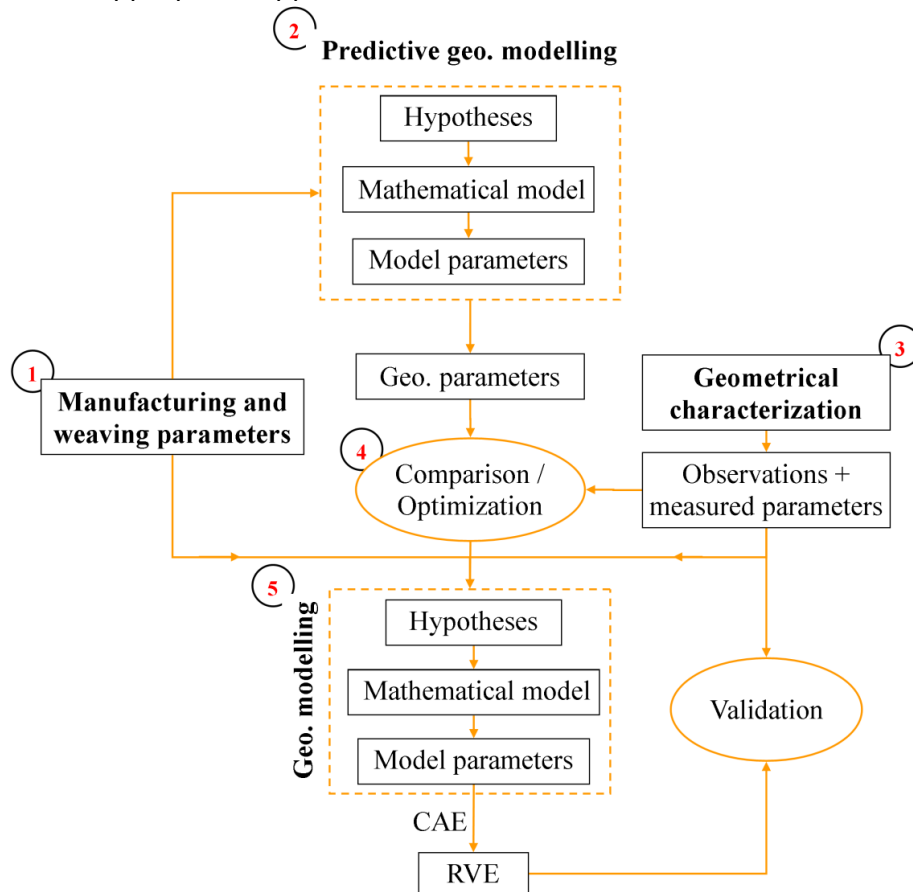


Figure 4.22: Geometrical modelling road map.

4.5. Predictive Geometrical Model

A predictive geometric model objectives are: to predict the geometrical properties of the novel architecture before fabrication on the weaving loom, to estimate the influence of input parameters on the final geometrical properties and to specify the machine requirement as the number of warp, weft, biases and binder yarns per unit length, the adequate yarns arrangement and the dimensions of the produced preform.

To develop this model, the work of Buchanan et al. (2010-b) has been taken as the basic statement. It is also the unique predictive model for the 3D multiaxis woven preform in the literature and it is based on his previous model (Buchanan et al., 2010-a) developed for the 3D orthogonal woven preform. Since the 3D orthogonal architecture has no interlacement between in-plane yarns like the present multiaxis architecture, similar path and cross section shape could be assumed for yarns in both architectures. Therefore, the assumed hypotheses in the literature regarding the yarns geometry for the orthogonal architecture are also treated.

4.5.1. Hypothesis of the Model

Ansar et al. (2011) reported the basic geometrical modelling approaches introduced in the literature for the 3D orthogonal woven preform. These basic approaches are introduced by Quinn (2003), Wu (2009) Buchanan et al. (2010-a) and for multiaxis 3D woven preform, Buchanan et al. (2010-b).

The basic hypotheses assumed in these models are related to the path, the cross section shapes and area of yarns;

1. The path of the yarns remains straight inside the unit cell (Figure 4.23). The yarn crimp is neglected.
2. The shape of the yarns cross section is constant along the yarn path.
3. The AR and the packing factor of the filaments inside the yarn are pre-assumed, constant along yarns path and unique for all in-plane yarns.
4. The packing factor and the AR values for a yarn set are unique despite of the yarn location in the preform. That means the same area and AR for inner and outer filler yarns.

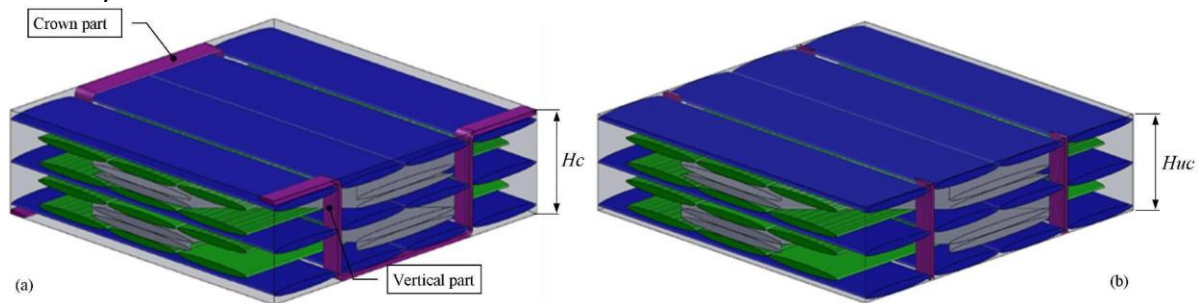


Figure 4.23: Definition of the thickness of the RVE. (a) Crowned configuration. (b) Uncrowned configuration.

The difference between these models is about the considered shape for the yarns cross-section and the assumed value AR and Pf, as it was reported in the literature survey (section 4.3.4). In Quinn's model (2003) the cross section shape is considered lenticular, the AR is equal to 12 and the packing factor is 0.8 for all yarns. The deviation of the predicted FVF and H for three carbon fabrics to measured values are 28.23%, 14.6%, 13% and -18%, -10%, -5.2% respectively. This deviation is reduced by the optimized model proposed in the same paper where it becomes +10.5%, -2.4%, -0.9% and -9%, 0%, +5% respectively. However, the binder yarn was not taken into consideration when computing the total preform thickness.

In Wu's model (2009), another parameter is suggested representing the ratio of the gap width between adjacent yarns comparing to the yarns width. Two models are treated in this paper, one for glass fabric with consideration elliptical cross section shapes for yarns, gap ratio to yarn width for filler yarn equals to 1 and packing factor equals to 0.7 for all yarns, but no details were provided concerning the computation the yarns cross section

dimensions for this sample. The second fabric is made of carbon fibres with rectangular cross section shape consideration, packing factor equals to 0.82. The predicted FVF and H for the first fabric were not validated to measured values, whereas the deviation of the predicted FVF and H to measured values is -1% and -0.22%. The width of yarns cross section was computed based on the unit cell dimensions and gap ratio, while the thickness is deduced by getting the preform thickness equal to measured value. However, no precessions were presented in this paper concerning the reason of the two assumed values for these fabrics.

Buchanan's model (2010-a) was applied to predict the geometrical parameters of 3D orthogonal woven composite made of carbon fibres and impregnated by VARTM method. In this model, the elliptical shape is considered for the yarns cross section, the aspect ratio is equal to 11 for in-plane yarns and 4 for binder yarn and the packing factor is equal to 0.7854 where rectangular packing array for the filaments within the yarns is considered. The computed FVF and H were compared to measured values and the deviation was -2.31% and 0% respectively. However, the binder yarn thickness was not taken into consideration when computing the preform thickness.

In Buchanan's model (2010-b) for the five axial woven preform, the same hypotheses were assumed excepting the packing factor that is equal to 0.9069, where hexagonal packing array for the filaments with the yarns is assumed. The model was applied for 3D multiaxis woven composite characterized by McIlhagger (2007) and it is made of carbon fibres (for in-plane yarns) and aramid fibres (for binder yarn). The reported deviation between predicted and measured value of FVF is 4.02%, 2.42%, 0.61% for three samples. The measured preform thickness was not reported.

For the manufactured samples listed in the table 3.2, Buchanan's model has been applied (2010-b) with two considerations of the filaments arrangement inside the yarns (hexagonal; $pf=0.9069$ and rectangular; $pf=0.7854$). The predicted H and FVF values by Buchanan's model of the five dry preforms and of the impregnated sample using VARTM method are listed in table 4.1. The obtained values are compared to the H values measured through the captured micrographs as it was detailed in section (3.7.3.1). They are Also compared to the FVF values computed by density method as detailed in (3.7.2.3) based on the component fibre density, the used resin density and the measured final composite density reported in section (3.7.3.2).

Significant deviation is noted between predicted values by Buchanan's model and measured values, especially for the dry preforms. For the sample-5, the deviation in the fibre volume fraction values (FVF) in the case of the after impregnation is less important than the deviation in the case of dry preform. That is attributed to the estimated value of the Pf whereas the yarns of the impregnated sample have higher Pf value so the deviation is less important. That is noted also when considering the rectangular array for the filaments arrangement ($Pf=0.7854$) comparing to the second consideration with hexagonal array ($Pf=0.9069$). Buchanan's model was developed for impregnated samples, therefore the assumptions in this model lead to high deviation in the case of the dry preforms.

Otherwise, the interpenetration among yarns is deduced when the yarns cross section dimensions are computed based on this model. That could be seen by application of the geometrical conditions (4.3, 4.6), table 4.2, that are deduced in the present paper based on the yarns path and unit cell dimensions as it will be detailed in the next section. The equation (4.6) is satisfied for all samples meaning that there is no interpenetration among warp and bender yarns. However, the other condition is not satisfied for all samples

4. Geometrical modelling of 3D multiaxis woven composite

excepting sample-3 (as it has higher yarns gap values as it is found). That means the interpenetration may be found among filler and binder yarns and also among bias and binder yarns.

Therefore, an optimized predictive geometric modelling is developed in this study for the 3D multiaxis woven preforms enabling the prediction of the geometrical parameters of this structure without interpenetration among yarns. In this model the same previous hypotheses are adopted excepting the one concerning the AR value. Therefore an optimization loop is proposed to compute the cross section dimensions of each set of yarns in the preform based on the geometrical conditions of this architecture instead of a fixed aspect ratio for all yarns. Respecting these geometrical conditions allow avoiding the yarns interpenetration. This geometric modelling is developed with consideration the elliptical cross section shape as in Buchanan's model. Nevertheless, other shapes could be considered.

Table 4.1: Comparison the predicted fiber volume fraction (FVF) and preform thickness (H) by Buchanan's model (2010-b) to the measured values with two considerations for the packing factor (Pf) value.

pf=0,7854	H [mm]			FVF_ weight [%]		
	model	measured	Dif. [%]	model	measured	Dif. [%]
Sample-1	3,44	5,8	-41	51,45	31,12	65
Sample-2	3,82	5,43	-30	35,11	25,02	40
Sample-3	3,44	4,04	-15	29,75	26,35	13
Sample-4	5,15	7,32	-30	46,75	33,13	41
Sample-5	6,23	9,35	-33	52,15	34,95	49
Sample-5C	6,23	6,8	-8	52,59	45,47	16

pf=0,9069	H [mm]			FVF_ weight [%]		
	model	measured	Dif. [%]	model	measured	Dif. [%]
Sample-1	3,2	5,8	-45	55,26	31,12	78
Sample-2	3,55	5,43	-35	37,72	25,02	51
Sample-3	3,2	4,04	-21	31,96	26,35	21
Sample-4	4,79	7,32	-35	50,22	33,13	52
Sample-5	5,8	9,35	-38	56,02	34,95	60
Sample-5C	5,8	6,8	-15	56,5	45,47	24

Table 4.2: Investigation of interpenetration between yarns in case of computation of the yarns cross section dimensions by Buchanan's model by verifying the geometric conditions of multiaxis structure expressed by equations (4.2 and 4.6).

	$n_w^{uc} l_w + l_b \leq L_f$	$\frac{l_\theta}{\cos(\theta)} + 2P + \frac{n_f^{uc}}{2} l_f + h_b \leq L_w$
Sample-1	5,20 6,14	8,12 5,66
Sample-2	5,20 9,4	9,59 9,08
Sample-3	5,20 9,9	8,23 10,42
Sample-4	6,64 9,92	12,66 9,97
Sample-5	7,93 9,8	15,27 10,5
Sample-5C	7,93 9,86	15,16 10,25

During the weaving process, the filler yarns at the two top and lower surfaces of the preform are undulated under the binder yarn, due to the tension applied on them. Consequently, the crown part of the binder yarns will be in the same plane as the filler yarns. However, according to the first hypothesis, a straight yarns path to simplify the RVE model, the filler's undulation wasn't taken into account. Hence, the crown part of binder will not be in the same plane of filler yarns on the top and lower surfaces of the preform. This simplification leads to propose two configurations illustrated in Figure 4.23, associated to the computation of the total thickness of the RVE. In the first case, denoted crowned configuration, (Figure 4.23-a), the crown part of the binder will be taken into consideration, and the thickness of the RVE is noted H_c . That is accompanied with an additional quantity of resin on two surfaces of the preform. In the second case, (Figure 4.23-b) denoted uncrowned configuration, the crown part of the binder yarn has not been considered. This assumption is used by Buchanan (2010-a, b) to compute the thickness of the RVE, which is noted H_{uc} .

4.5.2. Development of the Model

4.5.2.1. Yarns parameters

The first step of the geometrical model is dedicated to the computation of the cross section dimensions (l , h) of the constituent yarns. Contrary to the assumption introduced by Buchanan's model, the cross section dimensions are not computed based on unique assumed value of AR for all yarns where a method is developed to find the AR value for each yarns. This leads to a computation of the yarns cross section dimensions without interpenetration among yarn volumes. This method is introduced through the data-flow presented in Figure 4.24.

At the beginning, the aspect ratio values of yarns are initialized and they are assumed to be $AR=11$, for the in-plane yarns (warp, filler and bias), while the binder yarns are assumed to have $AR=4$ according to Buchanan's model (2010-b). From the initial values, the cross section dimensions (l_i , h_i) of the yarns, are computed by (4.1) where the elliptical shape was assumed for the yarn cross section and the packing factor equal to 0.9069 or 0.7854. Other cross section shapes could be considered in this model and the two cross section dimensions are computed via the area and the AR as listed in the table (4.3).

$$h_i = \frac{4 \mu_i 10^{-3}}{\pi P_f \rho_i l_i} = \sqrt{\frac{4 \mu_i 10^{-3}}{\pi P_f \rho_i AR_i}} \quad l_i = AR_i h_i \quad (i=w, f, \vartheta) \quad (4.1)$$

From the arrangement of the constituent yarns inside the structure, as shown in the Figure 3.34, the first geometrical condition is deduced (4.2) with the assumption of straight path for the in plane (no waviness for in-plane yarns in the through thickness).

$$\frac{l_\theta}{\sin(\theta)} + 2P + \frac{n_f^{uc}}{2} l_f + h_b + \frac{h_f+h_o}{\tan \alpha} \leq \frac{10}{\lambda_b^w} \quad (4.2)$$

The angle (α) represents the inclination of the through thickness part of binder yarn to the mid-plane of the preform, Figure 3.39. The expression $\frac{h_f+h_o}{\tan \alpha}$ is deduced from the waviness and the inclination of the through thickness part of the binder yarn.

4. Geometrical modelling of 3D multiaxis woven composite

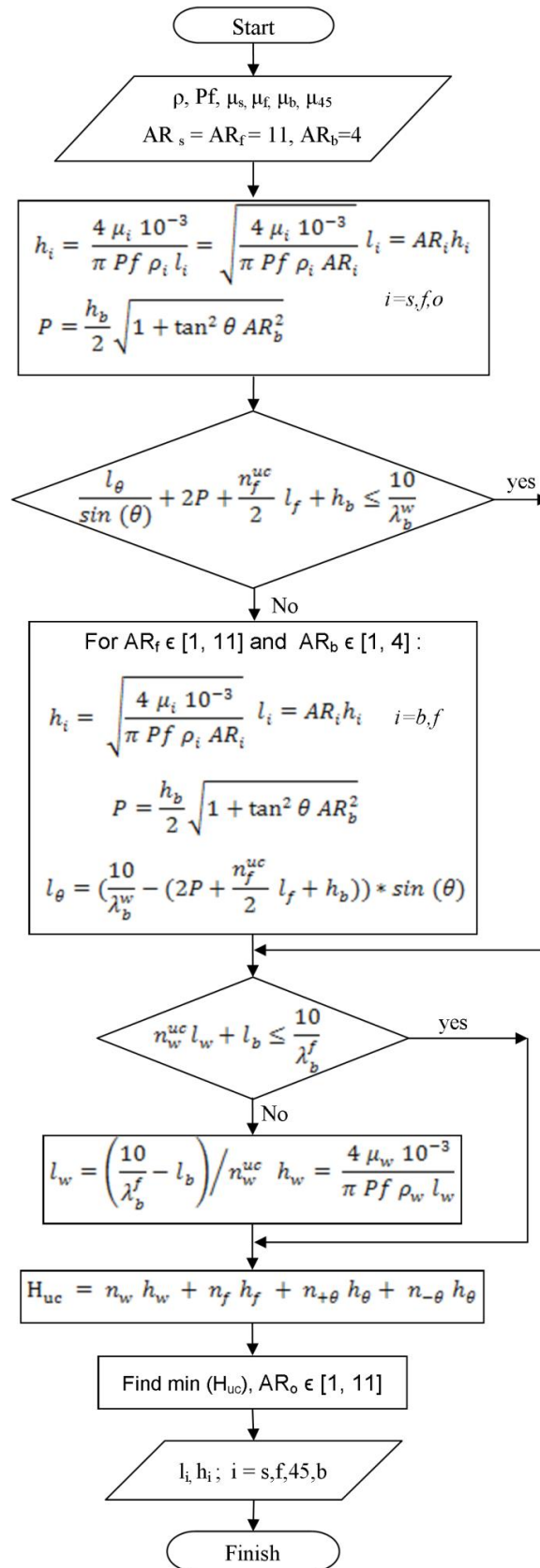




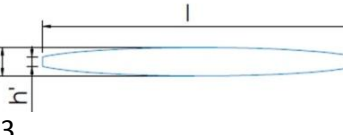


Figure 4.24: Flow chart for the optimization method dedicated to predict the cross section dimensions of constituent yarns.

4. Geometrical modelling of 3D multiaxis woven composite

Table 4.3: The considered cross section shapes.

Shape	Area in function of the two dimensions (l, h), h calculated by the aspect ratio $AR = \frac{l}{h}$	sections; S= 11mm ² and AR=11
rectangle	$S = lh, h = \sqrt{\frac{S}{AR}}$	
racetrack	$S = lh - (1 - \frac{\pi}{4})h^2, h = \sqrt{\frac{S}{(AR-1+\frac{\pi}{4})}}$	
ellipse	$S = \frac{\pi}{4}lh, h = \sqrt{\frac{4S}{\pi AR}}$	
lenticular	$S = \frac{1}{8h^2}(l^2 + h^2)^2 \tan^{-1}\left(\frac{2lh}{l^2-h^2}\right) - \frac{l}{h}(l^2 - h^2),$ $h = \frac{(AR^2 - 1) + \sqrt{(AR^2 - 1)^2 - S(AR^2 - 1) \tan^{-1}\left(\frac{2AR}{AR^2 - 1}\right)}/2}{(AR^2 + 1) \tan^{-1}\left(\frac{2AR}{AR^2 - 1}\right)}/4$	
cut ellipse	$S = \frac{lh}{2} \left[\frac{1}{\beta} + \frac{1}{\sqrt{1-1/\beta^2}} * \sin^{-1}(\sqrt{1-1/\beta^2}) \right]; \beta = \frac{h}{h'}$, $h = \sqrt{\frac{2S}{AR \left[\frac{1}{\beta} + \frac{1}{\sqrt{1-1/\beta^2}} * \sin^{-1}(\sqrt{1-1/\beta^2}) \right]}}$	

For the preform with high fibre volume fraction and low binder yarn tension, the applied compression during the impregnation process on the two outer faces of the preform causes waviness of the through the thickness part of the binder yarn and the angle $\alpha > \pi/2$, as in the case of impregnated and cured sample under 2bar, Figure 4.25, reported in the work of McIlhagger et al. (2007). While for a dry preform having low fibre volume fraction, a through the thickness part of binder yarn is straight, but the angle $\alpha < \pi/2$, as in the case of sample-2 Figure 3.47 and of sample-3 Figure a.3 of appendix. For other sample (1, 4, 5, 5C) the through the thickness part has quasi-straight path and angle $\alpha \approx \pi/2$, Figure a.1, a.4, a.5, a.6. The angle α is measured for the five dry preforms and impregnated sample and listed in table 3.7.

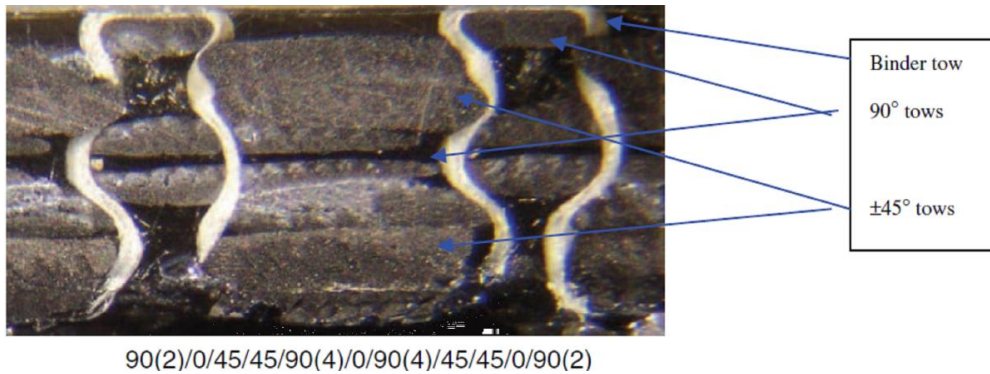


Figure 4.25: Waviness of the through thickness part of the binder yarn for impregnated and cured multiaxis woven sample under 2bar, (McIlhagger et al. 2007).

Hence for the predictive model, this angle is considered $\alpha = \pi/2$ and the path of through the thickness part of the binder yarn is considered straight (no waviness) according to previously treated predictive models in the literature. Thus, the expression $\frac{h_f + h_o}{2 \tan \alpha} = 0$ and the condition (4.2) becomes as (4.3). That reduces the number of variables in the condition (4.3) to three (l_θ, l_f, h_b) instead of four. This approximation induces an error for the two first cases. That will be treated in the next section.

By this condition the interpenetration between the bias and the binder yarns is verified.

$$\frac{l_\theta}{\sin(\theta)} + 2P + \frac{n_f^{uc}}{2} l_f + h_b \leq \frac{10}{\lambda_b^w} \quad (4.3)$$

The parameter P is computed from the equation (4.4) based on the Figure 3.38. Where, the outer surface of binder yarn is considered tangent to the filler and bias yarn in the association with elliptic cross section shape consideration for binder yarn. The equation (4.4) satisfies also the assumption of circular cross section shape for binder yarn. But for rectangular shape, the equation (4.5) is used Figure 4.47.

$$P = \frac{h_b}{2} \sqrt{1 + \tan^2 \theta AR_b^2} \quad (4.4-a)$$

$$P = \frac{h_b}{2} \left(1 + \frac{AR_b}{\tan \theta}\right) \quad (4.4-b)$$

If this condition (4.3) is not satisfied, the maximum value for the left expression of (4.3) is considered equal to $\frac{10}{\lambda_b^w}$. Two variables (l_f, h_b) are re-calculated by varying the value of $AR_f \in [1, 11]$ and $AR_b \in [1, 4]$ (acceptable physical configuration for the yarns cross section), l_θ is computed via (4.5) and P is computed via (4.4-a).

$$l_\theta = \left(\frac{10}{\lambda_b^w} - \left(2P + \frac{n_f^{uc}}{2} l_f + h_b\right)\right) * \sin(\theta) \quad (4.5)$$

The cross section dimensions of the warp yarns are verified by the condition (4.5) associated with the arrangement of the warp and binder yarns in the filler direction. This condition verifies the interpenetration between warp and binder yarns.

$$n_w^{uc} l_w + l_b \leq \frac{10}{\lambda_f^l} \quad (4.6)$$

If this condition is not satisfied, the cross section dimensions of the warp yarns are computed from (4.6) with condition $AR_w \in [1, 11]$

$$l_w = \left(\frac{10}{\lambda_f^l} - l_b\right) / n_w^{uc} \quad h_w = \frac{4 \mu_w 10^{-3}}{\pi P f \rho_w l_w} \quad (4.7)$$

This variation of (AR_f, AR_b) values until obtains the minimum preform thickness (H_{uc}) value, which is computed from (4.8). It is assumed that the yarns trend to have lower internal energy by getting lower preform thickness.

This model is not restricted to the elliptic shape, different shapes could be considered such as those listed in the table 4.3.

4.5.2.2. Unit cell parameters

After the definition of dimensions of all yarns in the unit cell, it's possible to compute, in the second step, all geometrical parameters characterizing the unit cell.

Concerning the unit cell thickness, two configurations of the binder yarn resulting in two approaches are used to compute the preform thickness; either crowned configuration (in this case the thickness is denoted H_c , Figure 4.23-a) or uncrowned configuration (in this case the thickness is denoted H_{uc} , Figure 4.23-b). In Buchanan's model the uncrowned

4. Geometrical modelling of 3D multiaxis woven composite

configuration is assumed. Here, two approaches are considered and the difference between these two approaches in function of the number of layers will be investigated.

$$\begin{aligned} H_{uc} &= n_w h_w + n_f h_f + n_{+\theta} h_\theta + n_{-\theta} h_\theta \\ H_c &= n_w h_w + n_f h_f + n_{+\theta} h_\theta + n_{-\theta} h_\theta + 2h_b \end{aligned} \quad (4.8)$$

Associated to the thickness, the unit cell volume can be deduced:

$$V^{uc} = L_x \cdot L_y \cdot H \quad (4.9)$$

With H is equal to H_c or H_{uc} for crowned or uncrowned configuration respectively.

The total length of each set of yarns in the unit cell can be computed with the assumption of straight yarns path. The length of the binder yarn is computed depending on the binder yarn configuration (crowned or uncrowned) with consideration $\alpha = \pi/2$.

$$\begin{aligned} L_w [mm] &= \frac{10 \cdot n_f^{uc}}{\lambda_f} \cdot n_w^{uc} \cdot n_w \quad L_f = \frac{10 \cdot n_w^{uc}}{\lambda_w} \cdot n_f^{uc} \cdot n_f \quad L_\theta = \left[\frac{10 \cdot n_f^{uc}}{\lambda_f \cos(\theta)} \right] n_\theta^{uc} \cdot n_\theta \\ L_b &= \left[\frac{10 \cdot n_f^{uc}}{\lambda_f} + 2(H_c - 2 \cdot h_b) \right] \cdot n_b^{uc} \quad \text{or} \quad L_b = 2H_{uc} \cdot n_b^{uc} \end{aligned} \quad (4.10)$$

The Volume of each yarn in the unit cell is defined based on the area of the yarns cross-section and its length in the unit cell:

$$V_i = S_i \cdot L_i \quad (i = w, f, \vartheta, b) \quad (4.11)$$

The overall volume of the yarns in the unit cell can be calculated as:

$$V_{fibre} = V_w + V_f + V_b + V_\theta + V_{-\theta} \quad (4.12)$$

The mass of the fibre in the unit cell as well the areal density can be calculated by:

$$M^{uc} = \sum_{i=w,f,b,\theta} L_i \mu_i \quad S^{uc} = \frac{M^{uc}}{L_x \cdot L_y} \quad (4.13)$$

Two methods are introduced in the literature to predict the fibre volume fraction in the unit cell. The first method, denoted FVF_{volume} and reported by Ansar et al. (2011), is based on the ratio of the total yarns volumes in the unit cell to the unit cell volume. In this method the yarns are considered, as solid volume and the resin within the yarns are not taken into consideration. That means that the packing factor of the filaments inside yarns is assumed to be equal to 1. This method allows evaluating the volume of the resin or the void restricted between yarns. The second method, called FVF_{weight} and reported by Buchanan et al. (2010-a, b), is based on the ratio of the total volume of the fibre to that of the unit cell. In the present study the FVF_{weight} method is followed to predict the fibre volume fraction since it is more accurate.

$$FVF_weight = \frac{S^{uc}}{\rho H} \quad (4.14-a)$$

$$FVF_volume = \frac{V_{yarns}}{V^{uc}} \quad (4.14-b)$$

In this formula H is equal to H_c or H_{uc} respectively for crowned or uncrowned configuration.

The specific proportion of each yarn relative to the total fibre volume can be defined:

$$V_{fi} = \frac{V_i}{V_{yarns}} \cdot 100 \quad (i = w, f, \theta, b) \quad (4.15)$$

Also the specific proportion of each yarn relative to the unit cell volume is estimated by:

$$V_i^{uc} = \frac{V_i}{V^{uc}} \cdot 100 \quad (i = w, f, \vartheta, b) \quad (4.16)$$

4.5.3. Results

Before carrying out the multiaxis weaving loom, the predictive geometric model was applied for 3D multiaxis woven preforms made of carbon fibre and the influence of the linear density of the warp and bias yarns and the angle (α) on the predicted FVF value was investigated in our previous work, (Labanieh et al., 2013). That helps to understand this architecture and to develop the required mechanisms on the weaving loom.

In the next step, this optimized predictive geometrical model is implemented for the manufactured dry preform and the impregnated sample, which have the manufacturing and weaving parameters presented in the table 3.2. The density of E-glass fibre is ($\rho = 2.85 \text{ gr/cm}^3$) while the aramid is ($\rho = 1.44 \text{ gr/cm}^3$). The hexagonal array ($Pf=0.9069$) and rectangular array ($Pf=0.7854$) for the arrangement of the filaments inside the yarns are considered.

From the geometrical characterization, it was noticed that the warp yarns as well as the bias yarns of one unit cell provided to the weaving zone by passing through the same “eye guide” are packed together and they appear as one yarn on the captured micrographs, Figure 3.41-47. Similarly, the double picks of filler yarns are packed as one yarn. This observation has to be taken into consideration in implementing the geometrical model.

4.5.3.1. Prediction of the geometrical parameters

The predicted fibre volume fraction and total thickness of the dry preforms and composite sample are listed in table 4.4. For the dry preform the assumption of rectangular array for the filaments arrangement ($Pf=0.7854$) and the crowned configuration for the binder yarn give less prediction error relative to the measured values. For the impregnated sample less deviation is obtained when considering the hexagonal array for the filaments arrangement ($pf=0.9069$) with the uncrowned configuration for binder yarns where the difference to the measured values is within the domain of the measurement incertitude.

The reason of the high deviation between predicted values for the dry preform comparing to measured value is the overestimation of the packing factor value, the simplifying assumption of unique packing factor and AR for all yarns and the assumed value of the angle ($\alpha = \pi/2$). That could be noted by comparing the assumed values of packing factor to the measured values listed in the table 3.10, as well as by observing the path of the binder yarn in the through thickness of the preform for the dry preforms. Where, the measured packing factor values in the dry preforms are less than 0.7854. And as in the crowned configuration an additional resin volume is considered, this volume recomposes little the overestimation of the packing factor value. Thus the deviation in the case of crowned configuration approach is less comparing to the predicted values by the uncrowned configuration approach.

The variation of the predicted FVF value by optimized predictive model with the two configurations for binder yarn versus the assumed value of packing factor is investigated and illustrated in the Figure 4.26. This relation is obtained by varying the assumed packing factor ($Pf \in [0.4, 0.9]$) to estimate the yarn cross section area and dimensions using the equation (4.1). Then the FVF is computed by following the geometrical model steps developed in the section (4.5.2.2). It could be seen that the FVF is proportional to the packing factor with quasi-linear relationship. The adequate assumed packing factor value which gives FVF close to the measured value could be deduced from this Figure 4.26 and measured value and they are between 0.55 and 0.65 and between 0.66 and 0.78 for uncrowned and crowned configuration respectively.

4. Geometrical modelling of 3D multiaxis woven composite

Table 4.4: fiber volume fraction and thickness of the dry preform and composite predicted by optimized predictive model with two configurations for filaments arrangement (Pf=0.7854) and (Pf=0.9069) also two configurations for binder yarn (crowned and uncrowned). The predicted values are compared to measured one.

	H [mm]					FVF_ weight [%]				
	measured	Predictive model (Pf=0,7854)				measured	Predictive model (Pf=0,7854)			
		crowned	dif.[%]	uncrowned	dif.[%]		crowned	dif.[%]	uncrowned	dif.[%]
Sample-1	5,80	5,07	-12,59	4,37	-24	31,12	35,55	14,22	40,56	30
Sample-2	5,43	4,60	-15,31	3,92	-27	25,02	29,45	17,69	34,19	36
Sample-3	4,04	3,88	-3,96	3,44	-14	26,35	26,67	1,23	29,75	12
Sample-4	7,32	6,69	-8,67	6,02	-17	33,13	36,25	9,43	40,00	20
Sample-5	9,35	8,67	-7,27	8,02	-14	34,95	37,69	7,84	40,52	15
sample-5C	6,8	8,78	29,11	8,13	19	45,47	37,52	-17,48	40,34	-11

	H [mm]					FVF_ weight [%]				
	measured	Predictive model (Pf=0,9069)				measured	Predictive model (Pf=0,9069)			
		crowned	dif.[%]	uncrowned	dif.[%]		crowned	dif.[%]	uncrowned	dif.[%]
Sample-1	5,80	4,50	-22,43	3,85	-33	31,12	39,98	28,48	46,00	47
Sample-2	5,43	3,96	-27,07	3,55	-34	25,02	34,15	36,50	37,72	50
Sample-3	4,04	3,61	-10,63	3,20	-20	26,35	28,63	8,66	31,96	21
Sample-4	7,32	5,94	-18,82	5,32	-27	33,13	40,76	23,04	45,22	36
Sample-5	9,35	7,68	-17,83	7,08	-24	34,95	42,51	21,63	45,90	31
sample-5C	6,8	7,78	14,40	7,17	5	45,47	42,34	-6,89	45,72	0,55

In comparison of the obtained result with the results of the geometrical parameters predicted by Buchanan's model, table 4.1, an important reduction in the difference between predicted FVF and H to the measured values is obtained by optimized model for both H and FVF (about 42%-95% for the dry performs due to the assumption of the crowned configuration for binder yarns). While for the impregnated sample with uncrowned configuration for two models, the optimized model provides better estimation when considering the packing factor equal to (0.9069) whereas Buchanan's model (2010-b) provides better estimation when considering the packing factor equal to (0.7854). Otherwise, the optimized model provides closer estimation to the measured value with no interpenetration between in-plane yarns and binder yarn.

The yarn cross section dimensions of the five dry preforms are listed in the table 4.5 where these parameters are computed from the optimized model with rectangular array assumption (pf=0.7854) inasmuch as better predicted FVF and H is obtained via this assumption. In this comparison the mean of the measured values is introduced, the "filler-inner" section is considered for the measured filler yarns cross section dimensions and the crown section is considered for the binder yarn cross section dimensions.

Important deviation in the predicted values of the yarns cross section area to the measured values about -45% due to the overestimation of the packing factor values, as it is noted for FVF in table 4.4. Regarding the AR values are generally overestimated between 4% and 70%. For binder yarns the comparison is not accurate because two cross sections shapes are observed in the geometrical characterization (section 3.7.3.5) and Figure (3.47), whereas

unique constant cross section shape is considered for the binder yarn in the predictive model.

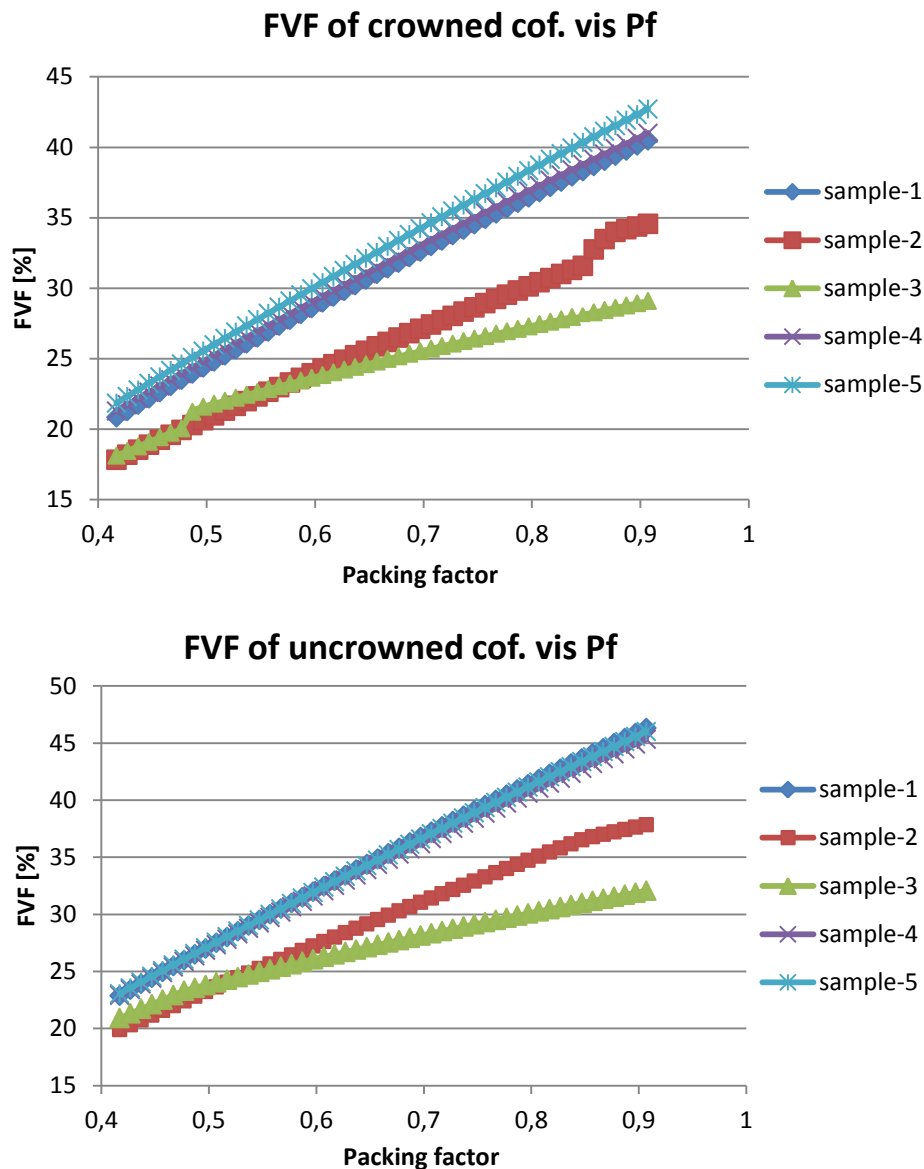


Figure 4.26: Variation of the FVF of dry preform predicted by optimized predictive model with two configurations of binder yarns versus assumed value of packing factor.

4.5.3.2. Binder yarn configuration

In the present predictive geometrical model two configurations for the binder yarn (crowned and uncrowned) are considered. In the crowned configuration and as a result of the straight path assumption for the filler yarns (no waviness in the through thickness direction), a supplementary resin layer with a thickness equal to the binder yarn thickness is created on the two outer faces of the preform. Thus, remarkable difference is noted in the FVF and the preform thickness resulting from these two configurations.

Rao et al. (2009) have shown the effect of two configurations when construction RVE of orthogonal woven composite serving in mechanical modelling to estimate the mechanical properties of this structure. He noted an underestimation for the elastic properties when considering the crowned configuration. That is attributed to the supplementary resin layer

4. Geometrical modelling of 3D multiaxis woven composite

associated with considering the crown part of the binder yarn. From geometric point of view, this layer leads to an increase of the predicted value of the preform thickness (H) and consequently decreases the predicted value of the FVF, as it is noted in table 4.4.

The influence of these two configurations of binder yarn on the value of the FVF has been evaluated in the previous works by the authors for dry preforms of carbon fibre designed with the aid of earlier predictive model, Labanieh et al. (2013). The difference in the predicted value of the FVF resulting from the two configurations (crowned and uncrowned) could be expressed by following equations:

$$Dif. FVF_{Huc} to FVF_{Hc} = \frac{FVF_{Huc} - FVF_{Hc}}{FVF_{Hc}} * 100 \quad (4.17)$$

$$Dif. FVF_{Huc} to FVF_{Hc} = \frac{2V_{fiber}^{uc} h_b - S_b L_y H_{uc}}{H_{uc} (S_b L_f + V_{fiber}^{uc})} * 100 \quad (4.18)$$

From these equations it could be noted that the difference in the FVF computed based on the configuration depends on binder yarn cross section area and dimensions and on the preform thickness and preform fibre volume in the uncrowned configuration. That means the volume of supplementary resin layer associated to binder crown part relative to the uncrown volume of the unit cell. Where, the volume of this resin layer is in function of the binder crown part thickness and the unit cell dimensions.

For the dry preforms with constant h_b , S_b (same binder yarn linear density, packing factor and AR_b) also same unit cell dimension in the filler direction L_f the difference in the FVF computed based on the two configurations decreases to less than 5% when the number of in-plane yarns layers exceed 20 layers, Figure 4.26.

Hence, when design 3D multiaxis woven preform with layer number less than 20 as well when construct RVE of this structure with the assumption of straight in-plane filler yarns path (no waviness) the two configurations (crowned and uncrowned) for binder yarns should be taken into consideration.

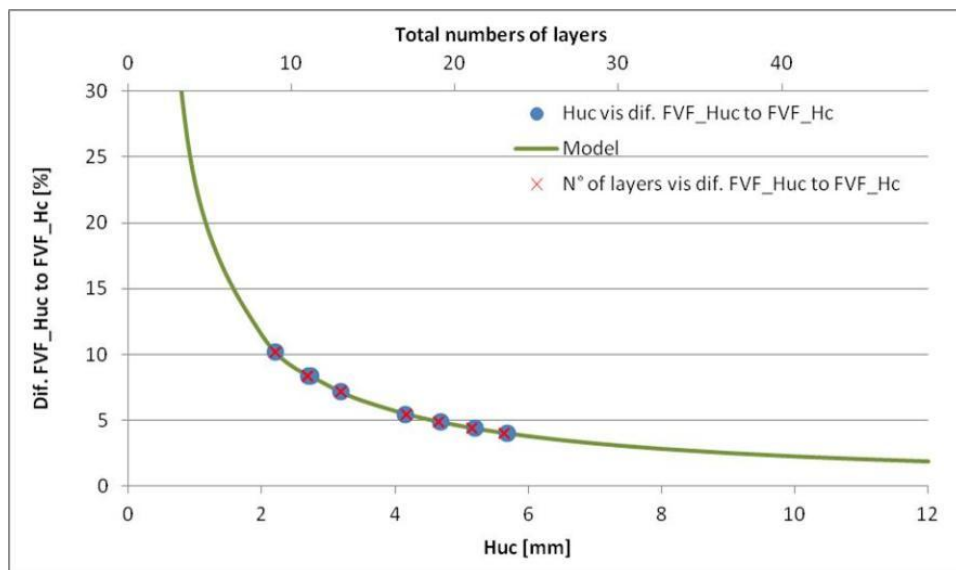


Figure 4.27: Difference in the fiber volume fraction value computed in the uncrowned configuration to that computed in the crowned configuration in function of the total number of layer in preform and of the total thickness of preform in the uncrown configuration, (Labanieh et al. 2013).

4. Geometrical modelling of 3D multiaxis woven composite

Table 4.5: The dimensions of the yarns cross section for the five manufactured dry preform, computed by the optimized predictive model.

	Sample-1			Sample-2			Sample-3			Sample-4			Sample-5		
	Model	Measured	Dif. [%]	Model	Measured	Dif. [%]	Model	Measured	Dif. [%]	Model	Measured	Dif. [%]	Model	Measured	Dif. [%]
Sw [mm ²]	1,33	2,07	-35,75	1,33	2,31	-42,42	1,33	2,34	-43,16	2,37	2,21	7,24	3,55	5,89	-39,73
ARw	11,00	6,83	61,04	11,00	7,81	-44,70	11,00	7,51	46,52	11,00	7,79	41,14	11,00	9,84	11,84
lw [mm]	4,32	4,03	7,19	4,32	5,00	-92,15	4,32	4,88	-11,48	5,76	4,91	17,31	7,05	8,36	-15,62
hw [mm]	0,39	0,59	-33,44	0,39	0,64	-38,64	0,39	0,65	-39,58	0,52	0,63	-16,88	0,64	0,85	-24,55
Sf-inner [mm ²]	0,89	1,29	-31,14	0,89	1,46	-39,16	0,89	1,52	-41,56	2,37	3,61	-34,38	2,37	3,53	-32,89
ARf	4,94	4,77	3,49	10,30	8,81	16,92	11,00	8,15	35,04	6,86	4,82	42,20	5,24	5,41	-3,17
lf [mm]	2,36	2,53	-6,57	3,41	3,70	-7,75	3,53	3,91	-9,79	4,55	4,39	3,61	3,98	4,60	-13,58
hf [mm]	0,48	0,53	-9,72	0,33	0,42	-21,10	0,32	0,48	-33,20	0,66	0,91	-27,14	0,76	0,85	-10,74
So [mm ²]	0,44	0,71	-37,44	0,89	1,55	-42,69	0,44	0,77	-42,32	1,18	1,83	-35,28	2,37	3,40	-30,33
ARo	4,85	3,10	56,12	9,87	5,05	95,59	11,00	6,37	72,73	6,45	5,59	15,33	4,76	5,40	-11,74
lo [mm]	1,66	1,49	11,11	3,34	3,13	6,77	2,49	2,42	3,06	3,12	3,41	-8,56	3,79	4,48	-15,39
ho [mm]	0,34	0,48	-28,83	0,34	0,62	-45,41	0,23	0,38	-40,33	0,48	0,61	-20,72	0,80	0,83	-4,14
Sb [mm ²]	0,15	0,27	-43,67	0,15	0,31	-50,94	0,15	0,35	-56,55	0,15	0,35	-56,55	0,15	0,32	-52,47
ARb	1,60	5,52	-71,11	1,68	3,55	-52,80	4,00	6,15	-35,00	1,74	6,15	-71,73	1,86	5,00	-62,90
lb [mm]	0,56	1,27	-56,24	0,57	1,10	-48,23	0,88	1,60	-44,99	0,58	1,60	-63,72	0,60	1,35	-55,61
hb [mm]	0,35	0,23	51,49	0,34	0,31	9,68	0,22	0,26	-15,38	0,33	0,26	28,31	0,32	0,27	19,66

4.6. Validation of the predictive geometrical model

The validation of the predictive geometrical model has been realized through the verification of the reliability of the assumed hypothesis and by comparing them to the observed states of the yarns inside the produced preform. That helps to develop geometrical modelling approach based on more realistic hypothesis serving in construction accurate model which will be used in the next mechanical modelling step in order to evaluate the mechanical properties of the manufactured 3D multiaxis woven preform.

As it was noticed earlier, table 4.5 and 4.6, an important deviation is observed between predicted cross section area and measured value for the dry preform and the impregnated sample. That may be explained by the overestimation of the packing factor value. The difference in the cross section area as well as the difference in the cross section dimensions of the yarns affects the mechanical properties and performance estimation.

The revealed differences are also resulting from the simplifying assumptions of the predictive model. We will treat here each hypothesis and compare them with the observation and the measurement in the geometrical characterization.

Table 4.6: Comparison of the component yarns parameters computed by geometric model for impregnated sample-5C with rectangular cross section shape consideration to the measured values.

		Measured (CV%)	predictive dif. [%]		Geometric model			
					initial	dif. [%]	optimized	dif. [%]
Warp	S_w [mm ²]	3,71 (5,29)	3,08	-17,06	3,71	0,00	3,29	-11,38
	AR_w	11,87 (19)	11,00	-7,33	11,87	0,00	11,87	0,00
	l_w [mm]	7,05 (7,11)	6,56	-6,88	6,64	-5,87	6,25	-11,39
	h_w [mm]	0,61 (15,5)	0,60	-2,16	0,56	-8,35	0,53	-13,72
Filler-inner	S_{fi} [mm ²]	3,09 (4,24)	2,05	-33,61	3,09	0,00	2,74	-11,38
	AR_{fi}	9,17 (56,11)	6,45	-29,72	4,92	-46,41	5,51	-39,99
	l_{fi} [mm]	4,95 (28,5)	4,10	-17,08	3,90	-21,24	3,88	-21,54
	h_{fi} [mm]	0,65 (48)	0,64	-3,29	0,79	20,46	0,71	7,16
Filler-outer Z1	S_{fz1} [mm ²]	2,77 (1,53)	-	-	2,77	0,00	2,45	-11,38
	AR_{fz1}	6,57 (0,1)	-	-	4,01	-38,94	10,65	62,12
	l_{fz1} [mm]	4,26 (1,72)	-	-	5,53	29,75	5,56	30,53
	h_{fz1} [mm]	0,7 (1,71)	-	-	1,38	96,83	0,52	-25,42
Filler-outer Z2	S_{fz2} [mm ²]	2,88 (1,1)	-	-	2,77	-3,82	2,45	-14,76
	AR_{fz2}	3,85 (0,9)	-	-	2,45	-36,28	2,79	-27,59
	l_{fz2} [mm]	3,6 (1,4)	-	-	1,94	-46,06	1,97	-45,41
	h_{fz2} [mm]	0,93 (0,7)	-	-	0,79	-14,89	0,71	-24,19
Binder-crown	S_b [mm ²]	0,13	0,13	1,31	0,13	0,00	0,13	0,00
	AR_{bc}	6,25	2,35	-62,40	6,50	4,00	6,50	4,00
	l_{bc} [mm]	0,93	0,63	-32,50	0,97	4,33	0,97	4,33
	h_{bc} [mm]	0,14	0,27	90,81	0,15	6,63	0,15	6,63
Bias	S_o [mm ²]	2,9 (5,52)	2,05	-29,26	2,90	0,00	2,57	-11,38
	AR_o	6,25 (24,13)	5,01	-19,84	4,90	-21,53	5,56	-10,97
	l_o [mm]	4,39 (11,1)	3,62	-17,60	3,77	-14,09	3,78	-13,86
	h_o [mm]	0,75 (15,8)	0,72	-3,73	0,77	2,53	0,68	-9,39
Thickness	H [mm]	6,8 (1,36)	7,72	13,51	7,77	14,26	7,04	3,51
	H_{unc}		7,18	5,65				
	FVF	45,47	42,68	-6,82	42,78	-5,92	45,47	0,00
	FVF_unc		45,62	-0,38				

- **In-plane yarn path:** in the predictive model the path of the yarns was considered straight for all constituent in-plane yarns. This assumption could be accepted, except for outer filler yarns on the two extreme surfaces of the preform, in light of no interlacements between in-plane yarns and the low percentage of the measured crimp for these yarns in the trough thickness direction of the preform, table 3.5. The outer filler yarns have more important crimp percentage value because of the tension applied on the binder yarns which pass over it. The consideration of this waviness for outer filler yarns makes the crown part of binder yarn on the same plane of the preform outer faces. Thus no supplementary resin packet is created when considering the crown configuration for binder yarn. That is contrary to the assumption of two configurations for binder yarn in the predictive model. The additional volume of resin affects the mechanical properties estimation and also the stress field distribution during the mechanical modelling. Furthermore, the inconsideration of the crown part of the binder yarn through the uncrowned configuration in the predictive model neglect the effect of the crown part on the in-plane structure response. So
- **Binder yarn path:** it was considered as composition of two straight segments connected by arc with respecting the centreline continuity in the crowned configuration while in the uncrowned configuration just one straight through thickness segment was considered. And these two configurations for binder yarns were proposed to avoid take the undulation of filler yarns under the binder yarn into consideration. The straight path assumption for through the thickness part could be accepted as approximation by observing the Figure 3.47. The inclination of this part relative to the mid-plane of the preform should be taken into consideration. However, the magnitude of the compression applied on the outer faces of the preform during the impregnation process affects the binder path as it was mentioned in (4.6.2) and it was illustrated in the Figure 4.27.
Regarding the crown part, the approximation of straight segment doesn't agree with the observed curved path as it was remarked in the Figure 3.47. That affects the mechanical response evaluation of this structure by a numerical approach using a geometrical model with this approximation for binder yarn.
- **Variation of the area and the shape of the yarn cross section along its path:** In light of monitoring the variation of the area of the yarns cross section across the different cut-planes in the geometrical characterization, table 3.9, the assumption of constant area along yarns path could be accepted excepting for outer filler yarn on the extreme surface of the performs, which is alternate between two section (filler-outer free section and filler outer under binder section) consequent to the binder yarn path.
Contrariwise, the assumption of maintaining constant AR value and shape for the yarns cross sections along with its path does not agree with the observation. Where, the coefficients of the variation of the AR between different cut-planes are more important, table 3.9, especially for bias yarns. Also the yarns cross-section shape varies along with its shape in function of the contact interaction with adjacent yarns in the preform as observed by the captured micrographs especially for impregnated sample.
Otherwise, the unique AR, Pf values for all in-plane yarns doesn't agree with measured values as shown in table 3.10 and detailed measured data for each sample

in appendix A. Furthermore, the value of AR for binder yarn cross section varies along with its path. For the through thickness part, the AR has less value where the binder thickness is more important whereas for the crown part the AR has more important value where the cross section becomes, Figure 3.47.

- **Filler yarns:** In the geometrical characterization, three different sections were specified for the filler yarns, section (3.7.3.6), regarding the area and the shape of the yarn cross section and depending on their position in the through thickness of the preform. However, these sections were not respected in the predictive model.
- **The shape of the yarns cross-section:** In the predictive model, the same shape (elliptical) was considered for all yarns. That consideration does not accord with observation in the geometrical characterization where the shape of the yarn cross-section depends on the contact with surrounding yarns, which refers to its position inside the preform. It could be concluded from the geometrical observation:
 - The in plane yarns, except filler yarns on the two extreme surfaces of the preform, have straight upper and lower contact zones with the two next layers. Therefore, the lenticular and elliptical shapes do not fit for this architecture, Figure 3.41, 3.43 and 3.49.
 - The filler yarns on the two extreme surfaces of the preform have one straight contact zone with the next layer. Further, they have semi-elliptic contact zone when binder yarn pass over associated with higher packing factor (filler-outer under binder section) or they have free contact zone associated with lower packing factor (filler-outer free), Figure 3.49.
 - The binder yarn has two cross section shapes depending on its position. A trough the thickness part has contact zones on its entire perimeter while the crown part has one contact zone with filler yarn and it has more flat cross section, Figure 3.47 and 3.49. These two sections are not taken into consideration in the predictive model.

Consequently, the predictive geometrical model contributes to estimate the FVF and H for dry preform and composite during a design procedure. The estimated geometrical parameters and predictive model could not be used to construct accurate RVE of the structure used into mechanical modelling to estimate the mechanical properties of the structure.

4.7. Geometrical model

In order to construct an accurate RVE, a geometrical model is developed based on the observations and the results obtained by the geometrical characterization. This model is also constructed on the meso-scale for one unit cell of the multiaxis 3D woven composite like the predictive model. The yarns and the matrix are represented as 3D solid volume.

Firstly, the assumed hypotheses in the predictive model are re-adapted to the observed state of the yarns in the geometrical characterization. Secondly, the computation approach used to compute the model parameters, is developed based on the earlier predictive model with respect the present hypotheses. Finally, the construction approach of the RVE is presented and the obtained results are analysed.

4.7.1. Hypothesis and method

As pointed out previously, the yarn path inside the preform is too complex and its cross section shape and area vary along its path. That is resulting from the multi-filaments

structure of the yarns, which gives the yarn high deformability and flexibility. Also that is related to the interaction with neighbour yarns depending on the preform architecture. The influence of this multi-filament structure of yarn could be remarked through observation of the captured micrographs for the manufactured samples (appendix-a) and through table 3.8 the deviation in the cross section area and AR for yarns over the different unit cell on the same cut plane. On the other side this deviation is related also to the loom apparatus performance.

As a result of this particularity of yarns structure, the construction of RVE with high details in term of the yarn path and the variation of the yarn cross section shape and area conduce to complex meshing process while mechanical modelling using finite element method. As well construction a geometrical model of the composite with these deep details without assuming any approximation requires extra detailed geometrical characterization and more geometric parameters. Therefore as reported in the literature, different approximations are considered regarding the yarns path and the variation of the yarns cross section area and dimensions to construct a geometrical model and RVE depending on the application and the analysed properties through the mechanical modelling.

In this study we are interested in estimation of the elastic properties of the manufactured 3D multiaxis woven composite and the effect of the novel yarns arrangement on the generated stress-strain field under extension and shear load. So in this section the assumed hypotheses are explored with justification of each assumed hypothesis based on the geometrical characterization.

In this model the yarns are considered as 3D solid volumes of composite material made of fibres and resin with fibre volume fraction equal to the packing factor. Thus, the stiffness matrix of the yarns parts depends on the packing factor value.

The coefficient variation of the area of the yarns cross section along its path (across cut-planes) is less than 10%, as illustrated in table 3.9, relating to the variation of the packing of the filaments inside the yarns. Therefore, the areas of the yarns cross section are considered constant (that means constant packing factor) along its trajectory like in the predictive model. This assumption agree with the necessity of mechanical modelling regarding assignment of the material stiffness properties of constituent yarns parts of FE model. The yarn part material in the mechanical modelling is considered as a composite material composed of filaments and matrix with a fibre volume fraction equal to the packing factor value of the filaments inside each yarn. Hence, tacking the variation of the packing factor into consideration implies the variation of the assigned materials stiffness matrix for the yarns parts along its trajectory in the FEA.

Concerning the cross section shape and the path of the yarns, contrary to the predictive model, they are not considered same for all the yarns, so for each yarn its cross section shape and its path are assumed individually depending on its type and its position inside the preform:

- For in-plane yarns including: filler-inner yarns, warp yarns in the 2 inner layers, and biases yarns ($\pm\theta^\circ$); the path is considered straight because of the low measured crimp percentage, which could be neglected table 3.5. While, the cross section shape is considered rectangular instead of elliptic, cut-elliptic or racetrack because of two raisons:

4. Geometrical modelling of 3D multiaxis woven composite

- 1- In case of consideration of rectangular cross section shape, we get a fibre volume fraction as near as possible to the measured values in comparison with the other shape consideration, which will be detailed in the next section and it is shown in table 4.7.
- 2- Contact surfaces between adjacent yarns layers (top and bottom contact zone of the yarns cross section) and also lateral contact surfaces between filler yarns of the middle layer and the vertical part of the binder yarns can be determined. Whereas, in the case of the other cross-section shapes considerations, contact lines instead of contact surfaces may be obtained. That implies getting matrix volume between two yarns surfaces with zero thickness causing meshing problem or that obligates to add matrix layer between two yarn layers causing less FVF value, as reported in the work of Lin et al. (2011).

Table 4.7: FVF of the different sample computed by geometric model with variant cross section consideration for in-plane yarns and compared to measured value.

FVF [%]	measured	ellipse dif. [%]	cut-ellipse dif. [%]	racetrack dif. [%]	rectangle dif. [%]
Sample 1	31,12	28,54 -8,29	30,04 -3,47	30,23 -2,86	31,12 0,00
Sample 2	25,02	22,64 -9,51	25,02 0,00	25,02 0,00	25,02 0,00
Sample 3	26,35	21,77 -17,38	24,09 -8,58	24,95 -5,31	25,31 -3,95
Sample 4	33,13	28,69 -13,40	31,93 -3,62	32,84 -0,88	33,13 0,00
Sample 5	34,95	29,26 -16,28	32,63 -6,64	33,45 -4,29	34,63 -0,92
Sample 5C	45,47	36,2 -20,39	40,42 -11,11	41,61 -8,49	42,78 -5,92

- For binder yarns, as mentioned in the geometrical characterization and in Figure 3.47; two parts are distinguished crown part and through the thickness part regarding the path and the cross section shape. For through the thickness part, rectangular shape is assigned for the cross section to have a contact surface with the filler yarns and straight path with undulation angle (α) with respect to the preform middle plane, Figure 4.28. For crown part, cut-ellipse shape is assigned to the cross section to have continuity with rectangular shape of through the thickness part in order to avoid meshing problem. Further, the yarn path is considered as part of ellipse with respecting the continuity condition with straight-line path of through the thickness part.
- For filler yarns on two extreme surfaces of the preform, as observed in the geometrical characterization (3.7.3.6), two cross sections are distinguished regarding area and shape; filler-outer under binder section (filler-OZ1 and filler-OZ2) and filler-outer free section (filler-OF). In association with the first hypothesis, there is no variation for cross section area along yarns path, only the filler-outer under binder section for filler yarns at extreme preform surface are considered. On another hand, as observed in the geometrical characterization, the filler yarns on the outer preform surface have semi elliptical cross section shape, Figure 3.49, resulting from the top contact zone with the binder yarn and straight bottom contact zone with the warp yarns, Figure 4.29. Concerning the yarn path, it is composed of three segments, Figure 4.29, the first segment corresponds to the shape of the binder yarn cross section, the second is a spline connected to the third straight segment with respecting the continuity

4. Geometrical modelling of 3D multiaxis woven composite

conditions. By this way, the undulation of the filler yarns on the extreme was taken into consideration; contrary to the predictive model. Thus the two configurations for binder yarns (crowned and uncrowned) are not required. Additional fine matrix volume δ (equal to 0.05mm) between the binder yarn and filler yarn was added to resolve the construction problem of the matrix volume by increase the undulation of the filler yarn about 0.05mm in addition to the cross section thickness of binder yarn, as illustrated in Figure 4.30. By increasing the undulation of filler under z, no modification is caused on the volume of matrix while a too small influence on the length of the outer filler yarn could be ignored.

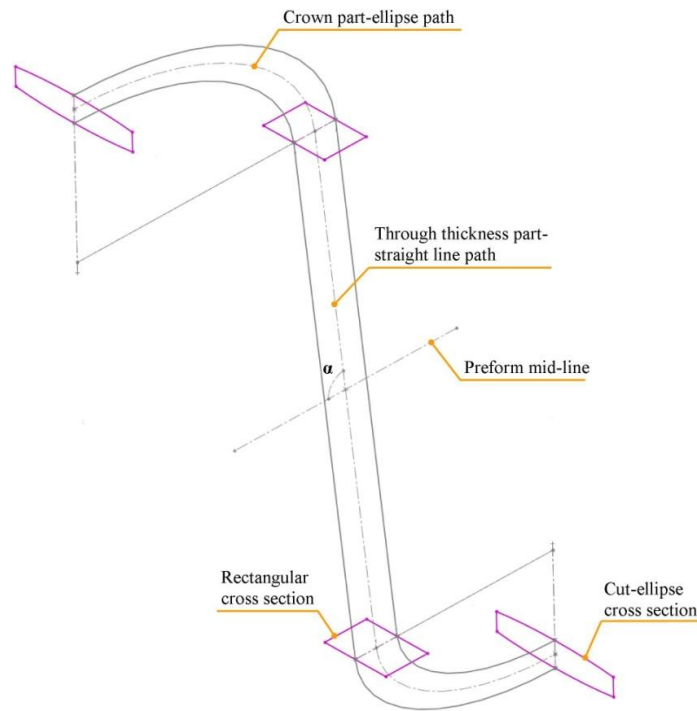


Figure 4.28: Assumptions concerning the cross section shape and path of the binder yarn.

- For warp yarns, which are in contact with filler yarns on the two extreme preform surfaces, their cross section shape varies in function of the path of the filler yarns, as shown in the Figure 4.31, in function of the undulation of filler yarns.

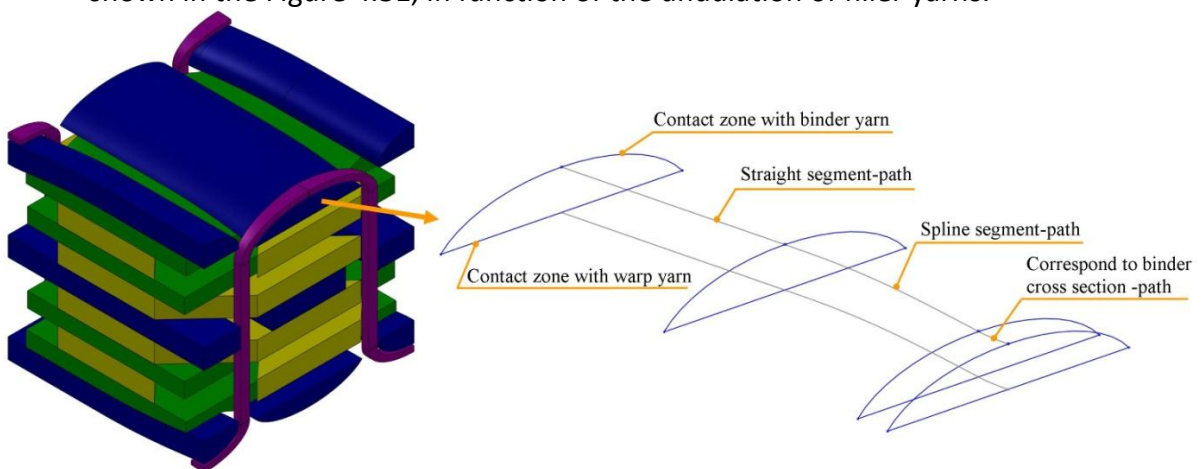


Figure 4.29: Assumptions concerning the cross section shape and path of the filler yarn at outer preform surfaces.

4. Geometrical modelling of 3D multiaxis woven composite

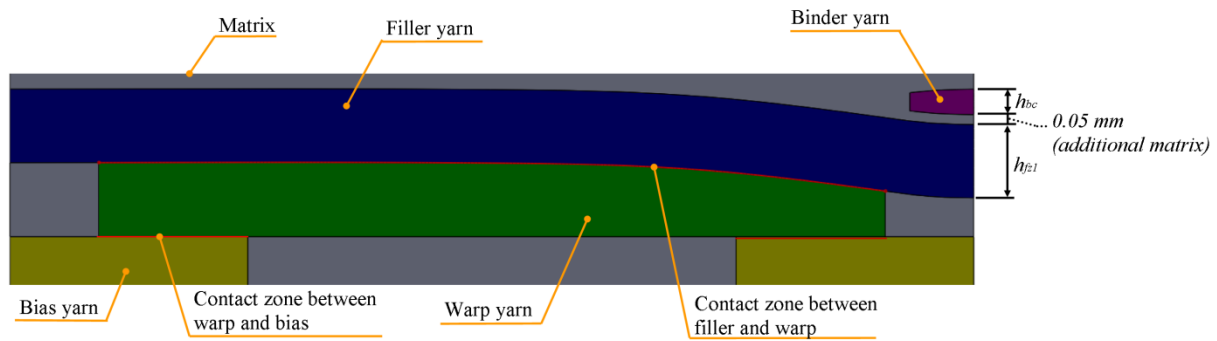


Figure 4.30: Front view of the RVE at filler-a cut plane illustrates the undulation of the filler yarn and the contact zone with warp yarn.

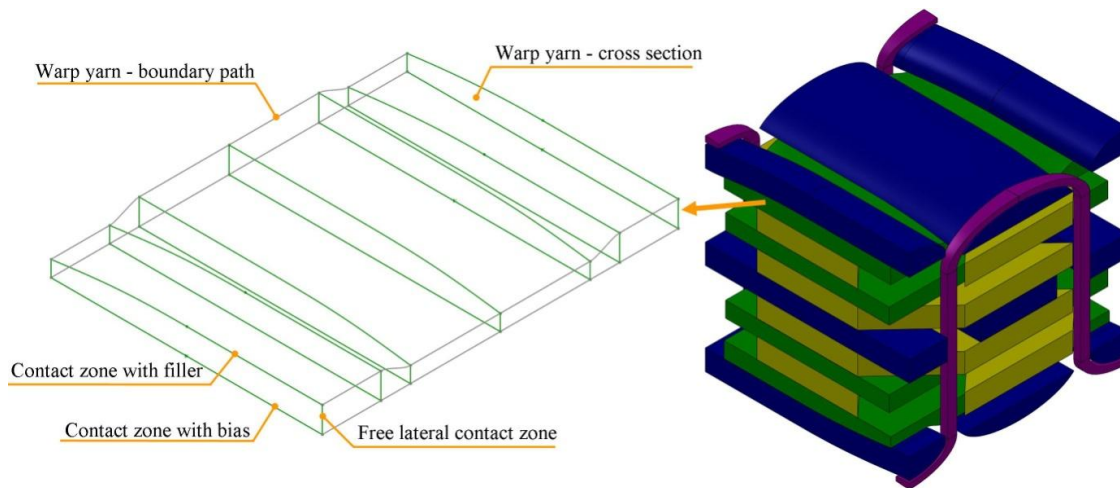


Figure 4.31: Assumptions concerning the cross section shape and path of the warp yarn near to extreme preform surfaces.

4.7.2. Development of the model

To calculate the model parameters including the yarn parameters and the unit cell parameters, a computational approach was developed, Figure 4.32. This approach is based on the earlier developed predictive geometrical model (4.6.2) and on the observed geometry of the yarns in association with the assumed hypotheses.

In this approach, the cross section area of all the component yarns in the model as well as the two in-plane unit cell dimensions (L_w , L_f) are equal to the means of the measured values, obtained by the geometrical characterization and reported in appendix A. Two major and minor dimensions of the yarns cross section are computed depending on the type and position of the yarn inside the preform with the condition of getting the fibre volume fraction of resultant RVE as close as possible to the measured value.

In the flow chart, Figure 4.32, the first step is dedicated to assign the value of the input parameters. These parameters include the manufacturing and weaving parameters of the produced preform and the following measured parameters: the area of the all yarns cross section, the two in-plane dimension of unit cell, the angle α defining the inclination of binder yarn and the AR_w and AR_{bc} of the warp and binder yarns. For the AR_{bt} of the cross section of the binder yarn on the through thickness part was assumed to 1.5 for all samples. In the second step, the width and height of the warp and binder yarns are computed using the geometrical equations detailed in the table 4.3 depending on the cross section shape consideration. This approach doesn't imply a specific cross section shape of yarns, it could be

4. Geometrical modelling of 3D multiaxis woven composite

applied for different cross section shapes. In the third step, we assume a value for the AR_{fm} of the filler-middle yarn within the range $[1, 11]$ and it will be considered a variable in the optimization loop. In fourth step, the dimensions of the filler-middle yarn cross section are computed as for the warp yarn. Then the width of the bias yarn cross section (l_o) could be computed from the equation 4.19, which is deduced from the position of bias yarn and its interlacement with binder yarn as illustrated in Figure 4.33 with rectangular cross section shape consideration for through the thickness part of the binder yarn.

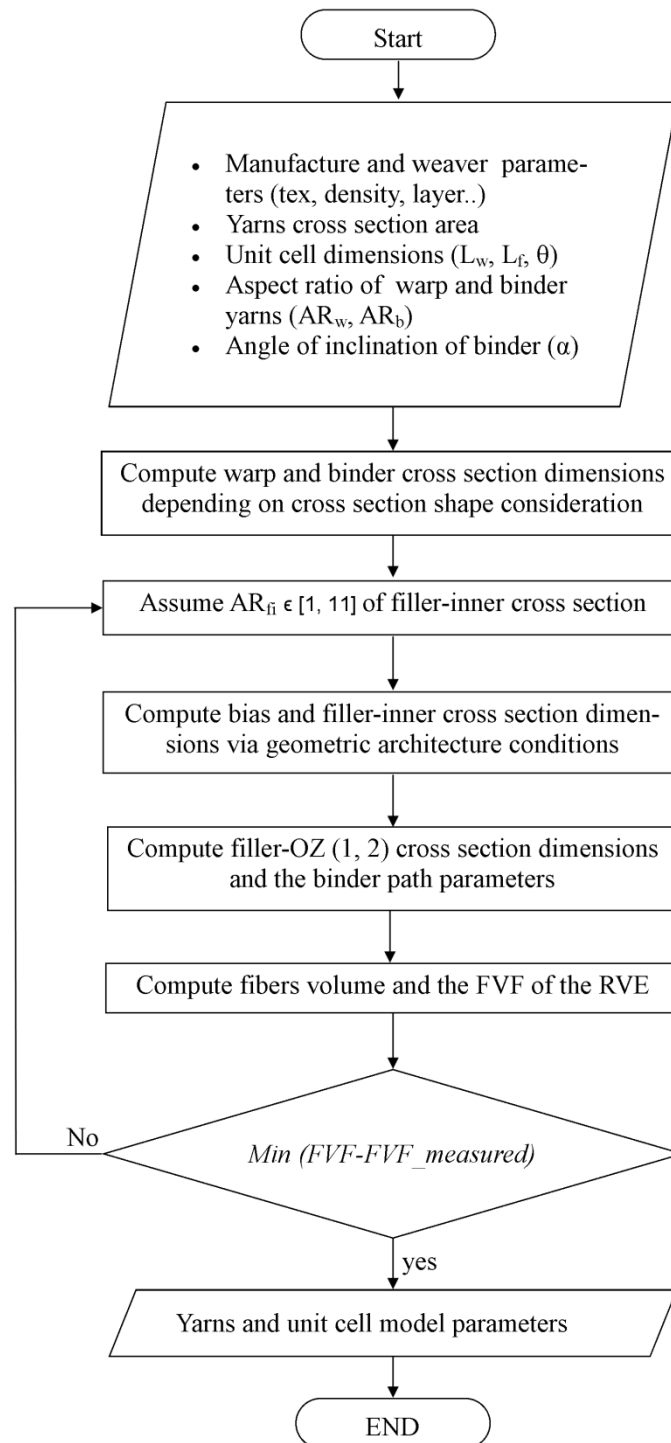


Figure 4.32: Computation approach in the geometric model to calculate yarns and unit cell parameters

4. Geometrical modelling of 3D multiaxis woven composite

$$l_o = \left(L_w - \frac{l_{bt}}{\tan \theta} - 2h_{bt} - l_{fi} - \frac{h_f + h_o}{\tan \alpha} \right) \cdot \sin \theta \quad (4.19)$$

The height h_o and the AR_o of bias yarn could be calculated based on the area and the shape cross-section consideration. The dimensions of the cross section of the two bias yarns ($+\theta$ and $-\theta$) are considered same since the configuration of the two yarns is symmetric relative to the middle plane between two binder yarns. In the fifth step, the cross section dimensions of the filler-OZ (1 and 2) are calculated as explained in the flow chart shown in Figure 4.34. This section is related to the path of the binder yarn defined in Figure 4.35.

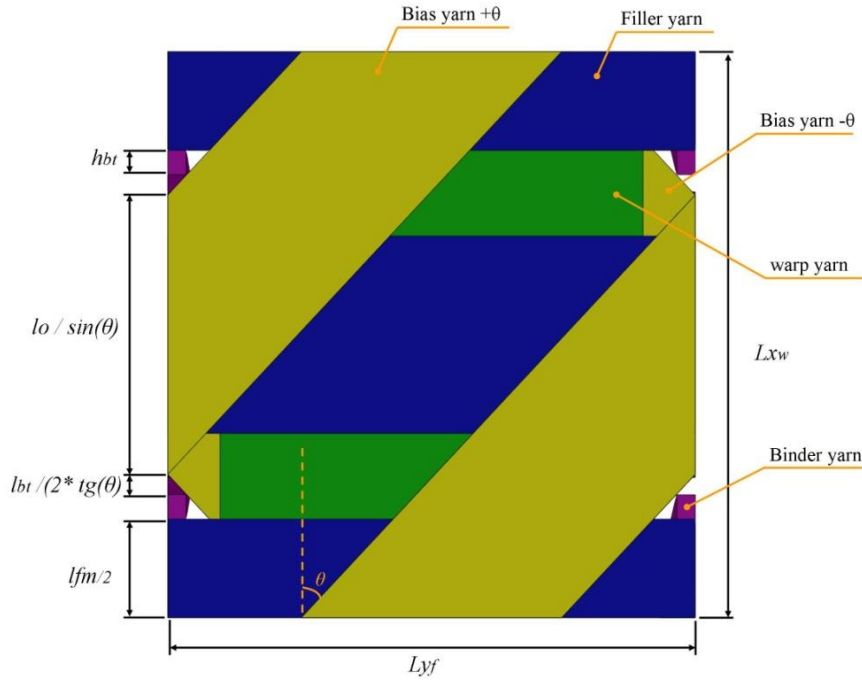


Figure 4.33: Transversal cut view for the RVE of sample-5 parallel to mid-plane, illustrating the path of the bias yarns and its position relative to binder and filler yarns.

Here, we have three possible configurations for the filler-OZ1 cross section, which are the same possible configuration for filler-OZ2 cross section, depending on the two conditions detailed in the flow chart Figure 4.34. These three configurations of cross section are illustrated in Figure 4.36.

In the sixth step, the fibre volume fraction of the unit cell is computed after calculating the total yarns lengths and volumes inside the unit cell as followed in the predictive model (4.14) with weight method. For the length of outer filler yarns under binder (L_{fz}) and the binder yarn (L_b), the formulations (4.20) and (4.21) are used since the undulation of filler-under z yarn was taken into consideration in the earlier predictive model and here the path of binder yarn was considered as combination of straight segment and semi-elliptical segment.

$$L_{fz} = \frac{L_f}{2} + l_{bc} + \frac{h_{bc} + \delta}{\sin \varphi}; \quad \varphi = \tan^{-1} \frac{h_{bc} + \delta}{\frac{L_f}{2} - l_{bc}} \quad (4.20)$$

$$L_b = \pi \sqrt{2(t_1^2 + j_1^2)} + 2(H - t_1 - t_2 - h_{bc}) \sin \alpha \quad (4.21)$$

In the seventh step, the obtained FVF of RVE for the assumed value of AR_{fi} is compared to the measured value of FVE. This loop is re-taken to compute new value of FVF for new assumed value of the AR_{fi} within the range [1, 11] until the minimum deviation between FVF of RVE and the measured FVF is obtained.

4. Geometrical modelling of 3D multiaxis woven composite

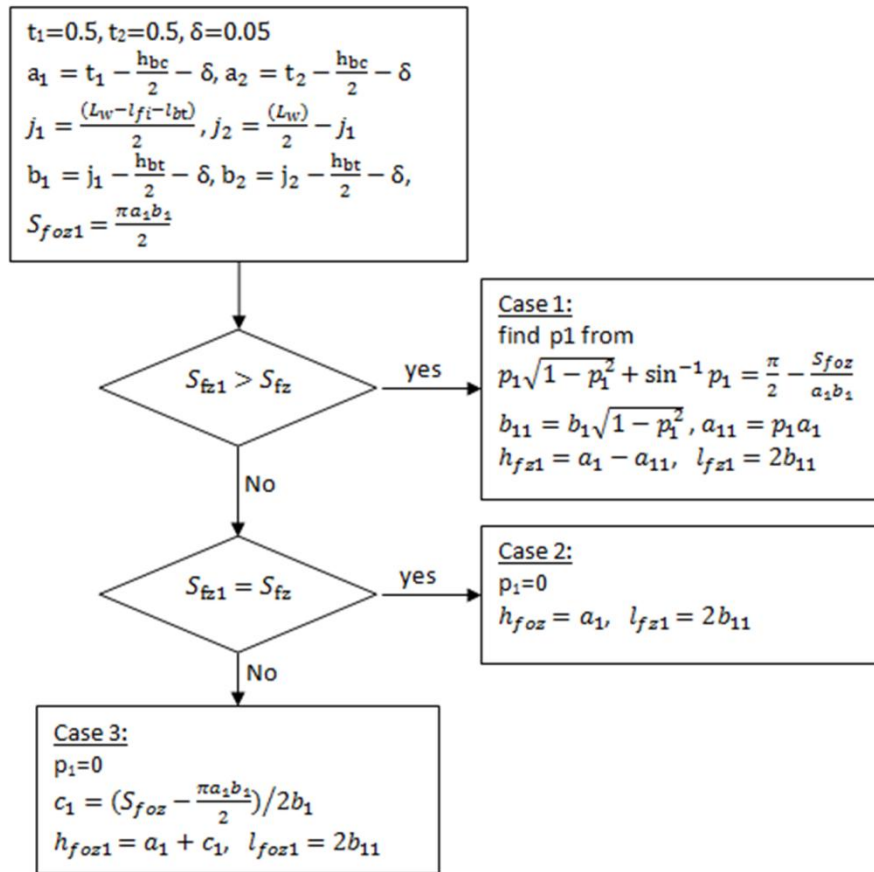


Figure 4.34: Computation approach to calculate filler_ under Z (1, 2) cross sections dimensions and binder path parameters.

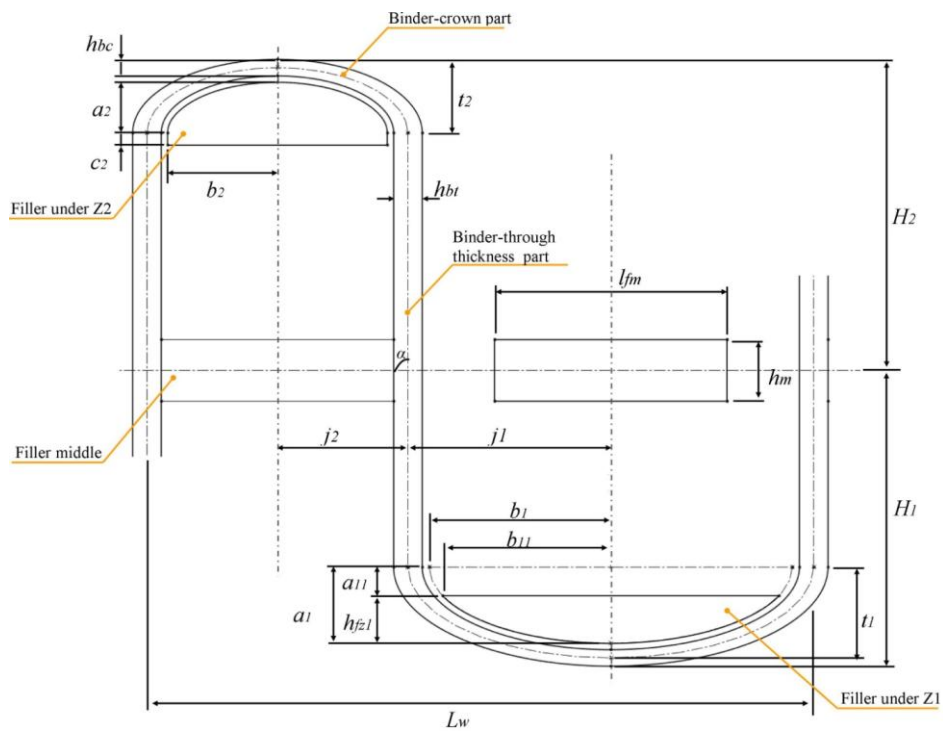


Figure 4.35: Path of the binder yarn and the sections of filler yarns at different position relative to binder yarn.

Consequently, the geometric model parameters allow construction RVE of the analysed 3D multiaxis woven preform with FVF as close as the measured FVF of this structure with more accurate hypotheses comparing to previous predictive models.

A code has been written in MATLAB software to model this approach enabling the computation of the model parameters for all samples in function of the input parameters.

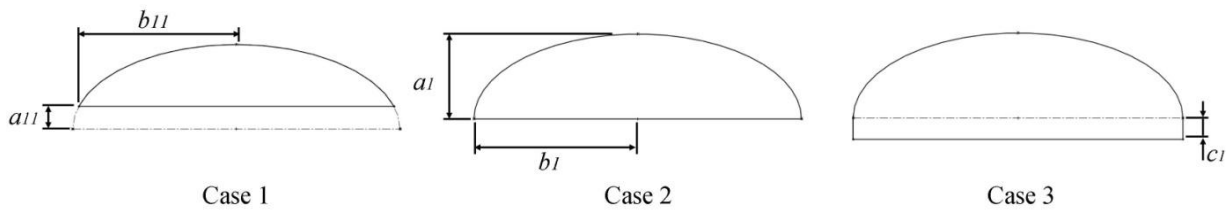


Figure 4.36: Three possible cases for the filler-under Z cross section.

4.7.3. Construction of the RVE

This section focuses on the construction of a RVE for a unit cell of a composite structure made with a textile reinforcement of the developed 3D multiaxis woven fabric. As it was introduced earlier in the section (4.7.1), the RVE of this structure is built on the meso-scale, where the yarns and the matrix are represented as 3D solid volumes.

In the literature (4.3.2), the Texgen and Wisetex software and also the work of Hivet and Boisse (2005) are based on the determination of the yarn path and assigning the yarn cross section at specified nodes along the yarn path. Then the sweep and loft functions were used to build the solid volume of the yarn. In the present approach based on Hivet's approach, the "SolidWorks" (CAD software) is used to construct the RVE by using the model parameters computed by the geometric modelling introduced in the previous section. This software provides many useful and practical tools to construct the solid volume and is available in our laboratory (GEMTEX). By this software, the contact surfaces (yarn-yarn) and (yarn-matrix) could be controlled more properly than with other textile geometric software such as Texgen and Wisetex. Also, the penetration between the volume features could be avoided as well as the cross section parameters and path parameters of the yarns could be controlled and managed more efficiently.

To construct a RVE for a unit cell of a composite, the first step is extruding the matrix volume based on the three dimensions of the unit cell (L_w, L_f, H). The yarn paths are sketched inside the cube, the cross section of yarns are sketched on specified plane perpendicular to the yarn path and they are defined depending on the variation of the shape of the yarn according to its position. The outline of the yarns cross section is derived from the path of the surrounding yarns that are in contact. The half of the warp yarn outline takes the shape of the filler-under z yarn path and it varies along its path in function of the contact with filler yarns, as illustrated in Figure 4.30.

A surface with zero thickness is arisen when lofting cut or sweeping cut of a yarn with curved cross section shape, which is in contact with curved yarn path, from the solid volume of the matrix cube. This problem appears when sweep-cut the filler-under z yarn from the matrix cube. Consequently in order to avoid this zero thickness surface it was an obligation to increase the undulation of filler-under z when the binder yarn passing over resulting in addition a layer of matrix with δ thickness separate between the binder crown part and the filler under z, Figure 4.30. For the same reason an additional layer of matrix is added on the

top and lower surface of RVE with a thickness of 0.02 mm. However, that increases the matrix volume about 2%.

After sketching the path and the cross sections of the yarns, they are lofted cut and swept cut from the matrix cube to obtain the matrix volume feature, Figure 4.37-a. In the next step, the same sketches are used to loft and sweep the independent yarns volume feature, Figure 4.37-b. Using the tools of the SolidWorks software, the RVE of the dry preform of this multiaxis 3D woven architecture also of the impregnated preform of this architecture could be obtained as well as for multiple unit cells, Figure 4.38.

4.7.4. Results

For five produced samples of the 3D multiaxis woven architecture using the developed multiaxis weaving loom, the model parameters are computed by the developed geometrical model. The computation is made using the manufacturing and weaving parameters of the five samples listed in table 3.2. The preform geometric parameters are measured through the geometrical characterization. The computation approach is applied with four assumptions regarding the shape of the in-plane yarns cross section (ellipse, cut-ellipse, racetrack and rectangular illustrated in table 4.3) and the closest FVF of the RVE to the measured RVE could be obtained by varying the value AR_{fi} for each shape consideration (listed in table 4.7). The racetrack and rectangular shape considerations provide the possibility to get approximately the exact FVF for RVE in comparison with the measured FVF. It means that these two cross section shapes with the assumed hypotheses lead to construct a realistic RVE. On the other side, the rectangular shape, as we investigated in the hypothesis section 4.7.1 assures the contact surfaces with the surrounding yarns and the binder yarns. Therefore, the rectangular shape has been adopted in the next steps of construction of the RVE. Otherwise, the assumption of elliptic cross-section shape in association with the assumed hypotheses causes high deviation in the FVF. This cross section shape leads to non-accurate geometrical model for the present 3D multiaxis woven architecture.

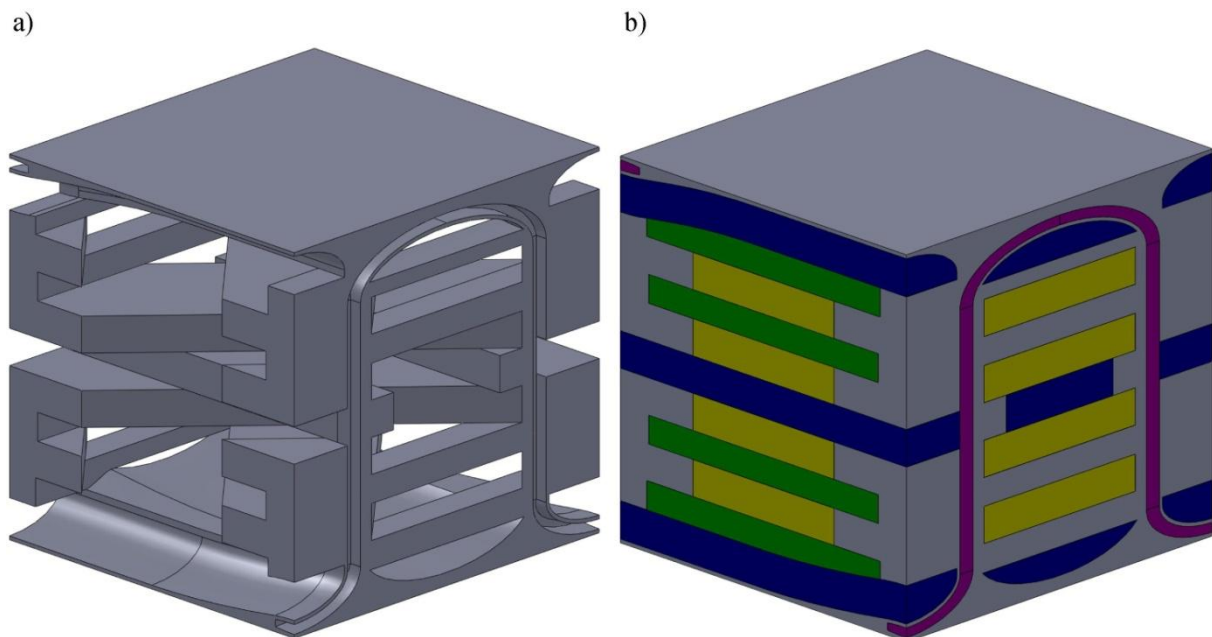


Figure 4.37: Isometric view of the constructed RVE of sample-5. a) construction of the matrix as a first step, b) formation the yarns inside the matrix.

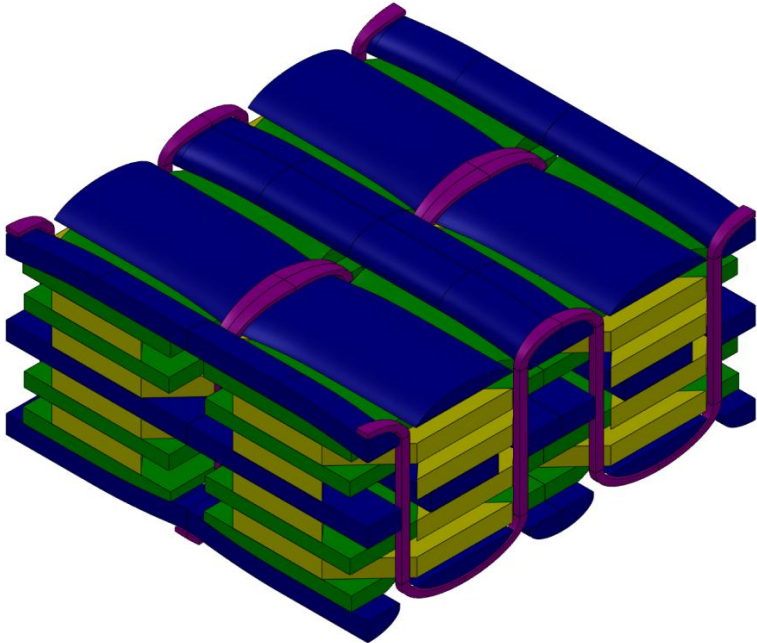


Figure 4.38: Isometric view of a representative volume of the preform illustrates the alternative movement and position of the binder yarns.

For the impregnated sample 5C, errors of -5.92% and 14.26% are observed between FVF and H of geometric model and the measured values respectively. These errors are induced essentially by the simplification of constant AR along preform and also by the incertitude of the measured values. These errors could be reduced by an optimization loop looking for the packing factor value of the in-plane yarns, with the condition of $Pf \leq 0.9069$, providing FVF of the geometric model equal to the measured value. Similar method was followed by Xu et al. (2013) to introduce additional resin packet around yarns within the composite to avoid contacts yarn/yarn. By this loop optimization the packing factor of all in-plane, table 4.8, is increased by 12% resulting in decreasing the in-plane yarns cross section area of about 11.4%. The effect of this correction in the packing factor value on the estimation of the mechanical properties of the analysed structure should be evaluated against the required complexity and numerical cost of perfect realistic geometric model.

Table 4.8: Optimized value of the yarns packing factor leading to obtain FVF of geometric model equal to measured value.

Yarns	Measured	Model-optimized
Warp	0,73	0.81
Filler-inner	0,58	0.65
Filler- outer free	0,55	0.62
Filler- outer under binder	0,65	0.73
Bias	0,62	0.69
Binder	0,9	0.9

Two dimensions of the yarns cross section obtained for the sample-5C with rectangular shape consideration are compared, in the table 4.6, to the average of the measured values also to the obtained values by the predictive model. A deviation has been noticed between

the measured and computed values especially for the filler yarn resulting from the assumed simplification as reported earlier.

The Figures 4.39 and 4.40 show comparison between the micrographs and the constructed RVE of the samples-5 and sample-5C respectively at four specified cut-planes. It could be noted the influence of the impregnation process on the arrangement and on the cross section shape of the yarns inside the preform. Furthermore, the geometrical properties of the sample 5 are listed in the table 4.9, whereas those of the sample 5C are given in the table 5.5.

4.8. Conclusion

The geometrical modelling approaches developed in the literature for the 3D multiaxis woven preform as well as for the 3D interlock woven preform are explored. They provide a method to develop a predictive model for 3D multiaxis woven preform. This model has been developed before manufacturing the multiaxis samples. It is based on previous researchers works to give a conception tool serving in design and predicting geometrical parameters (FVF and H) of multiaxis architectures in function of the weaving and manufacturing parameters. This model has been compared with the Buchanan's model (2010-b) developed for the same multiaxis architecture. Better estimation is obtained by present model with respect of the geometric conditions of the structure to avoid the interpenetration between the in-plane yarns.

The predictive model has been verified after the geometrical characterization of the manufactured performs by comparison the geometry of the yarns inside the preform to the assumed geometry. It has been concluded that inaccurate hypotheses have been assumed in the predictive model that affects the estimation of the mechanical properties and performance of this structure obtained by mechanical modelling. Thereby, the predictive geometrical modelling could not be used to construct accurate geometric model serving in the mechanical modelling using the finite element method.

Therefore, geometrical modelling has been developed as accurate as possible with more realistic hypothesis taking into consideration the waviness of the outer filler yarn and the cross section shape variations of the binder yarn along with its path. That leads to avoid the hypothesis of twofold configuration of the binder yarn. However, the approximation of constant AR value and cross section shape along with yarn path is maintained. The yarns cross section parameters are computed based on the measured values of the yarns cross section area and assuming AR value giving FVF as close as to the measured value. That is realized with respect of the geometrical architecture condition in order to avoid yarns volume interpenetration. In this model different cross section shapes have been considered (ellipse, cut-ellipse, racetrack and rectangular). It has been concluded that racetrack and rectangular shape provide geometrical model with FVF close to the measured value with respecting the yarn/yarn contact. Moreover, it has been observed that there is no interlacement between in-plane yarns in this architecture.

The necessity of RVE construction with less complexity and less numerical cost involve maintaining the approximation of constant AR value and shape of the yarns cross section along with its path. However, in addition the measurement incertitude, that causes an error in the FVF of geometrical model comparing to the measured value. This error could be minimized to zero by varying the packing factor of the in-plane yarns via optimization loop.

4. Geometrical modelling of 3D multiaxis woven composite

Table 4.9: Geometric parameters of the constructed RVE for sample 5.

Preform total thickness	H [mm]	9,71
Length of warp yarns in the unit cell	L _w [mm]	42
Length of filler yarns in the unit cell	L _f [mm]	58,87
Length of bias yarns in the unit cell	L _v [mm]	61,56
Length of binder yarns in the unit cell	L _b [mm]	27,06
areal density of the unit cell	S ^{uc} [gr/cm ²]	0,86
Total volume of yarns	V _{yarns} [mm ³]	647,43
Volume of unit cell	V ^{uc} [mm ³]	999.39
Fiber volume fraction computed by yarns volume	FVF_volume [%]	64,78
Fiber volume fraction	FVF_weight [%]	34,47
rate of warp fiber volume to total fibers	V _{fw} [%]	37,55
rate of filler fiber volume to total fibers	V _{ff} [%]	31,77
rate of bias fiber volume to total fibers	V _{fv} [%]	14,83
rate of binder fiber volume to total fibers	V _{fb} [%]	1,03

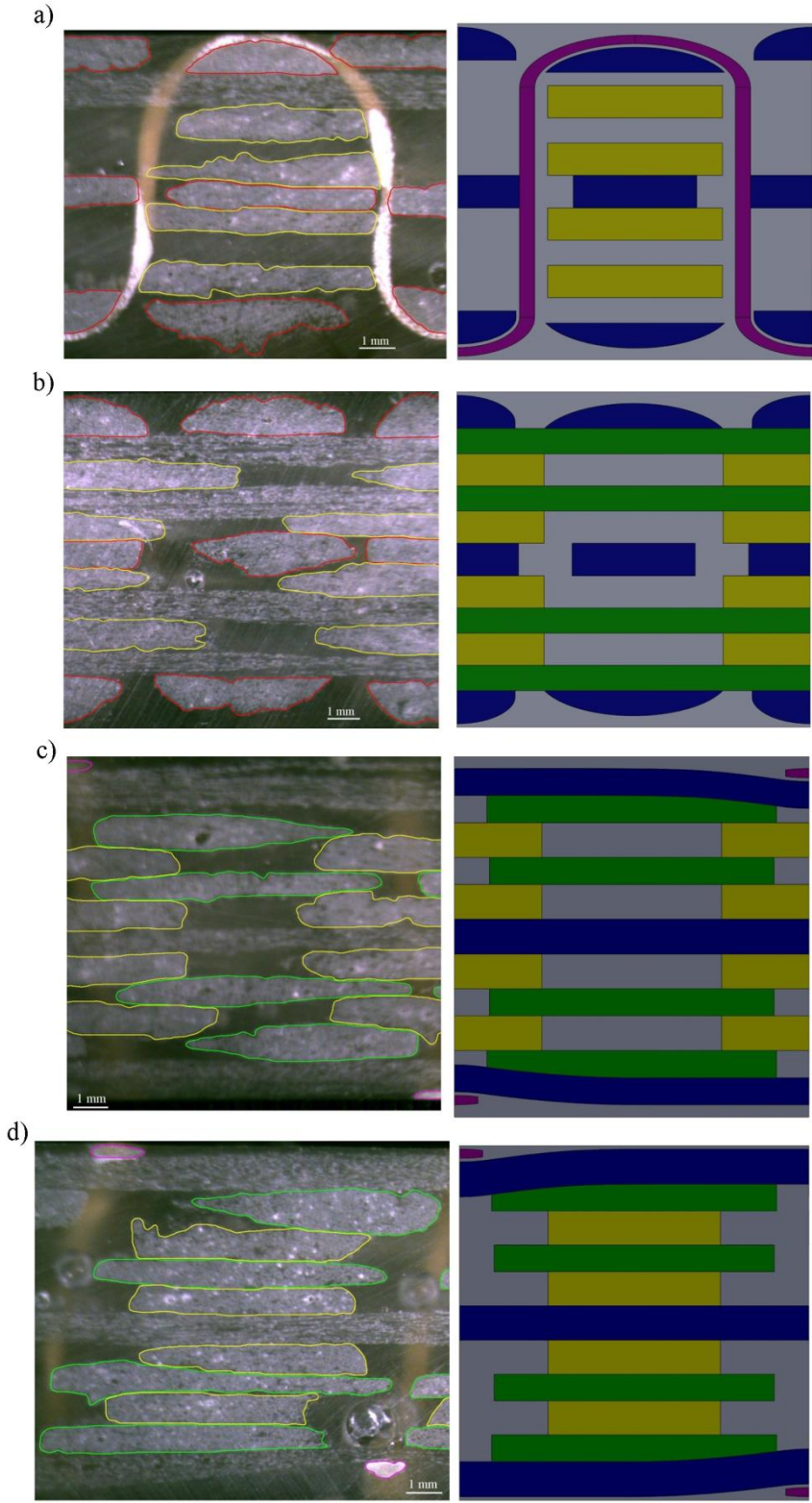


Figure 4.39: Comparison of the constructed RVE for sample-5 at four cut planes to the corresponding section of the real composite

4. Geometrical modelling of 3D multiaxis woven composite

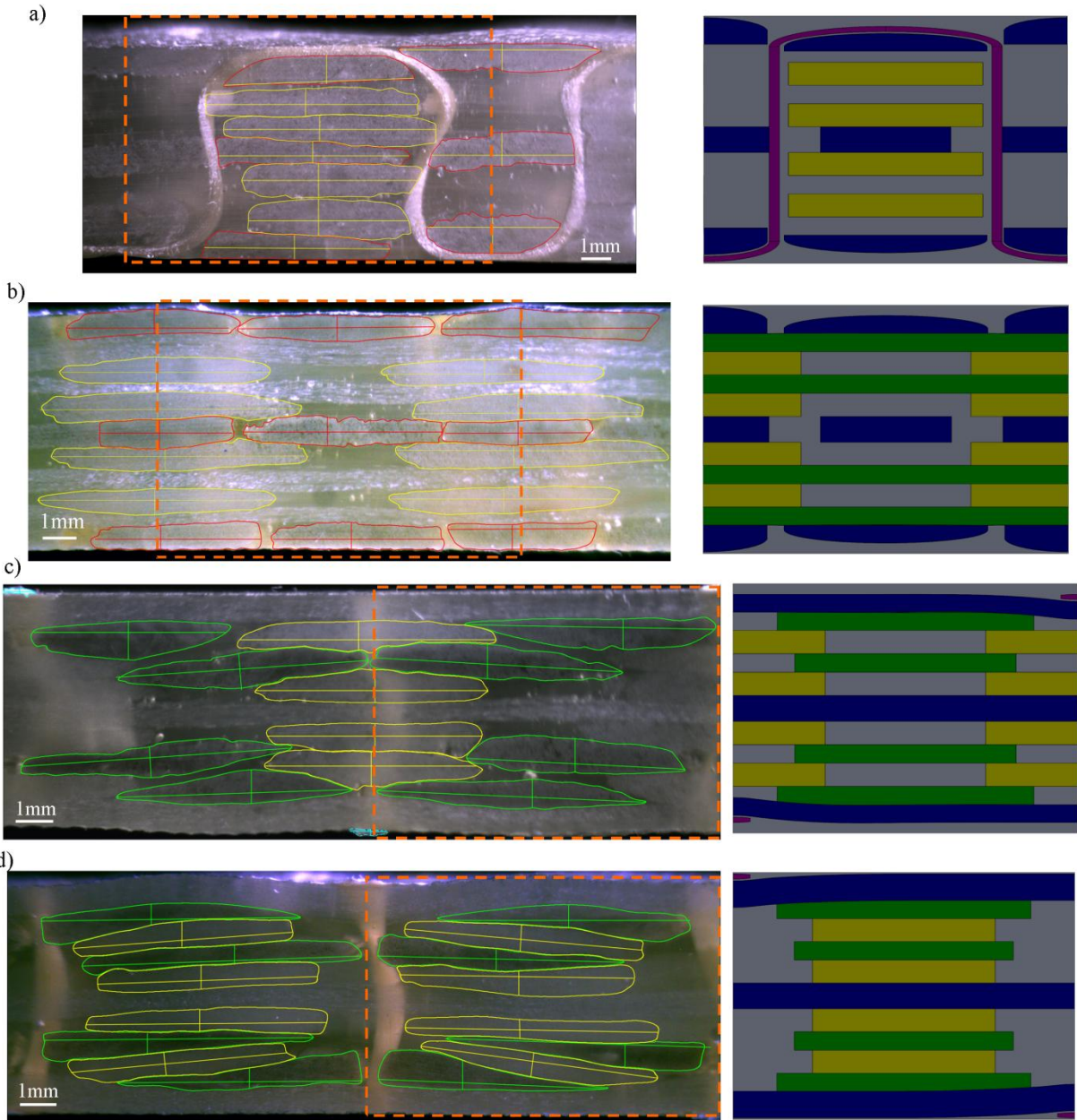


Figure 4.40: Comparison of the constructed RVE for sample-5C at four cut planes to the corresponding section of the real composite.

5. Evaluation the elastic properties of 3D multiaxis woven composite

5.1. Introduction

The investigation of the mechanical properties for any developed structure is indispensable to valorise and classify it from mechanic performances point of view among existing structures. Therefore, the present chapter is dedicated to the investigation of mechanical properties and advantages of developed multiaxis woven architecture using the technology presented in the chapter 3. Geometrical characterisation of the preform has been completed in the chapter 4. The investigation consists of evaluation of the multiaxis composite elastic modulus using numerical model. Then, a comparison of the obtained results to those of equivalent orthogonal woven composite, which is established in this study as well, is realized. Otherwise, in order to validate the numerical approach, the elastic properties of equivalent laminate composites are determined for both 3D woven architectures (multiaxis and orthogonal). They are evaluated using the Classical Laminate Theory. This mechanical investigation includes also the estimation of the effect of developed architecture on the in-plane off-axis properties of 3D woven reinforcement. Finally, the interest of the proposed technology regarding the in-plane bias yarns layer sequence is also explored in this chapter by evaluation of the layers sequence effect on the generated interlaminar stresses at the free-edge of composite.

In this chapter, at the first, the basic theories related to the mechanics of composites required to this study are outlined. Second, the investigation methodology is exposed. Finally, the obtained results are presented and commented.

5.2. Theory

5.2.1. Stress – strain relationship for composite materials

The relationship between stress and strain at a point of a material is described by Hook's law; it is also called constitutive equation. Both stress tensor and strain tensor are symmetric ($\sigma_{ij} = \sigma_{ji}$, $\epsilon_{kl} = \epsilon_{kl}$) (Crandall et al. 1978). The constitutive equation is expressed generally using contracted notation (5.1-b).

$$\sigma_{ij} = C_{ijkl}\epsilon_{kl} \quad (5.1-a)$$

$$\begin{Bmatrix} \sigma_1 \\ \sigma_2 \\ \sigma_3 \\ \sigma_4 \\ \sigma_5 \\ \sigma_6 \end{Bmatrix} = C_{ij} \begin{Bmatrix} \epsilon_1 \\ \epsilon_2 \\ \epsilon_3 \\ \epsilon_4 \\ \epsilon_5 \\ \epsilon_6 \end{Bmatrix}; \quad i, j = 1, 2, \dots, 6 \quad (5.1-b)$$

Where, C_{ij} is the stiffness matrix, σ_i is the stress tensor and ϵ_j is the engineering strain tensor. Also the compliance matrix S_{ij} is used to express the stress-strain relationship (5.2)

$$\epsilon_i = S_{ij}\sigma_j \quad (5.2)$$

$$[S] = [C]^{-1} \quad (5.3)$$

36 entries are required to obtain the stiffness or compliance tensor defining material properties. Based on a strain energy density function (Sokolnikoff 1956 and Jones 1999), it was proven that stiffness matrix is symmetric. Thus the number of entries of stiffness matrix is reduced to 21. These entries depend on the material symmetry (if it possesses or not planes or axis of symmetry).

5. Evaluation the elastic properties of 3D multiaxis woven composite

In the case of **anisotropic** material, which has no planes of symmetry and its properties depends upon its orientation; these 21 entries of stiffness matrix are independent. If the material has one plane of symmetry (e.g. plane 1-2), it is called **monoclinic** material. The entries $C_{i4} = C_{i5} = 0$ with $i \neq 4, 5$ mean that no shear- extension coupling has effect on plane 1-3 and 2-3. The number of independent entries in stiffness or compliance matrix becomes 13.

For **orthotropic** material, which has three planes of symmetry that coincides with the coordinate planes, the entries $C_{i4} = C_{i5} = C_{i6} = 0$ with $i \neq 4, 5, 6$. It means that there is no tensile-shear coupling effect in orthotropic material comparing to anisotropic material. The number of independent entries in stiffness or compliance matrix for orthotropic material becomes 9. These 9 entries are computed by 9 independent engineering modules ($E_1, E_2, E_3, \nu_{12}, \nu_{13}, \nu_{23}, G_{12}, G_{13}, G_{23}$) (5.4) particular to material type.

$$\begin{Bmatrix} \epsilon_1 \\ \epsilon_2 \\ \epsilon_3 \\ \epsilon_4 \\ \epsilon_5 \\ \epsilon_6 \end{Bmatrix} = \begin{bmatrix} \frac{1}{E_1} & \frac{-\nu_{12}}{E_1} & \frac{-\nu_{13}}{E_1} & 0 & 0 & 0 \\ \frac{-\nu_{12}}{E_1} & \frac{1}{E_2} & \frac{-\nu_{23}}{E_2} & 0 & 0 & 0 \\ \frac{-\nu_{13}}{E_1} & \frac{-\nu_{23}}{E_2} & \frac{1}{E_3} & 0 & 0 & 0 \\ 0 & 0 & 0 & \frac{1}{G_{23}} & 0 & 0 \\ 0 & 0 & 0 & 0 & \frac{1}{G_{13}} & 0 \\ 0 & 0 & 0 & 0 & 0 & \frac{1}{G_{12}} \end{bmatrix} \begin{Bmatrix} \sigma_1 \\ \sigma_2 \\ \sigma_3 \\ \sigma_4 \\ \sigma_5 \\ \sigma_6 \end{Bmatrix} \quad (5.4)$$

If the orthotropic material has one axis of symmetry that coincides with coordinate axis (e.g. "1"), it becomes **transversally isotropic** material (meaning that the material is isotropic at plane 2-3). And the number of engineering modules is reduced to 5 ($E_1, E_2, \nu_{12}, \nu_{23}, G_{12}$) where

$$E_2 = E_3, \nu_{12} = \nu_{13}, G_{12} = G_{13} \quad (5.5-a)$$

$$G_{23} = \frac{E_2}{2(1+\nu_{23})} \quad (5.5-b)$$

The **isotropic** material has infinite number of planes of symmetry meaning that the material properties are independent of the orientation. Hence, just two independents engineering constants are required to get stiffness or compliance matrix.

Since the composite material is made by a combination of matrix and fibre reinforcements, it is considered as heterogeneous and its constitutive equation depends upon the properties of the two components, their volume ratio and the geometry properties of the fibre reinforcement.

Generally, the unidirectional lamina is considered as transversally isotropic material with consideration of a coordinate axis along with yarn longitudinal axis, (Barbero, 2013). While the 2D woven fabric, which has three planes of symmetry, is considered orthotropic if the two in-plane axis of coordinates system coincide the warp and weft yarns main axis. The lamina made of 2D woven fabric is considered as orthotropic material. Regarding the laminate composite made by sacking different laminas with variant orientation, it is considered as anisotropic material. In special case if the staked layers are symmetric about its mid-plane, it becomes monoclinic material. The 3D woven composite with symmetric weave pattern to mid-plane of fabric is considered as orthotropic material.

Consequently, the stress-strain relationship of composite material is essentially related to geometric and material property symmetry of constitutive fibre reinforcement which should be taken into consideration during design and analysis of composite material.

5.2.2. Coordinate transformation

In the analysis of composite material, it is often required to know the material properties out of the principal coordinate (called “off-axis properties”). Therefore, the coordinate transformation approach of stress, strain and stiffness constants between local and global coordinates, have to be explored here. Also, as the manufactured composite material is an heterogeneous (resin and yarns oriented in different orientation), this approach it is required to transform the stress and strain in an element of the structure referred to the local coordinate system of this element to the global coordinate system of the structure and vice versa.

By considering local coordinate system with unit vectors (e'_i) and global coordinate system with unit vectors (e_j), the local stress σ' is obtained from global stress σ by (5.6), (Brabero, 2013).

$$\sigma'_{ij} = a_{ip}a_{jq}\sigma_{pq} \quad (5.6)$$

Where $[a]$ is the transformation matrix of the unit vectors composed of cosines of the angle between unit vectors (e_j) and (e'_i).

$$a_{ij} = \cos(e'_i, e_j) \quad (5.7)$$

The (5.6) could be rewritten (5.8) in contracted notation by 6x6 coordinate transformation matrix $[T]$ written as (5.9) and it could be obtained by a logarithm scribed by Brabero (2013) on *Matlab* software.

$$\sigma'_\alpha = T_{\alpha\beta}\sigma_\beta \quad \alpha, \beta = 1, 2, \dots, 6 \quad (5.8)$$

$$[T] = \begin{bmatrix} a_{11}^2 & a_{12}^2 & a_{13}^2 & 2a_{12}a_{13} & 2a_{11}a_{13} & 2a_{11}a_{12} \\ a_{21}^2 & a_{22}^2 & a_{23}^2 & 2a_{22}a_{23} & 2a_{21}a_{23} & 2a_{21}a_{22} \\ a_{31}^2 & a_{32}^2 & a_{33}^2 & 2a_{32}a_{33} & 2a_{31}a_{33} & 2a_{31}a_{32} \\ a_{21}a_{31} & a_{22}a_{32} & a_{23}a_{33} & a_{22}a_{33} + a_{23}a_{32} & a_{21}a_{33} + a_{23}a_{31} & a_{21}a_{32} + a_{22}a_{31} \\ a_{11}a_{31} & a_{21}a_{32} & a_{13}a_{33} & a_{12}a_{33} + a_{13}a_{32} & a_{11}a_{33} + a_{13}a_{31} & a_{11}a_{32} + a_{12}a_{31} \\ a_{11}a_{21} & a_{12}a_{22} & a_{13}a_{23} & a_{12}a_{23} + a_{13}a_{22} & a_{11}a_{23} + a_{13}a_{21} & a_{11}a_{22} + a_{12}a_{21} \end{bmatrix} \quad (5.9)$$

Similarly, the local strain (ε') is obtained from global strain (ε) by 6x6 coordinate transformation matrix $[T]$ (5.10)

$$\varepsilon'_\alpha = T_{\alpha\beta}\varepsilon_\beta \quad \alpha, \beta = 1, 2, \dots, 6 \quad (5.10)$$

To obtain the engineering local strain the equation (5.10) is rewritten (5.11) using $[\bar{T}]$ instead of $[T]$ where $[\bar{T}] = [R][T][R]^{-1}$ and R is obtained as (5.12)

$$\varepsilon'_\alpha = \bar{T}_{\alpha\beta}\varepsilon_\beta \quad (5.11)$$

$$[R] = \begin{bmatrix} 1 & 0 & 0 & 0 & 0 & 0 \\ 0 & 1 & 0 & 0 & 0 & 0 \\ 0 & 0 & 1 & 0 & 0 & 0 \\ 0 & 0 & 0 & 2 & 0 & 0 \\ 0 & 0 & 0 & 0 & 2 & 0 \\ 0 & 0 & 0 & 0 & 0 & 2 \end{bmatrix} \quad (5.12)$$

The stiffness matrix in the global coordinate system is transformed to the local coordinate system by (5.13)

$$[C'] = [T][C][T]^T \quad (5.13)$$

Inversely, the stiffness matrix could be transformed from local coordinate system to global coordinate system by (5.14)

$$[C] = [\bar{T}][C'][\bar{T}]^T \quad (5.14)$$

5.2.3. Homogenisation concept

The homogeneous material consists of one unique phase. It has the same physical and mechanical properties at any point. The heterogeneous material inasmuch as it is composed of more than one phases possessing different physical and mechanical properties, so its properties at any point is in function of the position of this point, (Berthelot, 2005).

In the mechanical analysis, the approach followed to find the mechanical properties of a representative volume element RVE of heterogeneous material as homogeneous one, is called homogenisation technique, (Berthelot, 2005 and Brabero, 2013). Consider a representative volume V of heterogeneous material composed of k phases which are considered as homogeneous linear elastic material and it is subjected to an external displacement or force on its external surface. To obtain the elastic stiffness properties of this volume as homogeneous material, the homogenisation technique is applied. This technique consists in finding the averaged stress $\bar{\sigma}_i$ and averaged strain $\bar{\varepsilon}_i$ over this volume. These averaged stress and strain could be obtained from the global stress σ_i and global strain ε_i at each element or point of this volume by implementing homogenisation formula based on elements volume

$$\bar{\sigma}_i = \frac{1}{V} \int_V (\sigma_i)_k dV \quad i=1, 2, \dots, 6 \quad (5.15)$$

$$\bar{\varepsilon}_i = \frac{1}{V} \int_V (\varepsilon_i)_k dV \quad i=1, 2, \dots, 6 \quad (5.16)$$

Then, the elastic stiffness and compliance matrix (C_{ij}, S_{ij}) of this volume as homogeneous material, could be predicted by

$$\bar{\sigma}_i = C_{ij} \bar{\varepsilon}_j \quad (5.17)$$

$$\bar{\varepsilon}_i = S_{ij} \bar{\sigma}_j \quad (5.18)$$

5.2.4. Micromechanics technique

As it was mentioned in the section (4.2), the composite material is heterogeneous at microscale and at mesoscale. At the microscale (yarns scale), the heterogeneity is resulting from the two constituent phases; fibre and matrix. At mesoscale, the heterogeneity is arisen from the different constituent yarns and matrix. The homogenisation technique is implemented to find the elastic properties of the composite material at these scales. Generally, in the mechanical modelling of composite material when implementing homogenisation technique to predict the elastic properties at one scale the constituent elements are considered as homogeneous material. For example, when implementing homogenisation technique to find the elastic properties of woven composite material at mesoscale, the impregnated yarns are considered as homogeneous material. Thus, the homogenisation approach has to be previously implemented at microscale to find the elastic properties of impregnated yarns as homogeneous material.

At the microscale, different homogenization techniques are developed to estimate the elastic properties of impregnated yarn (matrix plus fibre). In this study, the treated yarns are constituted of continuous parallel filaments as homogeneous material, whereas the yarns constructed from discontinuous fibre (short) yarns are out of the scope of this study. The homogenization techniques at this scale are based on construction of representative volume element (RVE) of this yarn called micromechanics model. Therefore, these homogenization techniques are called micromechanics techniques. The accuracy of obtained results for

elastic modulus is related to the accuracy of micromechanics model and the assumed hypotheses, (Brabero 2010). The developed micromechanics models in the literature are classified into empirical, semi-empirical, analytical and numerical. Only analytical models are outlined in this analysis.

Different analytical micromechanics models are developed in the literature to predict the elastic modulus of the continuous unidirectional fibre reinforced lamina with considering the constituent fibres and matrix as homogeneous material. These models could be also applied to predict the elastic modulus of impregnated yarns, since they are similarly composed of unidirectional continuous parallel filaments surrounded by matrix.

In these models, a RVE is constructed with considering the fibre and the matrix as homogeneous material. The fibre is considered as transversally isotropic material having axis of symmetry along with its longitudinal axis "1" while the matrix is considered as isotropic material. The difference between these models is about the assumptions regarding the fibre cross section shape, fibres arrangement, consideration of fibre/matrix interface (generally, it is assumed that they are perfectly bounded) and RVE size. However, for all models, the computed moduli are in function of the fibre volume fraction relative to total RVE volume.

The basic models in literature that we implemented in this analysis to find the elastic modulus of impregnated yarns, where it is considered as transversally isotropic material are:

Longitudinal modulus

Reuss model (called also the first Rule of Mixture) is often used to predict the longitudinal modulus ($E_1, \nu_{12} = \nu_{13}$) since it provides a good estimation for design use (Gibson, 2007). This model is based on the iso-strain assumption, where the strain in fibre ε_f and in matrix ε_m are assumed the same $\varepsilon_f = \varepsilon_m = \varepsilon_{RVE}$. For a representative volume V of fibre and matrix (with fibre volume fraction ν_f and matrix volume fraction ν_m ; $\nu_f + \nu_m = 1$, no void and matrix and fiber are perfectly bonded) subjected to an external load on its external surface, the averaged stress $\bar{\sigma}_i$ in this volume could be evaluated from the generated stress σ_i at each point of this volume by the equation (5.15). Thereby, the longitudinal modulus of this volume as homogeneous material is computed by

$$E_1 = \nu_f E_{f1} + \nu_m E_m \tag{5.19}$$

$$\nu_{12} = \nu_f \nu_{f12} + \nu_m \nu_{m12} \tag{5.20}$$

Transversal modulus

To predict the transversal modulus ($E_2 = E_3$) Voigt proposed a model (called the second Rule of mixture) based on iso-stress assumption. In this assumption, the elements are assembled in series and the stress in the fibre σ_f and in the matrix σ_m is considered even $\sigma_f = \sigma_m = \sigma_{RVE}$. The average strain in the RVE is computed from the equation (5.16). As a result of this assumption, the transversal modulus could be computed:

$$\frac{1}{E_2} = \frac{\nu_f}{E_{f2}} + \frac{\nu_m}{E_m} \tag{5.21}$$

Similarly, the in-plane shear modulus (G_{12}) could be computed by the assumption of even sheared stress. However, this model does not provide very accurate results due to non-validated equal shear assumption. As well as, for transverse modulus poor accurate value is obtained, (Gibson, 2007). Therefore, Chamis (1984 and 1987) proposed simplified micromechanics equations SME for transverse modulus and shear modulus (E_2, G_{12}). In this model E_2, G_{12} are computed by

$$E_2 = \frac{E_m}{1 - \sqrt{\nu_f(1 - E_m/E_{f2})}} \quad G_{12} = \frac{G_m}{1 - \sqrt{\nu_f(1 - G_m/G_{f2})}} \tag{5.22}$$

Chamis and Caruso (1986) have shown that a good agreement is obtained for the E_2 and G_{12} computed by SME compared to 3D finite elements models. Therefore, this model has been adopted in our analysis to obtain the transverse and shear modulus of impregnated yarns.

5.2.5. Mechanic modelling of woven composite at mesoscale

For woven composite material, different homogenisation techniques are developed at the mesoscale to estimate the macro elastic properties of this multi-phases structure as homogeneous material. Similar to the micromechanics techniques, in the literature it is possible to find different analytical and numerical models developed for a representative volume element RVE of woven composite at the mesoscale. At this scale, the RVE is defined based on the repeated unit of fibre reinforcement architecture.

Recent review papers deal with modelling of the mechanical behaviour of the 3D composite structure, O et al. (2011), Nehme et al. (2011), Hallal et al. (2013), Prodromou et al. (2011)). These papers detail the different models found in the literature, based on analytical models but also on numerical models. These models can be dissociated classically, as presented in the work of Ansar et al. (2011), Nehme et al. (2011), Prodromou et al. (2011), Ivanov (2011), in four categories. The majority, denoted here as analytical models, is based on the Classical Laminate Theory (Ishikawa and Chou (1982), Ko and Chou (1989), Karkkainen and Sankar (2006), Gibson (2007), Mallick (2008)) and orientation averaging techniques, where in the RVE, the constituents are represented as unidirectional segments (straight or curved to take into account the yarn crimp) then iso-strain or iso-stress conditions applied. Another group concerns the finite element models with different levels of detail to represent the yarns where the internal stress/strain fields can be evaluated to estimate the damage in addition to the elastic properties. The accuracy of the proposed models depends, from one side, on the accuracy of constructed geometric model for RVE (treated in the chapter "4") and, on the other side, on the hypotheses assumed through homogenisation approach. The third group is constituted by the inclusion methods, where the elastic properties of a composite can be calculated using a mean field approach based upon the equivalent inclusion theory. The last group is constituted by the approaches based on the cell method, presented in the work of Prodromou et al. (2011) and Ivanov et al. (2011). Related to these papers, a lot of applications concerned the determination, by these models, of the elastic properties of specific 3D-preform, in majority for the 3D-woven interlock (layer-to-layer interlock, through-the-thickness angle interlock or orthogonal interlock weaves) Cox and Dadkhah (1995), Rosario and Liu (2010), Nehme et al. (2011), Karkkainen and Sankar (2006), Buchanan et al. (2010), Stig and Hallstrom (2012), Wu et al. (2002) and Rao et al. (2009)) but also for braided (Li et al. (2010), Byun et al. (1991), Schultz and Garnich (2013) and Fang and Liang (2011)), knitted (Ramakrishna (1997), Huang and Ramakrishna (2000)) and NCF preform Tserpes and Labeas (2009)).

5.2.6. Classical laminate theory

To obtain the stress-strain relationship for a laminate composite material, which is used widely in the industry as structural material, the classical laminate theory CLT was upgraded through the works of many researchers for laminated plate such as Smith 1953, Pister and Dong 1959, Reissner and Stavsky 1961, Stavsky 1964, Lekhnitskii 1968 and Stavsky and Hoff 1969 and through the theory of Timoshenko and Woinowsky-Krieger 1959 for homogeneous and isotropic plates and shells. Now, the general CLT is implemented to define force-displacement equation in the laminate by following the procedure indicated by Whitney 1987 where plane stress state is assumed and interlaminar stresses are neglected. The basic

assumptions of this procedure, for static analysis of a laminate with (x, y, z) coordinated system (where origin of coordinate system is on the middle plane of laminate), are outlined by Gibson 2007 :

1. The plate consists of orthotropic laminae bonded together, with the principal material axes of the orthotropic lamina oriented along arbitrary directions with respect to the xy plane.
2. The thickness of the plate, t , is much smaller than the lengths along the plate edges.
3. The displacements u, v and w are small compared with the plate thickness.
4. The in-plane strains $\varepsilon_x, \varepsilon_y$ and γ_{xy} are small compared with unity.
5. Transverse shear strains γ_{xz} and γ_{yz} are negligible.
6. Tangential displacements u and v are linear functions of the z coordinate.
7. The transverse normal strain ε_z is negligible.
8. Each ply obeys Hook's law.
9. The plate thickness, t , is constant.
10. Transverse shear stresses τ_{xz} and τ_{yz} vanish on the plate surfaces defined by $z = \pm t/2$.

The assumption 5 and 6 accord with the Kirchhoff deformation hypothesis that cross section plane which is normal to natural middle surface remains straight and normal with deformation of the plate. The displacements of any point of plate is expressed according to assumption 6 and 7 as

$$\begin{aligned} u(x, y, z) &= u^0(x, y) - z\phi_x(x, y) \\ v(x, y, z) &= v^0(x, y) - z\phi_y(x, y) \\ w(x, y, z) &= w^0(x, y) \end{aligned} \quad (5.23)$$

Where u^0, v^0 and w^0 are natural middle surface displacements, and ϕ_x, ϕ_y are the rotation angle of deformed cross section plane with respect to initial un-deformed state. According to assumption 5 (refer to assumption that cross section plane will remain normal to middle surface):

$$\begin{aligned} \gamma_{xz} &= -\phi_x + \frac{\partial w}{\partial x} = 0 \text{ so } \phi_x = \frac{\partial w}{\partial x} \\ \gamma_{yz} &= -\phi_y + \frac{\partial w}{\partial y} = 0 \text{ so } \phi_y = \frac{\partial w}{\partial y} \end{aligned} \quad (5.24)$$

Thus governing equation in the laminate for in plane displacements are:

$$\begin{aligned} \varepsilon_x(x, y, z) &= \frac{\partial u_0}{\partial x} - z \frac{\partial^2 w}{\partial x^2} = \varepsilon_x^0(x, y) + zk_x \\ \varepsilon_y(x, y, z) &= \frac{\partial v_0}{\partial y} - z \frac{\partial^2 w}{\partial y^2} = \varepsilon_y^0(x, y) + zk_y \\ \gamma_{xy}(x, y, z) &= \frac{\partial u_0}{\partial y} + \frac{\partial v_0}{\partial x} - 2z \frac{\partial^2 w}{\partial y \partial x} = \gamma_{xy}^0(x, y) + zk_{xy} \end{aligned} \quad (5.25)$$

Where k_x is bending curvature associated with bending of the middle plane in the xz plane and k_y is bending curvature associated with bending of the middle plane in the yz plane. k_{xy} is twisting curvature associated with out-of-plane twisting of the middle surface xy .

The in-plane (associated with the plane xy) stress strain relationship in the lamina k of the laminate could be found by:

$$\begin{Bmatrix} \sigma_x \\ \sigma_y \\ \gamma_{xy} \end{Bmatrix}_k = \begin{bmatrix} \bar{Q}_{11} & \bar{Q}_{12} & \bar{Q}_{16} \\ \bar{Q}_{21} & \bar{Q}_{22} & \bar{Q}_{26} \\ \bar{Q}_{61} & \bar{Q}_{62} & \bar{Q}_{66} \end{bmatrix}_k \begin{Bmatrix} \varepsilon_x^0 + zk_x \\ \varepsilon_y^0 + zk_y \\ \gamma_{xy}^0 + zk_{xy} \end{Bmatrix} \quad (5.26)$$

In the laminate analysis, the forces and moments per unit length are often implied instead of stress in the constitutive equations. The forces and moments per unit length are obtained from the static equilibrium condition:

$$\begin{aligned}
 N_x &= \int_{-t/2}^{t/2} \sigma_x dz = \sum_{k=1}^N \left\{ \int_{z_{k-1}}^{z_k} (\sigma_x)_k dz \right\} \\
 M_x &= \int_{-t/2}^{t/2} \sigma_x z dz = \sum_{k=1}^N \left\{ \int_{z_{k-1}}^{z_k} (\sigma_x)_k z dz \right\}
 \end{aligned} \quad (5.27)$$

Where z_k is the distance from the middle surface of laminate to the outer surface of the lamina k and z_{k-1} is the distance from the middle surface to the inner surface of the lamina k .

By substituting equation (5.25) and (5.26) in (5.27) the constitutive equation of laminate is reformulated using forces and moments per unit length.

$$\begin{aligned}
 A_{ij} &= \int_{-t/2}^{t/2} (\bar{Q}_{ij})_k dz = \sum_{k=1}^N (\bar{Q}_{ij})_k (z_k - z_{k-1}) \\
 B_{ij} &= \int_{-t/2}^{t/2} (\bar{Q}_{ij})_k z dz = \frac{1}{2} \sum_{k=1}^N (\bar{Q}_{ij})_k (z_k^2 - z_{k-1}^2) \\
 D_{ij} &= \int_{-t/2}^{t/2} (\bar{Q}_{ij})_k z^2 dz = \frac{1}{3} \sum_{k=1}^N (\bar{Q}_{ij})_k (z_k^3 - z_{k-1}^3)
 \end{aligned} \quad (5.28)$$

$$\begin{Bmatrix} N_x \\ N_y \\ N_{xy} \\ M_x \\ M_y \\ M_{xy} \end{Bmatrix} = \begin{bmatrix} A_{11} & A_{12} & A_{16} & B_{11} & B_{12} & B_{16} \\ A_{21} & A_{22} & A_{26} & B_{21} & B_{22} & B_{26} \\ A_{61} & A_{62} & A_{66} & B_{61} & B_{62} & B_{66} \\ B_{11} & B_{12} & B_{16} & D_{11} & D_{12} & D_{16} \\ B_{21} & B_{22} & B_{26} & D_{21} & D_{22} & D_{26} \\ B_{61} & B_{62} & B_{66} & D_{61} & D_{62} & D_{66} \end{bmatrix} \begin{Bmatrix} \varepsilon_x^0 \\ \varepsilon_y^0 \\ \varepsilon_{xy}^0 \\ k_x \\ k_y \\ k_{xy} \end{Bmatrix} \quad (5.29)$$

Where A_{ij} are the entries of extensional stiffness matrix, D_{ij} are the entries of bending stiffness matrix and B_{ij} are the entries of extensional-bending coupling effect matrix which could be zero depending on material property and geometry symmetry of the laminate.

5.2.7. Interlaminar stresses

The reason of appearance of the interlaminar stresses in the composite material is attributed to the mismatch of Poisson's coefficients and the coefficients of mutual influence between adjacent constitutive components, (Mallick 2007). The coefficients of mutual influence represent the influence of shear stresses on extensional strains and the influence of normal stresses on shear strain. Consider a laminate subjected to uniform uniaxial extension in "x" axis direction, if the constitutive laminas are not bonded, dissimilar transverse strain ε_y is induced (depends on ν_{xy} of laminas) so dissimilar transverse stress σ_y is generated in each lamina. However, since the constitutive laminas are perfectly bonded, the transverse strain is unique throughout the laminate, and in addition to the transverse stress σ_y generated in the laminas, equilibrant interlaminar stress σ_{yz} is induced at laminas interface, Figure 5.1. Similarly, the uneven coefficient of mutual influence $\eta_{xy,x}$ between laminas causes dissimilar shear stress σ_{xy} . However, since the laminas are perfectly bonded that leads to developing even shear stress σ_{xy} throughout the laminate, equilibrium interlaminar shear stress σ_{xz} is induced. Because of the last shear stress σ_{xz} the equilibrium in the Z direction is assured by the moment of normal stress σ_z generated at the interface, Figure 5.1, brought from Mallick (2007).

5. Evaluation the elastic properties of 3D multiaxis woven composite

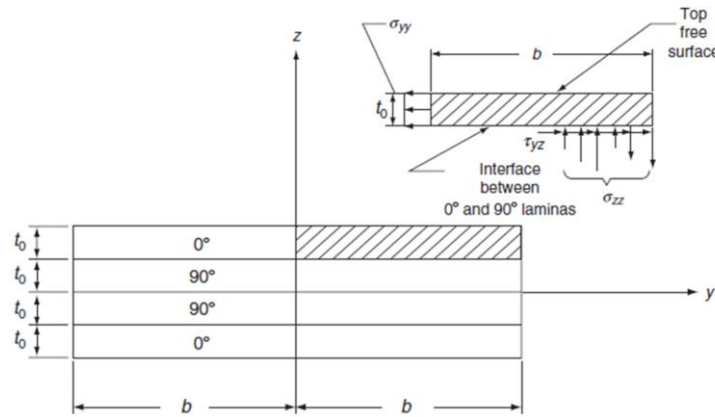


Figure 5.1: the origin of interlaminar stresses (σ_{yz}, σ_{zz}) in cross-ply laminate (Mallick 2007).

In the Classical Laminate Theory, where the plane stress state is assumed, these interlaminar stresses ($\sigma_z, \sigma_{xz}, \sigma_{yz}$) are neglected. This assumption is validated when predicting the in-plane stresses in the interior region far away from geometric discontinuities in a symmetric balanced angle-ply (+/-45°) laminate subjected to uniform axial extension (Gibson, 2007 and Brabero, 2013). However, this plane stress state assumption does not exist at region near to the geometric discontinuities, such as free edge or hole as shown by Pipes and Pagano (1970) based on the 3D elasticity solution. Where the in-plane stresses (σ_y, σ_{xy}) decrease to zero and it is equilibrated by interlaminar stresses which is increasing considerably as approximate to free-edge. That is shown in Figure 5.2 brought from Pipes and Pagano (1970) depicting the evaluation of the gradient of 3D stresses at the interface of two laminas (45 and -45) in function of the distance from laminate centre along with its width (y/b). The existence of the interlaminar stresses near the free-edge could be also proven by the stress equilibrium equations from the theory of elasticity, as outlined by Gibson, 2007.

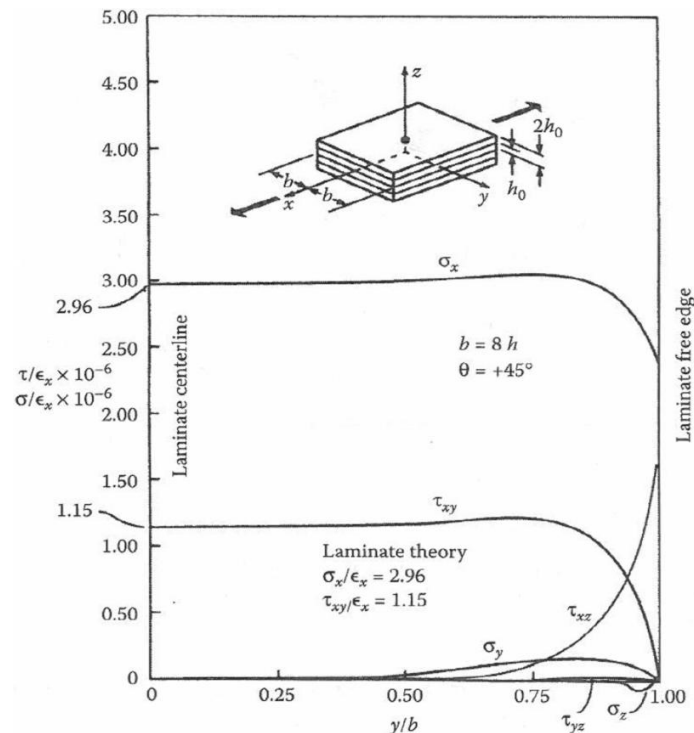


Figure 5.2: the 3D stresses distribution along with the “y” axis at the mid-plane interface of laminate subjected to uniaxial extension in “x” direction, (Pagano and Pipes, 1971).

On the other side, the laminate stacking sequence influences the interlaminar stresses as it has been found analytically and experimentally, (Pipes and Pagano 1971, Whitney and Browning 1972, Whitney and Kim 1977 and Mallick 2007).

As a result of high interlaminar stresses at the geometric discontinuities (free edge) in the composite, the delamination can initiate before the in-plane stresses attain the failure stress predicted by the in-plane failure criteria. Especially that the interlaminar strength is generally less than fibre and matrix strength. Therefore, these stresses should be identified and minimized when design a composite structure.

To evaluate the interlaminar stresses in a composite structure, the 3D stresses distribution should be predicted, which is not possible by CLT method based on plane stress state. Pipes and Pagano (1970) have released this evaluation for angle-ply laminate using the finite difference solution technique. First, the RVE of this laminate with geometry width b is equal to thickness; H is subjected to simple uniform uniaxial extension in the “ x ” axis direction, Figure 5.2. Second, the 3D stresses were predicted in this volume using the finite difference solution technique. Then the interlaminar stresses are evaluated at the interface of two laminas (45 and -45) along with the “ y ” axis, as mentioned earlier in Figure 5.2. It has been found that the interlaminar shear stress σ_{xz} is the largest interlaminar stress at the free-edge ($y=b$) on laminate boundary plane “ y ”. By investigating different laminate geometry (width/thickness), it has been concluded that the region of disturbance is restricted, a width equal to the laminate thickness.

A number of researchers have used other methods to evaluate the interlaminar stresses at the laminate free-edge, as outlined by Tahani and Nosier 2003 and Gibson 2007. The higher-order plate theory by Pagano (1974), the boundary layer theory by Tang and Levy (1975), the perturbation technique by Hsu and Herakovich (1977) and the 3D finite elements by Wang and Crossman (1977) and Whitcomb et al. (1972).

5.3. Methods

5.3.1. Evaluation of elastic modulus of developed 3D mutiaxial woven composite

In order to evaluate the elastic properties of the 3D multiaxis woven composite fabricated using previously developed technology (detailed in the chapter 3), the homogeneous technique is used at meso-scale by developing numerical model using the finite elements. This approach provides more accurate estimation comparing to analytical models regarding estimation the stress/strain field in the structure. It is also low cost comparing to the experimental investigation. In the analytical models such as CLT, the plane stress is assumed and the out-of-plane stresses are neglected. While, the 3D finite element model allows investigating 3D stresses induced at each element of the analysed structure. Thus the interlaminar stresses induced at the free edge and contact interface could be evaluated and located in RVE more accurately by 3D FE modelling, (Gibson, 2007). However, the accuracy of the FEM depends on the accuracy of developed geometric model of this structure and the assumed hypothesis.

In this section, the followed numerical approach is outlined to evaluate the elastic modulus of the sample-5C of 3D multiaxis woven composite. This sample is made of glass and aramid fibre with the manufacture, weaving and geometrical parameters are detailed in the table (3.2, 4.6) and it is impregnated using a VARTM.

Finite element model

For produced 3D multiaxis woven composite samples, a finite element model is constructed based on the geometrical model adapted in the chapter 4, Figure 5.3-a. This model is constructed at the mesoscale for a RVE of this structure inasmuch as periodicity of the fibre woven reinforcement. The yarns and matrix are represented as 3D deformable solid volumes. The same hypotheses of geometrical model (detailed in the section 4.7) are adopted. However, in the geometric model, four possible cross section shapes could be considered for the in-plane yarns: elliptical, cut elliptical, racetrack and rectangular shape. For this FE model only rectangular cross section shape is considered for three following reasons:

1. When considering the rectangular shape, least deviation for FVF computed by the geometric modelling to the measured values is obtained in comparison with the other shape considerations.
2. To simplify the meshing process and to avoid the generation of matrix element with zero thickness at yarn/yarn contact zone like in the case of elliptical and cut-elliptical cross section shape.
3. Representation of the yarn/yarn contact zone is more accurate with rectangular and racetrack cross section shape configuration where the contact zone is a surface, Figure 5.3-a. Whereas, in the case of elliptical and cut-elliptical consideration the contact zone is line involving add supplementary matrix volume between yarns to avoid zero thickness elements.

Abaqus package is used as FE analysing software. Each yarn of the reinforcement as well as the matrix pocket is imported independently from SolidWorks software, which is used to construct the RVE. Then, parts are assembled to construct the FE model.

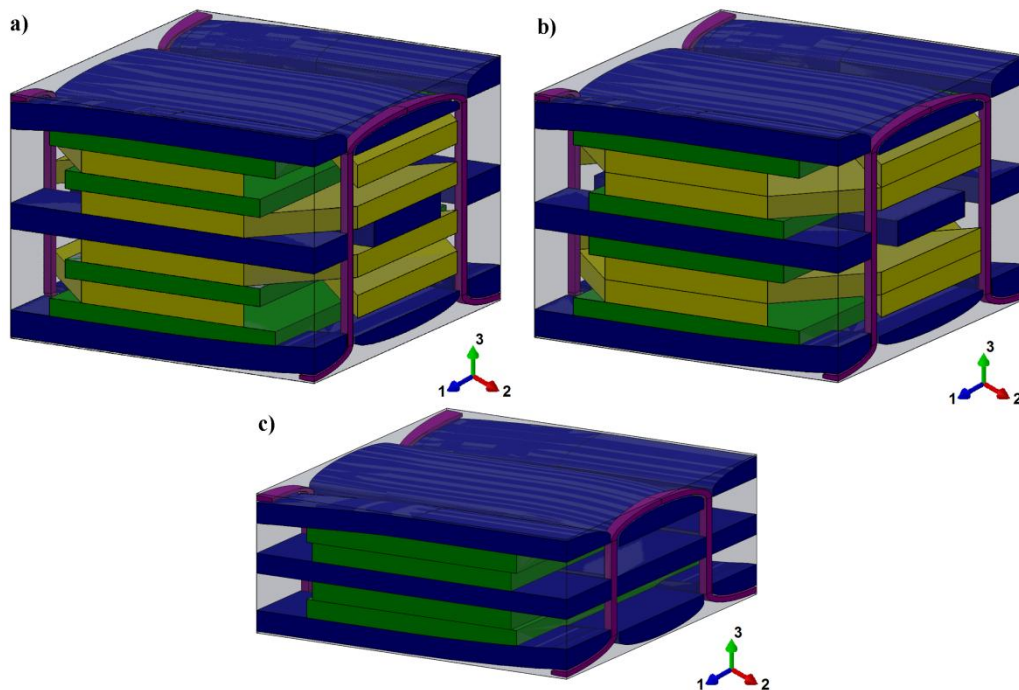


Figure 5.3: 3D volume solid model of RVE of: 3D multiaxis woven composite (a), multiaxis architecture-2 (b), equivalent 3D orthogonal woven composite (c).

Materials stiffness

The yarns are considered as homogeneous transversally isotropic material while the matrix is considered as homogeneous isotropic material. To obtain the elastic modulus of the yarns as homogenous material at mesoscale the micromechanics techniques are implemented. The rule of mixture (5.19, 5.20) and Chamis micromechanics models (5.22) are implemented, as followed by Ivanov et al. (2010) Xu et al. (2013) and Jacques et al. (2014) in the mechanic modelling of 2D woven composite. The E-glass fibre is used for all in-plane yarns while 149 aramid yarns are used for binder yarns. The epoxy resin is used as matrix. The mechanical properties of these materials are listed in the table (5.1). The elastic stiffness matrixes of constituent yarns are computed by micromechanics technique using the packing factor parameter for each yarn instead of fibre volume fraction within yarns. The packing factor values are acquired by the geometrical characterization (3.7.2.6) and optimized for geometric model, table 4.8, as detailed in geometrical modelling approach (4.7.4).

Table 5.1: Elastic modulus of used materials

E-Glass fibre* (isotropic)	E [GPa]	80
	ν	0.22
Aramid-149 fibre* (transversally isotropic)	E_l [GPa]	81.8
	E_t [GPa]	5.10
	G_{lt} [GPa]	1.82
	ν_{lt}	0.31
	ν_{tt}	0.31
Resin Epoxy* (isotropic)	E [GPa]	3.5
	ν	0.35

* Lee M., 1992, Handbook of Composite Reinforcements, ISBN: 978-0-471-18861-2

Parts orientation

Since the yarns are considered as transversally isotropic material, the orientation of each yarn in the structure with respect to the principle longitudinal woven fabric axis (aligned with warp yarn axis) has to be defined. Thus, local coordinate systems $(1', 2', 3')^k$ for each yarn k of the reinforcement are assigned with considering the principle axis $1'$ aligned with longitudinal axis of the yarn. The global coordinate system (1, 2, 3) is defined for the FE model where the “1” axis is aligned with the longitudinal warp yarn axis and the “2” axis is aligned with the longitudinal filler yarn axis. It could be mentioned here for binder yarn, its local coordinate axis “1” follows the path of the yarn centreline with rotation the coordinate system around “2” axis. So the axis “1” of the through the thickness part of binder yarns is aligned with the reinforcement global axis “3” while the axis “1” of the crown part is aligned with the reinforcement global axis “1”, Figure 5.4.

Contact condition

Each yarn in the woven composite structure has contact surface with the adjacent yarns as well as with surrounding matrix. The composite structure contains yarns/yarns contact surfaces and yarn/matrix contact surfaces. These contact surfaces have been indicated and shown in the section (4.7) for the analysed 3D multiaxis woven composite sample. Some researchers, who investigated about the elastic properties of the woven composite structure using the 3D FE method like the followed method in this study, considered a simplification regarding the yarn/yarn contact. This simplification consists of adding supplementary volume of matrix separating the pair surfaces of two yarns in contact, as mentioned in the

5. Evaluation the elastic properties of 3D multiaxis woven composite

work of Nehme et al. (2011), Ivanov et al. (2010) Xu et al. 2013 and Jacques et al. (2014). This has been done in order to simplify the contact condition in the FE model. As a result of this approximation, the FE model includes only yarn/matrix contact surfaces. This additional volume of matrix changes the fibre volume fraction of RVE and that could be recompensed by rectifying the filaments packing factor inside yarns. Xu et al. (2013) modified the packing factor values 18.5% and 16.1% for two analysed 2D woven reinforcement. However, the stress field distribution within the FE model could be affected by this approximation as well as the gradients of interlaminar shear stress generated at the yarn/yarn contact surfaces. Hivet and Boisse (2005, 2008) and Wendling (2014) proposed a consistent 3D geometric modelling for 2D and 3D interlock layer-to-layer woven fabrics. In this modelling approach, the shape of the yarns cross section is defined based on the contact conditions between adjacent yarns and matrix, Figure 4.20-a. That ensures accurate estimation of stress field.

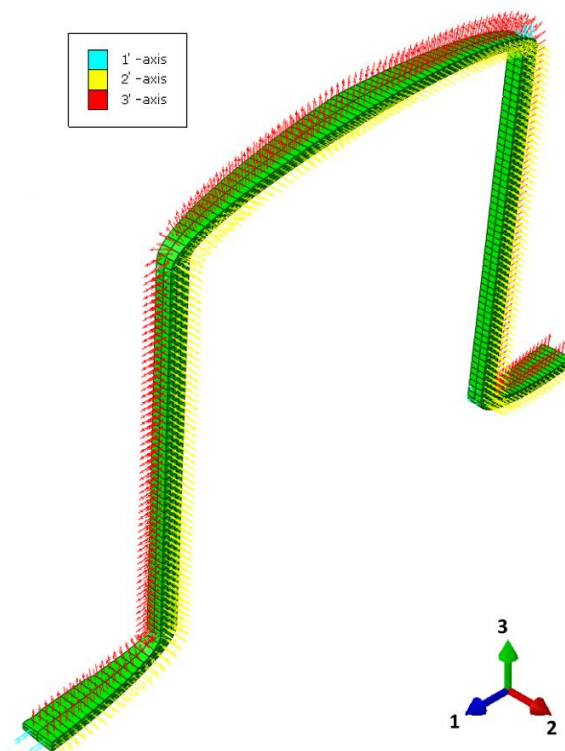


Figure 5.4: Local coordinate system (1^{\wedge} , 2^{\wedge} , 3^{\wedge}) of the binder yarn elements and global coordinate system (1, 2, 3).

The investigation of these interlaminar stresses is necessarily required to be observed in the present analysis as it was previously reported in the section (5.2.7). That is way both the yarn/yarn contact surfaces and yarn/matrix contact surfaces are respected when construction the geometric model for the RVE of 3D multiaxis woven composite. It was mentioned in section 4.7.1, also during the construction the 3D FE model.

The contact pairs between adjacent yarns surfaces and also those between adjacent yarns and matrix surfaces in the FE model are defined. Some yarns surfaces are in contact with more than one adjacent yarns surfaces and/or matrix. Therefore, the surfaces are partitioned to assure that each one belongs to one contact pair, Figure 5.5. In total, 168 contact pairs are defined in the FE model of the analysed multiaxis woven composite.

The cohesive model zone approach developed by Dudgale 1960, Barenblatt 1962, Hillerborg 1976 is applied to investigate delamination failure behaviour of laminated composite and 2D

5. Evaluation the elastic properties of 3D multiaxis woven composite

woven composite. The defined traction-separation formula leads to evaluate crack initiation, crack propagation and matrix-yarns de-bonding. In the FE analysis, either a cohesive element with thin thickness could be created in the contact zone between the contact surfaces pair or the cohesive interaction behaviour, could be assigned to the contact property. However, this approach increases highly the computation cost, especially for the current analysis of 3D solid volume model containing 168 contact pairs. The FE analysis job has been aborted after many attempts for one increment. That is why, in this analysis dedicated to evaluate the linear elastic properties of the present 3D multiaxis woven composite using small extension values (table 5.2), it was assumed that no failure initiates at load level. The surfaces of contact pairs in the FE model are tie constrained. However, when evaluate strength and delamination failure behaviour of this model, the tie constraint could be replaced by the cohesive zone model for contact pair located within concentrated stress zone, which could be determined through the last analysis. This last approach is applied to decrease computation cost as mentioned by Römelt and Cunningham (2012).

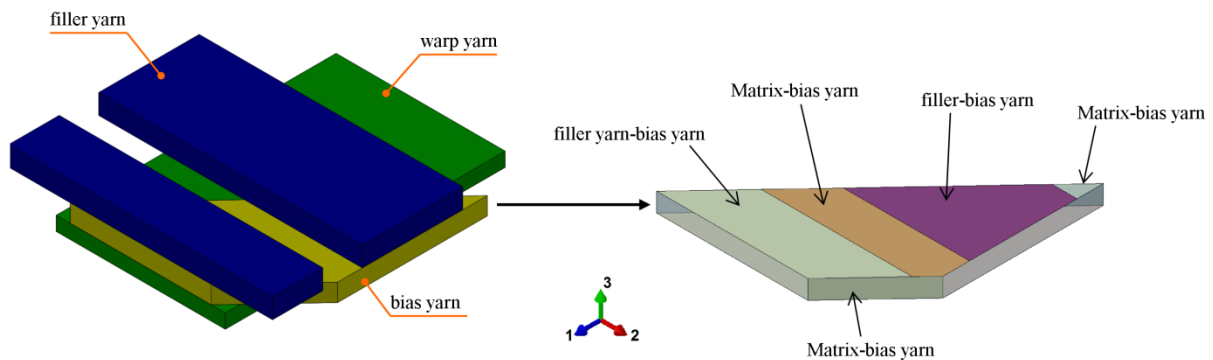


Figure 5.5: Partitioning the upper bias yarn face.

Boundary condition

Due to the material and geometry periodicity of the woven reinforcement, the strain and the stress responses of RVEs of this structure, when it is subjected to external load, are the same in despite of its location in the reinforcement plates, (Karkkainen and Sankar 2006, Barbero 2013). Therefore, in the numerical analysis of such structure using FE method the periodic boundary conditions are implemented as it is reported in the work of (Karkkainen and Sankar 2006, Rao et. al. 2009, Lin et. al. 2011, Nehme et. al. 2011, Römelt and Cunningham, 2012) for evaluating the elastic properties of 2D plain or 3D interlock woven composite. Similarly, regarding the material and geometry periodicity of the treated 3D multiaxis woven composite, the periodic boundary conditions are applied in this analysis in order to evaluate its elastic properties.

Table 5.2: Six boundary condition cases

	Case 1	Case 2	Case 3	Case 4	Case 5	Case 6
$\bar{\epsilon}_1$	1×10^{-3}	0	0	0	0	0
$\bar{\epsilon}_2$	0	1×10^{-3}	0	0	0	0
$\bar{\epsilon}_3$	0	0	1×10^{-3}	0	0	0
$2\bar{\epsilon}_4$	0	0	0	1×10^{-3}	0	0
$2\bar{\epsilon}_5$	0	0	0	0	1×10^{-3}	0
$2\bar{\epsilon}_6$	0	0	0	0	0	1×10^{-3}

5. Evaluation the elastic properties of 3D multiaxis woven composite

In this type of boundary condition, the following constraining equations are applied as reported by Barbero (2013), Miehe C. and Dettmar J., (2004) and Suilc et al. (2000):

$$\begin{aligned} u_i \left(\frac{L_w}{2}, y, z \right) - u_i \left(-\frac{L_w}{2}, y, z \right) &= L_w \varepsilon_{i1}^g \\ u_i \left(x, \frac{L_f}{2}, z \right) - u_i \left(x, -\frac{L_f}{2}, z \right) &= L_f \varepsilon_{i2}^g \\ u_i \left(x, y, \frac{H}{2} \right) - u_i \left(x, y, -\frac{H}{2} \right) &= H \varepsilon_{i3}^g \end{aligned} \quad (5.30)$$

Where u_i ($i=1, 2, 3$) is the displacement of RVE referred to global coordinate system (1, 2, 3), L_w is length of the RVE in warp direction corresponding to "1" global coordinate axis, L_f is length of the RVE in filler direction corresponding to "2" global coordinate axis and H is total thickness of the RVE corresponding to "3" global coordinate axis. ε_{ij}^g is the macro strain of RVE (where it is referred to global coordinate system). The macro strain ε_{ij}^g could be rewritten in contracted subscript (ε_{β}^g) using the contraction rule (5.31) reported by Barbero (2013). This strain is equal to the average strain over the RVE by equation (5.16) ($\varepsilon_{\beta}^g = \bar{\varepsilon}_{\beta}$).

$$\begin{aligned} \varepsilon_{ij}^g &= \varepsilon_{\beta}^g \quad (i, j = 1, 2, 3) \\ \beta &= i \text{ if } i = j \\ \beta &= 9 - i - j \text{ if } i \neq j \end{aligned} \quad (5.31)$$

In order to evaluate the value of stiffness matrix entries of a composite structure, six boundary condition cases are applied. Each BC case leads to predict one column of the stiffness matrix. In each case only one macro strain is equal to 1×10^{-3} whereas all other macro strain are zero, as it is listed in the table 5.2. Thus, the applied displacements at each boundary surfaces for each BC case are reported in table 5.3.

Table 5.3: The applied displacement on each boundary surfaces for each boundary condition cases

		Case 1	Case 2	Case 3	Case 4	Case 5	Case 6
Boundary surface "1"	$u \left(\frac{L_x}{2}, y, z \right) - u \left(-\frac{L_x}{2}, y, z \right)$	$L_x \cdot 10^{-3}$	0	0	0	0	0
	$v \left(\frac{L_x}{2}, y, z \right) - v \left(-\frac{L_x}{2}, y, z \right)$	0	0	0	0	0	$\frac{L_x}{2} \cdot 10^{-3}$
	$w \left(\frac{L_x}{2}, y, z \right) - w \left(-\frac{L_x}{2}, y, z \right)$	0	0	0	$\frac{L_x}{2} \cdot 10^{-3}$	0	0
Boundary surface "2"	$u \left(x, \frac{L_y}{2}, z \right) - u \left(x, -\frac{L_y}{2}, z \right)$	0	0	0	0	0	$\frac{L_y}{2} \cdot 10^{-3}$
	$v \left(x, \frac{L_y}{2}, z \right) - v \left(x, -\frac{L_y}{2}, z \right)$	0	$L_y \cdot 10^{-3}$	0	0	0	0
	$w \left(x, \frac{L_y}{2}, z \right) - w \left(x, -\frac{L_y}{2}, z \right)$	0	0	0	0	$\frac{L_x}{2} \cdot 10^{-3}$	0
Boundary surface "3"	$u \left(x, y, \frac{H}{2} \right) - u \left(x, y, -\frac{H}{2} \right)$	0	0	0	$\frac{H}{2} \cdot 10^{-3}$	0	0
	$v \left(x, y, \frac{H}{2} \right) - v \left(x, y, -\frac{H}{2} \right)$	0	0	0	0	$\frac{H}{2} \cdot 10^{-3}$	0
	$w \left(x, y, \frac{H}{2} \right) - w \left(x, y, -\frac{H}{2} \right)$	0	0	$H \cdot 10^{-3}$	0	0	0

Meshing

The parts of the FE model, which are imported independently to Abaqus CAE, are meshed independently as well. The parts of in-plane yarns are meshed with a 10-node quadratic tetrahedron elements C3D10 type in light of partitioning process executed when surfaces contact pairs are selected as explained in previous section. The element size is 0.3 mm and the mesh is verified where the portion of elements with aspect ratio more than 5 is 0 %. While the parts of binder yarns are meshed with an 8-node linear brick element C3D8 with element size 0.1 to have at least two element in the through thickness of the crown part.

5. Evaluation the elastic properties of 3D multiaxis woven composite

Like the in-plane yarns parts, the matrix part is meshed with a 10-node quadratic tetrahedron elements C3D10. The mesh is also verified where the portion of elements with aspect ratio more than 5 is 1.48 %. The number of elements and nodes is listed in table 5.4.

Table 5.4: Number of elements and nodes for FE models

		Multiaxis	Multiaxis-Inv	Orthogonal
Total number of nodes		395 611	380 222	225 657
Total number of elements	Type: C3D10	234 583	224 865	127 663
	Type: C3D8	2 370	2 388	1 708

Numerical approach to predict elastic modulus

After applying each BC case (table 5.3), the local stresses in each element σ'_β of FE model is computed by FE method with respect to the local coordinate system $(1', 2', 3')^k$ of this element k associated to the orientation of the yarn or the matrix to which this element belong to. The local stress tensor of each element is transformed to global coordinate system of RVE $(1, 2, 3)$ using the inverse of the coordinate transformation equation (5.8 and 5.9).

$$\sigma_\alpha = [T_{\beta\alpha}]^{-1} \sigma'_\beta \quad (5.32)$$

Where, σ_α is the element stress tensor relative to the global coordinate system.

Then, the average stress tensor $\{\bar{\sigma}_\alpha\}$ over the RVE (which represents the macro stress of RVE relative to global coordinate system) is computed by homogenization equation (5.15) with respect to elements volume (V^k) and RVE volume (V^{RVE}). Consequently, the entries value of one column of the stiffness matrix of RVE could be computed by equation (5.1) through applying associated BC case.

For example, after applying the first BC case $\bar{\epsilon}_{11} = \bar{\epsilon}_1 = 1 \times 10^{-3}$ the entries value of the first column $C_{\alpha 1}$ of stiffness matrix could be computed as

$$C_{\alpha 1} = \bar{\sigma}_\alpha / \bar{\epsilon}_1; \quad \bar{\sigma}_\alpha = \frac{1}{V^{RVE}} \int_V \sigma_\alpha (x_1, x_2, x_3) dV = \frac{1}{V^{RVE}} \sum_{k=1}^N \{\sigma_\alpha\}^k V^k \quad (5.33)$$

The compliance matrix [S] is obtained from the stiffness matrix [C] by equation (5.3). Then, the elastic modulus could be computed as following with respect to the global coordinate system of RVE $(1, 2, 3)$:

$$\begin{aligned} E_1 &= \frac{1}{S_{11}}, E_2 = \frac{1}{S_{22}}, E_3 = \frac{1}{S_{33}} \\ \nu_{12} &= -S_{21}E_1, \nu_{13} = -S_{31}E_1, \nu_{23} = -S_{32}E_2 \\ G_{12} &= \frac{1}{S_{66}}, G_{31} = \frac{1}{S_{55}}, G_{23} = \frac{1}{S_{44}} \end{aligned} \quad (5.34)$$

To release this approach a python script is written post-treating the output data base of the FE analysis.

5.3.2. Evaluation of elastic modulus of equivalent orthogonal woven composite

In order to observe the influence of insertion the bias yarns into 3D woven reinforcement regarding geometrical and mechanical elastic properties, the present composite is compared to equivalent 3D woven composite without bias yarns. The equivalent 3D woven architecture is the 3D orthogonal interlock. The similarity architecture features are: first, the binder yarns pass through whole the thickness of the reinforcement for each column of filler yarns, second, there is no interlacement between the in-plane yarns.

5. Evaluation the elastic properties of 3D multiaxis woven composite

The geometric model of RVE of the equivalent 3D orthogonal woven composite is constructed using the same developed geometrical modelling approach introduced in the section (4.7) for the multiaxis woven composite with omitting bias yarns from that model and considering the closed-packing weave configuration in the warp direction. The measured yarn parameters (such as cross section area of warp, filler and binder yarns) and the unit cell dimensions are retained the same. Then, the model and geometric parameters are computed by the geometrical modelling approach. So the geometrical parameters for the equivalent orthogonal structure are as listed in table (5.5) and the model is constructed by SolidWorks CAE software, Figure (5.3-c).

In the next step, in order to evaluate the elastic properties of this equivalent 3D orthogonal woven composite, a FE model of this structure is constructed based on the last geometric model and the same numerical mechanic modelling approach is followed as that for multiaxis 3D woven composite (section 5.3.1).

Table 5.5: Geometric parameters and geometric properties of the RVEs of 3D orthogonal woven composite and 3D multiaxis woven composite.

		Multiaxis	Orthogonal
Composite total thickness	H [mm]	6,99	3,91
Length of warp yarns in the unit cell	L_w [mm]	41,12	41,12
Length of filler yarns in the unit cell	L_f [mm]	58,08	58,08
Length of bias yarns in the unit cell	L_v [mm]	28,24	0
Length of binder yarns in the unit cell	L_b [mm]	23,62	17,45
areal density of the unit cell	S^{uc} [gr/cm²]	0,85	0,58
Total volume of yarns	V_{yarns} [mm³]	434,96	290,53
Volume of unit cell	V^{uc} [mm³]	695	388,81
Fibre volume fraction computed by yarns volume	FVF_volume [%]	62,56	74,72
Fibre volume fraction	FVF_weight [%]	45,47	55,7
rate of warp fibre volume to total fibres	V_{fw} [%]	35,29	51,24
rate of filler fibre volume to total fibres	V_{ff} [%]	32,06	47,96
rate of bias (+/-θ) fibre volume to total fibres	V_{fv} [%]	31,76	0
rate of binder fibre volume to total fibres	V_{fb} [%]	0,89	0,8

5.3.3. Evaluation of elastic modulus of equivalent laminate composite

In order to validate the FE modelling approach used in the present study, the elastic properties of the equivalent laminate is conducted by the analytical method based on the classical laminate theory (section 5.2.6). Regarding that the crimp percentage of the in-plane yarns are quite poor (table 3.5) and that the proportion of binder yarns relative to the total volume of yarns is too low as indicated in the table (5.5) (where the portion of binder in the multiaxis structure and the orthogonal structure is 0.89 % and 0.97% respectively). Thus, the in-plane elastic properties of the present multiaxis woven composite, as well for equivalent orthogonal woven composite (presented in the previous section), should be near to that of equivalent laminate, as determined by Cox (1995).

The followed approach to obtain the equivalent laminate is based on consideration of the same RVE dimensions of multiaxis composite and the same number, orientation and stacking sequence of constitutive layers with omitting the binder yarns and ignoring the waviness of

outer filler yarns path. The thickness of each lamina h_k is identical to the thickness of associated yarn (whose this lamina represents) in the multiaxis composite FE model. Therefore, the volume v_k of lamina k is equal to

$$v_k = L_w L_f h_k \quad (k=w, fo, fi, -\theta, +\theta) \quad (5.35)$$

Where w is warp yarns lamina, fo is outer filler yarns lamina, fi is inner filler yarns lamina, $-/+ \theta$ is bias $+/-\theta$ yarns lamina.

The volume fraction of fibre in each lamina is deduced from:

$$FVF_k [\%] = \frac{v_{filament}}{v_k} 100 = \frac{P f_k v_{yarn-k}}{v_k} 100 \quad (5.36)$$

Where v_{yarn-k} is the volume of yarn k in the FE model and $P f_k$ is the packing factor of yarn k obtained from table (4.).

The stiffness matrix of each lamina $[C']^k$ with respect to the local coordinate system of this lamina associated to that of the corresponding yarn is deduced based on the analytical micromechanics model (5.19, 5.20, 5.22). Then, the lamina stiffness matrix is transformed to the global coordinate system of laminate by (5.14) where the transformation matrix [T] is obtained based on the angle between "1" axis of global coordinate system to "1'" axis of local coordinate system.

The general classical laminate theory is implemented to deduce the $\begin{bmatrix} A & B \\ B & D \end{bmatrix}$ matrix (defining the membrane and bending elastic properties of laminate) by the equation (5.28). Then the in-plane stiffness matrix (with considering in-plane stress hypothesis) and the elastic modulus of laminate are obtained from equation (5.37)

$$[C] = \frac{1}{H} [A] \quad (5.37)$$

This approach is scripted by MATLAB software. It is implemented for equivalent 3D orthogonal woven composite and for multiaxis one.

5.3.4. Evaluation of in-plane off-axis properties

To proceed the investigation of the influence of the insertion of the bias yarns into the 3D woven reinforcement, the in-plane off-axis properties of the developed 3D multiaxis woven composite is predicted and compared to that of the equivalent 3D orthogonal woven composite. This investigation is performed using the equivalent laminate models. Where the analytical approach is implemented to predict the variation of the Young's tensile modulus (E_1) and shear modulus (G_{12}) of equivalent laminate in function of the angle, denoted α , between the extension axis "x" and the "1" global axis of laminate (correspond to warp yarn axis) as illustrated in Figure 5.6.

$$E_x = f_1(\alpha), G_{xy} = f_2(\alpha) \quad (5.38)$$

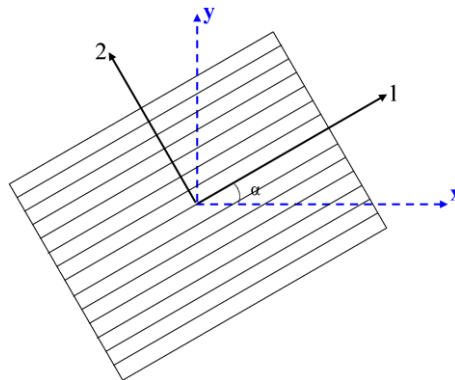


Figure 5.6: Illustration of transformation angle (α).

The approach is based on coordinate transformation concept. The stiffness matrix of laminates is transformed by equations (5.13) with variation of angle (α). Where, this angle represents the transformation angle of global coordinate system (1, 2, 3) to the coordinate system (x, y, z). And the transformation is occurred in the 1-2 plane and the axis “z” aligned with the axis “3” which is rotation axis. The equation (5.13) could be rewritten in function of α as

$$\begin{aligned}
 C'_{11} &= C_{11}\cos^4(\alpha) + C_{22}\sin^4(\alpha) + 2(C_{12} + 2C_{66})\sin^2(\alpha)\cos^2(\alpha) \\
 C'_{12} &= (C_{11} + C_{22} - 4C_{66})\sin^2(\alpha)\cos^2(\alpha) + C_{12}(\sin^4(\alpha) + \cos^4(\alpha)) \\
 C'_{22} &= C_{11}\sin^4(\alpha) + C_{22}\cos^4(\alpha) + 2(C_{12} + 2C_{66})\sin^2(\alpha)\cos^2(\alpha) \\
 C'_{16} &= (C_{11} - C_{12} - 2C_{66})\sin(\alpha)\cos^3(\alpha) - (C_{22} - C_{12} - 2C_{66})\sin^3(\alpha)\cos(\alpha) \\
 C'_{26} &= (C_{11} - C_{12} - 2C_{66})\sin^3(\alpha)\cos(\alpha) - (C_{22} - C_{12} - 2C_{66})\sin(\alpha)\cos^3(\alpha) \\
 C'_{66} &= (C_{11} + C_{22} - 2C_{12} - 2C_{66})\sin^2(\alpha)\cos^2(\alpha) + C_{66}(\sin^4(\alpha) + \cos^4(\alpha)) \quad (5.39)
 \end{aligned}$$

Where [C'] is the stiffness matrix of laminate at angle α (x, y, z) coordinate axis and [C] is the stiffness matrix of laminate at (1, 2, 3) coordinate system.

5.3.5. Evaluation of interlaminar stresses

As mentioned earlier in the section (5.2.7), it is necessary, when new textile reinforcement is designed to optimize the layers stacking sequence in the structure. It is done to minimize the gradient of the interlaminar stresses appeared at the geometric discontinuities. The influence of bias yarns layers stacking sequence in multiaxis woven composite on interlaminar stress is evaluated. In addition to the already reported FE model for RVE of multiaxis woven architecture possessing the following yarns layer stacking sequence $[90/0/\theta/0/-\theta/90]_s$, a second FE model is developed with modified yarns-layer stacking sequence $[90/0/\theta/-\theta/0/90]_s$. All developed technologies proposed in the literature to produce 3D multiaxis woven preform containing bias layers in the through-thickness (not only as outer layer) adopted the second architecture without the possibility to produce the first one. Here, the generated interlaminar stresses in structure for both architectures is predicted and compared in order to valorise the solution technology proposed in this project enabling obtain both architectures.

The RVE of the second architecture of multiaxis woven composite is called “Multiaxis-Inv”. And it is created following the same geometrical modelling approach, as for the first architecture, assuming the same geometrical parameters. The RVE of this architecture is shown in Figure 5.3-b.

The investigation about interlaminar stresses is performed following the same approach outlined by Pipes and Pagano (1970) and other researchers. The generated interlaminar stresses on the boundary surface of composite structure issued from applying simple uniform uniaxial extension are predicted. In the present approach, the 3D FE technique is used to predict the 3D stresses distribution in the RVE as in the work of Wang and Crossman (1977) and Whitcomb et al. (1972).

The developed FE models are subjected to simple uniform uniaxial extension in the global “1” axis direction. So the boundary surface “1” is subjected to displacement in “1” axis direction $u\left(\frac{L_x}{2}, y, z\right) - u\left(-\frac{L_x}{2}, y, z\right) = L_x \varepsilon_1$ where, $\varepsilon_1 = 1.10^{-3}$ and it is not constrained in the two other direction; v and w are not equal to zero. As well, the displacements (u, v, w) of

the other boundary surfaces (2, 3) are not constrained neither. The normal and shear stresses ($\sigma_2, \sigma_3, \sigma_4, \sigma_5, \sigma_6$) on the free-edge should then be equal to zero

The evaluation of the generated out of plane stresses ($\sigma_1, \sigma_4, \sigma_5$) at the boundary surface “2” is investigated. Path-2 is defined at a surface passing via the two points $(0, \frac{L_y}{2}, -\frac{H}{2})$ and $(0, \frac{L_y}{2}, +\frac{H}{2})$ and the three stresses are evaluated along with this path. That allows seeing the evaluation of interlaminar stresses through the thickness at the free edge of RVE. Furthermore, that helps to locate at which interface surfaces between yarn layers the interlaminar stress attains the maximum values.

5.4. Results

5.4.1. Elastic modulus

The elastic modulus of two architectures of 3D multiaxis woven composite and that of equivalent 3D orthogonal woven composite have been evaluated at mesoscale using the finite element method and following the outlined approach. The Figure 5.7 shows the displacement magnitude in deformed FE model under 6 applied boundary conditions cases reported in table 5.2.

Further, the extension stiffness, coupling stiffness and bending stiffness matrix of equivalent laminates; Multiaxis, Multiaxis-Inv and orthogonal architectures have been evaluated using the Classical Laminate Theory. The results of this computation are as following:

a- For laminate equivalent to 3D multiaxis woven architecture:

- extensional stiffness matrix

$$[A] = \begin{bmatrix} 160.06 & 36.24 & 0 \\ 36.24 & 153.76 & 0 \\ 0 & 0 & 41.68 \end{bmatrix} GPa.mm$$

- coupling stiffness matrix

$$[B] = \begin{bmatrix} -0.03 & -0.002 & 0 \\ -0.002 & -0.011 & 0 \\ 0 & 0 & -0.004 \end{bmatrix} GPa.mm^2$$

- Bending stiffness matrix

$$[D] = \begin{bmatrix} 616.29 & 117.75 & 24.41 \\ 117.75 & 761.16 & 24.41 \\ 24.41 & 24.41 & 140.99 \end{bmatrix} GPa.mm^3$$

b- For laminate equivalent to 3D multiaxis-Inv woven architecture:

- extensional stiffness matrix

$$[A] = \begin{bmatrix} 160.06 & 36.24 & 0 \\ 36.24 & 153.76 & 0 \\ 0 & 0 & 41.68 \end{bmatrix} GPa.mm$$

- coupling stiffness matrix

$$[B] = \begin{bmatrix} -0.016 & -0.001 & 0 \\ -0.001 & -0.005 & 0 \\ 0 & 0 & -0.002 \end{bmatrix} GPa.mm^2$$

- Bending stiffness matrix

$$[D] = \begin{bmatrix} 573.71 & 124.58 & 16.31 \\ 124.58 & 764.51 & 16.31 \\ 16.31 & 16.31 & 147.08 \end{bmatrix} GPa.mm^3$$

c- For laminate equivalent to 3D orthogonal woven architecture:

5. Evaluation the elastic properties of 3D multiaxis woven composite

- extensional stiffness matrix

$$[A] = \begin{bmatrix} 121.03 & 13.85 & 0 \\ 13.85 & 114.81 & 0 \\ 0 & 0 & 17.832 \end{bmatrix} GPa.mm$$

- coupling stiffness matrix

$$[B] = \begin{bmatrix} 0.278 & 0.02 & 0 \\ 0.02 & 0.094 & 0 \\ 0 & 0 & 0.035 \end{bmatrix} GPa.mm^2$$

- Bending stiffness matrix

$$[D] = \begin{bmatrix} 141.03 & 21.439 & 0 \\ 21.439 & 222.49 & 0 \\ 0 & 0 & 27.364 \end{bmatrix} GPa.mm^3$$

The in-plane elastic moduli of these equivalent laminate structures have been obtained from extensional stiffness matrix $[A]$ from equation (5.37). The elastic modulus of estimated values for these structures (by two methods) are listed in table 5.6 and shown in Figure 5.8, 5.9, 5.10.

Table 5.6: Elastic modulus of multiaxis, multiaxis-Inv and orthogonal architectures of woven composite computed by FE method and that of equivalent laminates computed by CLT. The modulus values are expressed in GPa.

	E_1	E_2	E_3	ν_{21}	ν_{13}	ν_{23}	G_{23}	G_{13}	G_{12}
Multiaxis_by FE model	22,45	22,26	10,15	0,23	0,32	0,32	3,18	3,29	6,22
Multiaxis-Inv_by FE model	22,71	22,23	10,66	0,23	0,31	0,31	3,22	3,34	6,44
Laminate_multiaxis_by CLT	22,02	21,17	-	0,23	-	-	-	-	6,07
Orthogonal_by FE model	26,37	24,66	11,26	0,12	0,34	0,32	3,28	3,88	4,08
Laminate_orthogonal_by CLT	27,90	26,51	-	0,11	-	-	-	-	4,19

The differences in the in-plane elastic moduli (E_1 , E_2 , ν_{21} , G_{12}) of multiaxis computed by FE to those of equivalent laminate computed by CLT are (-1.96%, -5.15%, -0.12%, -2.53%) is determined respectively. While these differences in the in-plane elastic modulus (E_{11} , E_{22} , ν_{21} , G_{12}) for orthogonal by FE to that of equivalent laminate are (5.47%, 6.99%, -1.64%, 2.6%) respectively. These differences could be attributed at first to the approximation when developing equivalent laminates models concerning that the binder yarns have been ignored. Although the ratio of these yarns is too low 0.89 % and 0.97% relative to total fibre volume in multiaxis and orthogonal structure respectively. Second, these differences are higher for G_{12} and E_{22} which may be explained by accuracy of Chamis's analytical approximation model used to compute G_{12} and E_{22} of yarns in FE modelling and that of laminas in CLT. Further, the difference is also referred to the elements size finesse in the FE model obtained by meshing process. The last process was restricted to computation capacity which was increasing as the elements finesse increases. However, the differences are low and it could be concluded that two followed approaches give an acceptable prediction for the magnitude of the elastic modulus of composite structures at mesoscale.

The elastic moduli of multiaxis architecture are compared to those of orthogonal architecture to determine the effects of bias yarns insertion into the 3D woven reinforcement. The differences in the modulus of the multiaxis to that of orthogonal obtained by two approaches (FE and CLT) are listed in table 5.7. The tensile modulus of multiaxis architecture is lower than that of orthogonal. That is resulting from the low portion of fibre in the bias layer. The portion of bias yarns relative to the total fibre volume in the multiaxis structure is 15.97% while the warp and filler yarns portions are 34.89% and 32.85%

5. Evaluation the elastic properties of 3D multiaxis woven composite

respectively. That is noticed also during the construction of equivalent laminates where the FVF of bias lamina is 37.7% while for warp lamina and filler lamina the FVF are 55.9% and 47.6% respectively. The reason of this limitation is attributed to multiaxis woven reinforcement architecture. The bias yarns are maintained in position inside the structure by binder yarns which alternate their up/down position, and which require two filler insertions for one cycle, as explained previously in chapter 3. Consequently, one translation for bias yarns could be carried out per weaving cycle. That involves creating gaps between adjacent bias yarns of the same layer in the preform, Figure 4.33. This gap will be rich resin pocket inside the composite. Thus the portion of bias yarns is lower comparing to other in-planes portion. Contrariwise, the insertion of bias yarns into 3D woven preform leads to increase the in-plane Poisson's coefficient (ν_{21}) about 95.04% and the in-plane shear modulus (G_{12}) about 52.45% by comparing the modulus obtained by FE method, even for this low proportion of bias yarns. Consequently, the multiaxis architecture allows overcoming the poor in-plane shear properties of 3D orthogonal woven preform.

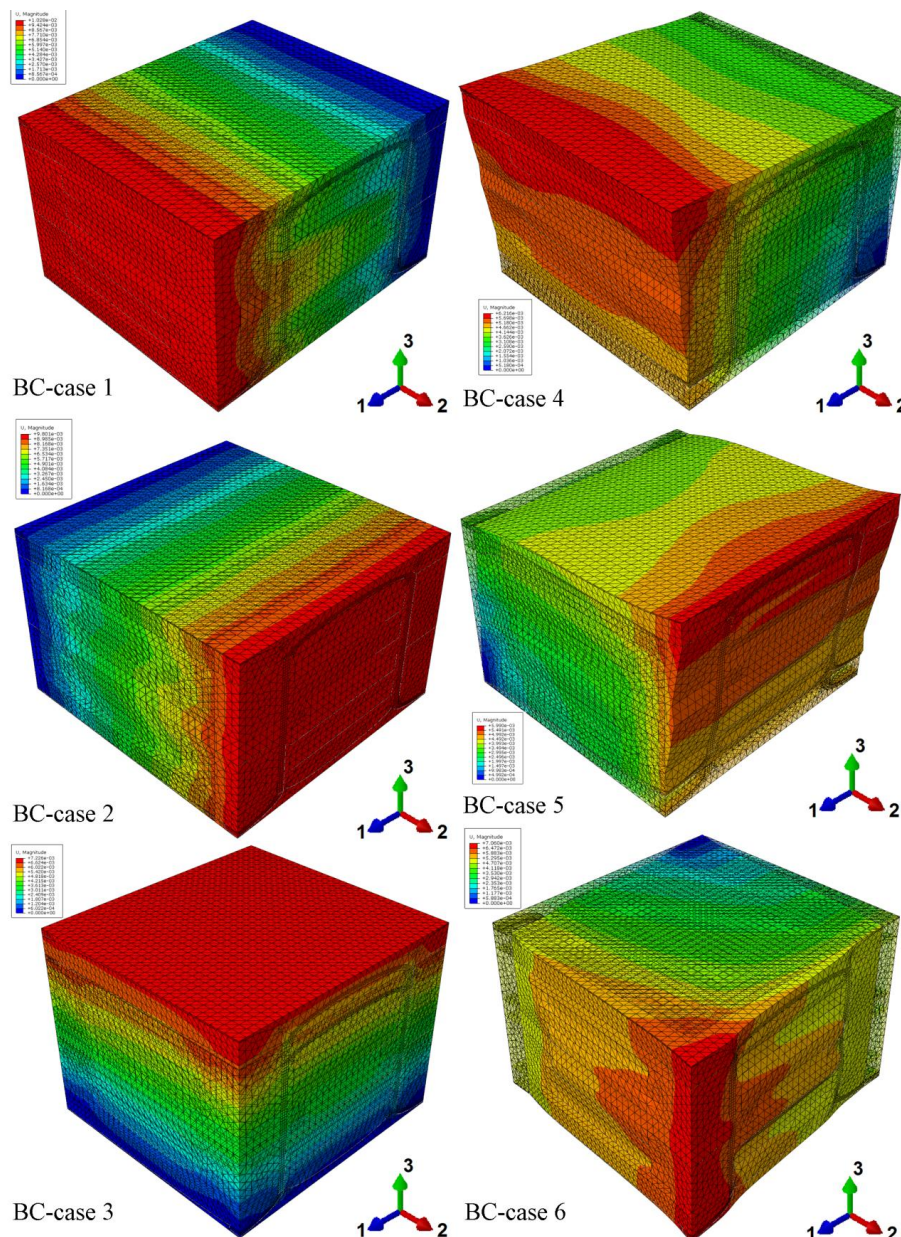


Figure 5.7: Displacement fields in the FE model of 3D multiaxis woven composite under the six BC cases.

5. Evaluation the elastic properties of 3D multiaxis woven composite

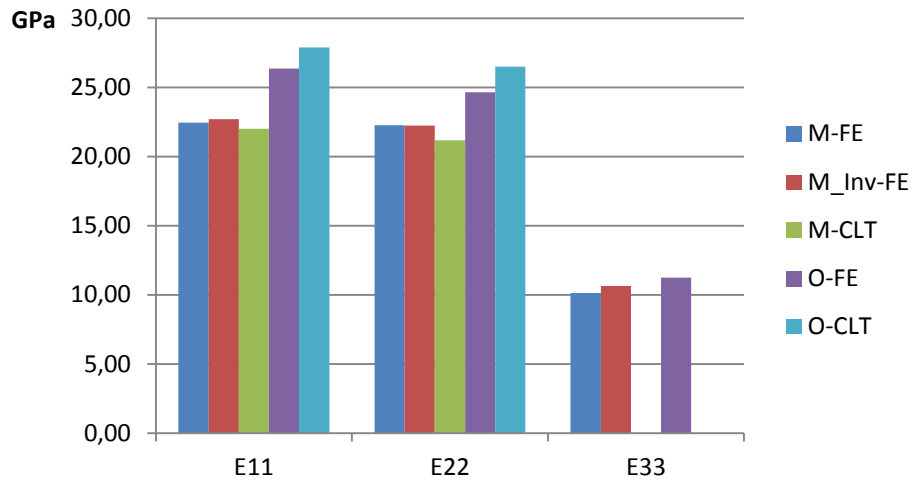


Figure 5.8: Tensile elastic modulus of 3D multiaxis woven composite (noted: M), of 3D multiaxis-Inv woven composite (noted: M_Inv) and 3D orthogonal woven composite (noted: O) using both FE method and CLT.

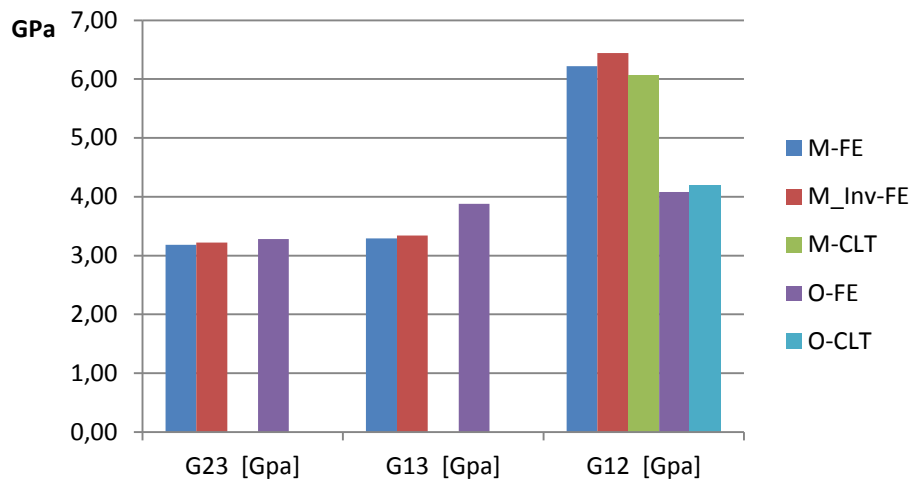


Figure 5.9: Shear elastic modulus of 3D multiaxis woven composite (noted: M), of 3D multiaxis-Inv woven composite (noted: M_Inv) and 3D orthogonal woven composite (noted: O) using both FE method and CLT.

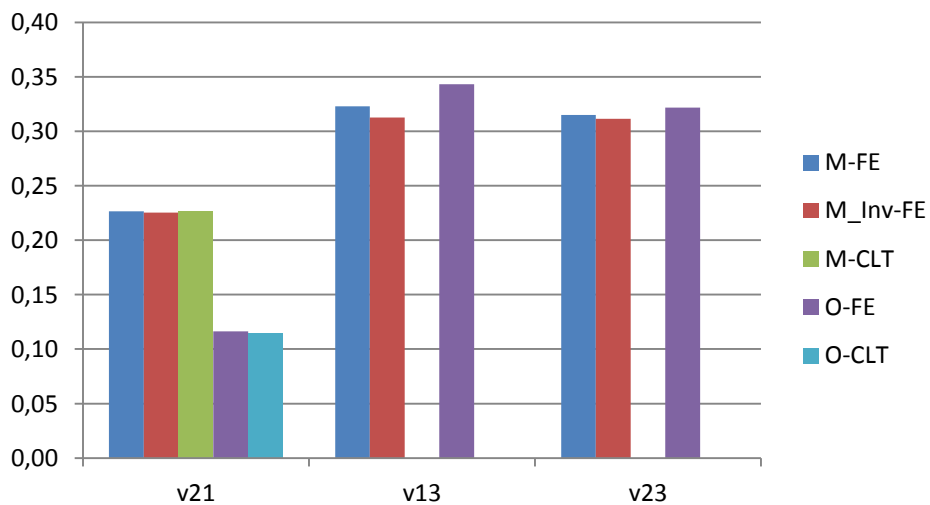


Figure 5.10: Poisson's coefficients of 3D multiaxis woven composite (noted: M), of 3D multiaxis-Inv woven composite (noted: M_Inv) and 3D orthogonal woven composite (noted: O) using both FE method and CLT.

5. Evaluation the elastic properties of 3D multiaxis woven composite

Table 5.7: Difference in the elastic modulus of multiaxis relative to the orthogonal obtained by two methods FE and CLT.

Multiaxis/ orthogonal	Difference [%]								
	in E11	in E22	in E33	in v21	in v13	in v23	in G23	in G13	in G12
By FE	-14,86	-9,72	-9,87	95,04	-5,90	-2,09	-3,05	-15,21	52,45
By CLT	-21,07	-20,14	-	98,01	-	-	-	-	44,83

The extension-bending coupling stiffness matrix of the equivalent laminates obtained by CLT is quasi-zero matrix for the tree structures. That is referred to the material and the geometry symmetry of these structures. By comparing the bending matrix entries of orthogonal to multiaxis ones, an important difference is noted (about 409%, 242% and 415%) for D_{11} , D_{22} and D_{66} respectively. These differences could not only be attributed to the fact that the multiaxis architecture contains bias yarns comparing to orthogonal architecture, but also to the differences in the total thickness between the two composites (for multiaxis $H=6.99$ mm and for orthogonal $H=3.91$ mm). And the bending modulus estimated by the CLT formulas (5.28) is proportional to the cube of layer distance from the mid-plane in the through thickness direction.

On the other side, the influence of the modification of yarn layers sequence (insertion warp yarns layers between two opposite bias layers) carried out by our technology on the bending properties of equivalent laminate could be compared. This modification leads to an increase D_{11} and D_{16} about 7.42% and 49.6% respectively. It leads to decrease D_{12} and D_{66} 5.4% and 4.1%. Thus, there is no significant influence of this modification excepting that it augments the normal-shear bending coupling for about 49.6%, but it is still low $D_{16}=D_{26}=24.41$ GPa.mm³ comparing to normal bending $D_{11}=616.29$ GPa.mm³.

5.4.2. In-plane off-axis properties

The in-plane off-axis properties of both 3D multiaxis woven composite and 3D orthogonal woven composite have been estimated through the evaluation of developed equivalent laminates properties for both architectures. This evaluation is achieved by investigating the variation of the in-plane modulus (E_x , G_{xy}) in function of angle (α) using (5.39) as explained in section 5.3.4. In this case, the angle (α) represents the angle created between the extension axis "x" and the global laminate axis "1" corresponding to the warp yarns axis.

The Figure (5.11) illustrates the variation of E_x and G_{xy} of the both equivalent laminates. It could be noticed the symmetry of the polar diagram referred to the material and geometry symmetry with respect to the planes (13 and 23). Thus, the investigation of the variation for a range $[0^\circ, 45^\circ]$ is sufficient. The critical angle for off-axis modulus values is $\alpha = 45^\circ$ degree.

Both the tensile modulus E_x and the shear modulus G_{xy} of orthogonal architecture shows high variation with the angle (α) comparing to the tensile modulus E_x and shear modulus G_{xy} of multiaxis architecture. The tensile modulus E_x of orthogonal degrades from 27.9 GPa at $\alpha = 0^\circ$ to 13.24 GPa at $\alpha=45^\circ$ (about -52.54%). While, the shear modulus G_{xy} increase from 4.19 GPa at $\alpha = 0^\circ$ to 12.14 GPa at $\alpha=45^\circ$ (about +189%). That is attributed to the absence of the bias in-plane yarns. Whereas, the tensile modulus E_x of multiaxis decreases from 22.02 GPa at $\alpha = 0^\circ$ to 17.03 GPa at $\alpha=45^\circ$ (about -22.6%). While, the shear modulus G_{xy} increase from 6.07 GPa at $\alpha = 0^\circ$ to 8.8 GPa at $\alpha=45^\circ$ (+44.9%). This rate of variation in multiaxis is referred to uneven portions for bias and warp yarns volume relative to the total fibre volume. The

5. Evaluation the elastic properties of 3D multiaxis woven composite

comparison of the variation of E_x and G_{xy} in function of angle α is in a range $[0^\circ, 45^\circ]$ between multiaxis and orthogonal is shown in Figure (5.12).

It could be concluded that in addition to the improvement brought to in-plane shear properties and in-plane Poisson's coefficient to 3D woven composite as result of the insertion of bias yarns. That also leads to reduce the sensibility of interlock woven composite to extension direction. This improvement is related to the portion of bias yarns relative to the total fibre volume in the preform.

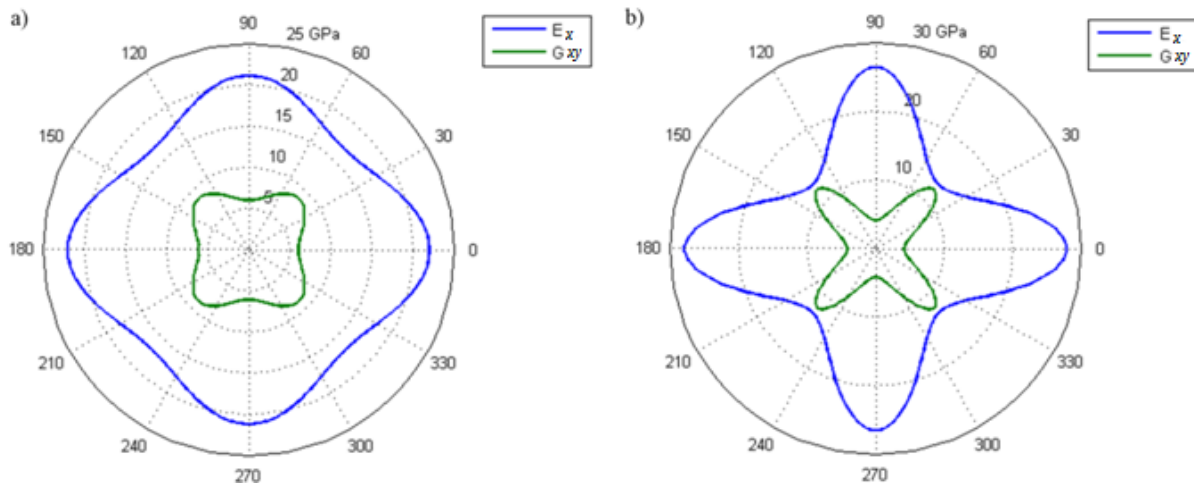


Figure 5.11: Polar representation for variation of the E_x and G_{xy} modulus of equivalent laminate to multiaxis architecture (a) and equivalent laminate to orthogonal architecture orthogonal (b) in function of angle between extension axis and warp yarns axis.

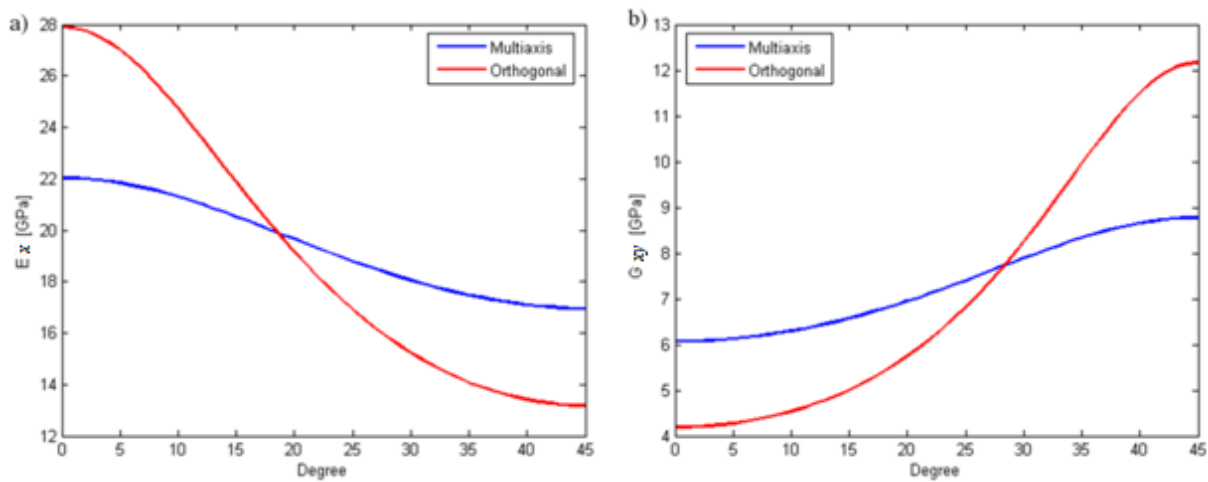


Figure 5.12: Comparison between equivalent laminate to multiaxis architecture and equivalent laminate to orthogonal architecture orthogonal relative to the variation of the tensile modulus E_x (a) and shear modulus G_{xy} (b) in function of angle between extension axis.

5.4.3. Interlaminar stresses

The distribution of the interlaminar stresses ($\sigma_3, \sigma_4, \sigma_5$) along with the path-1 and path-2 for the three FE models; multiaxis woven composite, multiaxis-Inv woven composite and orthogonal woven composite are illustrated in Figure 5.13, 5.14, 5.15 respectively. The mentioned stresses gradients do not represent the tensile and shear strength of samples but the resulting stresses from applying predefined simple extension ($\epsilon_1 = 1 \times 10^{-3}$).

5. Evaluation the elastic properties of 3D multiaxis woven composite

In the table 5.8 the maximum values of the generated interlaminar stresses and their location in three structures along with the two paths after applying the mentioned extension are given. The stresses values are expressed in [MPa]. Further, slash symbol “/” is used to express the interface surface between two components.

The interlaminar stresses generated in the orthogonal architecture have lower values comparing to the two multiaxis architectures. That may be explained by the absence of the bias yarns. In two multiaxis structures on the interface of the bias yarns with adjacent yarns or matrix, the interlaminar stresses get the highest values. The σ_3 is the highest interlaminar stress generated in the orthogonal on the free-edge (boundary surfaces “2”) while the σ_5 , σ_4 stresses could be neglected. However, in the multiaxis-Inv architectures the σ_5 stress gets highest values on the path-2 at the interface of opposite bias yarns while the σ_4 stress could also be neglected face to σ_5 and σ_3 . That agrees with the result of Pipes and Pagano (1970) for angle-ply (45/-45) laminates where the interlaminar stresses are only investigated on the boundary surface “2”. It coincides also with the result of Herakovich (1982), who studied the interlaminar stresses in laminates with different stacking sequence, and found that the σ_{23} stress gets the highest value at (45/-45) interface, Figure 5.14. That is noticed also for multiaxis architecture. Due to the insertion of warp yarn layer between the two opposite layers of bias yarns, the maximum values of σ_{13} shear stress decrease on the boundary surface “2” at warp-bias yarn layers interface for about -55% , Figure 5.13.

Table 5.8: Maximum interlaminar stresses values and its location along path-1 and path-2 for the three structures.

	σ_3 -max		σ_5 -max		σ_4 -max		σ_1 average
	Value	Location	Value	Location	Value	Location	
Multiaxis	4,8	Filler-inner	±3,2	Bias /matrix,	±1,34	bias - θ /filler	22,1
Multiaxis-Inv	-4,97	Bias θ and - θ	±7,22	Bias θ /bias - θ	±0,79	bias - θ /matrix	22,2
Orthogonal	-1,95	matrix	-0,21	binder/matrix	±0,37	filler-inner/matrix	28,7

“/” represents the interface surface between two components. All stress values are expressed in MPa.

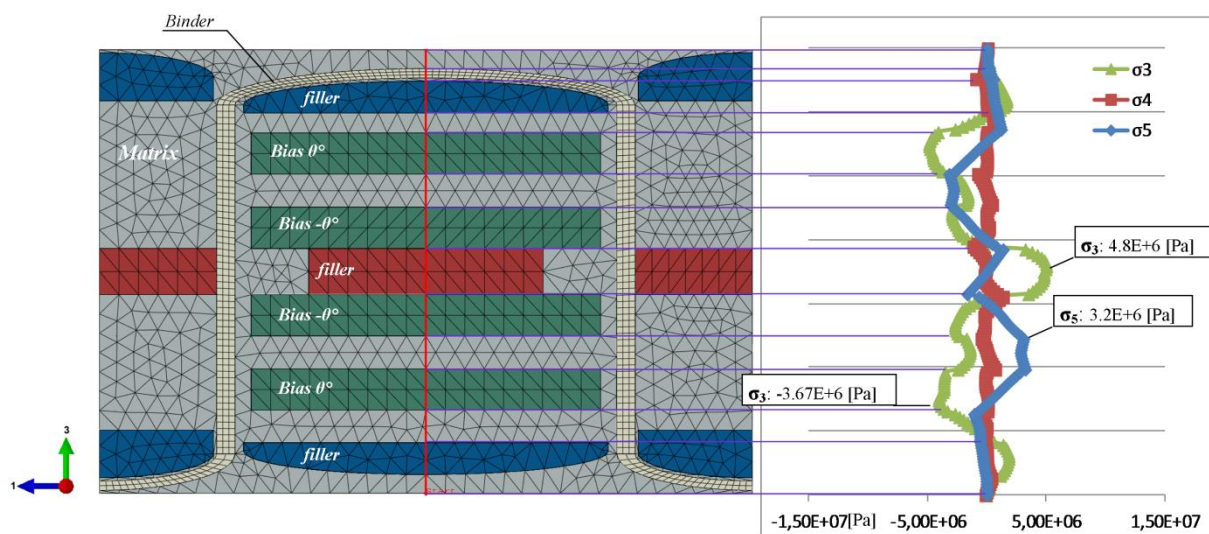


Figure 5.13: Evaluation of caused interlaminar stresses on FE model of multiaxis woven composite along with path-2 after applying uniaxial extension $\epsilon_1 = 1 \times 10^{-3}$.

5. Evaluation the elastic properties of 3D multiaxis woven composite

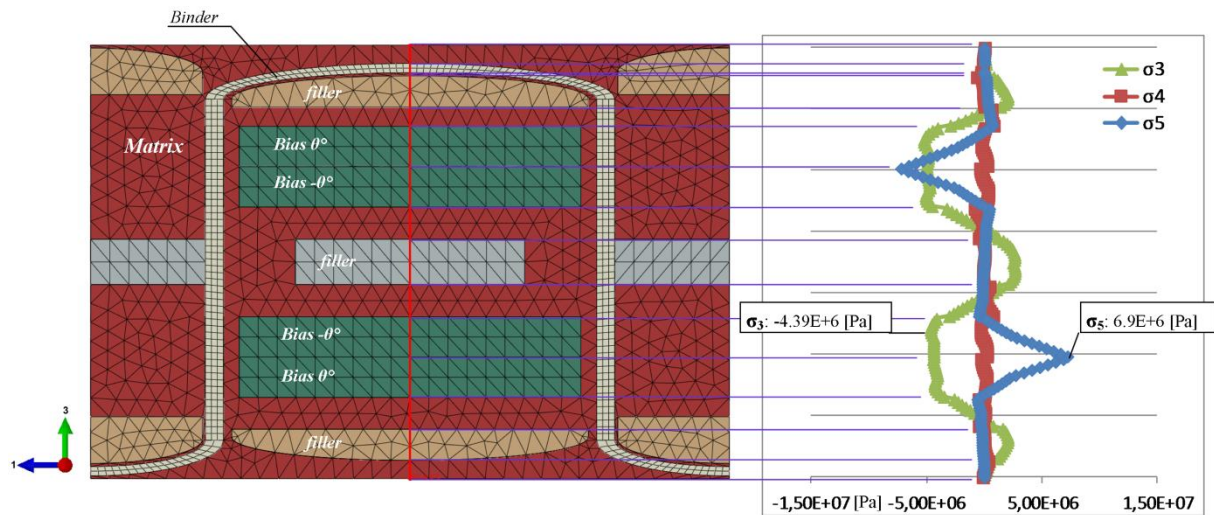


Figure 5.14: Evaluation of caused interlaminar stresses on FE model of multiaxis-Inv woven composite along with path-2 after applying uniaxial extension $\varepsilon_1 = 1 \times 10^{-3}$.

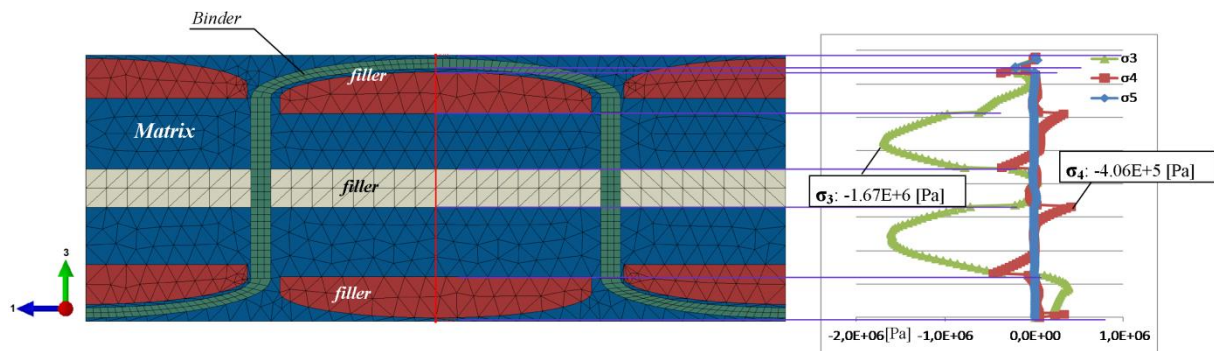


Figure 5.15: Evaluation of caused interlaminar stresses on FE model of orthogonal woven composite along with path-2 after applying uniaxial extension $\varepsilon_1 = 1 \times 10^{-3}$.

5.5.Conclusion

The elastic properties of the developed 3D multiaxis woven composite have been evaluated at mesoscale by 3D finite element method based on earlier developed geometrical model. These properties have also been compared to the properties of orthogonal architecture. The comparison made evident the influence of insertion the bias yarns to the 3D woven reinforcement. Further, two equivalent laminates to multiaxis woven composite and to orthogonal woven composite have been developed. Then the elastic moduli of these equivalent laminates have been evaluated by CLT to get approximate estimation for two woven composites, Cox (1995). This procedure allowed the validation of the 3D FE modelling approach generating acceptable approximate results.

Important improvements are observed, for 3D woven composites concerning the in-plane shear modulus and in-plane Poisson's coefficient, thanks to multiaxis architecture and insertion of bias yarns. However, no effect is brought to the out-of-plane modulus. Also, the reduction of tensile modulus in the multiaxis composite is visible because of the lower portion of bias yarns which could be inserted comparing to warp and filler yarns. This is due to the restriction of proposed architecture and the used technology that should be further improved. Otherwise, the high sensibility of the in-plane modulus of 3D woven composites to the angle between the extension direction and main structure axis, is reduced by the

insertion of bias yarns. That is related to the portion of bias yarns relative to the total fibre volume in the preform.

On the other side, the presence of bias yarns in the 3D woven composite increases the risk of delamination failure at the geometry discontinuities. Thus, higher interlaminar shear stress σ_{13} appeared on the free edge of multiaxis woven composite after applying uniaxial simple uniform extension comparing to the orthogonal composite.

All technological solutions proposed in the literature, as it has been shown in chapter 3, make possible insertion of two opposite biases yarns layers within the woven perform without the possibility to insert warp yarns layer between them. The technology developed in this project makes the separation of two opposite biases yarns layers by warp yarn layer possible. FE models have been developed for two multiaxis architectures, with change the in-plane yarns layers sequence ($[90/0/\theta/-\theta/0/90]_s$ and $[90/0/\theta/0/-\theta/90]_s$) based on the developed geometrical model, in chapter 4. The elastic properties of both multiaxis composite architectures and the influence of this change on the generated interlaminar stresses have been evaluated. No effect of this layers sequence change on the in-plane elastic modulus is observed, but an increase is noted for normal-shear coupling bending stiffness. However, the high interlaminar stresses generated at the bias $+\theta/-\theta$ interfaces decreased considerably by the insertion of warp yarns layer between the two opposite bias yarns layers. That technique also reduces the delamination damage initiation.

6. General conclusion

6.1. Conclusion

The low delamination resistance, poor through the thickness properties and poor toughness of laminates composite material are a result of the absence of the fibre reinforcement in the through the thickness direction of composite structure. Different textile technologies could be used to produce preforms with through the thickness fibre reinforcements. Among these technologies, braiding and weft knitting process are applied to produce 3D complex shape composite products. The weaving and stitching processes are suitable to fabricate flat (planar) 3D composite structure. Although the improvement of through the thickness properties and toughness, an important degradation of the in-plane properties is observed as a result of the microstructure damages induced by textile machinery and the geometry of yarns set up by textile technology. Besides, the woven composites show poor in plane off axis properties and poor in-plane shear properties because of absence of in-plane biases yarns. Further, crimp of in-plane yarns into through the thickness of preform contributes to decrease in-plane properties. On the other side, although, stitching technology has no restriction concerning orientation of in-plane yarns, it causes important microstructure damages to in-plane yarns.

The 3D multiaxis weaving technology is developed to overcome the drawbacks of standard weaving process by enabling aligning in-plane yarns in biases direction in addition to warp and filler yarns with minimization the effect of weaving machinery on fibres. However, this technology is still under development and few works have been realized to characterize the geometry and the mechanical performance of produced preform.

A novel prototype loom has been constructed enabling weave multiaxis multilayer preform. The guide blocks technique was used to control bias yarns position in the weaving zone and achieve the required transversal displacement. The bias yarns should be maintained into position inside the preform by binder yarns and their orientations in $\pm\theta^\circ$ are obtained by controlling number of binder per unit length in warp and weft direction. These two parameters could be controlled by developed loom in order to enable bias yarns orientation could variations. Uniform layers of bias yarns are obtained in means of closed rotative motion of guide blocks inside frames and rotative motion of feeding bobbins since they are mounted on rotative chain. Further, bias layers are edge to edge across fabric width. Symmetric structure regarding layers order is produced relative to mid-plane of structure. As well the number of layers could be controlled on this loom. The present architecture samples are made of 11 in-plane yarn layers. Warp yarns layer could be inserted between two opposite $+\theta^\circ$ and $-\theta^\circ$ bias layers contrary to all other developed multiaxis loom. Controlling bias yarns folding at the fabric edge minimized the fabric width shrinkage. Thus beating of inserted filler yarns is achieved with minimum friction between reed blades and warp and bias yarns.

The delicate fibres, having low flexibility such as glass fiber, could not be used as binder yarns because of the high bending curvature induced by insertion system of the binder yarn. Where, the available gaps between crossing of opposite bias yarns to insert binder needles is too close to bias guide blocks frames resulting in high bending curvature for binder yarns.

The characterizing parameters of the 3D multiaxis woven preform have been defined and classified into three groups: manufacturing, weaving and geometrical parameters. Five samples of the 3D multiaxis woven preform have been produced on the developed loom

with variation of the manufacturing and weaving parameters to evaluate their influence on the geometrical parameters. Further, the geometry of the yarns involving the shape, area and AR of the yarns cross-section and the yarns path inside the structure have also been investigated. The five samples have been analysed in the dry state (after loom). The last sample has been impregnated with resin epoxy using VARTM method, then its geometrical parameters and yarns geometry have been investigated to evaluate the influence of the impregnation process.

Too low crimp percentage has been found for the in-plane yarns of this architecture since there are no interlacements between these yarns. The contact interaction between adjacent yarns governs the yarns cross-section shape and dimensions inside the structure. The cross section area and shape of filler yarns are related inherently to its position relative to binder yarn. Low variation of the yarns cross-section area along its path has been noticed for the five samples. However, the variation of the AR value of the yarns cross section along its path is more important and its related to the yarns gap value. The high yarn gap value causes rearrangement of the yarns inside the structure resulting in high variation of the yarns cross-section shape and AR value. The packing factor of the constituent filaments inside the yarns is inversely proportional to the yarn cross-section area. Regarding the outer filler yarns (on the two outer preform faces) the packing factor value is affected by its position and the tension applied on the binder yarns.

The pressure associated with the impregnation process causes compaction of the preform thickness without remarkable influence on the other unit cell dimensions. That results in increasing the FVF of the impregnated sample relative to dry state about 10%. By using the two computation methods of FVF (FVF-weight and FVF-volume), this increasing in the FVF is attributed to compaction of the yarns cross section thus increasing the packing factor value whereas the yarns gap are slightly affected.

The geometrical modelling approaches developed in the literature for the 3D multiaxis woven preform as well as for the 3D interlock woven preform are explored. They provide a method to develop a predictive model for 3D multiaxis woven preform. This model has been developed before manufacturing the multiaxis samples. It is based on previous researcher's works to give a conception tool serving in design and predicting geometrical parameters (FVF and H) of multiaxis architectures in function of the weaving and manufacturing parameters. This model has been compared with the Buchanan's model (2010-b) developed for the same multiaxis architecture. Better estimation is obtained by present model with respect of the geometric conditions of the structure to avoid the interpenetration between the in-plane yarns.

The predictive model has been verified after the geometrical characterization of the manufactured performs by comparison the geometry of the yarns inside the preform to the assumed geometry. It has been concluded that inaccurate hypotheses have been assumed in the predictive model that affects the estimation of the mechanical properties and performance of this structure obtained by mechanical modelling. Thereby, the predictive geometrical modelling could not be used to construct accurate geometric model serving in the mechanical modelling using the finite element method.

Therefore, more accurate geometrical modelling has been developed with more realistic hypothesis taking into consideration the waviness of the outer filler yarn and the cross section shape variations of the binder yarn along with its path. That leads to avoid the

hypothesis of twofold configuration of the binder yarn. However, the approximation of constant AR value and cross section shape along with yarn path is maintained. The yarns cross section parameters are computed based on the measured values of the yarns cross section area and assuming AR value giving FVF as close as to the measured value. That is realized with respect of the geometrical architecture condition in order to avoid yarns volume interpenetration. In this model different cross section shapes have been considered (ellipse, cut-ellipse, racetrack and rectangular). It has been concluded that racetrack and rectangular shape provide geometrical model with FVF close to the measured value with respecting the yarn/yarn contact. Moreover, it has been observed that there is no interlacement between in-plane yarns in this architecture.

The necessity of RVE construction with less complexity and less numerical cost involves maintaining the approximation of constant AR value and shape of the yarns cross section along with its path. However, in addition the measurement incertitude, that causes an error in the FVF of geometrical model comparing to the measured value. This error could be minimized to zero by varying the packing factor of the in-plane yarns via optimization loop.

The elastic properties of the developed 3D multiaxis woven composite have been evaluated at mesoscale by 3D finite element method based on earlier developed geometrical model. These properties have also been compared to the properties of orthogonal architecture. The comparison made evident the influence of insertion the bias yarns to the 3D woven reinforcement. Further, two equivalent laminates to multiaxis woven composite and to orthogonal woven composite have been developed. Then, the elastic modulus of these equivalent laminates have been evaluated by CLT to get approximate estimation for two woven composites, Cox (1995). This procedure allowed the validation of the 3D FE modelling approach generating acceptable approximate results.

Important improvements are observed, for 3D woven composites concerning the in-plane shear modulus and in-plane Poisson's coefficient, thanks to multiaxis architecture and insertion of bias yarns. However, no effect is brought to the out-of-plane modulus. Also, the reduction of tensile modulus in the multiaxis composite is visible because of the lower portion of bias yarns, which could be inserted comparing to warp, and filler yarns. This is due to the restriction of proposed architecture and the used technology that should be further improved. Otherwise, the high sensibility of the in-plane modulus of 3D woven composites to the angle between the extension direction and main structure axis is reduced by the insertion of bias yarns. That is related to the portion of bias yarns relative to the total fibre volume in the preform.

On the other side, the presence of bias yarns in the 3D woven composite increases the risk of delamination failure at the geometry discontinuities. Thus, higher interlaminar shear stress σ_{13} appeared on the free edge of multiaxis woven composite after applying uniaxial simple uniform extension comparing to the orthogonal composite.

FE models have been developed for two multiaxis architectures, with change the in-plane yarns layers sequence ($[90/0/\theta/-\theta/0/90]_s$ and $[90/0/\theta/0/-\theta/90]_s$) based on the developed geometrical model. The elastic properties of both multiaxis composite architectures and the influence of this change on the generated interlaminar stresses have been evaluated. No effects of this layers sequence change on the in-plane elastic modulus are observed, but an increase is noted for normal-shear coupling bending stiffness. However, the high interlaminar stresses generated at the bias $+\theta/-\theta$ interfaces decreased

considerably by the insertion of warp yarns layer between the two opposite bias yarns layers. That technique also reduces the delamination damage initiation.

6.2. Perspective

The developed prototype loom is not automated that limited the sample production. In future work, this obstacle could be resolved enabling more detailed study of the manufacturing and weaving effect and the impregnation process effect on the geometrical properties of the final composite. Also, manufacturing new samples with other type of fiber like carbon and aramid fiber. On the other side, the fibre volume fraction could be improved by modifying manufacturing and weaving parameters in the aids of the optimized predictive model.

The geometrical model has been developed with the consideration of constant AR value for the yarn cross section along its path inside the structure. The effect of this approximation on the mechanical properties estimation should be evaluated in light of the model complexity and numerical computation cost.

Validation of the mechanical modelling approach by comparing the obtained results with the experimental results is also required. And, the geometrical and mechanical modelling should be optimized to ensure accurate estimation for the mechanical properties. Furthermore, the mechanical modelling approach should be extended to estimate also the strength, failure initiation and failure mechanism of this structure.

As a result of the good in-plane off-axis elastic properties and shear resistance of the 3D multiaxis woven composite comparing to the 3D woven composite, promising potential application for this type of fibre reinforced composite in the protection and construction is expected. That prompts to study the impact damage and ballistic impact behaviour of this architecture.

Reference

- Agrawal S, Singh KK, Sarkar P., 2013, Impact damage on fibre-reinforced polymer matrix composite - A review, *Journal of Composite Material*, vol.: 48(3), p.:317–32.
- Anahara M., Yasui Y., Omori H., 1991, Three-dimensional textile and method of producing the three dimensional textile, European patent : 0-426-878-A1.
- Ansar M, Xinwei W, and Chouwei Z, 2011, Modeling strategies of 3D woven composites: A review. *Composite Structures*, vol.: 93(8), p.: 1947-1963.
- Atas C, Icten BM, Küçük M., 2013, Thickness effect on repeated impact response of woven fabric composite plates. *Composite Part B Eng.* vol.: 49, p.: 80–5.
- Behera B. K. and Hari B. K., 2010, *Woven textile structure: theory and application*. Cambridge: Woodhead Pub.
- Berthelot J.M. and Cole J. M., 1999, *Composite Materials: Mechanical Behavior and Structural Analysis*. Springer-Verlag New York Inc.
- Berthelot, J.M., 2005, *Matériaux Composite*, 4th edition, Lavoisier, Paris, France.
- Bibo G., Hogg P., Backhouse R, Mills a., 1998, Carbon-fibre non-crimp fabric laminates for cost-effective damage-tolerant structures, *journal of Composite Science Technology*, vol.: 58(1), p.: 129–43.
- Bibo GA, Hogg IJ, Kempb M., 1997, mechanical characterization of glass- and composites made with non-crimp fabrics. vol.: 57 p.: 1221-41.
- Bilisk A. K., 2000, multiaxial three dimensional (3D) woven carbon preform, United States patent: 6-129-122.
- Bilisk A. K., 2011, “multiaxis three dimensional woven fabric” chapter of “advances in modern woven fabric technology”, Edited bySavvas Vassiliadis, InTech.
- Bilisk K., 2010, Multiaxis 3D weaving: comparison of developed two weaving methods (tube-rapier weaving versus tube-carrier weaving) and effects of bias yarn path to preform properties, *Fibers and polymers*, vol.: 11(1), p.: 104-114.
- Bilisk K., 2012, Multiaxis three dimensional weaving for composite: A review, *Textile research journal* vol.: 82(7), p.: 724-743.
- Bilisk K., 2013, three-dimensional braiding for composites: A review, *Textile Research Journal*, vol. 83(13), p.: 1414-1436.
- Bilisk A. K., Mohamed M. H., 1994, Multiaxial 3D weaving machine and properties of multiaxial 3D woven carbon/epoxy composites, *Proceeding of American society of composite*, p.: 868-82.
- Bilisk A. K., Mohamed M. H., 2010, Multiaxis three-dimensional (3D) flat woven preform-tube carrier weaving, *Textile Research Journal*, vol.: 80(8), p.: 696-711.
- Boisse P., Hivet G., Rocher JE., Vidal Sallé E., and Wendling A. (2010), Modélisation et maillage de la géométrie d'une maille élémentaire de renfort de composite tissé, presentation in GDR MIC n°3371 « Mise en oeuvre des matériaux Composites et propriétés induites ».
- Booth J. E., 1968, *Principle of textile testing*, 3rd edition, Butterworths, England.

- Boussu F., 2011, The use of warp interlock fabric inside textile composite protection against ballistic impact, *Textile Research Journal*, vol.: 81(4), p.: 344-354.
- Brabero E.J., 2010, *Introduction to composite Materials Design-Second edition*, Taylor and Francis, LLC.
- Brabero E.J., 2013, *Finite Element Analysis of Composite Materials Using Abaqus*, Taylor and Francis, LLC.
- Bryn L., Islam M. A., Lowery W. L., Harries H. D., 2004, Three dimensional woven forms with integral bias fibers and bias weaving loom, United States patent: 6-742-547.
- Buchanan S, Grigorash a., Quinn JP, McIlhagger a. T, Young C., 2010-a, Modelling the geometry of the repeat unit cell of three-dimensional weave architectures, *Journal of the Textile Institute*, vol.: 101(7), p.: 679–85.
- Buchanan S, Quinn J, McIlhagger A, Grigorash A, and Archer E., 2010-b, Modeling the geometric characteristics of five-dimensionally woven composites, *Journal of Reinforced Plastics and Composites*, vol.: 29(23), p.: 3475-3479.
- Buchanan S., Grigorash A., Archer E., McIlhagger A., Quinn J., Stewart G. 2010, Analytical elastic stiffness model for 3D woven orthogonal interlock composite, *Journal of Composites Science and Technology*, vol.: 70, p.: 1597–1604
- Byun J.-H., 2000, the analytical characterization of 2-d braided textile composites, *Composites Science and Technology*, vol.: 60(5), p.: 705-716.
- Byun J.-H., Whitney T. J., Du G.W. and Chou T.W., 1991, Analytical characterization of two-step braided composites, *Journal of Composite Materials*, vol.: 25, pp.: 1599-1618.
- Callus PJ, Mouritz a. P, Bannister MK, Leong KH., 1999, Tensile properties and failure mechanisms of 3D woven GRP composites, *Journal of Composite Part A*, vol.: 30(11), p.:1277–87.
- Cartié DDR, Troulis M, Partridge IK., 2006, Delamination of Z-pinned carbon fibre reinforced laminates, *Journal of Composite Science and Technology*, vol.: 66(6), p.: 855–61.
- Caruso J.J. and Chamis C.C. 1986, Assessment of simplified composite micromechanics using three-dimensional finite element analysis, *Journal of Composite Technology and Research*, vol.: 8(3), p.: 77-83.
- Chamis C.C., 1984, Simplified Composite Micromechanics Equations for Hygral, Thermal and Mechanical Properties, *SAMPE Quarterly*, vol.: 15(3), p.: 14-23.
- Chamis C.C., 1987, Simplified Composite Micromechanics Equations for Mechanical, Thermal and moisture-related Properties, in Weeton, J.W., Peters, D.M., Thomas K.L., eds, *Engineer's guide to composite materials*, ASM International Materials Park, OH.
- Chang P, Mouritz AP, Cox BN., 2006, Properties and failure mechanisms of z-pinned laminates in monotonic and cyclic tension. *Composites A*, vol.: 37, p.: 1501–13.
- Chang P, Mouritz AP, Cox BN., 2007, Flexural properties of z-pinned laminates, *Composites A*, vol.: 38, p.: 224–51.
- Chang P, Mouritz AP, Cox BN., 2008, Elevated Temperature Properties of Pinned Composite Lap Joints, *Journal of Composite Material*, vol.: 42(8), p.: 741–69.

- Chen X., Taylor L.W., Tsai L.J., 2011, An overview on fabrication of three-dimensional woven textile preforms for composites, *Textile Research Journal*, vol.: 81(9), p.: 932-944.
- Chou T.W., 1992, *Microstructural design of fiber composites*. Cambridge: Cambridge University Press, pp.382–390.
- Chou, T. W. and Ko, F. K., 1989, *Textile structural composites*. In *Composite Materials Series*, Vol. 3, Elsevier, Amsterdam.
- Cox B. N., Dadkhah M. S., Morris W. L., 1995-a, On the tensile composites failure of 3D woven, *Composite: Part A*, vol.: 27, p.:447–58.
- Cox B. N., Dadkhah M. S., Morris W. L., Flintoff J. G., 1994, Failure mechanisms of 3D woven composites in tension, compression, and bending, *Acta Materialia Material*, vol.: 42(12), p.: 3967-84.
- Cox B.N., Dadkhah M.S, Inman R V, Morris WL, Zupon J, 1992, Mechanisms of Compressive Failure In 3d Composites, *Acta Metal Materials*, vol.:40(12), p.: 3285–98.
- Cox B.N., Dadkhah M.S, Morris WL and Flintoff J.G., 1993, Failure mechanisms of 3D woven composites in tension, compression and bending, *Acta Metall Mater*; vol.: 42, p.: 3967–3984.
- Cox B.N., Dadkhah M.S., 1995-b, The Macroscopic Elasticity of 3D Woven Composites, *Journal of Composite Materials*, vol.: 29(6), p.: 785–819.
- Crandall S.H., Dahl N.C. and Lardner T.J., 1978, *An Introduction to the Mechanics of Solids* (2d ed. with SI units) McGraw-Hill, Inc., New York.
- Curtis P. T., 1988, Crag test methods for the measurement of the engineering properties of fibre reinforced plastics, technical report, Controller HSMO London.
- Curtis PT, Bishop SM., 1984, An assessment of the potential of woven carbon fibre-reinforced plastics for high performance applications. *Composites*, vol.: 15(4), p.: :259–65.
- Du G. w. and Popper P., 1994, Analysis of a circular braiding process for complex shapes, *Journal of the Textile Institute*, vol.: 85(3), p.: 316-337.
- Durville D., 2005, Numerical simulation of entangled materials mechanical properties, *Journal of Materials Science*, vol.: 4, n° 22, p.: 5941-5948.
- Durville D., 2008, Finite element simulation of the mechanical behaviour of textile composites at the meso-scope scale of individual fibres, *Recent Advances in Textile Membranes and Inflatable Structures*, Ed. E. Oñate and B. Kröplin. Springer.
- Edgren et al., 2008, Damage tolerance analysis of NCF composite sandwich panels. *Composites Science and Technology*, vol.: 68, p.: 2635–2645.
- Fang G., Liang J., 2011, A review of numerical modeling of three-dimensional braided textile composites. *Journal of Composite Materials*, vol.:45(23), p.: 2415–2436.
- Farley G. L., 1993, Method and apparatus for weaving a woven angle ply fabric, United State Patent 5,224,519.
- Frain G., Hoschek J. and Kim M.-S., 2002, *Hand book of computer aided geometric design*, Elsevier Science B. V., the Netherlands.
- Fukuta K., Aoki E. and Nagatsuka Y., 1986, 3-D fabrics for structural composites, presented in 15th Textile Research Symposium, Philadelphia, PA.

- Gause L.W. and Alper J.W., 1987, Structural properties of braided graphite epoxy composites, *Journal of Composite Tech. & Res.*, vol.: 9, p.: 141-150.
- Gay D., 1997, *Matériaux composites*, 4^{ème} éd. Paris: Hermès, 672 p. (Matériaux) ISBN 2-86601-586-X.
- Gegauff C, 1907, Strength and elasticity of cotton threads, *Bull Soc Ind Mulhouse*, vol.:77, p.:153-76.
- Gibson R. F., 2007, *Principles of composite material mechanics*, second Edition. USA: Taylor and Francis Group.
- Guenon V.A., Chou T.W. and Gillespie J.W., 1989, Toughness properties of a three-dimensional carbon-epoxy composite, *Journal of Material Science*, vol.:24, p.: 4168-4175.
- Hallal A, Younes R., Fardoun F., Nehme S., 2012, Improved analytical model to predict the effective elastic properties of 2.5 D interlock woven composites, *Composite Structures*, vol.:89(10), p.: 3009-3028.
- Hallal, A., Younes, R., Fardoun, F., 2013, Review and comparative study of analytical modeling for the elastic properties of textile composites, *Composites: Part B*, vol.: 50, P.: 22-31.
- Head A. A., Ko F. K., and Pastore C. M., 1989, *Handbook of Industrial Braiding*, Atkins and Pearce.
- Hearle J.W. S. and Shanahan W. J., 1978, An energy method for calculations in fabric mechanics, *Journal Textile Institute*, vol.:69(4), p.:81–110
- Herakovich C.T., 1982, Influence of layer thickness on the strength of angle-ply laminates, *Journal of Composite Material*, vol.: 16, p.:216-227.
- Hivet G, Boisse P., 2005, Consistent 3D geometrical model of fabric elementary cell, Application to a meshing preprocessor for 3D finite element analysis, *Finite Element Analysis and design*, vol.: 42(1), p.:25–49.
- Hivet G, Boisse P., 2008, Consistent mesoscopic mechanical behaviour model for woven composite reinforcements in biaxial tension, *Composite Part B Eng*, vol.:39(2), p.:345–61.
- Hogg PJ, Ahmadnia A, Guild FJ., 1993, The mechanical properties of non-crimped fabric based composites, *Journal of Composite*, vol.: 24(5), p.:423–32.
- Hsu PW, Herakovich CT., 1977, Edge effects in angle-ply composite laminates. *J Compos Mater*, vol.: 11, p.: 422–428.
- Hu J., 2004, *Structure and mechanics of woven fabrics*, Woodhead publishing limited, Cambridge, England.
- Huang Z. M., Ramakrishna S., 2000, Micromechanical modeling approaches for the stiffness and strength of knitted fabric composites: a review and comparative study, *Composites: Part A*, vol.: 31 p.: 479–501.
- Huang Z-M, Zhang Y, Ramakrishna S., 2001, Modeling of the progressive failure behavior of multilayer knitted fabric-reinforced composite laminates, *Composite Science Technology*, vol.: 61(14), p.: 2033–46.

- Hwang S.J, 1988, Characterisation of the effect of the three dimensional state of stress on damping of laminated composites, PhD. Dissertation Mechanical Engineering Department, University of Idaho
- Ishikawa T and Chou T.W., 1982, Stiffness and strength behaviour of woven fabric composites, *Journal of Material Science*, vol.:17, p.:3211–20.
- Ishikawa T. and Chou T.W., 1982, Elastic behaviour of woven hybrid composites, *Journal of Composite Materials*, vol.: 16(I), p.:2-19.
- Ishikawa T. and Chou T.W., 1983, One-dimensional micromechanical analysis of woven fabric composites, *AZAA Journal*, vol.: 21(12), p.: 1714-1721.
- Ivanov D. S., Ivanov S. G., Lomov S. V., Verpoest I., 2011, Unit cell modelling of textile laminates with arbitrary inter-ply shifts. *Composites Science and Technology*, vol.: 72, p.: 14–20.
- Ivanov D. S., Lomov S. V., Ivanov S. G., & Verpoest I., 2010, Stress distribution in outer and inner plies of textile laminates and novel boundary conditions for unit cell analysis, *Composites Part A: Applied Science and Manufacturing*, 41(4), 571–580.
- Jacques S, De Baere I, Van Paepegem W., 2014, Application of periodic boundary conditions on multiple part finite element meshes for the meso-scale homogenization of textile fabric composites. *Composite Science Technology*, vol.:92, p.:41–54.
- Jones R.M., 1999, *Mechanics of Composite Material Second Edition*, Taylor and Francis, Inc., Philadelphia, PA.
- Kamiya R. et al., 2000, Some recent advances in the fabrication and design of three-dimensional textile preforms : a review, *Knowledge Creation Diffusion Utilization*, vol.: 60, p.: 33-47.
- Karkkainen R.L. and Sankar B. V., 2006, A direct micromechanics method for analysis of failure initiation of plain weave textile composites, *Composites Science and Technology*, vol.: 66(1), p.: 137–150.
- Kassapoglou C., 1990, Determination of interlaminar stresses in composite laminates under combined loads, *Journal of Reinforced Plastic Composite*, vol.: 9(1), p.: 33 –58.
- Kaw A.K., 2006, *Mechanics of composite material*, Taylor & Francis Group, United States of America.
- Kemp A., 1958, An extension of peirce’s cloth geometry to the treatment of nonlinear threads, *Journal Textile Institute*, 49:44–48.
- Ko FK, Chou TW, 1989, *Composite materials series – textile structural composites*, vol.: 3, Amsterdam: Elsevier Science.
- Koh TM, Isa MD, Chang P and Mouritz AP, 2012, Improving the structural properties and damage tolerance of bonded composite joints using z-pins, *Journal of Composite Materials*, vol.: 46, p.: 3255-3265
- Kowalski M., Legrand X., Koncar V., 2010, Conception d’un démonstrateur permettant de tisser une étoffe multicouche et multiaxiale, *Projet de fin d’étude*, ENSAIT.

- Koziol M., 2012, Experimental study on the effect of stitch arrangement on mechanical performance of GFRP laminates manufactured on a basis of stitched performs, *Journal of Composite Materials*, vol.: 46, p.: 1067-1078.
- Koziol M., 2013, Effect of thread tension on mechanical performance of stitched glass fibre-reinforced polymer laminates - experimental study, *Journal of Composite Materials*, vol.: 47, p.: 1919-1930
- Kregers AF, Melbardis YG., 1978, Determination of the deformability of three-dimensional reinforced composites by the stiffness averaging method, *Polymer Mechanics*, vol.:1, p.:25–31
- Labanieh, a. R., Legrand, X., Koncar, V., Soulat, D., 2013, Novel optimization method to estimate the geometrical properties of a multiaxial 3D woven performs, *Journal of Reinforced Plastics and Composites*, vol.: 32, p.: 700-712.
- Lapeyronnie P, Le Grogneq P, Binétruy C, Boussu F., 2011, Homogenization of the elastic behavior of a layer-to-layer angle-interlock composite, *Composite structure* vol.: 93(11), p.: 2795–807.
- Lefebvre M., Boussu F. and Coutellier D., 2013, Influence of high-performance yarns degradation inside three-dimensional warp interlock fabric, *Journal of Industrial Textiles*, vol.: 42, p.: 475-488.
- Lekhnitskii S.G., 1968, Anisotropic plates (translation from the 2nd Russian ed.) in Tsai S.W. and Cheron . eds. Gordon and Breach Science Publishers, New York.
- Leong KH, Lee B, Herszberg I, Bannister MK., 2000, The effect of binder path on the tensile properties and failure of multilayer woven CFRP composites, vol.: 60, p.: 149–56.
- Li D.S., Li J.L., Chen L., Lu Z-X, Fang D-N., 2010, Finite Element Analysis of Mechanical Properties of 3D Four-Directional Rectangular Braided Composites Part 1: Microgeometry and 3D Finite Element Model. *Applied Composite Material*, vol.:17, p.: 373–387.
- Lief E. Asp, and Sicomp AB, 2007, Local models for NCF composite materials mechanical performance prediction , 16th international conference on composite materials, Kyoto, Japon.
- Lima M., Fanguero R., Costa A., Rosiepen C., Rocha V., 2009, Multiweave _a prototype weaving machine for multiaxial technical fabrics, *Indian journal of fibre and textile research*, vol.(34), p.: 59-63.
- Lin H, Zeng X, Sherburn M, Long A C, Clifford M J, 2011, Automated geometric modelling of textile structures. *Textile Research Journal*, vol.: 82(16), p.: 1689-1702.
- Lomov S, Ivanov D, Verpoest I, Zako M, Kurashiki T, Nakai H, et al. ,2007, Meso-FE modelling of textile composites: Road map, data flow and algorithms. *Composite Science Technology*, vol.: 67(9), p.: 1870–91.
- Lomov S, Verpoest I and Robitalle F, 2005, Manufacturing and internal geometry of textiles, in: Woodhead publishing limited, *Design and Manufacture of Textile composites*. P.: 1-61.
- Lomov S. V., Ivanov D.S., Perie G. and Verpoest I., 2008, Modelling 3D fabrics and 3D reinforced composites: challenges and solutions, 1st World conference on 3D Fabrics, Manchester.

- Lomov S., Verpoest I., Robitaille F., 2005, Manufacturing and internal geometry of textiles chapter of Design and manufacture of textile composites Edited by Long A.C., Woodhead Publishing Limited and CRC Press LLC.
- Lomov SV, Huysmans G, Luo Y, Parnas RS, Prodromou a., Verpoest I, and Phelan F.R. ,2001, Textile composites: modelling strategies. Composite Part A. vol.:32(10), p.:1379–94.
- Lucas P., Zanella G., 2007, Mise en oeuvre des composites TP, Compounds à fibres courtes et longues. Techniques de l'ingénieur, AM 5 235, 8.
- Mahadik Y, Brown K a. R, Hallett SR., 2010, Characterisation of 3D woven composite internal architecture and effect of compaction. Composite Part A, Applied Science Manufacture, vol.: 41(7), p.:872–880.
- Mallick P. K., 2007, Fibre reinforced composite material manufacture and design, CRC Press, Taylor & Francis Group.
- McIlhagger R, Quinn JP, McIlhagger a. T, Wilson S, Simpson D, Wenger W., 2007, The influence of binder tow density on the mechanical properties of spatially reinforced composites. Part 1 – Impact resistance. Composite Part A - Applied Science Manufacture, vol.: 38(3), p.:795–801.
- Miehe C. and Dettmar J., 2004, A framework for micro–macro transitions in periodic particle aggregates of granular materials. Computer Method Applied Mechanics and Engineering; vol.: 193, p.: 225–56.
- Mohamed M. H., Bilisk A. K., 1995, Multilayer three-dimensional fabric and method for producing, United states patent: 5-467-760.
- Mood GI., 1996, Multi-axial yarn structure and weaving method, United States patent: 5-540-260.
- Mouritz A. P, Cox BN, 2010, A mechanistic interpretation of the comparative in-plane mechanical properties of 3D woven, stitched and pinned composites. Composite Part A Applied Science Manufacture, vol.: 41(6), p.:709–28.
- Mouritz A. P, Cox BN., 2000, A mechanistic approach to the properties of stitched laminates. Composite Part A, vol.: 31(1), p.: 1–27.
- Mouritz A. P., 2007, Compression properties of z-pinned composite laminates. Composite Science Technology, vol.: 67(15-16), p.:3110–20.
- Mouritz A. P., Bains C, Herszberg I., 1999, Mode I interlaminar fracture toughness properties of advanced textile fiber glass composites. Composite Part A, vol.: 30(7), p.: 859–70.
- Nanayakkara a., Feih S, Mouritz a. P., 2012, Experimental impact damage study of a z-pinned foam core sandwich composite, Journal Sandwich Structure Material, vol.: 14(4), p.: 469–86.
- Nayfeh SA., Rohrs JD., Rifni O. et al., 2006, Bias weaving machine, United State Patent: 7-077-167.
- Nehme S, Hallal a., Fardoun F, Younes R, Hagege B, Aboura Z, et al., 2011, Numerical/analytical methods to evaluate the mechanical behavior of interlock composites. Journal of Composite Material, vol.: 45(16), p.: 1699–716.
- Ogin S. L., 2000, Textile-reinforced composite materials, chapter of Handbook of technical textile edited by Horrocks A. R. Anand S. C., Woodhead publishing Limited, England.

- Padaki N V., Alagirusamy R, Deopura BL, Fanguero R., 2010, Influence of Preform Interlacement on the Low Velocity Impact Behavior of Multilayer Textile Composites. *Journal of Industrial Textiles*, vol.: 40(2), p.: 171–85.
- Pagano N.J. and Pipes R.B., 1971, The influence of stacking sequence on laminate strength, *Journal of Composite Materials*, vol.: 5(1), p.: 50-57.
- Pagano N.J., 1974, On the calculation of interlaminar normal stress in composite laminate. *Journal of Composite Materials*, vol.:8, p.: 65 –81.
- Pandita S.D., Falconet D., Verpoest I., 2002, Impact properties of weft knitted fabric reinforced composites, *Composite Science Technology*, vol.: 62, p.: 1113–1123.
- Peirce F., 1937, The geometry of cloth structure, *Journal Textile Institute*, vol.:28(3), p.:45–96.
- Peters S.T. 1982, *Handbook of composites*, second edition, Chapman & Hall, UK.
- Pipes, R. B., and Pagano, N. J., 1970, interlaminar stresses in composite laminates under uniform axial extension, *Journal of Composite Materials*, vol.: 4, p.: 538-548.
- Pister K.S. and Dong S.B. 1959, Elastic bending of layered plates in proceeding of the American Society of civil Engineers (*Journal of Engineering Mechanics Division*), 85, EM4, p.: 1-10.
- Prodromou A.G., Lomov S.V., Verpoest I., 2011, The method of cells and the mechanical properties of textile composites, *Composite Structures* vol.: 93, p.: 1290–1299.
- Provost B., Boussu F., Coutellier D., Vallee D., Rondot F. and Nussbaum J., 2013, Armouring solutions against high-velocity impact using 2D laminates and 3D warp interlock composites, *Journal of Industrial Textiles*, vol. 43(4), p.:606-626.
- Quinn J, McIlhagger R, McIlhagger A., 2003, A modified system for design and analysis of 3D woven preforms. *Composites Part A: Applied Science and Manufacturing*, vol.:34(6), p.:503–9.
- Ramakrishna S., 1997, Characterization and modeling of the tensile properties of plain weft-knit fabric-reinforced. composites, *Composites Science and Technology*, vol.: 57, p.: 1-22.
- Ramakrishna S., Cuong N. K., Hamada H., 1997, Tensile properties of plain weft knitted glass fiber fabric reinforced epoxy composites, *Journal of reinforced plastics and composites*, vol.: 16(10), p.: 946-966.
- Rao, M.P., Sankar, B.V. & Subhash, G., 2009, Effect of Z-yarns on the stiffness and strength of three-dimensional woven composites, *Composites Part B: Engineering*, vol.: 40(6), p.: 540–551.
- Reissner E. and Stavsky Y, 1961, Bending and stretching of certain types of heterogeneous aeolotropic elastic plates, *Journal of Applied Mechanics*, vol.: 28, p.: 402-408.
- Risicato J.V., Kelly F., Soulat D., Legrand X., Trümper W., Cochrane C., Koncar V., 2014. A Complex Shaped Reinforced Thermoplastic Composite Part Made of Commingled Yarns With Integrated Sensor, *Applied Composite Materials*, doi:10.1007/s10443-014-9400-9
- Robert M. J. 1999, *Mechanics of composite materials*, 2nd ed., Taylor & Francis Group, United States of America.

- Robitaille F., Long A. C., and Rudd C. D., 2002, Geometric modelling of textiles for prediction of composite processing and performance characteristics, *Plastics, Rubber and Composites*, vol.: 31(2), p.:66–75.
- Römelt P. and Cunningham P. R., 2012, A multi-scale finite element approach for modelling damage progression in woven composite structures, *Journal of Composite Structures*, vol.: 94(3), p.: 977–986.
- Rudov-Clark S, Mouritz a. P, Lee L, Bannister MK., 2003, Fiber damage in the manufacture of advanced three-dimensional woven composites, *Composite Part A, Applied Science Manufacture*, vol.: 34(10), p.: 963–70.
- Ruzand JM., Guenot G., 1994, Multiaxial three-dimensional fabric and process for its manufacture, *International patent WO: 94/20658*.
- Rybicki E.F. approximate three dimensional solutions for symmetric laminates under in-plane axial loading, *Journal of Composite Materials*, vol.:5(3), p.: 354-360
- Scardino F., 1989, An introduction to textile structures and their behavior, in: T.W.C.a.F.K.Ko (Ed), *Textile Structural Composites*, p.:1-24.
- Schultz J.A., Garnich M., 2013, Meso-scale and multicontinuum modeling of a triaxial braided textile composite, *Journal of Composite Materials*, vol.: 37(3), p.: 303-314.
- Searles K., Odegard G., and Kumosa M., 2001, Micro- and meso-mechanics of 8-harness satin woven fabric composites: I - evaluation of elastic behaviour, *Composites Part A: Applied Science and Manufacturing*, vol.: 32, p.: 1627–55.
- Seltzer R, González C, Muñoz R, Llorca J, Blanco-Varela T., 2013, X-ray microtomography analysis of the damage micromechanisms in 3D woven composites under low-velocity impact, *Composite Part A Applied Science Manufacture*, vol.: 45, p.: 49–60.
- Sherburn M., 2007, *Geometric and Mechanical Modelling of textiles*, thesis submitted to The University of Nottingham, <http://eprints.nottingham.ac.uk/10303/>.
- Sih G.C. and Skudra A.M., 1986, *Failure mechanics of composites*, New York: Elsevier Science Publishers BV.
- Sluis O. van der, Schreurs P.J.G., Brekelmans W.A.M., Meijer H.E.H., 2000, Overall behaviour of heterogeneous elastoviscoplastic materials: effect of micro-structural modelling, *Mechanics of Material*, vol.: 32, p.: 449-462.
- Smith C.B., 1953, Some new types of orthotropic plates laminated of orthotropic material, *Journal of Applied Mechanics*, vol.:20, p.: 286-288.
- Sokolnikoff I.S., 1956, *Mathematical Theory of Elasticity*, McGraw-Hill, Inc., New York.
- Solden J.A. and Hill B.J., 1998, Conventional weaving of shaped preforms for engineering composites, *Composite Part A*, vol.: 29, p.:757–762.
- Stavsky Y, 1964, on the general theory of heterogeneous aeolotropic plates. *Aeronautical Quarterly*, vol.: 15, p.: 29-38.
- Stavsky Y., and Hoff N.J., 1969, *Mechanics of composite sutures*, in Dietz, A.G.H. ed., *Composite Engineering Laminates*, MIT Press, Cambridge, MA.

- Stickler P., Ramulu M., Johnson P., 2000, Experimental and numerical analysis of transverse stitched T-joints in bending. *Composite Structures*, vol.: 50(1), p.:17–27.
- Stig F., Hallstrom S., 2012, A Modelling Framework for Composites containing 3D Reinforcement. *Composite Structures*, doi: 10.1016/j.compstruct.2012.03.009
- Tahani M., Nosier A., 2003, Edge effects of uniformly loaded cross-ply composite laminates, *Materials and design*, vol.:24, p.:647–658.
- Tan P., Tong L. and Steven G.P., 1997, Modelling for predicting the mechanical properties of textile composites-A review, *Journal of composite part-A*, vol.: 28, p.:903–22.
- Tan P., Tong L., Steven G.P. and Ishikawa T., 2000, Behavior of 3D orthogonal woven CFRP composites Part I, Experimental investigation, *Composite Part A*, vol.: 31, p.: 259–71.
- Tan P., Tong L., Steven G.P. and Ishikawa T., 2000, Behavior of 3D orthogonal woven CFRP composites Part II, FEA and analytical modelling approaches, *composite part A* vol.: 31, p.: 259–71.
- Tang S. and Levy A., 1975, A boundary layer theory-part II: extension of laminated finite strip, *Journal of Composite Material*, vol.: 9, p.: 42 –52.
- The Hong Kong cotton spinner association, 2001, Textile handbook, Hong kong productivity council.
- Timoshenko S.A., Woinowsky –Kreiger S., 1959, theory of plates and shells, 2d ed. McGraw-Hill, Inc, New York.
- Tong L., Mouritz A.P. and Bannister M.K. 2002, 3D fibre reinforced composites, Elsevier Science Ltd. UK.
- Tserpes K.I. and Labeas G.N., 2009, Mesomechanical analysis of non-crimp fabric composite structural parts, *Composite Structures*, vol.: 87, p.: 358-369.
- Uchida H., Yamamoto T., Takashima H., Yamamoto Tet., Nishlyama S., Shinya M., 1999, Three-dimensional weaving machine, United States patent 6-003-563.
- Vallons K., Adolphs G, Lucas P., Lomov S.V. and Verpoest I., 2014, The influence of the stitching pattern on the internal geometry, quasi-static and fatigue mechanical properties of glass fibre non-crimp fabric composites, *Composites: Part A*, vol.: 56, p.: 272–279.
- Vasiliev V.V. and Morozov E.V., 2001, *Mechanics and analysis of composite materials*, Elsevier Science Ltd.
- Wang ASD, Crossman FW., 1977, Some new results on edge effect in symmetric composite laminates. *Journal of Composite Material*, vol.:11, p.:92–106.
- Wang Y., Li J. and Do P. B., 1995, Properties of composite laminates reinforced with e-glass multiaxial non-crimp fabrics, *Journal of Composite Materials*, vol.: 29(17), p.: 2317-2333.
- Wendling a., Hivet G, Vidal-Sallé E, Boisse P., 2014, Consistent geometrical modelling of interlock fabrics, *Finite Element Analysis and Design*, vol.: 90, p.:93–105.
- Whitcomb J.D., Raju I.S. and Goree J.G. 1972, Reliability of the finite element method for calculating free edge stresses in composite laminates, *Composite Structure*, vol.: 15(1), p.: 23 –37.

- Whitney J.M. and Browning C.E., 1972, Free-edge delamination of ensile coupon, *Journal of Composite Materials*, vol.: 6(2), p.: 300-303.
- Whitney J.M. and Kim R.Y., 1977, Effect of stacking sequence on the notched strength of laminated composites, *Composite material: testing and design (Fourth conference) ASTM STP 617*, p.: 229-242.
- Whitney J.M., 1987, *Structural Analysis of laminated Plates*, Technomic Publishing Co., Inc., Lancaster, PA.
- Wu Z., 2009, three-dimensional exact modelling of geometric and mechanical properties of woven composites. *Acta Mechanica Solida Sinica*, The Chinese Society of Theoretical and Applied Mechanics, vol.:22(5), p.:479–486.
- Wu Z.J., Brown D. and Davies J.M., 2002, An analytical modelling technique for predicting the stiffness of 3-D orthotropic laminated fabric composites, *Composite Structures*, vol.: 56, p.: 407–412.
- Xu J, Lomov S V., Verpoest I, Daggumati S, Van Paepegem W, Degrieck J and Olave M., 2013, A progressive damage model of textile composites on meso-scale using finite element method: static damage analysis, *Journal of Composite Material*.
- Yasui Y., Anahara M., Hori F., Mita Y., 1993, Production of three-dimensional woven fabric, *Japanese Patent Publication: 05-106-140*.
- Zako, M., Y. Uetsuji, and T. Kurashiki, 2003, Finite element analysis of damaged woven fabric composite materials, *Composites Science and Technology*, vol.: 63 p.: 507-516.

Appendix A

This appendix is dedicated to present the micrographs captured for the cross sections of the five fabricated samples table 3.2, characterized in the section 3.7, at the specified cut-plane defined in section 3.7.2.1 and Figure 3.40. The averages of the yarn parameters have been measured at each cut-plane also the standard deviation (σ) are presented for each sample. The measured yarn parameters include the area and the two dimensions (the width " l " and the height " h ") of the yarns cross section. Then aspect ratio " $AR=l/h$ " which indicates the change of the cross section shape has been computed. Also, the measured unit cell dimensions, the two in-plane dimensions of the unit cell (L_w and L_f) and the preform thickness (H), are listed. Finally, the geometrical parameters of the manufactured samples are listed in table a.13 computed by the geometrical modeling approach with the consideration of rectangular cross section shape.

Sample-1

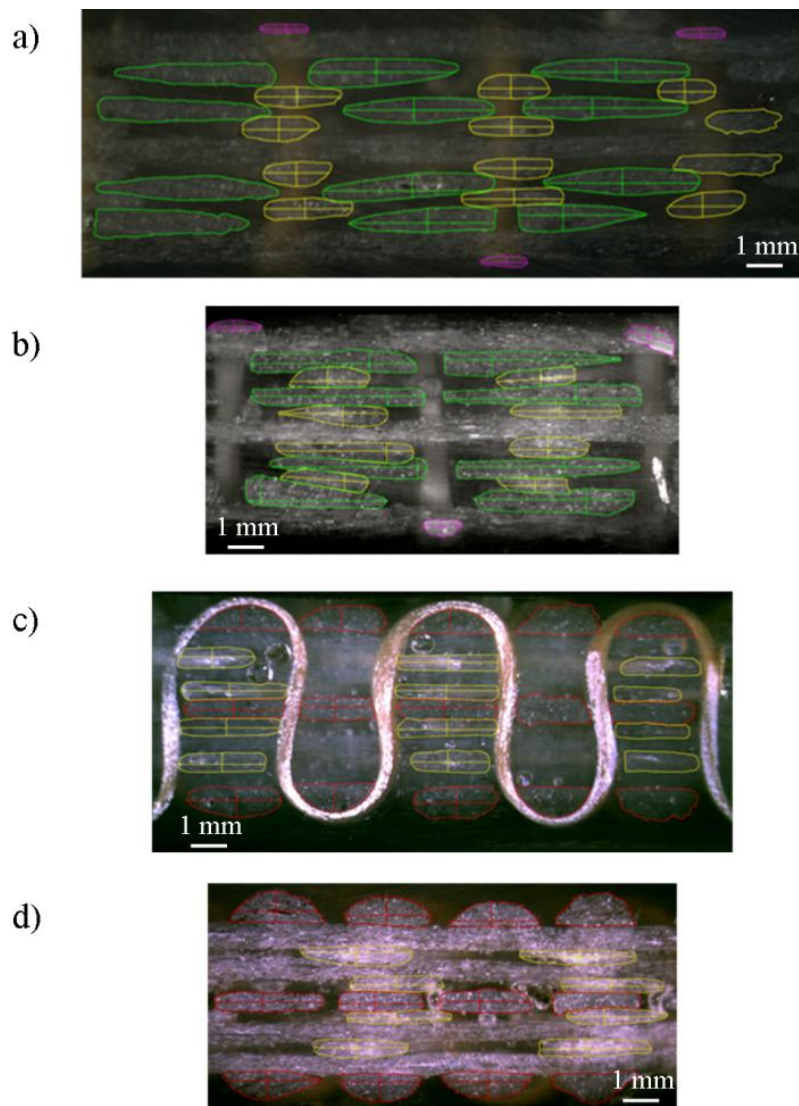


Figure a.1: Micrographs for the cross sections of the sample-1, green outline for warp, red outline for filler, yellow outline for biases and magenta outline for binder. a) at cut plane filler-a, b) at cut plane filler-b, c) at cut plane warp-a, d) at cut plane warp-b.

Appendix A

Table a.1: Mean and standard deviation of the measured parameters (width “l”, thickness “h”, area “S” and aspect ratio “AR”) at each cut plane of sample-1.

Yarn		Cut plane		S [mm ²]	l [mm]	h [mm]	AR	
Filler	outer Z 1	warp-a	average	1,21	2,37	0,65	3,64	
			σ	0,02	0,08	0,00	0,13	
	outer Z 2		average	1,30	2,16	0,82	2,64	
			σ	0,04	0,11	0,05	0,28	
	inner-1		average	1,28	2,74	0,45	6,08	
			σ	0,06	0,01	0,01	0,23	
	inner-2		average	1,299	2,04	0,63	3,24	
			σ	0,12	0,01	0,06	0,29	
	outer free		average	1,72	2,46	0,79	3,15	
			σ	0,24	0,13	0,09	0,25	
	outer		warp-b	average	1,46	2,36	0,74	3,25
				σ	0,26	0,23	0,16	0,58
	inner-1			average	1,29	2,71	0,46	5,80
				σ	0,21	0,39	0,06	0,01
inner-2	average	1,36		2,41	0,64	3,78		
	σ	0,1		0,08	0,06	0,53		
Warp	filler-a	average		2,15	4,03	0,64	6,39	
		σ		0,24	0,35	0,05	0,96	
	filler-b	average		1,99	4,03	0,55	7,47	
		σ		0,13	0,37	0,07	1,37	
Biases	warp-a	average		0,69	1,54	0,47	3,39	
		σ		0,09	0,16	0,08	0,96	
	warp-b	average		0,71	1,25	0,42	4,62	
		σ		0,09	0,25	0,06	0,83	
	filler-a	average	0,74	1,51	0,56	2,77		
		σ	0,07	0,25	0,07	0,88		
	filler-b	average	0,71	1,67	0,46	3,76		
		σ	0,07	0,19	0,06	0,89		
	Binder	filler-a	average	0,27	1,27	0,23	5,68	
			σ	0,02	0,05	0,04	1,11	

Table a.2: Preform thickness and the two unit cell dimensions measured for the sample-1 on four cut-planes

	H [mm]		L _w [mm]		L _f [mm]	
	Average	σ	Average	σ	Average	σ
warp-a	6,07	0,06			6,06	0,17
warp-b	5,72	0,19			6,21	0,40
filler-a	6,36	0,03	5,80	0,26		
filler-b	5,60	0,10	5,66	0,39		

Sample-2

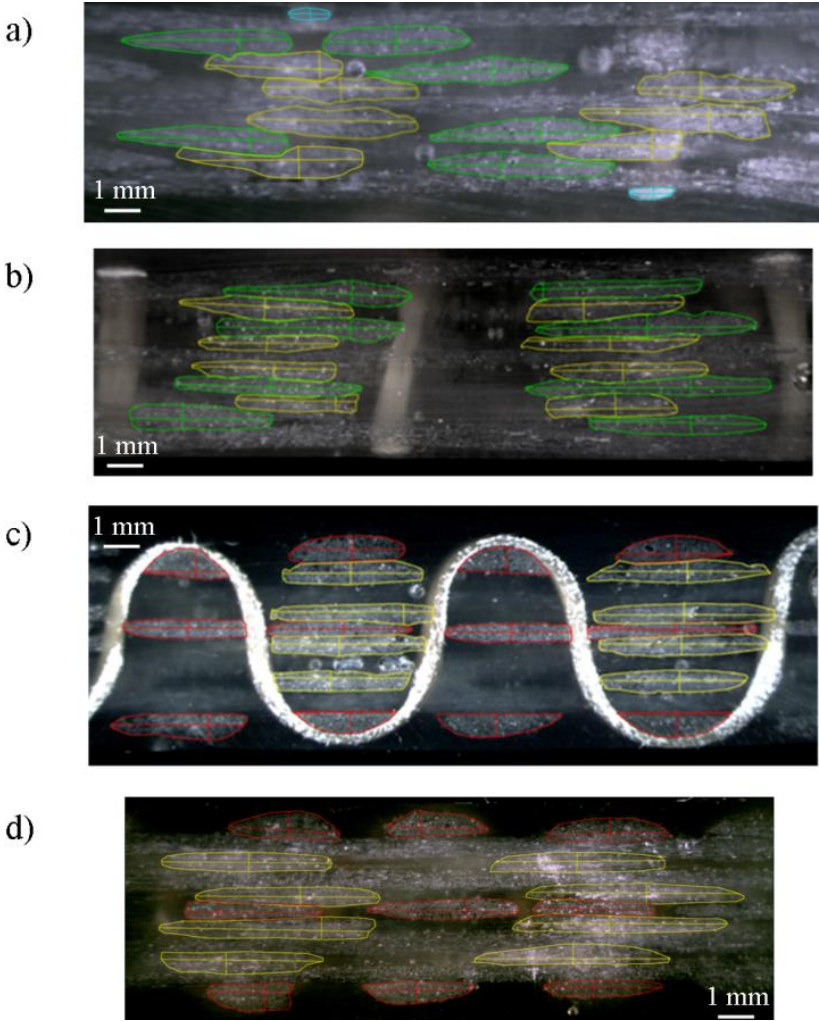


Figure a.2: Micrographs for the cross sections of the sample-2, green outline for warp, red outline for filler, yellow outline for biases and magenta outline for binder, a) at cut plane filler-a, b) at cut plane filler-b, c) at cut plane warp-a, d) at cut plane warp-b.

Table a.3: Mean and standard deviation of the measured parameters (width “l”, thickness “h”, area “S” and aspect ratio “AR”) at each cut plane of sample-2.

Yarn		Cut plane		S [mm ²]	l [mm]	h [mm]	AR	
Filler	outer Z 1	warp-a	average	1,30	2,92	0,65	4,51	
			σ	0,22	0,19	0,05	0,04	
	outer Z 2		average	1,25	2,34	0,76	3,07	
			σ	0,01	0,17	0,02	0,32	
	inner-1		average	1,48	4,24	0,39	11,31	
			σ	0,10	0,48	0,09	3,71	
	inner-2		average	1,53	3,38	0,48	7,09	
			σ	0,01	0,05	0,01	0,00	
	outer free		average	1,77	3,20	0,66	4,88	
			σ	0,21	0,30	0,04	0,60	
	outer		warp-b	average	1,44	2,73	0,64	4,33
				σ	0,15	0,36	0,07	0,89
	inner-1			average	1,64	3,97	0,40	9,90
				σ				
inner-2	average	1,29		3,39	0,42	8,15		
	σ	0,23		0,29	0,07	0,67		
Warp	filler-a	average		2,43	5,17	0,68	7,61	
		σ		0,10	0,47	0,05	0,47	
	filler-b	average		2,18	4,84	0,61	8,31	
		σ		0,20	0,69	0,11	2,36	
Biases	warp-a	average		1,46	3,04	0,55	5,52	
		σ		0,12	0,31	0,03	0,61	
	warp-b	average		1,56	3,56	0,53	6,74	
		σ		0,17	0,39	0,05	1,06	
	filler-a	average	1,66	2,86	0,81	3,71		
		σ	0,17	0,51	0,17	1,05		
	filler-b	average	1,53	3,06	0,60	5,29		
		σ	0,15	0,36	0,09	1,31		
Binder	filler-a	average	0,31	1,10	0,31	3,53		
		σ	0,03	0,02	0,00	0,07		

Table a.4: Preform thickness and the two unit cell dimensions measured for the sample-2 on four cut-planes.

	H [mm]		L _w [mm]		L _f [mm]	
	Average	σ	Average	σ	Average	σ
warp-a	5,73	0,07			8,96	0,24
warp-b	5,07	0,09			9,20	0,31
filler-a	5,29	0,36	9,38	0,41		
filler-b	5,57	0,36	9,69	0,19		

Sample-3

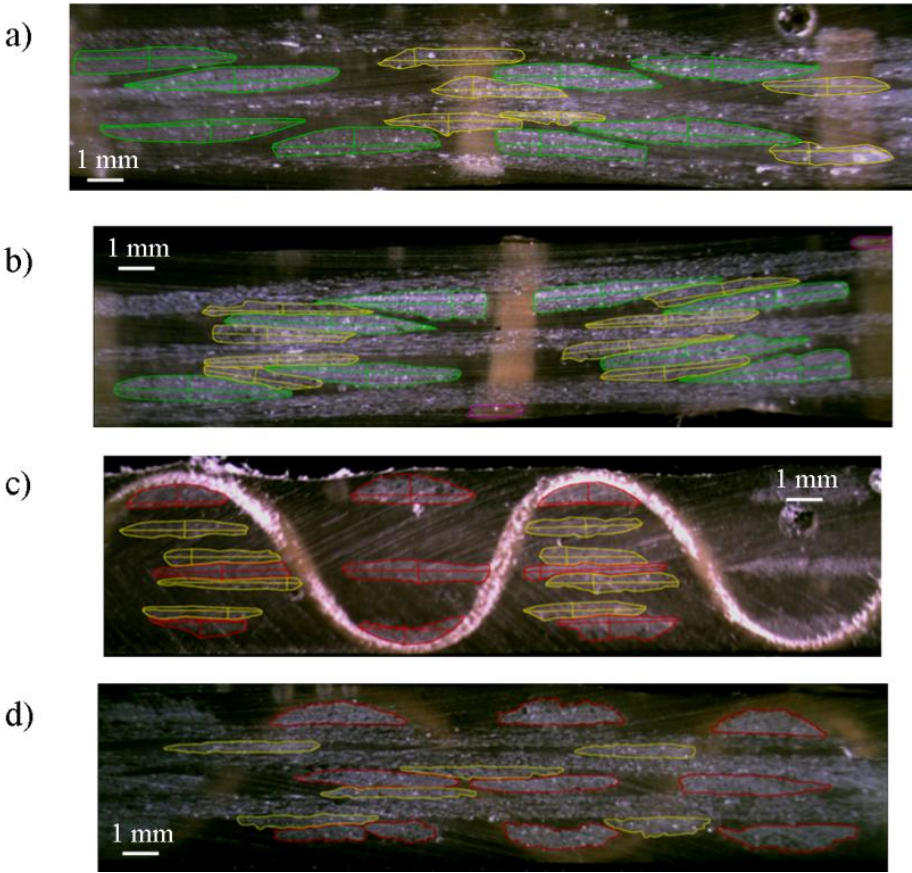


Figure a.3: Micrographs for the cross sections of the sample-3, green outline for warp, red outline for filler, yellow outline for biases and magenta outline for binder, a) at cut plane filler-a, b) at cut plane filler-b, c) at cut plane warp-a, d) at cut plane warp-b.

Table a,5: Mean and standard deviation of the measured parameters (width “l”, thickness “h”, area “S” and aspect ratio “AR”) at each cut plane of sample-3,

Yarn		Cut plane		S [mm ²]	l [mm]	h [mm]	AR	
Filler	outer Z 1	warp-a	average	1,22	0,59	2,70	4,55	
			σ	0,04	0,02	0,08	0,24	
	outer Z 2		average	1,18	0,54	2,53	4,75	
			σ	0,05	0,07	0,04	0,64	
	inner-1		average	1,20	0,37	3,77	10,32	
			σ	0,14	0,05	0,13	1,55	
	inner-2		average	1,73	0,53	4,08	7,98	
			σ	0,22	0,10	0,26	1,85	
	outer free		average	1,68	0,68	3,18	4,71	
			σ	0,14	0,07	0,08	0,38	
	outer		warp-b	average	1,78	3,61	0,62	6,05
				σ	0,36	0,58	0,11	1,81
	inner-1			average	1,59	4,29	0,44	9,74
				σ	0,14	0,41	0,03	1,63
inner-2	average	1,57		3,51	0,58	6,67		
	σ	0,43		0,34	0,21	2,94		
Warp	filler-a	average		2,25	0,67	4,85	7,72	
		σ		0,32	0,14	0,67	2,90	
	filler-b	average		2,16	0,58	4,98	8,84	
		σ		0,14	0,09	0,39	2,10	
Biases	warp-a	average		0,76	2,28	3,22	5,40	
		σ		0,10	0,25	0,35	1,48	
	warp-b	average		0,72	2,50	3,54	7,41	
		σ		0,10	0,39	0,56	2,23	
	filler-a	average	0,81	2,33	3,29	5,67		
		σ	0,06	0,28	0,39	1,21		
	filler-b	average	0,80	2,80	3,96	9,07		
		σ	0,28	1,00	1,42	3,70		
Binder	filler-a	average	0,35	0,26	1,60	6,51		
		σ	0,06	0,07	0,11	2,26		

Table a.6: The preform thickness and the two unit cell dimensions measured for the sample-3 on four cut-planes.

	H [mm]		L _w [mm]		L _f [mm]	
	Average	σ	Average	σ	Average	σ
warp-a	4,56	0,08			10,45	0,44
warp-b	3,81	0,14			10,39	0,31
filler-a	4,04	0,13	9,62	1,08		
filler-b	4,01	0,27	9,36	0,53		

Sample-4

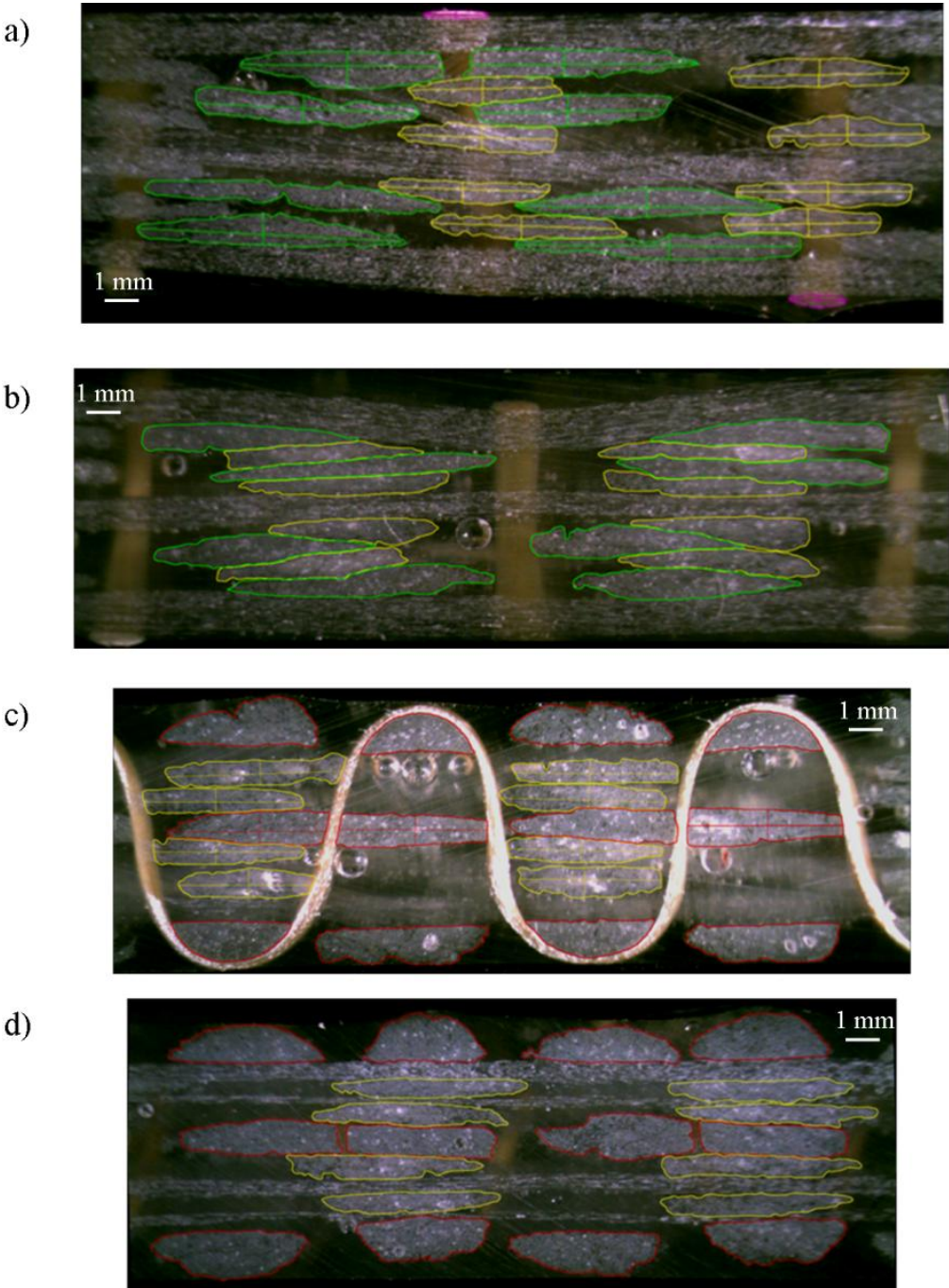


Figure a.4: Micrographs for the cross sections of the sample-4, green outline for warp, red outline for filler, yellow outline for biases and magenta outline for binder, a) at cut plane filler-a, b) at cut plane filler-b, c) at cut plane warp-a, d) at cut plane warp-b,

Table a.7: Mean and standard deviation of the measured parameters (width “l”, thickness “h”, area “S” and aspect ratio “AR”) at each cut plane of sample-4,

Yarn		Cut plane		S [mm ²]	l [mm]	h [mm]	AR	
Filler	outer Z 1	warp-a	average	2,81	3,49	1,02	3,42	
			σ	0,23	0,25	0,02	0,30	
	outer Z 2		average	2,76	3,29	1,12	2,95	
			σ	0,12	0,09	0,07	0,11	
	inner-1		average	3,67	4,73	0,87	5,50	
			σ	0,08	0,27	0,10	0,97	
	inner-2		average	3,83	4,36	0,87	4,99	
			σ	0,30	0,16	0,05	0,09	
	outer free		average	4,27	4,54	0,99	4,59	
			σ	0,13	0,19	0,04	0,39	
	outer		warp-b	average	3,75	3,96	1,17	3,41
				σ	0,41	0,36	0,12	0,47
	inner-1			average	3,49	4,35	1,10	4,05
				σ	0,31	0,06	0,21	0,83
inner-2	average	3,45		4,12	0,81	5,11		
	σ	0,03		0,04	0,03	0,24		
Warp	filler-a	average		3,93	7,10	0,74	9,98	
		σ		0,21	1,55	0,13	3,31	
	filler-b	average		3,43	6,27	0,70	9,14	
		σ		0,27	0,61	0,08	2,05	
Biases	warp-a	average		1,98	3,10	0,70	4,49	
		σ		0,15	0,25	0,08	0,77	
	warp-b	average		1,83	3,72	0,58	6,51	
		σ		0,12	0,18	0,05	0,62	
	filler-a	average	1,82	3,18	0,65	4,99		
		σ	0,19	0,25	0,07	0,79		
	filler-b	average	1,71	3,62	0,52	7,12		
		σ	0,13	0,25	0,08	1,39		
Binder	filler-a	average	0,35	1,60	0,26	6,51		
		σ	0,06	0,11	0,07	2,26		

Table a.8: Preform thickness and the two unit cell dimensions measured for the sample-4 on four cut-planes.

	H [mm]		L _w [mm]		L _f [mm]	
	Average	σ	Average	σ	Average	σ
warp-a	7,72	0,16			10,11	0,19
warp-b	7,07	0,08			9,83	0,04
filler-a	7,74	0,34	9,50	0,03		
filler-b	6,71	0,41	10,34	0,35		

Sample-5

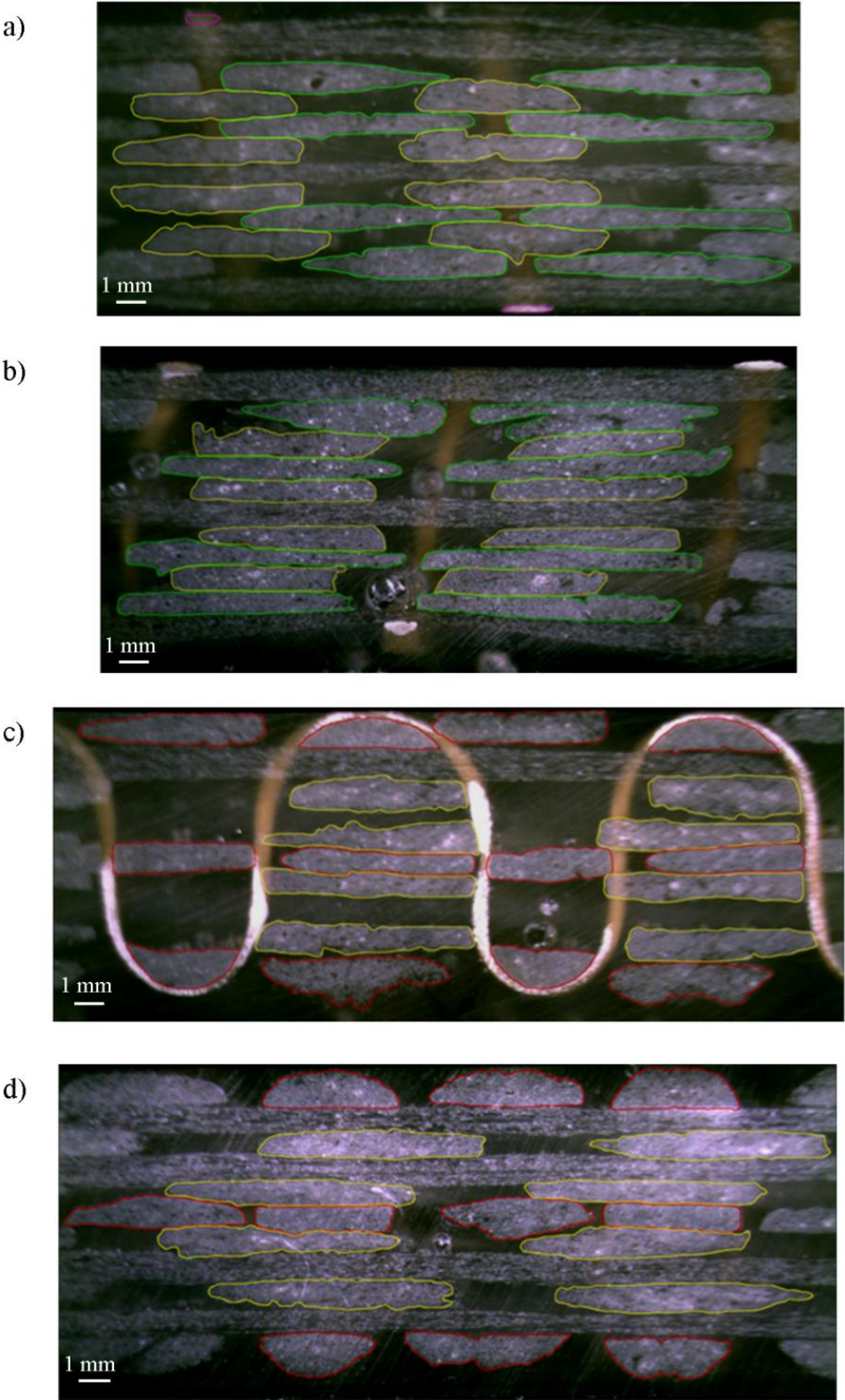


Figure a.5: Micrographs for the cross sections of the sample-5, green outline for warp, red outline for filler, yellow outline for biases and magenta outline for binder, a) at cut plane filler-a, b) at cut plane filler-b, c) at cut plane warp-a, d) at cut plane warp-b,

Table a.9: Mean and standard deviation of the measured parameters (width “l”, thickness “h”, area “S” and aspect ratio “AR”) at each cut plane of sample-5,

Yarn		Cut plane		S [mm ²]	l [mm]	h [mm]	AR	
Filler	outer Z 1	warp-a	average	2,83	4,07	0,92	4,45	
			σ	0,08	0,18	0,03	0,36	
	outer Z 2		average	2,90	3,15	1,13	2,79	
			σ	0,07	0,20	0,00	0,18	
	inner-1		average	3,57	4,07	0,96	4,27	
			σ	0,28	0,34	0,10	0,80	
	inner-2		average	3,65	5,34	0,62	8,74	
			σ	0,14	0,78	0,08	2,41	
	outer free		average	4,80	5,23	1,09	4,97	
			σ	0,43	0,44	0,21	1,13	
	outer		warp-b	average	3,69	4,06	1,12	3,69
				σ	0,25	0,55	0,11	0,78
inner-1	average	3,90		4,90	1,09	4,58		
	σ	0,03		0,43	0,13	0,95		
inner-2	average	3,08		4,10	0,73	5,64		
	σ	0,50		0,60	0,23	0,91		
Warp	filler-a	average		5,78	8,16	0,90	9,25	
		σ		0,25	0,73	0,12	1,82	
	filler-b	average		5,96	8,70	0,76	11,53	
		σ		0,54	0,69	0,08	1,84	
Biases	warp-a	average		3,29	4,26	0,83	5,24	
		σ		0,19	0,28	0,10	0,82	
	warp-b	average	3,51	5,08	0,81	6,35		
		σ	0,25	0,24	0,08	0,77		
	filler-a	average	3,69	4,33	0,91	4,78		
		σ	0,18	0,26	0,07	0,56		
	filler-b	average	3,13	4,24	0,75	5,73		
		σ	0,27	0,28	0,08	0,88		
Binder	filler-a	average	0,32	1,35	0,27	5,09		
		σ	0,01	0,34	0,05	2,14		

Table a.10: Preform thickness and the two unit cell dimensions measured for the sample-5 on four cut-planes

	H [mm]		L _w [mm]		L _f [mm]	
	Average	σ	Average	σ	Average	σ
warp-a	9,01	0,13			10,74	0,09
warp-b	9,37	0,10			10,32	0,46
filler-a	9,92	0,09	9,74	0,09		
filler-b	9,50	0,51	9,83	0,52		

Sample-5C

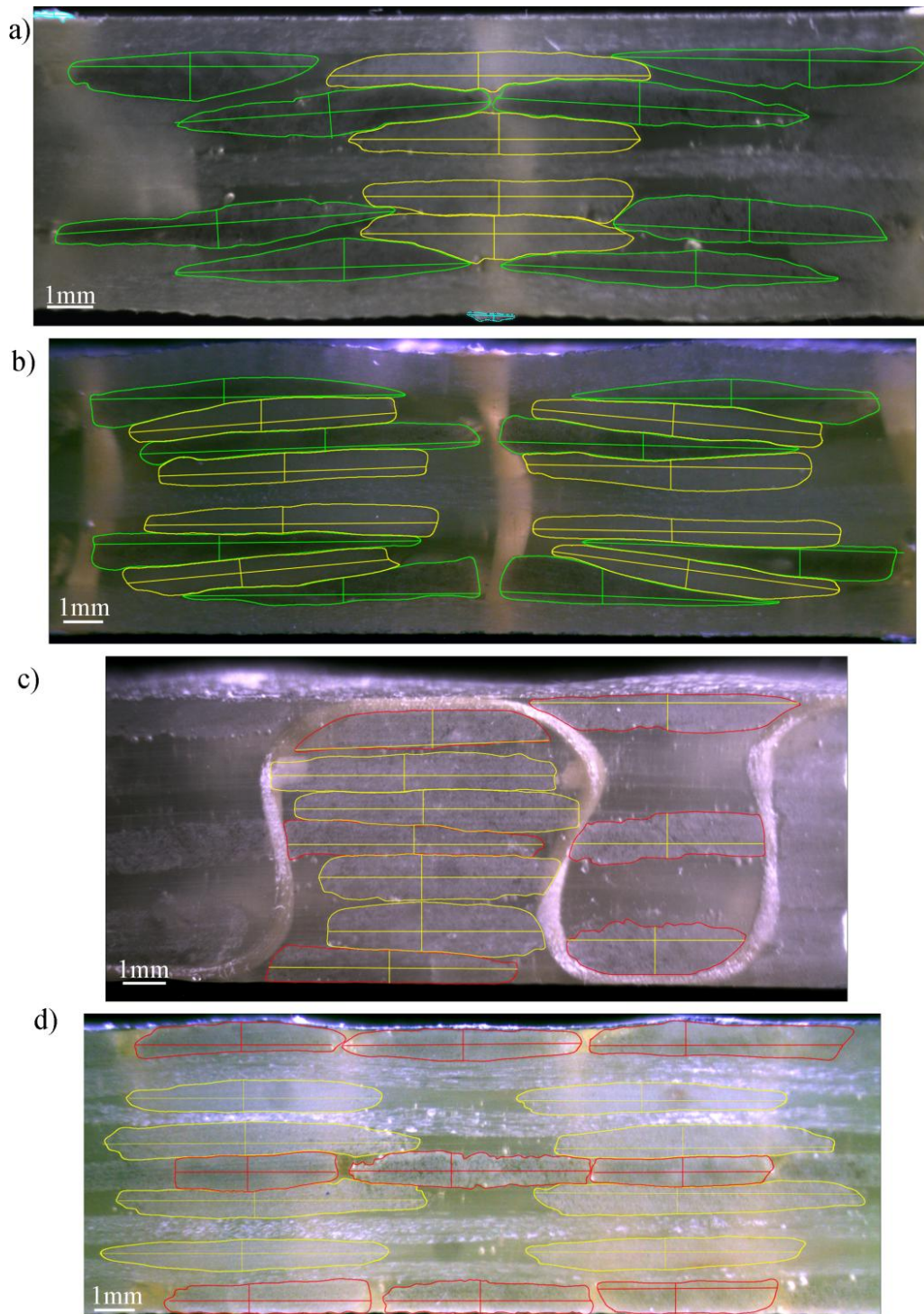


Figure a.6: Micrographs for the cross sections of the sample-5C (after impregnation), green outline for warp, red outline for filler, yellow outline for biases and magenta outline for binder, a) at cut plane filler-a, b) at cut plane filler-b, c) at cut plane warp-a, d) at cut plane warp-b,

Table a.11: Mean and standard deviation of the measured parameters (width “l”, thickness “h”, area “S” and aspect ratio “AR”) at each cut plane of sample-5C,

Yarn		Cut plane		S [mm ²]	l [mm]	h [mm]	AR	
Filler	outer Z 1	warp-a	average	2,72	4,26	0,70	6,07	
			σ	0,04	0,07	0,01	0,00	
	outer Z 2		average	2,89	3,60	0,94	3,85	
			σ					
	inner-1		average	3,03	5,77	0,48	12,14	
			σ	0,11	0,14	0,04	0,63	
	inner-2		average	3,22	3,33	1,02	3,25	
			σ					
	outer free		average	3,24	5,06	0,77	6,62	
			σ	0,18	0,16	0,06	0,56	
	outer		warp-b	average	3,25	4,90	0,71	6,94
				σ	0,17	0,46	0,04	0,57
	inner-1			average	3,82	5,63	0,81	6,92
				σ				
inner-2	average	2,78		3,94	0,74	5,38		
	σ	0,19		0,25	0,08	0,90		
Warp	filler-a	average		4,39	6,68	0,91	7,50	
		σ		0,35	0,78	0,10	1,54	
	filler-b	average		3,71	7,05	0,61	11,87	
		σ		0,20	0,50	0,09	2,26	
Biases	warp-a	average		3,01	4,13	0,78	5,34	
		σ		0,04	0,33	0,06	0,77	
	warp-b	average		2,86	4,60	0,71	6,58	
		σ		0,30	0,42	0,06	0,96	
	filler-a	average	3,21	4,63	0,85	5,51		
		σ	0,08	0,41	0,09	0,90		
	filler-b	average	2,85	4,73	0,63	7,58		
		σ	0,19	0,26	0,07	1,20		
Binder	filler-a	average	0,13	0,93	0,14	6,52		
		σ	0,02	0,3	0,07	1		

Table a.12: Preform thickness and the two unit cell dimensions measured for the sample-5 on four cut-planes

	H [mm]		L _w [mm]		L _f [mm]	
	Average	σ	Average	σ	Average	σ
warp-a	6,98	0,12			9,71	0,1
warp-b	7,02	0,10			9,64	0,28
filler-a	6,67	0,04	10,37	0,22		
filler-b	6,81	0,03	10,19	0,29		

Appendix A

Table a.13: Geometrical parameters of the constructed RVE for manufactured samples with rectangular cross section shape consideration.

		Sample-1	Sample-2	Sample-3	Sample-4	Sample-5	Sample-5C
Preform total thickness	H [mm]	6	5,92	4,37	7,72	9,71	6,99
Length of warp yarns in the unit cell	Lw [mm]	24,56	36,32	41,68	39,89	42	41,12
Length of filler yarns in the unit cell	Lf [mm]	33,96	56,40	56,94	59,53	58,87	58,08
Length of bias yarns in the unit cell	Lv [mm]	16,70	26,14	28,19	28,14	61,56	28,24
Length of binder yarns in the unit cell	Lb [mm]	15,13	17,67	16,33	22,04	27,06	23,62
areal density of the unit cell	S^{uc} [gr/cm ²]	0,46	0,38	0,27	0,62	0,86	0,85
Total volume of yarns	V_{yarns} [mm ³]	123,19	256,48	225,41	470,23	647,43	434,96
Volume of unit cell	V^{uc} [mm ³]	211,13	505,43	432,87	763,95	999,39	695
Fiber volume fraction-without considering Pf	FVF_volume [%]	58,35	50,75	52,07	61,55	64,78	62,56
Fiber volume fraction	FVF_weight [%]	29,77	25,18	24,25	31,41	25,65	45,47
rate of warp fiber volume to total fibers	V_{fw} [%]	41,23	34,79	44,38	30,88	37,55	35,29
rate of filler fiber volume to total fibers	V_{ff} [%]	35,56	31,89	33,50	45,58	31,77	32,06
rate of bias fiber (+θ) volume to total fibers	V_{fo} [%]	9,76	15,59	9,79	10,95	14,83	15,88
rate of binder fiber volume to total fibers	V_{fb} [%]	3,68	2,14	2,54	1,65	1,03	0,89

Publication

Articles in Journals

Labanieh A. R., Legrand X., Koncar V., Soulat D., 2014, Développement et optimisation de préformes tissées 3D-multiaxiales, Development and optimization of the 3D multiaxis woven performs, *Revue des composites et des matériaux avancés*, vol.: 24(1), p.: 111-124.

Labanieh A. R., Legrand X., Koncar V., Soulat D., 2014, Evaluation of the elastic behavior of multiaxis 3D-woven preforms by numerical approach. *Journal of Composite Materials*, vol.: 48(26), p.: 3243-3252.

Labanieh, A. R., Legrand X., Koncar V., Soulat D., 2013, Novel optimization method to estimate the geometrical properties of a multiaxial 3D woven preforms. *Journal of Reinforced Plastics and Composites*, vol.: 32, p.: 700-712.

Conference papers

Labanieh A. R., Legrand X., Koncar V., Soulat D., 2014, Development of the 3D multiaxis weaving technology and geometrical characterization of the produced performs, ECCM16 - 16TH European Conference On Composite Materials, Seville, Espagne.

Labanieh A. R., Legrand X., Koncar V., Soulat D., 2013, Development in the multiaxis 3D weaving technology, 4th ITMC Lille Metropole International Conference, ENSAIT, Roubaix, France.

Labanieh A. R., Legrand X., Koncar V., Soulat D., 2013, Conception and characterization of multiaxis 3D woven performs, TexComp-11, Leven, Belgium.

Labanieh A. R., Legrand X., Koncar V., Soulat D., 2013, Développement et optimisation de préformes tissées 3D-multiaxiales, JNC 18 - Ecole Centrale Nantes, France.

Labanieh A. R., Legrand X., Koncar V., Soulat D., 2012, Evaluation of stiffness properties of 3D multi-axial woven composites, 12th World Textile Conference AUTEX, p.: 1523, Zadar, Croatia.

Development of 3D multiaxis woven Preform for composites structures. Technology, modelling and optimisation

Abstract: 3D weaving technology is developed in response to the poor delamination resistance of laminated composite structures by insertion through the thickness fibre reinforcements. However, this technology is limited relatively to a possibility to insert in-plane yarns oriented other than 0° and 90° . This results in reduction of the in-plane off axis tensile properties and the in-plane shear resistance. Therefore, 3D multiaxis weaving technology has been developed in order to enable this insertion. In the thesis, a novel technique able to produce 3D multiaxis woven preforms is presented with the possibility to control the sequencing of yarn layers. The constitutive yarns and unit cell parameters of the produced samples have been measured with investigation of yarns geometry (cross section shape and path) within the structure, by analyzing the captured micrographs for the samples cross section. Predictive geometrical model has been developed. This model is indispensable design tool providing approximate estimation of the geometrical properties of the dry preforms and composites. Moreover, a geometric modelling approach is improved helping to construct an RVE of this structure as accurate as possible based on the elaborated geometrical characterization. Based on the developed RVE, a mechanical modelling has been also improved and completed using the finite element method serving firstly, to evaluate the bias yarns effect on the elastic stiffness and in-plane off-axis properties in comparison with equivalent 3D orthogonal woven composite. Secondly, it helps to investigate the influence of the in-plane layers sequence on the induced interlaminare stresses at the composite free edges.

Keywords: 3D fibre reinforced composite, 3D multiaxis weaving, geometrical characterization, geometrical modelling, finite element, homogenisation.

Résumé: La technologie de tissage 3D a été développée comme une réponse à la faible résistance au délaminage des structures de composite stratifiées en insérant des renforts fibreux dans l'épaisseur de la structure. Pourtant, cette technologie ne permet pas de positionner des fibres dans le plan autre que dans les directions à 0° et 90° . Cela implique de faibles résistances au cisaillement dans le plan. Pour cela une technologie de tissage 3D multiaxial a été développée permettant une insertion de fils dans d'autres orientations du plan. Dans cette thèse, une nouvelle technique dédiée à produire des préformes 3D multiaxial tissées avec la possibilité de contrôler l'ordre des couches est présentée. Les paramètres des fils constitutifs et de la cellule unitaire des échantillons fabriqués sont mesurés avec l'investigation de la géométrie des fils (section et trajectoire) au sein de la structure. Associé à ces développements expérimentaux, un modèle géométrique, en tant qu'outil de conception permettant de décrire les préformes élaborées, a été développé. Cette modélisation géométrique permet de générer un VER, à l'échelle mésoscopique de la structure. Afin d'évaluer l'influence de ces préformes 3D sur les caractéristiques mécaniques, une chaîne numérique par éléments finis a été mise en place afin de calculer le comportement élastique équivalent. Les résultats sur les propriétés élastiques permettent de quantifier l'apport des fils dans le plan, comparativement aux structures 3D tissées. L'influence de l'ordre des couches dans l'épaisseur est également mis en évidence sur la minimisation des contraintes interlaminaires sur les dans le composite.

Mots clés: renfort fibreux, tissage 3D multiaxial, caractérisation géométrique, modélisation géométrique, élément finis, homogénéisation.